The Hamburg Ocean-Atmosphere Parameters and Fluxes from Satellite Data (HOAPS):
A Climatological Atlas of Satellite-Derived
Air-Sea Interaction Parameters over the World Oceans

by

H. Grassl[1,2], V. Jost[2], J. Schulz[3]
M. R. Ramesh Kumar[3,4], P. Bauer[5], and P. Schluessel[2]

[1] Max-Planck-Institute for Meteorology, Hamburg Germany

[2] Meteorological Institute, University of Hamburg, Germany.

[3] German Aerospace Centre, Cologne, Germany.

[4] National Institute of Oceanography, Dona Paula, Goa, India.

[5] ECMWF, Reading, UK

7 November 2000

Table of Contents

Abstract

The present atlas is based on the newly available data set known as the Hamburg Ocean Atmosphere Parameters and Fluxes from Satellite Data (HOAPS), for the global oceans. It presents the basic fields of air-sea interaction parameters such as sea surface temperature, specific humidity at air and sea surface temperature, difference in humidity, Dalton number, wind speed and the air sea fluxes such as latent heat, sensible heat and longwave radiation. The atlas also provides the hydrological cycle parameters over the global oceans such as evaporation, precipitation and freshwater flux. The data set covers the period July 1987 to December 1998 and provides the mean monthly, seasonal and annual fields of different variables. It is intended to provide a climatological data base for scientists and students in the field of climatology, meteorology, oceanography, and air-sea interaction. The document describes the various satellite sensors used and details the method by which the fluxes are derived from those satellite data. This printed atlas is accompanied by a CD-ROM containing the data of all individual monthly averages of the considered parameters as well as the figures and this text.

Fields with higher temporal and spatial resolution are also freely available to interested users for non-commercial scientific research. For details of how to access the fields see: http://www.mpimet.mpg.de/Depts/Physik/HOAPS.

Chapter I   Introduction

Oceans play a very important role in the global climate system. They absorb most of the incoming shortwave solar radiation entering the earth atmosphere system and redistribute heat and energy with the oceanic environment by both horizontal and vertical oceanic movements. This energy is then further transported back into the atmosphere in the form of energy fluxes such as latent and sensible heat fluxes, and longwave radiation, which are the main sources of energy for the atmospheric circulation. The tropical oceans are the regions of net radiation gain. This excess energy is transported to higher latitudes by the atmosphere and the oceans to maintain the energy balance. Further, the tropical oceans are the regions where active air-sea interaction processes such as Monsoons, El Niño and Southern Oscillations take place. Thus the study of air-sea interaction parameters, fluxes and the hydrological cycle of the global oceans is quite important for our understanding of climate variability. Of the three major oceans, the Pacific Ocean has the largest longitudinal extension reaching over 140°. On the western part of the Pacific Ocean, there exists one of the warmest regions in the world, the so called warmpool, in the eastern equatorial Pacific, a well developed cold tongue extends towards the west. This large thermal gradient and the corresponding atmospheric circulation over this region has profound influence on the global weather and climate.

In the past, several authors have made important contributions in the form of atlases mostly using ship data (Baumgartner and Reichel, 1975; Hastenrath and Lamb, 1977, 1978, 1979a; and 1979b; Isemer and Hasse, 1987; Oberhuber, 1988; da Silva et al., 1994; Josey et al., 1999). All the above studies have provided useful information on the various aspects of air-sea interaction parameters and fluxes. But the major drawback of most of these studies has been scarcity of data over large regions such as the Indian Ocean and the Southern Ocean. Typically satellite data sets have a much better spatial as well as temporal resolution than ship data which is quite important for computing monthly averages.

Over the past decade there has been significant progress in the development of remote sensing methods to determine atmospheric and oceanic parameters from data of the Special Sensor Microwave/Imager (SSM/I) and the Advanced Very High Resolution Radiometer (AVHRR) that are of sufficient accuracy for the parameterisation of energy and freshwater fluxes at the sea surface. The operational application of recently developed retrieval schemes to data of these two radiometers results in this new atlas called the Hamburg Ocean Atmosphere Parameters and Fluxes from Satellite Data (HOAPS). HOAPS covers a period of 12.5 years from the beginning of the SSM/I data record in July 1987 to December 1998. The present climatology is subdivided in three parts: basic state variables, energy fluxes, and water balance components. It consists of global fields of sea surface temperature, saturation specific humidity at sea surface temperature, specific air humidity, the humidity difference, wind speed, the Dalton number used for the parameterisation of latent heat flux, latent heat flux, sensible heat flux, net longwave radiation at the surface, evaporation, rainfall, and the freshwater flux computed as their difference.

In this atlas we are presenting monthly averages of 1° latitude and longitude resolution in addition to seasonal and annual means. The seasonal means of winter, spring, summer and autumn are representative of the mean of December, January, February (DJF); March,

April, May (MAM); June, July, August (JJA), and September, October, November (SON), respectively.

Chapter II describes the necessary parameterisations and used retrievals and gives a rational for their use. Chapter III is devoted to the basic state variables such as sea surface temperature; specific humidity at sea surface temperature; surface specific air humidity; difference in humidity; Dalton number and wind speed. In Chapter IV, the air-sea fluxes such as latent and sensible heat fluxes and longwave radiation net flux are presented. Chapter V describes the hydrological cycle parameters evaporation, rainfall, and freshwater flux. A brief summary is presented in Chapter VI.

Chapter II   Data and Methodology

II.1. Data sources and quality control

To derive a climatology from satellite data major demands on the used instruments are that they must deliver accurate and stable measurements over a long time which is only achievable with an on-board calibration or algorithms that consider the aging of a certain radiometer. Additionally, the swath width must be large enough to sample the earths surface during a couple of days. The classical instruments that cover those demands are the Advanced Very High Resolution Radiometer (AVHRR) and the Special Sensor Microwave/Imager (SSM/I). Measurements of sea surface temperature are most suitable in the infrared range where the surface has a high emissivity. On the other hand this high emissivity prevents the extraction of wind speeds or near surface atmospheric humidity with high accuracy from infrared measurements. For those parameters the microwave spectral range is much better suited since the ocean surface emissivity is rather small in the microwave spectral range compared to the infrared. A disadvantage of this physical constraints for the construction of the climatology was that up to the Tropical Rainfall Measuring Mission (TRMM) no satellite with both above mentioned types of radiometers has been launched. So any estimate of parameterized quantities like latent heat flux will suffer from the lack of simultaneity. However, it is expected that this error is rather small because the sea surface temperature is a relative inert quantity compared to the atmospheric variables derived from SSM/I measurements.

a. AVHRR

The AVHRR is flown on board the Polar Orbiting Environmental Satellites (POES), also known as NOAA satellites. Main characteristics like the available channels and geometrical features of the AVHRR are shown in Table 1. The infrared window channels are best suited for estimates of sea surface temperature in cloud free cases. Despite the broad swath a complete coverage of the earths surface is achieved within one or two weeks depending on the actual cloud coverage. Some problematic regions with almost persistent cloud coverage are the extended stratocumulus fields to the west of Africa, the Inter Tropical Convergence Zone (ITCZ), and arctic and antarctic regions during winter. Therefore, the quality of an estimation of sea surface temperature is highly dependent on

the quality of the used aerosol and cloud detection schemes. A description of errors occurring in sea surface temperature by different quality of cloud detection during day and night can be found in Reynolds (1993). If measurements of the sea surface temperature are hampered for weeks by persistent cloudiness or long periods of darkness as over polar regions the estimates could be biased through the more difficult cloud detection in the infrared range. What consequences this has on the combination of AVHRR and SSM/I is not fully explored.

Table 1: AVHRR radiometer characteristics

channel	wavelength (μm)	spatial resolution (mrad)
1	0.58 - 0.68	1.39
2	0.725 - 1.1	1.41
3	3.55 - 3.93	1.51
4	10.3 - 11.3	1.41
5	11.5 - 12.5	1.30
S/N (channels 1, 2)[a]	3 at 0.5% reflectivity	
NE ΔT (channels 3 - 5)[b]	0.12 K	
scan angle	± 55.4°	
pixels per line	2048	
swath width	~ 3000 km	
scan rate	1 line per 1/6 s	
integration time	20 μs	
calibration	internal black body and space view	

    a. S/N, **signal to noise ratio**
    b. NE ΔT, **noise equivalent temperature difference**

Because of the amount of AVHRR raw data at the best resolution and the resulting problems of handling such big data set it was decided to use the NOAA/NASA Oceans Pathfinder sea surface temperature product (http://podaac.jpl.nasa.gov/sst). This product is freely available and delivers daily fields of gridded sea surface temperature with a spatial resolution of $(9 \text{ km})^2$, but with significant data gaps in the geographical distribution due to the cloud problem. The consequence is that for constructing the flux climatology only sea surface temperature maps averaged over one week have been used.

b. SSM/I

One of the most advanced sensors for monitoring winds, atmospheric humidity, and rainfall is the SSM/I aboard the satellites of the Defense Meteorological Satellite Program (DMSP). The SSM/I is a passive microwave radiometer measuring emitted and reflected radiation from the Earth's surface and the atmosphere at four frequencies 19.35, 22.235, 37.0, and 85.5 GHz at vertical and horizontal polarisation as indicated in Table 2. The SSM/I instrument scans conically at a constant scan angle of 45° that corresponds to an Earth incidence angle of 53.1°. The swath width of almost 1400 km is only half that of the AVHRR. However, this is sufficient to

cover 82% of the earth surface in 24 hours. Figure II.1 shows the daily coverage of one SSM/I. The data gaps north and south of the equator are covered through the east-west shift of the DMSP satellite orbit so that full global coverage is obtained within three days.

Table 2: SSM/I radiometer characteristics

channel	frequency (GHz)[a]	NE ΔT (K)[b]	spatial resolution (km)[c]
1	19.35 v	0.35	43 x 69
2	19.35 h	0.35	43 x 69
3	22.235 v	0.60	40 x 50
4	37.0 v	0.30	29 x 37
5	37.0 h	0.30	29 x 37
6	85.5 v	0.70	13 x 15
7	85.5 h	0.60	13 x 15
scan angle	45° (i.e. zenith angle of 53°)		
pixels per line	128 at 85.5 GHz, 64 at lower frequencies		
swath width	1394 km, conical scan		
scan rate	1 line per 1.9 s		
calibration	internal black body and space view		

a. v, vertical polarisation; h, horizontal polarisation
b. NE ΔT, noise-equivalent temperature difference
c. 3 dB footprint
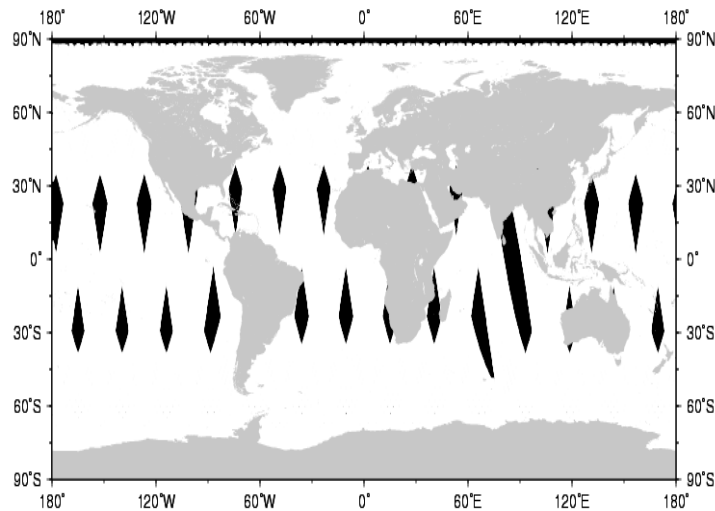
Figure II.1: Typical daily coverage with data from one SSM/I over oceans. Black areas are not covered.

SSM/I data are sampled every 25 km (A-Scan) at the three lower frequencies and every 12.5 km (B-Scan) at 85 GHz. All retrievals used in this study fall back upon the A-scan data and do not consider effects through different ground resolution at different frequencies. Some more characteristics of the SSM/I instrument are listed in Table 2 whereas a detailed description can be found in Hollinger et al. (1987).

Table 3: DMSP satellite equator crossing times and time periods of their use within the HOAPS climatology.

Satellite	Approx. Equatorial crossing times (UTC)	Time period
DMSP F-8	0615/1815	July 1987 - December 1990
DMSP F-10	0830/2030	January 1991 - December 1991
DMSP F-11	0530/1730	January 1992 - December 1998

SSM/Is have been flown on different DMSP satellites since July 1987. For the construction of HOAPS data from the DMSP satellites F8, F10 and F11 have been used for periods indicated in Table 3. The three satellites have different orbits that cause different local observing times throughout the period covered by the climatology.

The SSM/I data used have been the so called compact antenna temperature tapes (Remote Sensing Systems, F. Wentz) which contain the SSM/I brightness temperature data set with the highest consistency. In order to remove defective data (caused by wrong geocoding or calibration errors) in an early stage of the procedure we checked the brightness temperatures with a routine described by Wentz (1991). Furthermore, depending on the respective satellite the SSM/I brightness temperatures were corrected with regard to the different scan angle deviations (Fuhrhop and Simmer, 1996).

II.2. Parameterisations and Retrieval Schemes

As a sort of review this section describes the used parameterisations, satellite retrievals, and empirical assumptions that have been used to build the present climatology. The kind of assumptions that have been made influence the accuracies of the derived fluxes in different ways.

a. Parameterisations

Turbulent heat fluxes

Latent and sensible heat fluxes are parameterised using the bulk aerodynamic approach given by:

$$Q_L = \rho L_E C_E U (q_s - q_a)$$
$$Q_S = \rho c_p C_T U (T_s - \theta_a)$$

(1)

where ρ is the air density, c_p is the specific heat of air at constant pressure, U is the wind speed, L_E is the latent heat of evaporation, C_T is the Stanton number, C_E is the Dalton number, T_s is sea surface temperature, θ_a is the potential air temperature, q_s is the saturation specific humidity at the surface, and q_a is the specific humidity at the atmospheric measurement level (10m). The evaporation rate is then simply given by:

$$E = Q_L / (L_E \rho_0) \tag{2}$$

where ρ_0 is the freshwater density (as a function of temperature). Major components of (1) like U, T_S, and q_a are derivable from satellite data as described in section II.2.b or can be diagnosed from those like q_S. All other variables have to be chosen empirically or inserted from other sources like re-analyses, in situ data, or alternative satellite data. The use of re-analyses data might be superior to empirical assumptions but prevents a model independent determination of the energy fluxes. Schulz et al. (1997) discussed the errors that were introduced using a constant pressure and different assumptions for the not measurable surface air temperature within the bulk approach. Errors in surface pressure compensate each other through their contrary effect on q_S and ρ. Errors in T_a have a twofold effect; they directly enter the equation for the sensible heat flux and they alter the values of the transfer coefficients in all flux equations. In the present version a constant relative humidity of 80% has been assumed to compute the surface air temperature from the measured atmospheric specific humidity. The fixed relative humidity leads to a positive (negative) bias in the sensible heat flux where the actual humidity is higher (lower) than 80%. The Stanton and Dalton numbers or transfer coefficients are computed following the approach of Smith (1988). The 80% humidity assumption can cause large errors in the transfer coefficients in regions where the atmospheric surface layer is strongly stable stratified and may lead to totally erroneous values for the sensible heat flux. If conditions are more unstable then assumed errors in the transfer coefficients are in the order of 10% for moderate wind speeds (Schulz et al., 1997) and much lesser for high wind speeds because the stability dependence is no longer important.

Longwave net flux

The longwave net flux R_L at the sea surface is computed from the atmospheric back radiation $R_L^{\downarrow}$ and the sea surface temperature T_S:

$$R_L = \bar{\varepsilon} R_L^{\downarrow} - \bar{\varepsilon} \sigma T_S^4 \tag{3}$$

where $\bar{\varepsilon}$ is the spectrally integrated surface emissivity (which is close to 0.89, Gardashov et al., 1988) and σ is the Stefan-Boltzmann constant.

b. Retrieval Schemes

Sea surface temperature

As mentioned in section a. we decided to use the NOAA/NASA Oceans Pathfinder Sea Surface Temperature product instead of the widely used optimum interpolated sea surface temperature from Reynolds and Smith (1994) to establish a climatology that is based exclusively on satellite data. The pathfinder product is based on the use of different AVHRR sensors on different platforms. The used algorithm is essentially the non linear algorithm of Walton (1988) with a correction term for the sensor calibration drift with time. Issues that are still not resolved in this data set are that no independent water vapour data set, e.g. SSM/I data, have been used to

further correct the influence of water vapour on the retrieval as indicated by Emery et al. (1994) and secondly that it is not considered that any radiometer measures the ocean skin temperature and not the bulk temperature as pointed out by Schluessel et al. (1990). The influence of an additional explicit water vapour correction on the accuracy of the retrieval is not fully explored over the whole time series but it can have significant impact on the results especially for tropical atmospheres. The second point can be seen somewhat more relaxed since inaccuracies in the atmospheric humidity and wind speed estimates contribute much stronger to the flux error budget than the neglected bulk-skin temperature difference does.

Specific air humidity

To obtain the specific air humidity at the reference level of 10 m an algorithm of Schluessel et al. (1995) has been employed. This algorithm is based on an older two-step regression method of Schulz et al. (1993) which uses SSM/I frequencies at 19, 22, and 37 GHz to estimate the integrated water vapour content of the atmospheric boundary layer w_B and relate that to the specific humidity at the reference level. The method of Schluessel et al. (1995) improves that technique slightly in obtaining the specific humidity directly from the brightness temperatures which avoids the error propagation that occurs in the two-step method. Additionally it corrects a negative humidity bias in the Arctic Ocean. The theoretical standard error for this globally valid retrieval is stated to be 1.1 g kg^{-1} for an instantaneous SSM/I measurement. Schulz et al. (1997) have shown in comprehensive comparisons to ship measured q_a that this retrieval works very well. Nevertheless in comparisons to TOGA-COARE data some systematic underestimations of q_a occur that might be related to the mid-tropospheric humidity. Schulz et al. (1997) reported that the correlation between the surface q_a and the water vapour content in the lowest 500 m of the atmosphere is much lower than for extra tropical atmospheric conditions.

Recently, some alternatives to the used technique have been reported by Chou et al. (1995 and 1997). They estimate q_a from the total water vapour content W and w_B using an EOF (empirical orthogonal function) method using different EOFs for six classes of W. The reached accuracy for q_a differs not much from our method since the weights for w_B in the EOF analysis are two orders of magnitude larger than that for W. Some corrections of dry and wet biases at the low and high end of the humidity spectrum have been introduced, respectively. At the low end Chou et al. (1997) used only W within the EOF analysis to correct for an underestimation of q_a during wintertime over extra tropical oceans. Such a correction is not necessary for the direct retrieval of Schluessel et al. (1995) since the radiosonde data set that have been used for the radiative transfer calculations contained much more dry humidity profiles and gives those profiles a larger weight in the regression analysis. The other correction of Chou et al. (1997) concerns a positive humidity bias during summer in regions where warm air moves over a colder ocean surface. In those cases they constrained the surface air humidity to the saturation humidity at sea surface temperature. A side effect of this is that in each case with an overestimated w_B a positive bias will be automatically corrected for. This correction has also been adopted in the climatology presented here.

Surface wind speed

Because the wind induced ocean surface roughness and the foam coverage at high wind speeds modify the radiation field at passive microwave frequencies the estimation of wind speeds using SSM/I data is possible.

For estimations of wind speed the retrieval of Schluessel and Luthardt (1991) with improvements described by Schluessel (1995) has been used. This retrieval is based on radiative transfer simulations with subsequent linear regression between the simulated brightness temperatures and the given wind speeds. The algorithm employs the three lower frequencies of the SSMI/I where the main predictor is the polarisation difference at 37 GHz. The other frequencies are used to correct for atmospheric influences. The method discriminates between rain free, light rain and strong rain situations where in the latter case no wind speed can be retrieved.

The theoretical accuracy of the method is 1.4 m s^{-1} for rain free and 1.6 m s^{-1} for light rain situations (Schluessel, 1995). Taurat (1996) compared this method together with other passive microwave retrievals published by Goodberlet et al. (1989) and Stogryn et al. (1994) as well as scatterometer measurements from the ERS-1 satellite to ECMWF analysis data and ship measurements in the North Atlantic. The performance of the passive microwave algorithms is very similar and biases are obtained for wind speeds larger than approximately 15 m s^{-1}. Standard deviations between satellite and in situ measurements are close to 2 m s^{-1}.

Downwelling longwave radiation

Schluessel et al. (1995) described a retrieval scheme of the atmospheric back radiation under clear and cloudy conditions from SSM/I measurements using three channels at 22, 37, and 85 GHz. This retrieval scheme is based on the following consideration: about 80% of the downwelling radiation is emitted from the lowest 500 m of the atmosphere (Schmetz, 1989) and is mostly emitted in the water vapour bands near 6.3 µm and above 20 µm, and to a lesser extent in the CO_2 band at 15 µm. As shown by Schulz et al. (1993) the SSM/I measurements contain information on the boundary layer water vapour content. Schluessel et al. (1995) conclude that the radiation emerging from the lower 500 m should be proportional to the product of the mean layer temperature and the absorption by the water vapour of that layer, since the emitted flux density is proportional to the fourth power of the temperature according to the Stefan-Boltzmann law. Radiative transport calculations then showed that functions f_1 and f_2 are in fact closely correlated:

$$f_1(T_{22v}, T_{37h}) = \sigma(T_{22v}^4 - T_{37h}^4) \propto f_2(T_S, w_B) = \sigma T_S^4(1 - e^{-w_B}) \tag{4}$$

where T_{22v} and T_{37h} are the brightness temperatures for the 22 GHz vertically polarised and 37 GHz horizontally polarised channels, respectively.

The RMS error for the retrieval scheme has been theoretically estimated to be 30 Wm^{-2} on the instantaneous time scale. It has been partly validated using simultaneously obtained pyrgeometer measurements, radiosonde data and cloud observations from the TOGA-COARE and CEPEX experiments. The radiosonde data and the cloud observations have been used within

radiative transfer simulations as another means for comparison. Considering hourly means, Schanz and Schluessel (1997) stated a bias of -3 Wm^{-2} and a standard deviation of 14 Wm^{-2} for the comparison of pyrgeometer measurements and satellite retrieval and a bias of +3 Wm^{-2} and the same standard deviation for the comparison of radiative transfer simulations with satellite retrieval. For monthly averages a RMS error less than 10 Wm^{-2} is expected.

Combining the back-radiation retrieval with AVHRR derived sea surface temperature using equation (3) gives the net flux at the sea surface.

Rainfall

The derivation of global precipitation fields is only possible if satellite measurements are employed. The number of surface based rain gauges or radar sites is simply too low to derive fields from such data. Because of this many algorithms for rainfall estimation employing infrared and passive microwave (PMW) satellite measurements have been developed.

Estimates from infrared measurements are based on an empirical correlation between the rain rate at the surface and the cloud top temperature. Arkin (1979) and Arkin and Meisner (1987) applied this technique to measurements of the GOES (Geostationary Operational Environmental Satellite) satellite series and were able to produce 8 maps per day of the GPI (GOES precipitation index) over the area 40°S - 40°N covered by geostationary satellites.

On the contrary to infrared rainfall estimates, estimates from passive microwave radiation measurements are based on the interaction of the radiation field and the precipitation elements. Two basic approaches can be distinguished, the so called emission and scattering estimates. Emission estimates make use of the strong contrast of brightness temperatures at low frequencies (e.g. 19 GHz) caused by the emission from cloud and rain particles compared to the radiometrically relative cold surface. This method is even suitable for detecting light rain. Scattering estimates employ the strong decrease of brightness temperatures at high frequencies (e.g. 85 GHz) which is caused by scattering of radiation by cloud and rain drops as well as ice particles.

The Algorithm Intercomparison Project-3 (AIP-3) conducted by the Global Precipitation Climatology Project (Ebert, 1996) has revealed that on an instantaneous basis the passive microwave algorithms perform much better than infrared or mixed IR/PMW algorithms which is documented by significant differences in spatial correlation. So one of the advantages of PMW retrievals is obviously the rain detection. Certainly, for climatological aspects the quality of monthly mean values is more important. Results from Ebert et al. (1998) concerning AIP-3 indicate that algorithms using geostationary data have slightly higher correlations than PMW algorithms. But due to the small sample size (AIP-3 uses data from the Tropical Ocean Global Atmosphere Coupled Ocean Atmosphere Response Experiment which lasted from Nov. 1992 to February 1993 in the tropical West Pacific) the differences in correlation among IR and PMW algorithms is not significant so that only a few algorithms with very low spatial and time correlations can be discarded. Another comparison study called Precipitation Intercomparison Project 2 (PIP-2) conducted by the WetNet programme focussed only on PMW algorithms and on instantaneous rain rates. Results and major conclusions of this project are described in Smith et al. (1998). Different to the AIP-3 project it was stated that the results are not conclusive with respect to performance against an exact calibration standard, since the validation data used in PIP-2 are not of the quality as in AIP-3.

Since we had to chose one algorithm for the use in our climatology we apply the winner-looser system of PIP-2 (Smith et al., 1998) to the AIP-3 results for instantaneous and quasi monthly averages because the AIP-3 is the most comprehensive intercomparison study with probably the best validation data. This gave an indication which algorithm might be best suited for the climatology at least in the case of tropical rainfall situations. The final ranking procedure uses the bias, adjusted RMS, and correlation coefficient as measures of the performance of the algorithms. It turns out that the algorithm of Bauer and Schluessel (1993) is on position six at the instantaneous time scale and on position nine at the monthly time scale. If only bias and adjusted RMS are considered the algorithm climbs to the third position at monthly time scale with only two physical iterative algorithms in front, one based on Wilheit et al. (1991) and the other one is the high resolution version of the FSU profile algorithm (Smith et al., 1994). These two algorithms are not adequate for processing a ten year time series since they have too heavy computer demands. The consideration of bias and adjusted RMS only for the ranking is justified by the fact that for almost all SSM/I algorithms in AIP-3 the correlation coefficients are statistically not different.

The Bauer algorithm is of the type called physical rain map algorithm which use an 8-stream adding-doubling radiative transfer model and a conceptual cloud model to create a database from which a relationship between surface rain rates and brightness temperatures at 19, 22, and 85 GHz is accomplished by non-linear regression analysis. Beam filling is considered by randomly defining partial cloud cover within the beam patterns, allowing the regression analysis to find the optimum fit of rain rates and brightness temperatures.

The cutoff threshold for the algorithm is 0.3 mm h^{-1} so that any estimate lower than that is set to zero. The accuracy is estimated to be 0.5 mm h^{-1} (Bauer and Schluessel, 1993).

Because of the early degradation of the 85 GHz channel aboard the DMSP-F8 satellite in January 1989 an alternative retrieval scheme only employing lower frequencies has been used from January 1989 until the launch of DMSP-F10 in January 1991. Schluessel (1995) showed that despite the larger error an estimation of rainfall for climatological purposes remains possible.

Sea-ice coverage

Since all retrieval schemes described above work only over open oceans, sea ice and land surfaces have to be excluded from the analysis. While it is easy to smash out land surfaces one has to use a special retrieval scheme to determine if the surface is covered by ice or not. Within this climatology the NASA team sea ice algorithm that determines first, multi year, and total ice concentration has been used. It is based on algorithms developed for the Scanning Multi-channel Microwave Radiometer by Cavalieri et al. (1984) and Gloersen and Cavalieri (1986). The adjustment of the method to the SSM/I is described in Cavalieri et al. (1991). The accuracy of this retrieval varies with seasons and is most critical during summer when the ice surface is covered by melting ponds. This can lead to large errors in the derived quantities, because then the emissivity within a SSM/I pixel is much higher than that of open water. Therefore the criteria for flagging a grid box ice covered or not has to be done very carefully. The averaging procedure for temporary ice covered grid boxes is described in the next section.

II.3. Operational Application

In this subsection the operational application of the retrieval schemes is briefly explained. The fields of sea surface temperature are available as daily fields with a spatial resolution of $(9 \text{ km})^2$. These daily fields are averaged over 5 days and projected onto a regular grid with a resolution of $0.25° \times \times \pm \times \times 0.25°$. Remaining data gaps are closed using a distance weighted interpolation scheme including adjacent measurements. If, after the interpolation procedure, data gaps remain the monthly average is filled in. For the determination of quasi instantaneous parameters from SSM/I measurements that need T_S values (e.g. the bulk parameterisation) the pentad mean T_S of the grid box where the SSM/I footprint is located has been used.

As the passive microwave retrieval schemes are only applicable over open ocean any contamination with land and ice surfaces has to be avoided. This is achieved by using an enlarged land mask so that SSM/I retrievals are performed not closer than 50 km to the coastline. Ice surfaces are excluded using the scheme provided by Cavalieri et al. (1991). Each SSM/I measurement with an ice concentration $> 0\%$ is rejected. The remaining pixels can then be used for the retrieval of the desired quantities. To avoid errors due to faulty single SSM/I measurements each wavelength is checked with a simple threshold scheme. Measurements where the brightness temperature is larger than 300 K or lower than 100 K are rejected.

After this screening procedure the rainfall scheme is directly applied. For SSM/I derived basic state variables additional threshold schemes are applied to assure that measurements are rain free. If the polarisation difference at 37 GHz is lower than 20 K the pixel is rejected. For wind speed retrievals the scheme for light rain conditions is applied when $20 \text{ K} < \Delta_{37} < 55 \text{ K}$ and $160 \text{ K} < T_{19h} < 190 \text{ K}$ otherwise the scheme for rain free situations is applied.

If all necessary parameters for the computation of energy fluxes are available then the fluxes are computed in the SSM/I swath oriented coordinate system. It must be noted that evaporation and rainfall are estimated simultaneously only in situations with light rain. For stronger rainfall an estimation of evaporation is not possible.

With these procedures the retrievals are applied to the time series from July 1987 - December 1998. All quantities are averaged over each month and projected onto a regular grid with 1° resolution in longitude and latitude. Because of the projection of the satellite-derived parameters onto a regular grid the number of SSM/I measurements sampled into each grid box depends on the orbit characteristic and the size change of the grid boxes with latitude. Moving northwards the grid boxes become smaller so that less SSM/I pixels are sampled per box. But the number of overpasses is increasing northwards (32 overpasses per $1° \times 1°$ grid box at the equator and 65 overpasses at 60° N). Both effects are almost cancelling so that the number of measurements per grid box is almost constant (Berg and Chase, 1992). The freshwater flux is then simply computed as difference of the monthly evaporation and rainfall in each grid box.

During the spatial and temporal averaging grid boxes are flagged ice-covered if more than 50% of the measurements in that grid box are flagged as ice. On one hand some valid measurements near the ice margin are destroyed and the ice coverage is a bit enhanced by this con-

straint. On the other hand the Cavalieri scheme often classifies SSM/I pixels near the ice margin wrongly as ice-free. Because of the large errors that can arise if ice covered pixels are used in the computations of the mean values the rigid constraint of excluding pixels is justified.

Seasonal and annual averages are computed from the individual monthly means on the regular grids.

Chapter III   Basic State Variables

III.1. Sea Surface Temperature (Fig. III.1 to III.17)

The most important feature of the sea surface temperature distribution is the large east-west gradient in the Pacific Ocean. Another important feature is the summer monsoonal cooling in the Arabian Sea, whereas the rest of the northern oceans exhibit warmer sea surface temperatures. Further there exists a warm pool region in the western Pacific and eastern Indian Ocean during most part of the year. The southern Indian Ocean region experiences very little annual variation and remains cool throughout the year. The north Indian Ocean and the Arabian Sea in particular undergo dramatic variations with onset of summer monsoon (Figures III.6 to III.9). With the development of the strong cross equatorial flow, relatively cooler waters appear along the coasts of Somalia and Arabia (Figure III.15) due to upwelling processes.

The meridional T_S gradient is strong in the north Pacific Ocean during the winter (Figure III.13) as compared to the summer (Figure III.15) when it is quite weak.

III.2. Specific Humidity at Sea Surface Temperature (Fig. III.18 to III.34)

The distribution of the surface specific humidity is the same as for the T_S charts as they are related to each other by the Clausius-Clapeyron-Equation. The maximum q_s values can be expected in the warm pool regions of the eastern Indian and western Pacific Oceans and the lowest values are found in the regions where T_S is low. On a seasonal scale, the maximum values are to be found in spring, summer and autumn seasons (Figures III.31, 32, and 33) as compared to the winter season (Figure III.30). The largest values are to be found in the north Atlantic ocean during the summer and autumn seasons especially in the Gulf of Mexico (Figures III.32 and 33).

III.3. Specific Humidity at Air Temperature (Fig. III.35 to III.51)

The distribution of the specific air humidity follows the T_s pattern to a certain extent. The highest values are observed in the warm pool region, i.e the eastern Indian Ocean and western Pacific Ocean. The maximum q_a values are observed in the Bay of Bengal and the adjacent South China Sea (>20 g kg^{-1}) during the summer monsoon (Figures III.40 to III.43), even though the extent of the warm pool area is much larger.

III.4. Difference in Humidity (Fig. III.52 to III.68)

The distribution of difference in humidity shows that the maximum differences are seen in the Arabian Sea and Bay of Bengal during the winter months (December, January and February; Figures III.52, 53, and 63). On an annual scale also the Persian Gulf, Red Sea and the northern Arabian Sea are the regions of the largest difference in humidity (Figure III.68). Minimum values are found in the eastern equatorial Pacific and along the western African coasts, especially in the summer and autumn season, while differences in humidity are generally low throughout the year at high latitudes north and south of 40°.

III.5. Wind Speed (Fig. III.69 to III.85)

The maximum wind speed (> 12 m s^{-1}) is observed over the North Atlantic Ocean during the winter months (Figures III.69, 70, and 80) and they gradually decrease in their intensity in spring (Figures III.71, 72, and 73). In the winter months, the minimum wind speed is found in the northern Indian Ocean, both in the Arabian Sea and Bay of Bengal. With the summer monsoon, i.e from June till September (Figures III. 74 to 77), a strong cross equatorial flow develops over the western equatorial Indian Ocean, which brings along copious amount of moisture into the Arabian Sea and the Indian subcontinent. Other regions of high wind speed throughout the year is the subpolar storm tracks along 40^0S where the values exceed 10 m s^{-1} (Figure III.85).

III.6. Dalton number (Fig. III.86 to III.102)

The Dalton number, often called transfer or exchange coefficient, is very important for computing the latent heat flux as well as the evaporation. It is dependent upon the atmospheric stability and wind speed. The lowest values are observed in the eastern equatorial Pacific and the Atlantic throughout the year (Figures III.86 to 97) and highest values are observed in the northern Arabian Sea during the winter, spring and autumn seasons (Figures III.98, 99, and 101). Another region of large transfer coefficients is observed off the west Australian coast on annual scale (Figure 102).
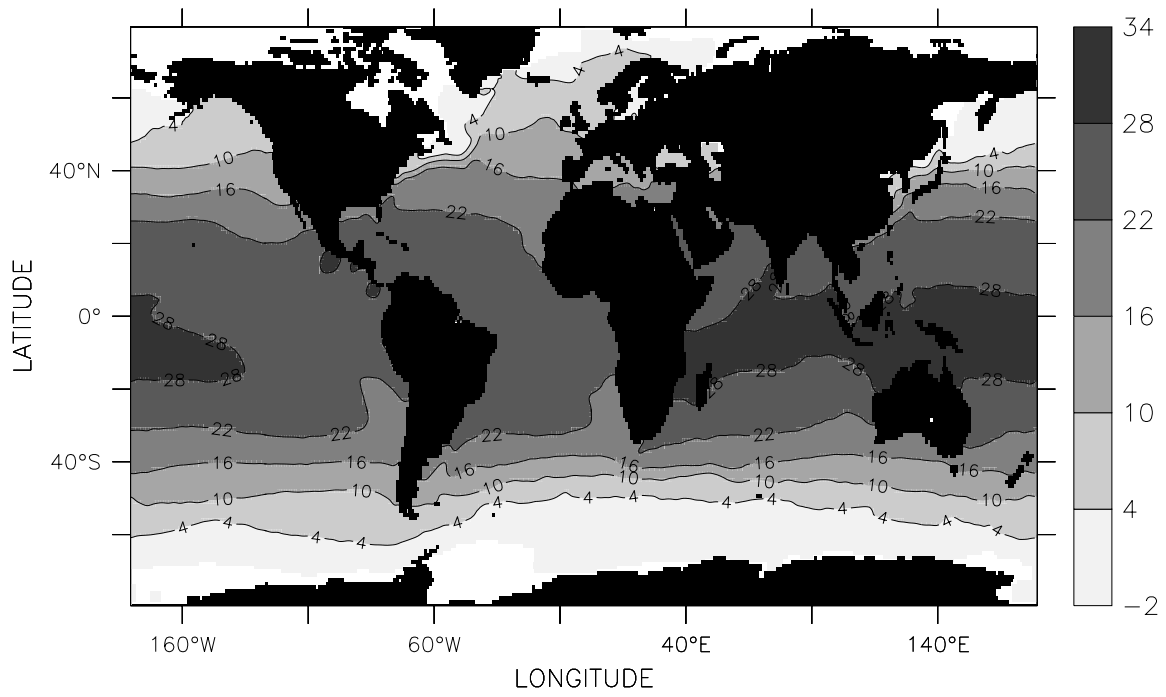
Fig.III.1 Sea Surface Temperature (°C), January
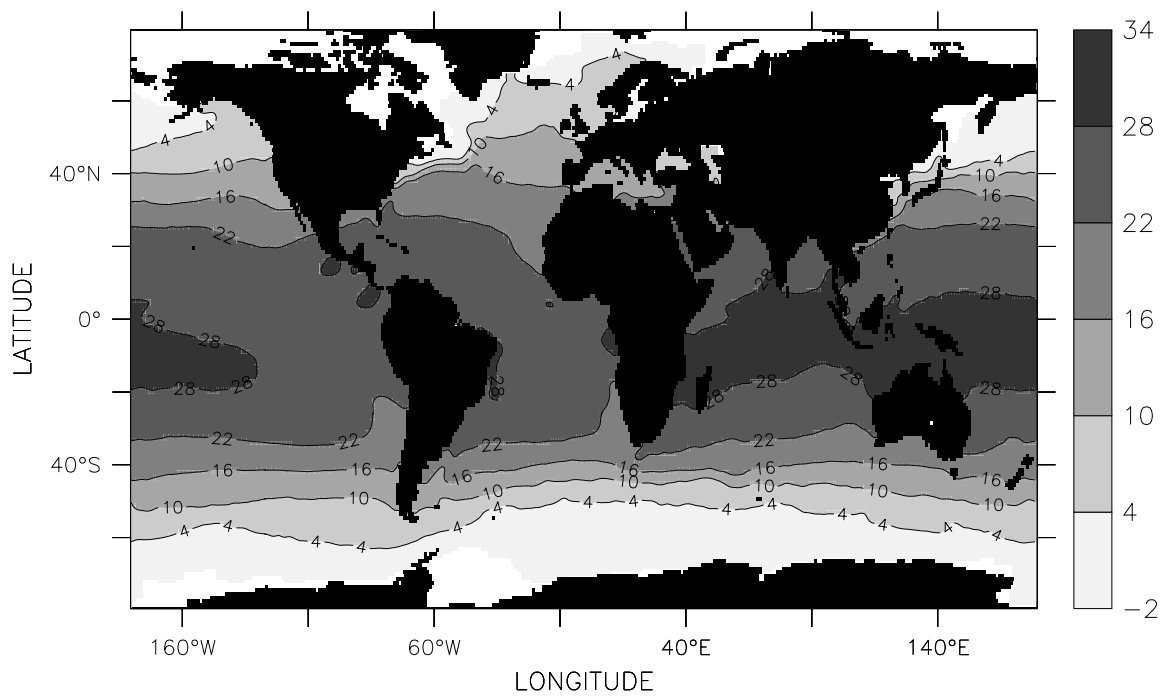
Fig.III.2 Sea Surface Temperature (°C), February
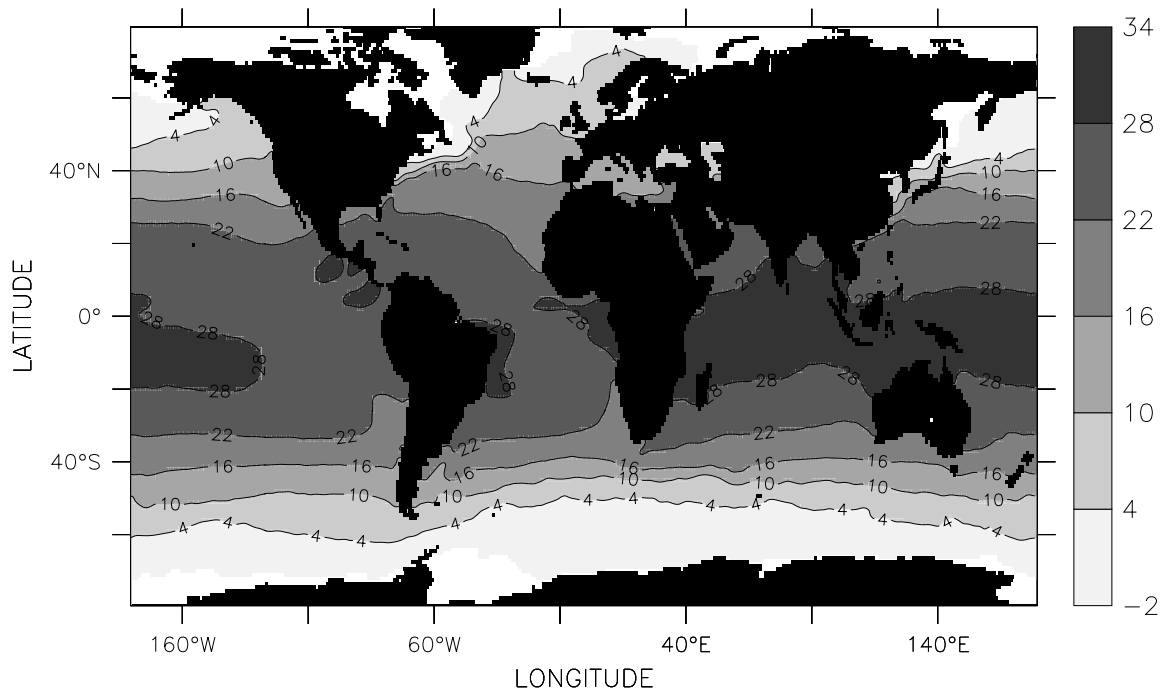
Fig.III.3 Sea Surface Temperature (°C), March
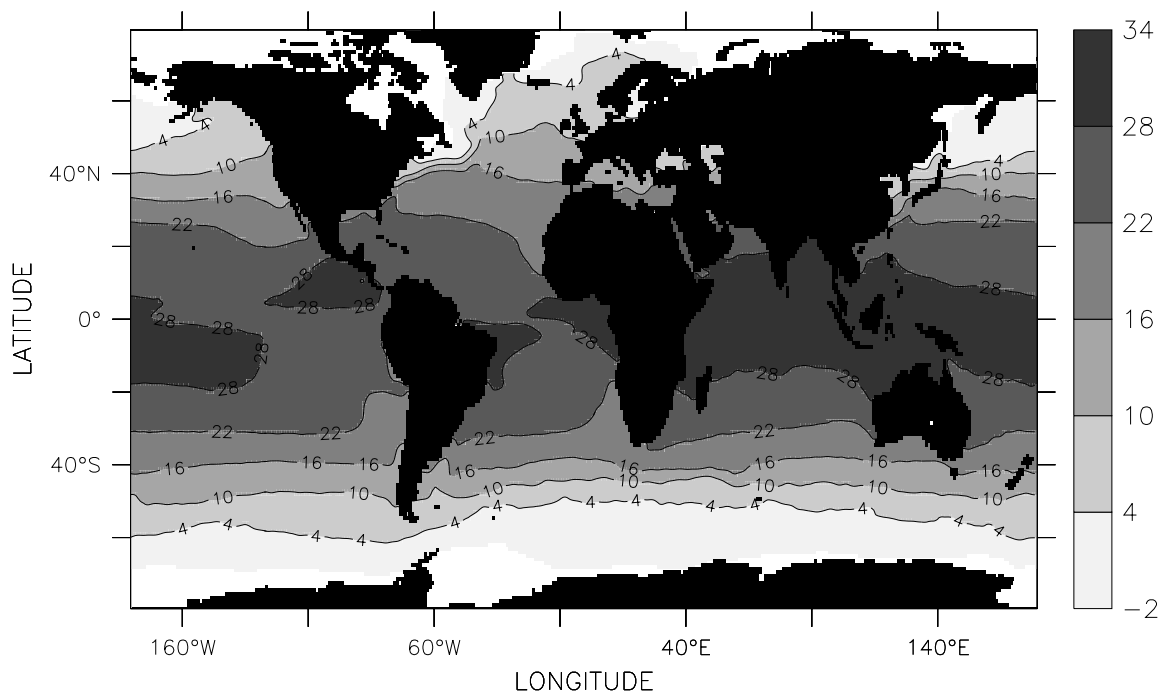
Fig.III.4 Sea Surface Temperature (°C), April
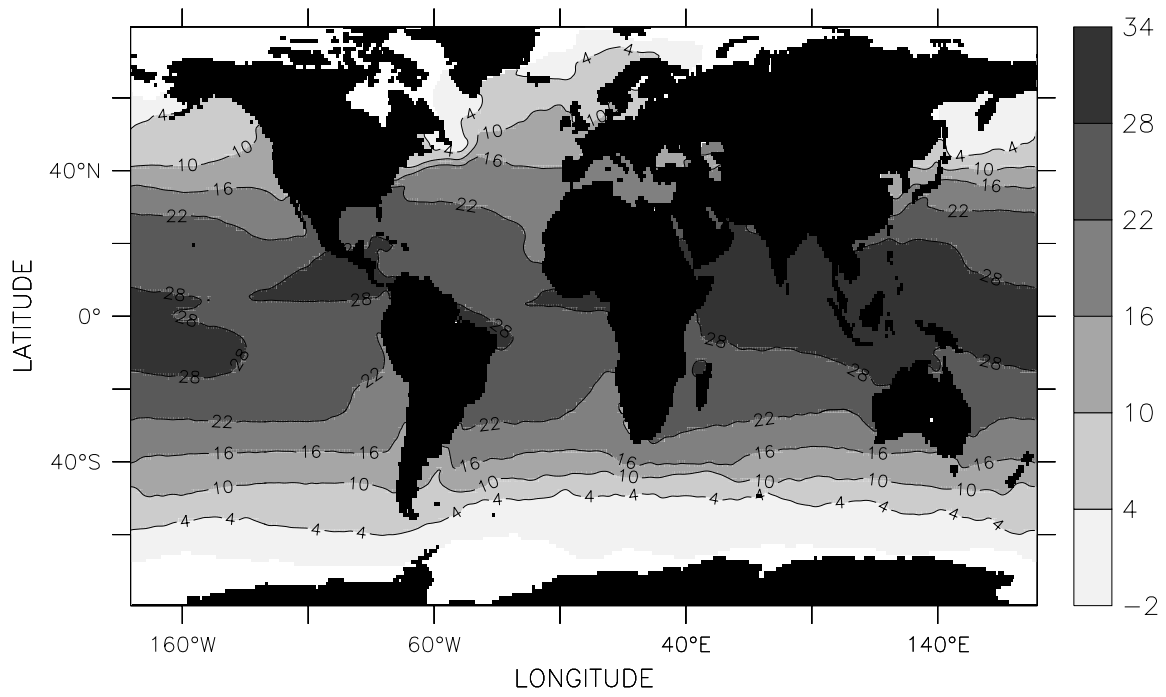
Fig.III.5 Sea Surface Temperature (°C), May
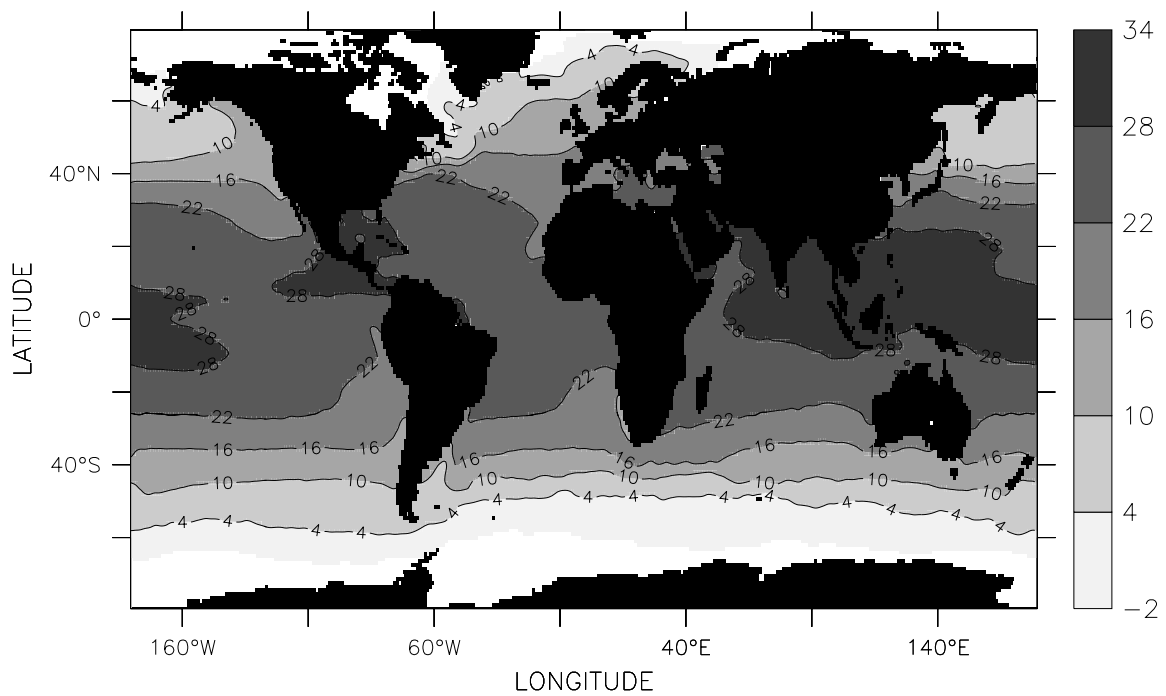
Fig.III.6 Sea Surface Temperature (°C), June

17
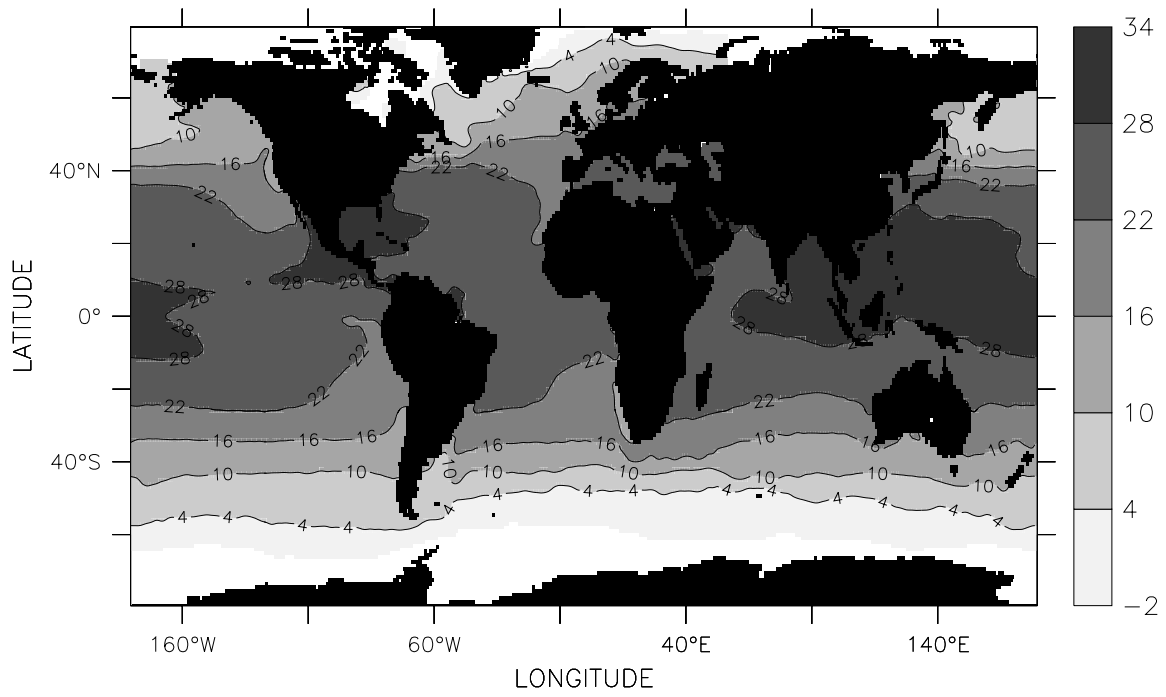
Fig.III.7 Sea Surface Temperature (°C), July
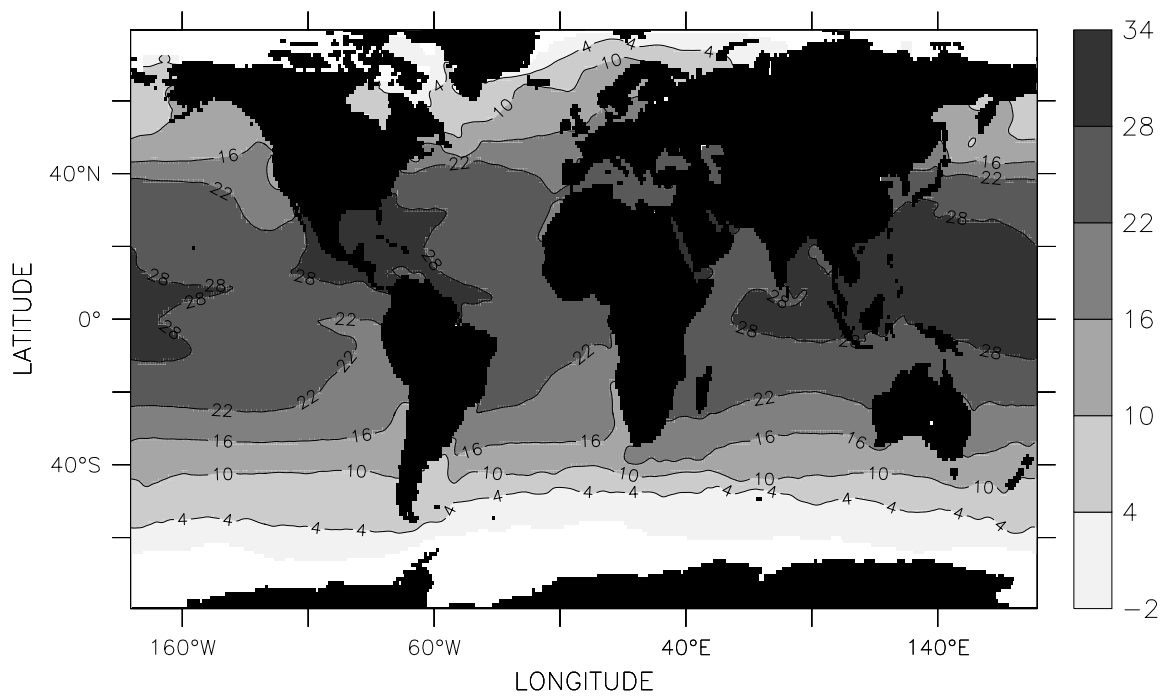
Fig.III.8 Sea Surface Temperature (°C), August
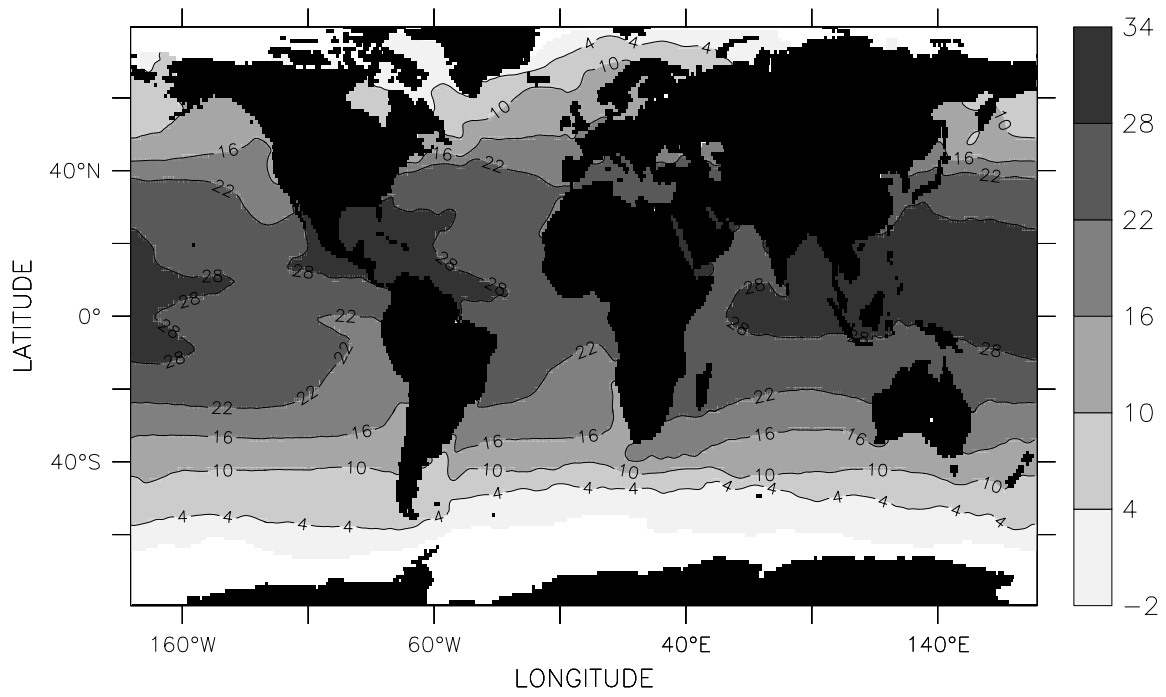
Fig.III.9 Sea Surface Temperature (°C), September
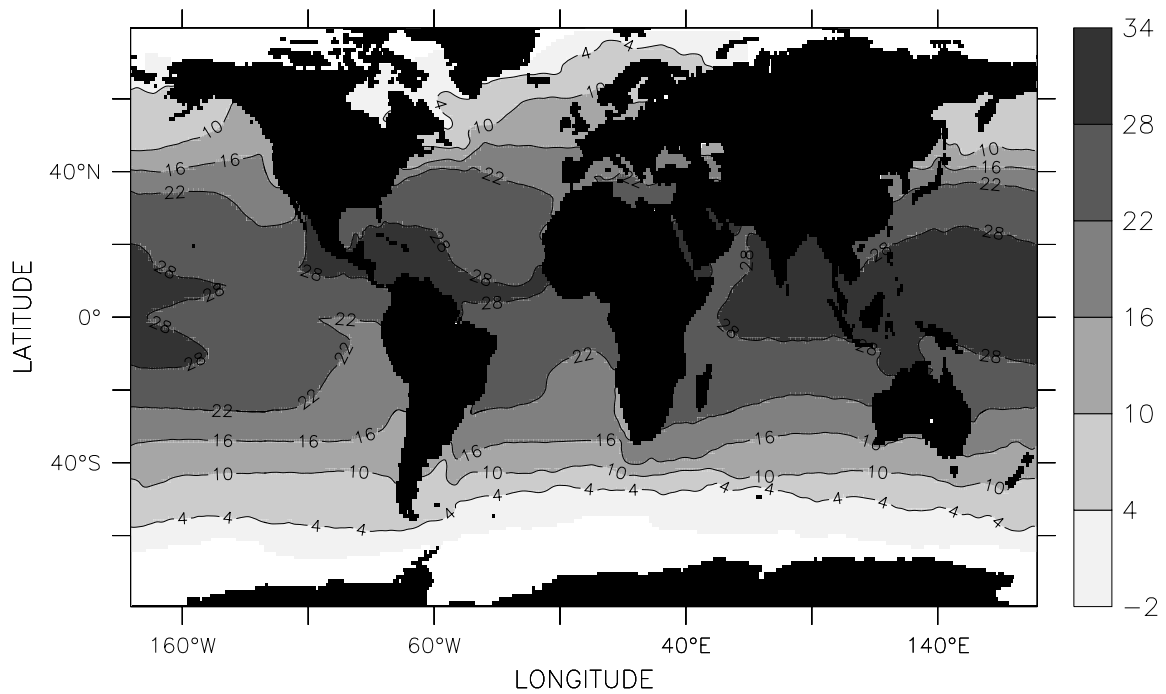
Fig.III.10 Sea Surface Temperature (°C), October

19
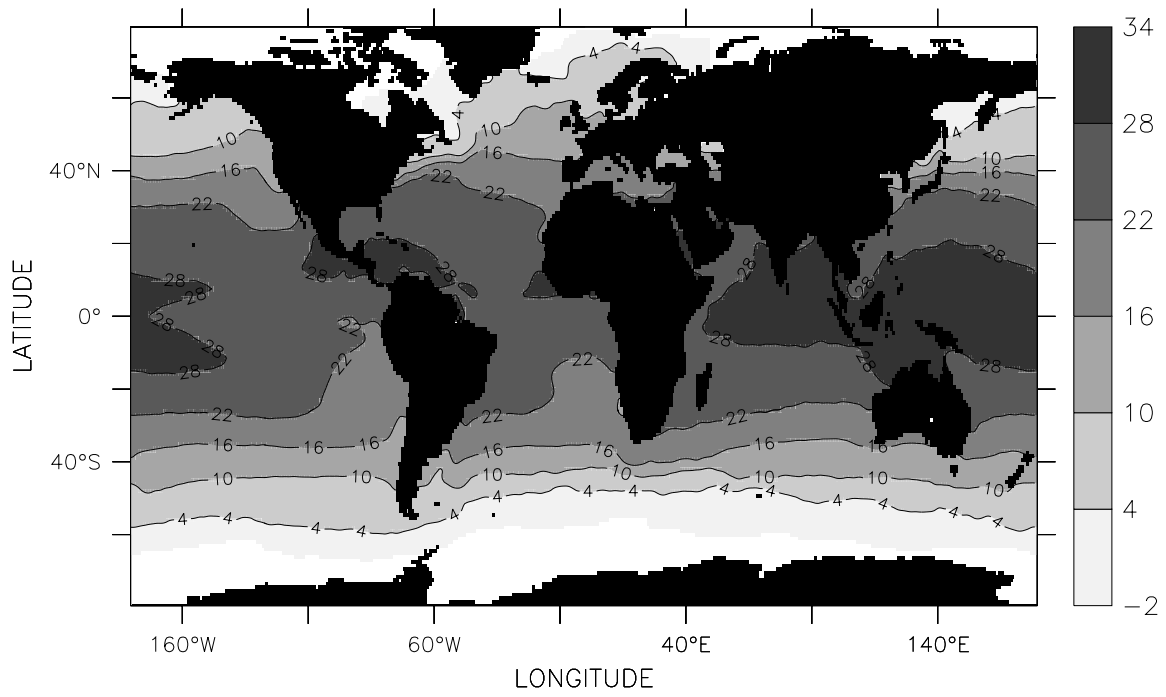
Fig.III.11 Sea Surface Temperature (°C), November
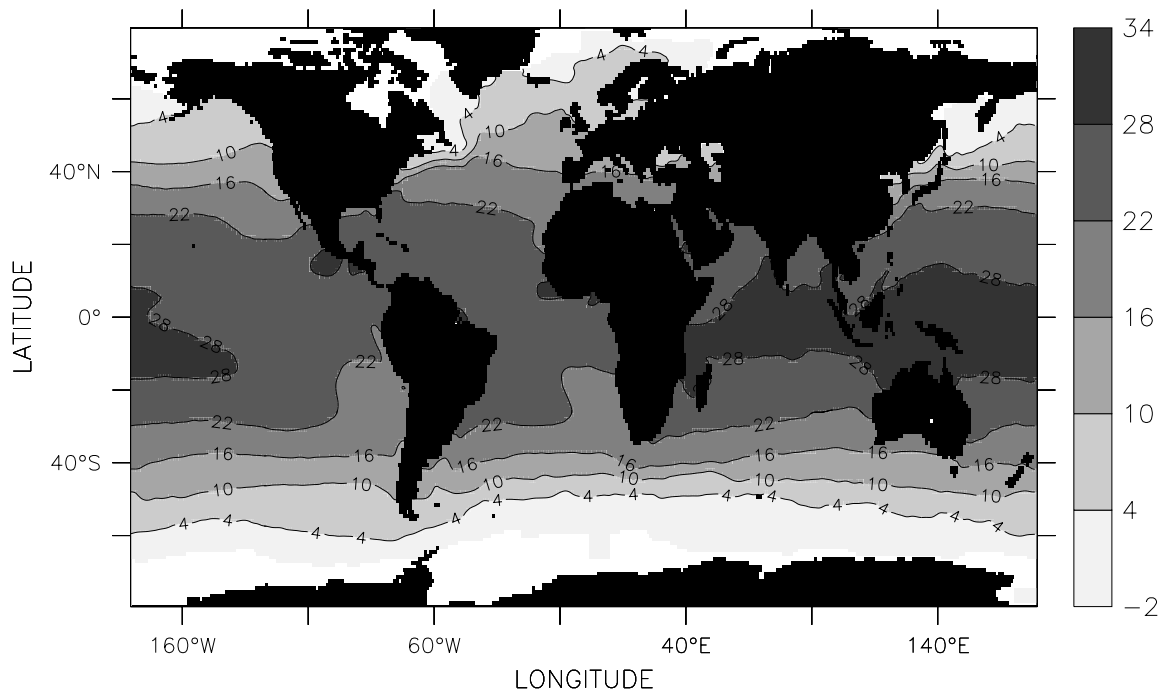
Fig.III.12 Sea Surface Temperature (°C), December
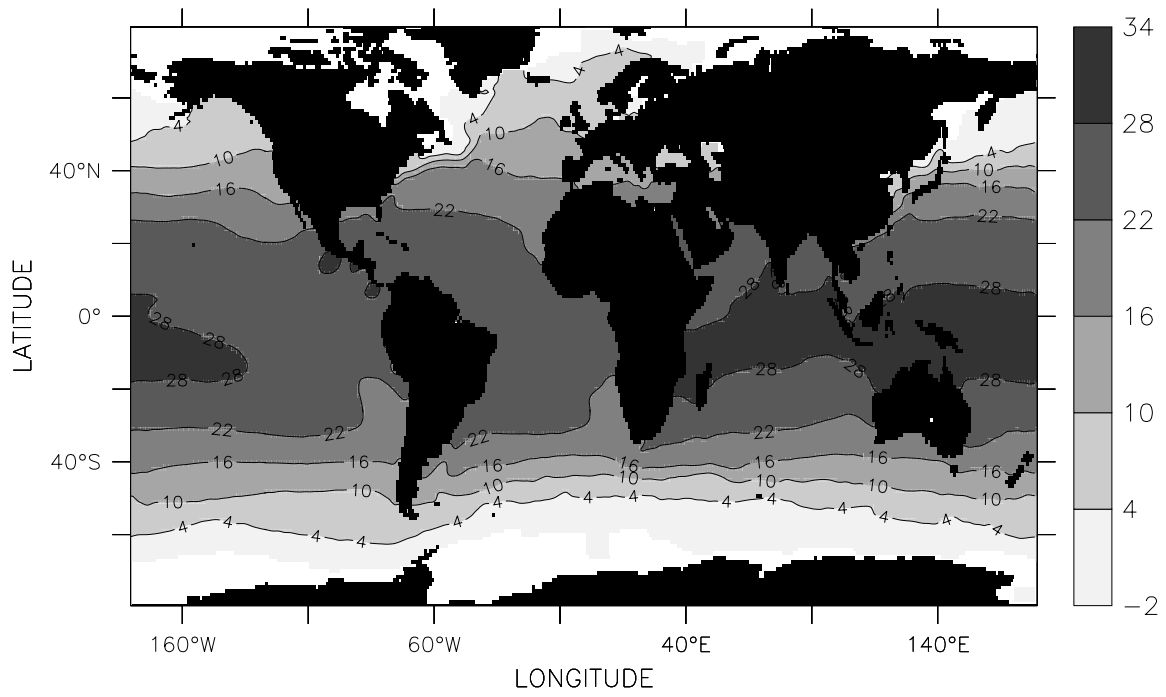
Fig.III.13 Sea Surface Temperature (°C), DJF
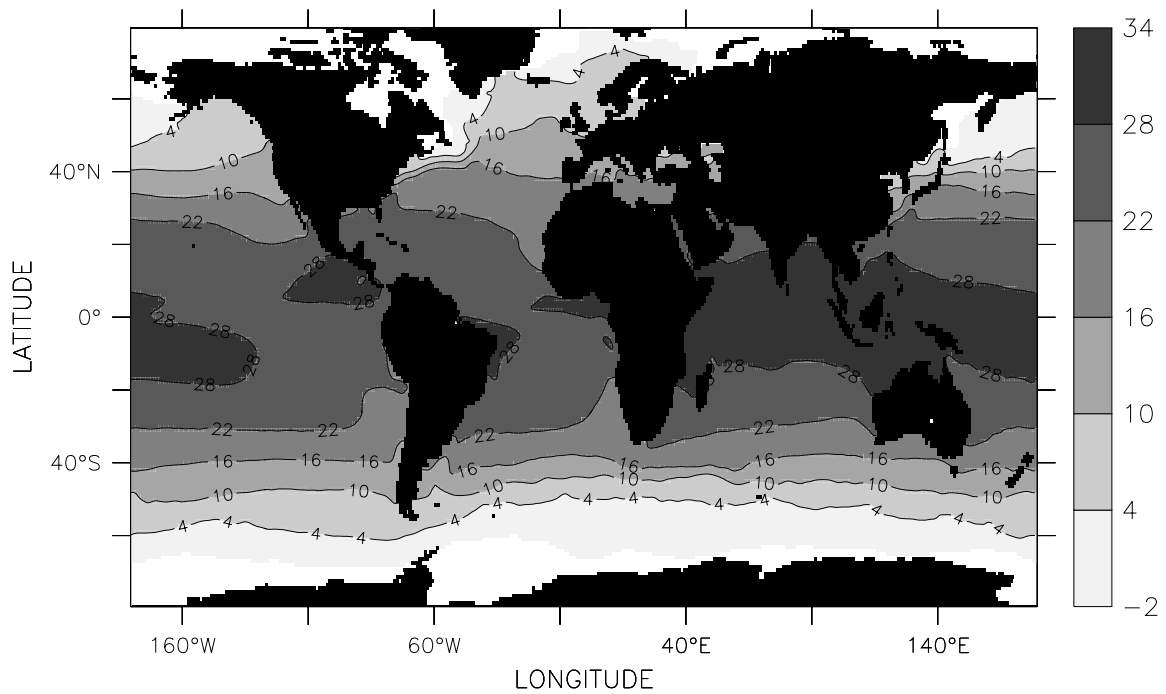
Fig.III.14 Sea Surface Temperature (°C), MAM
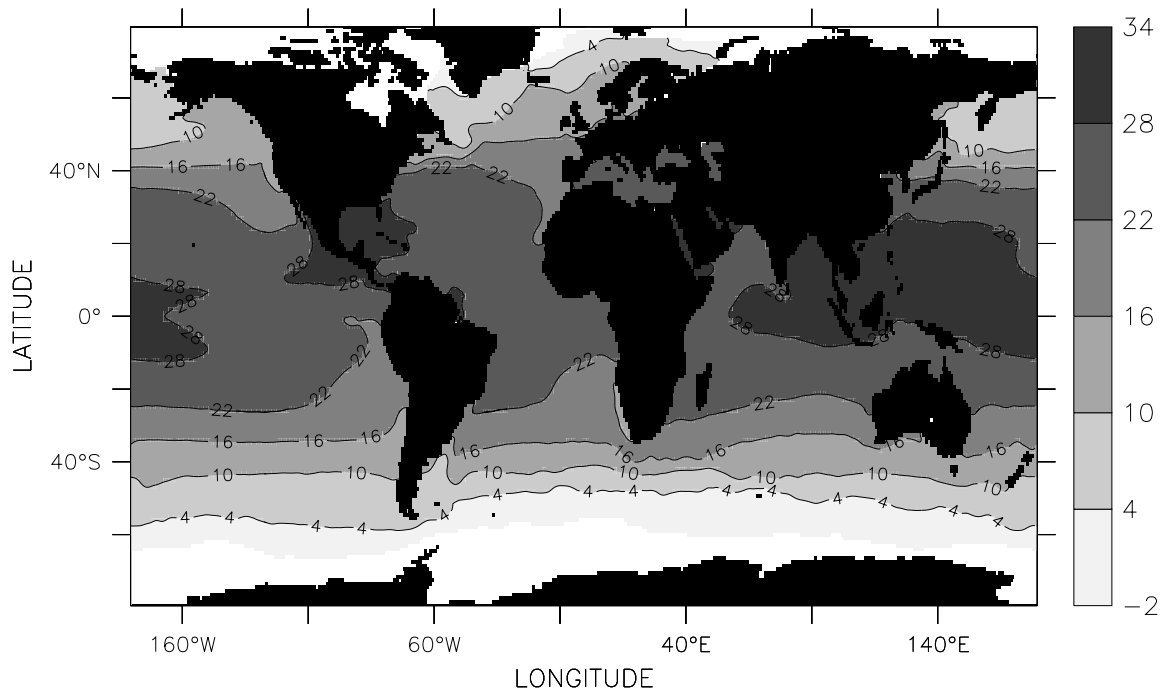
Fig.III.15 Sea Surface Temperature (°C), JJA
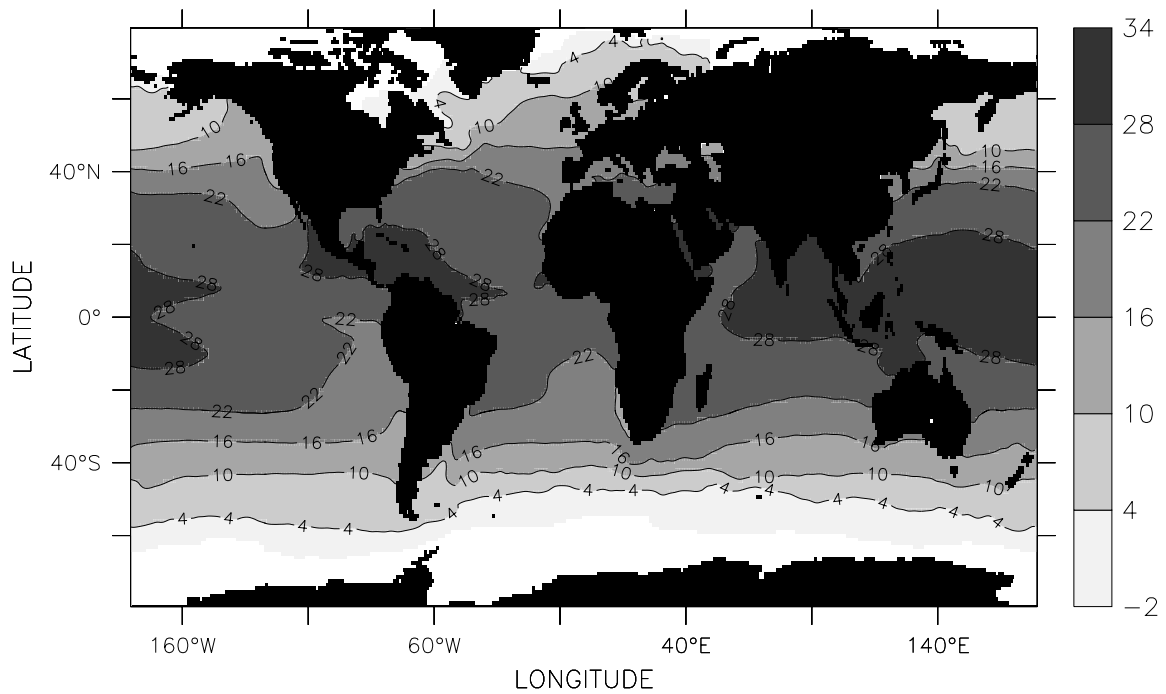
Fig.III.16 Sea Surface Temperature (°C), SON

22
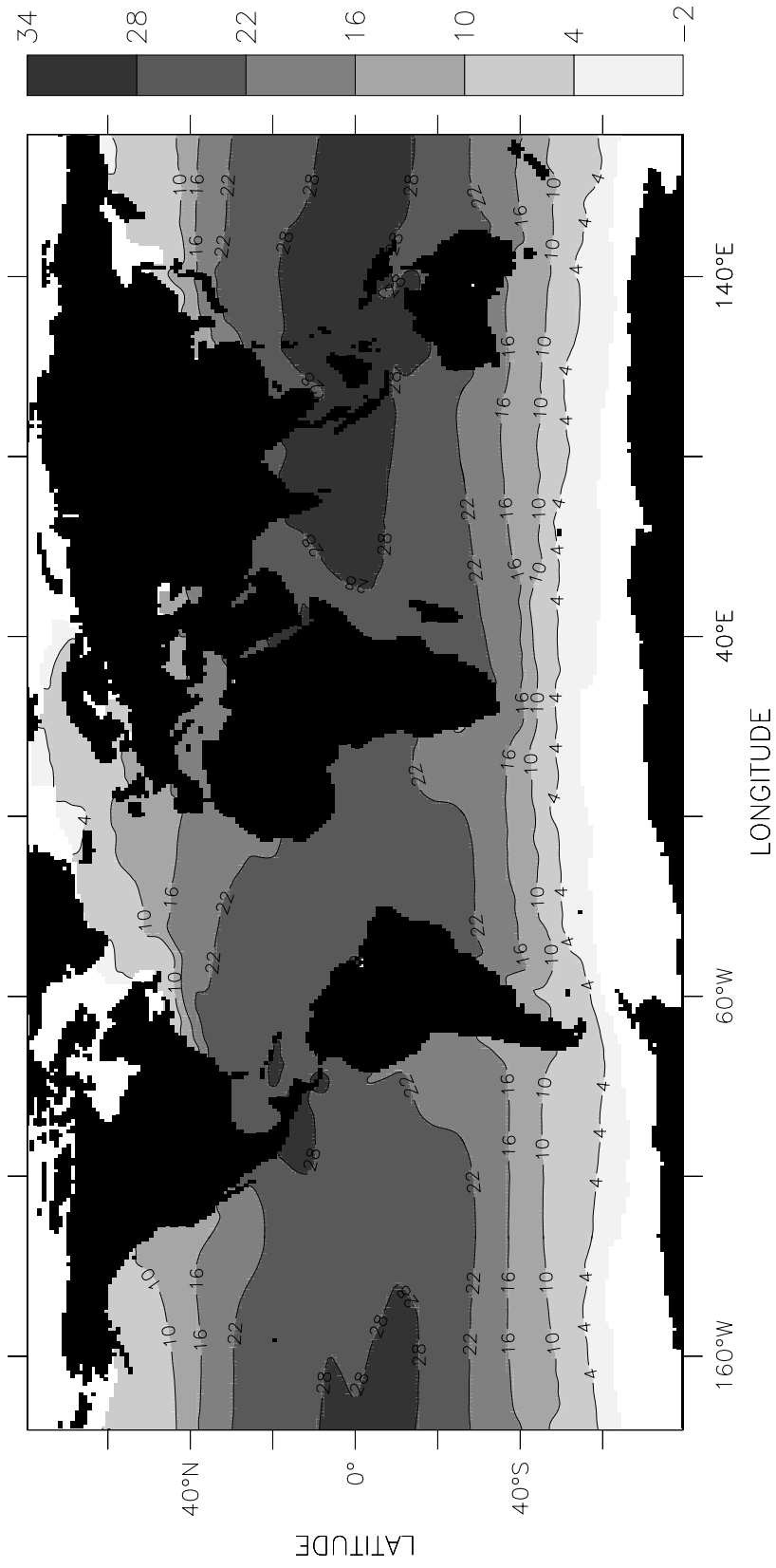
Fig.III.17 Sea Surface Temperature (°C), Annual
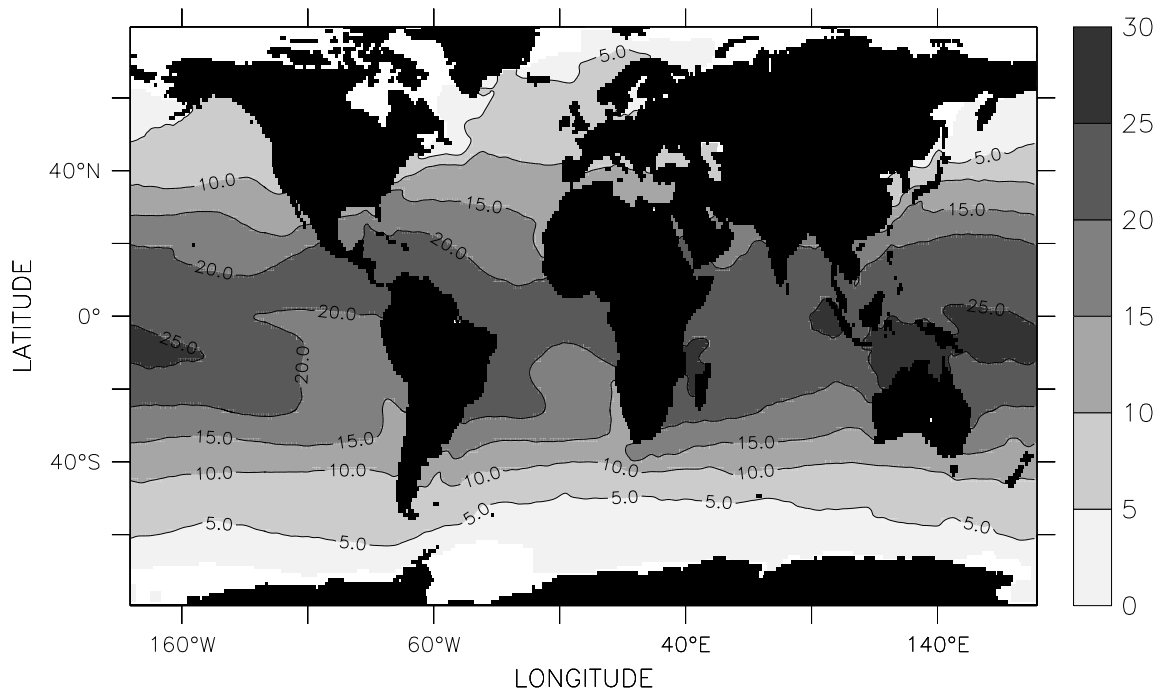
Fig.III.18 Surface Humidity (g/kg), January
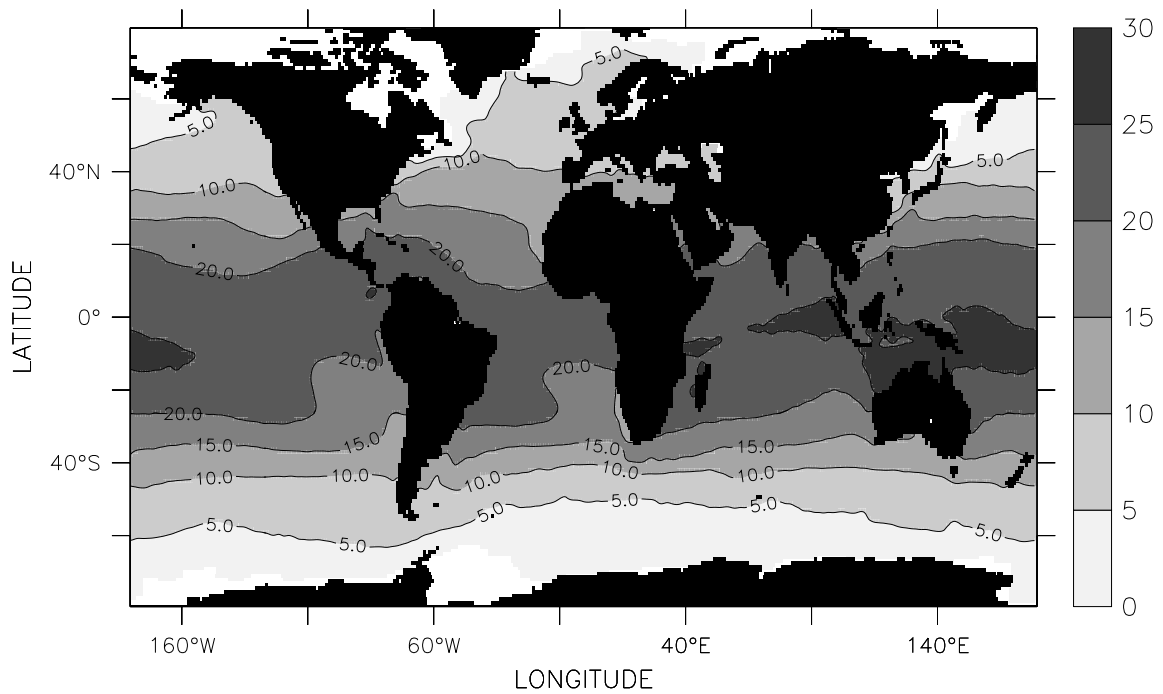
Fig.III.19 Surface Humidity (g/kg), February
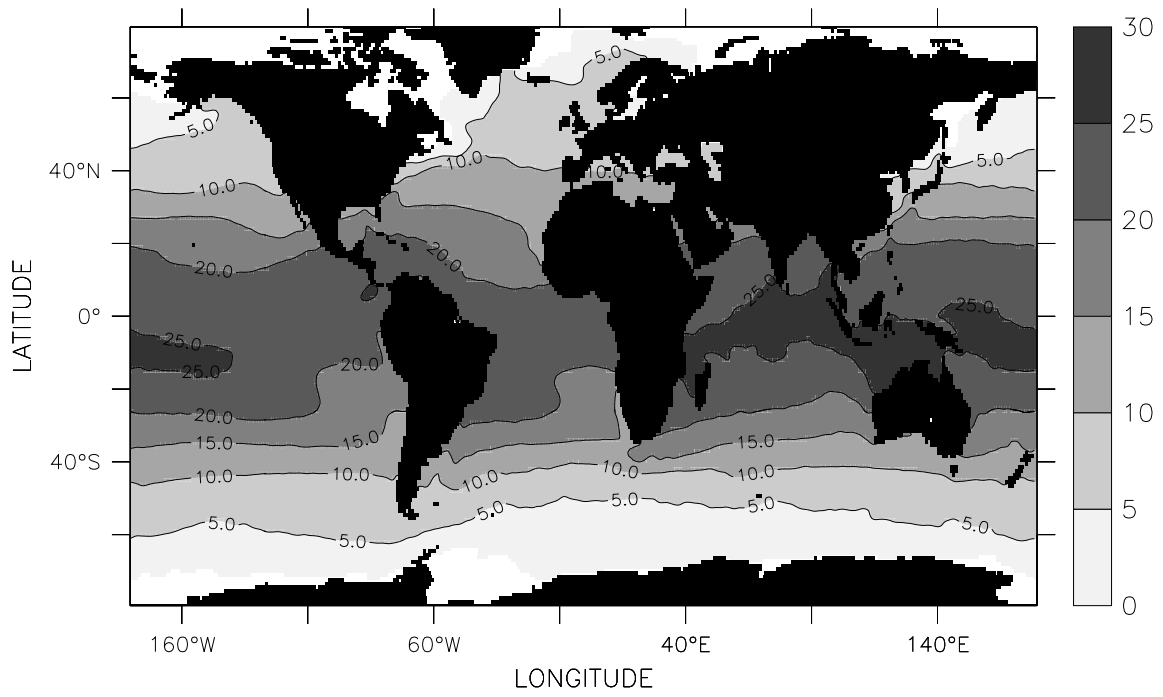
Fig.III.20 Surface Humidity (g/kg), March
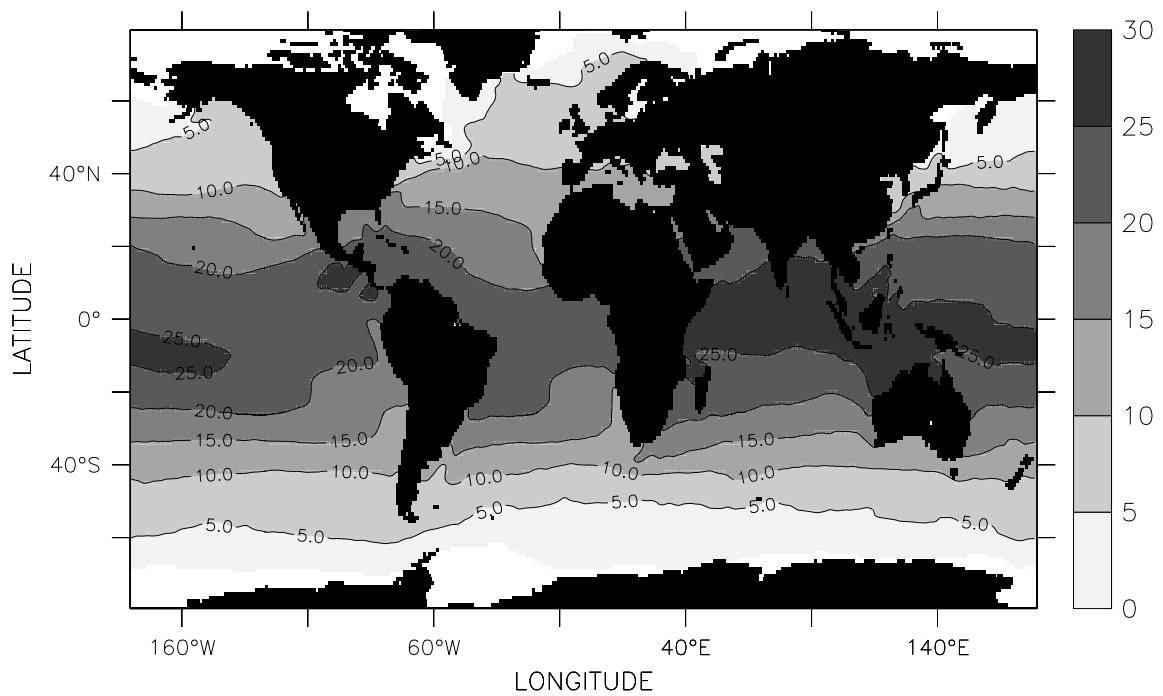
Fig.III.21 Surface Humidity (g/kg), April

25
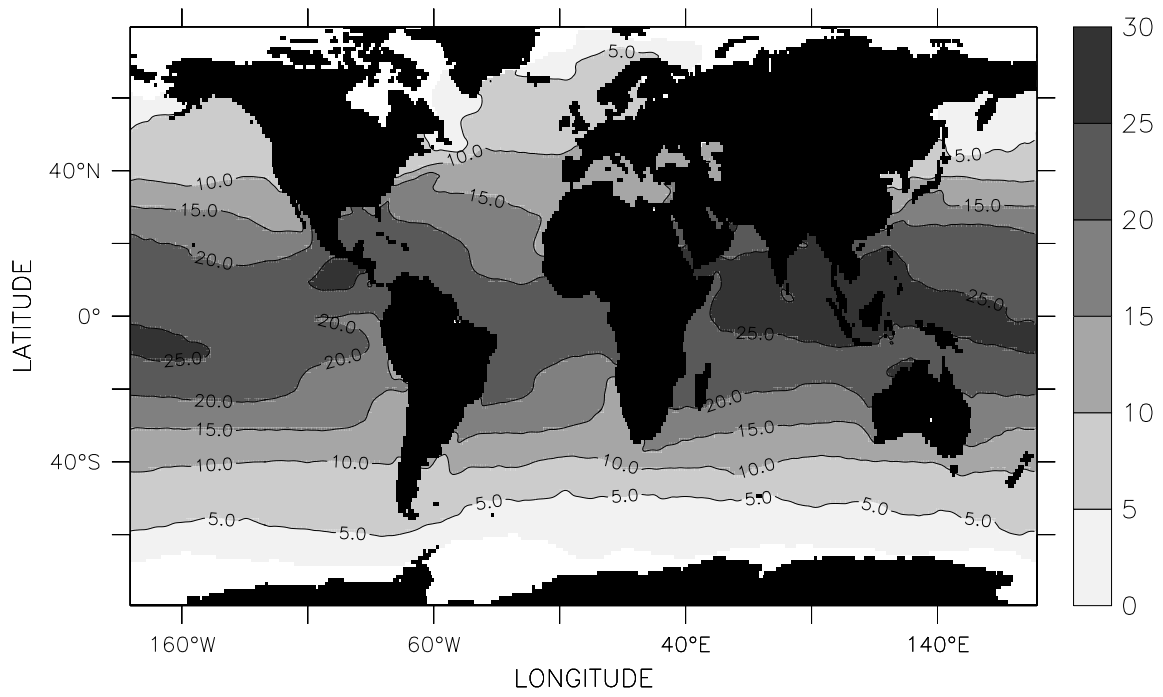
Fig.III.22 Surface Humidity (g/kg), May
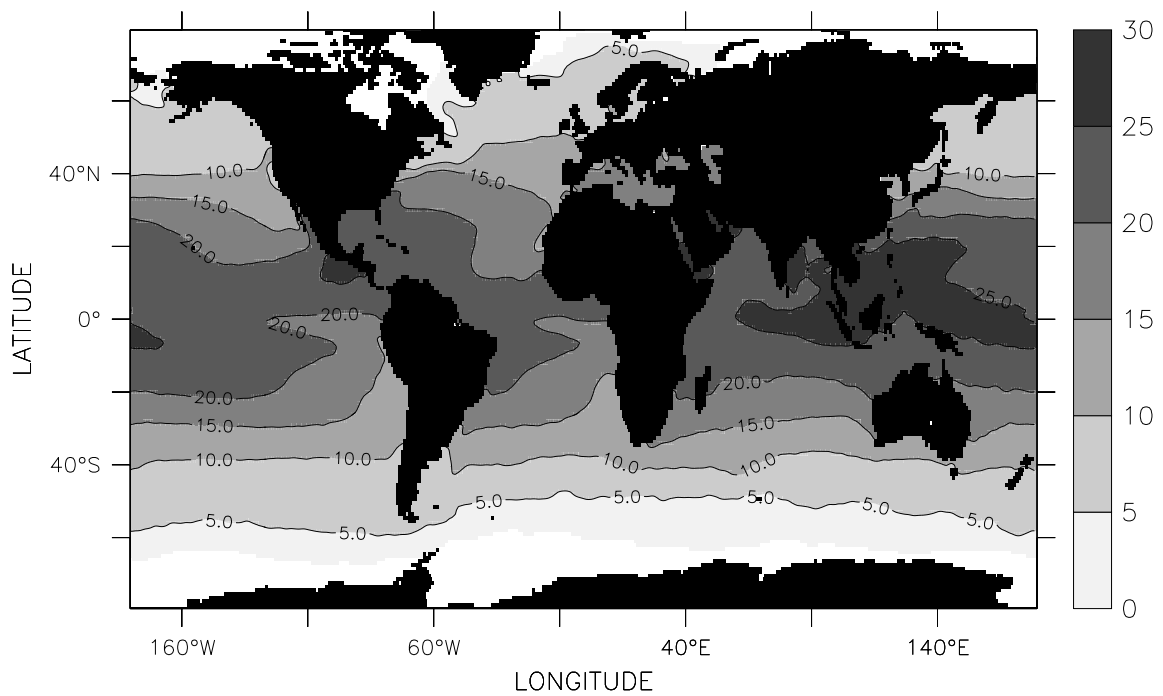
Fig.III.23 Surface Humidity (g/kg), June
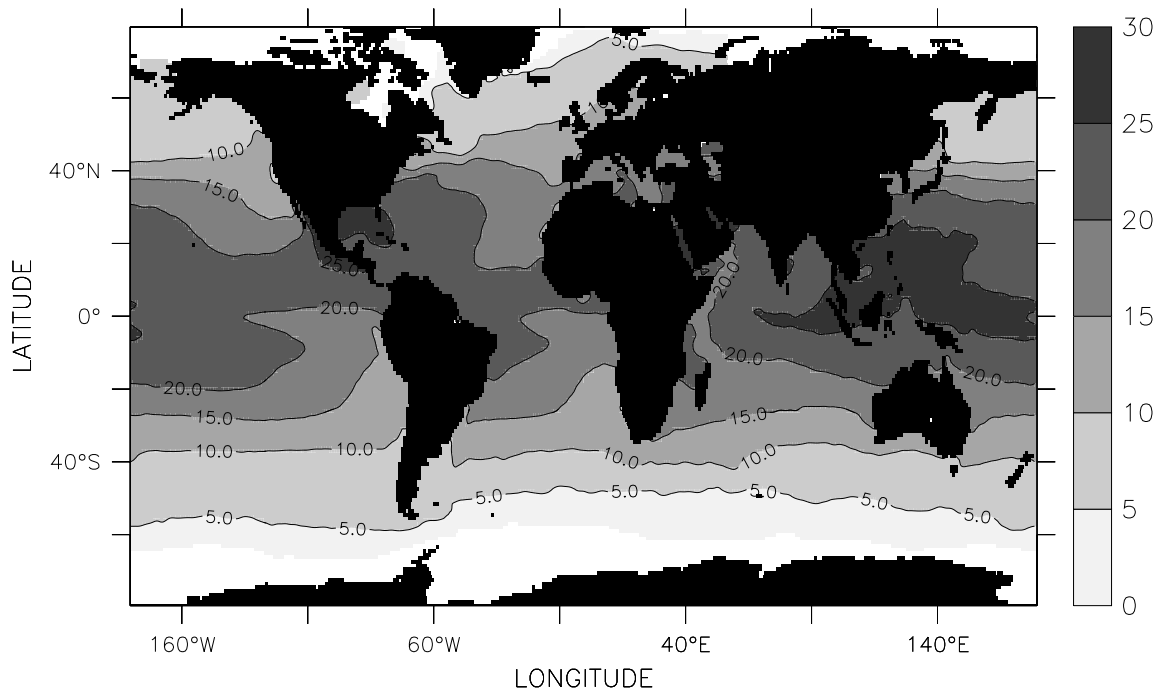
Fig.III.24 Surface Humidity (g/kg), July
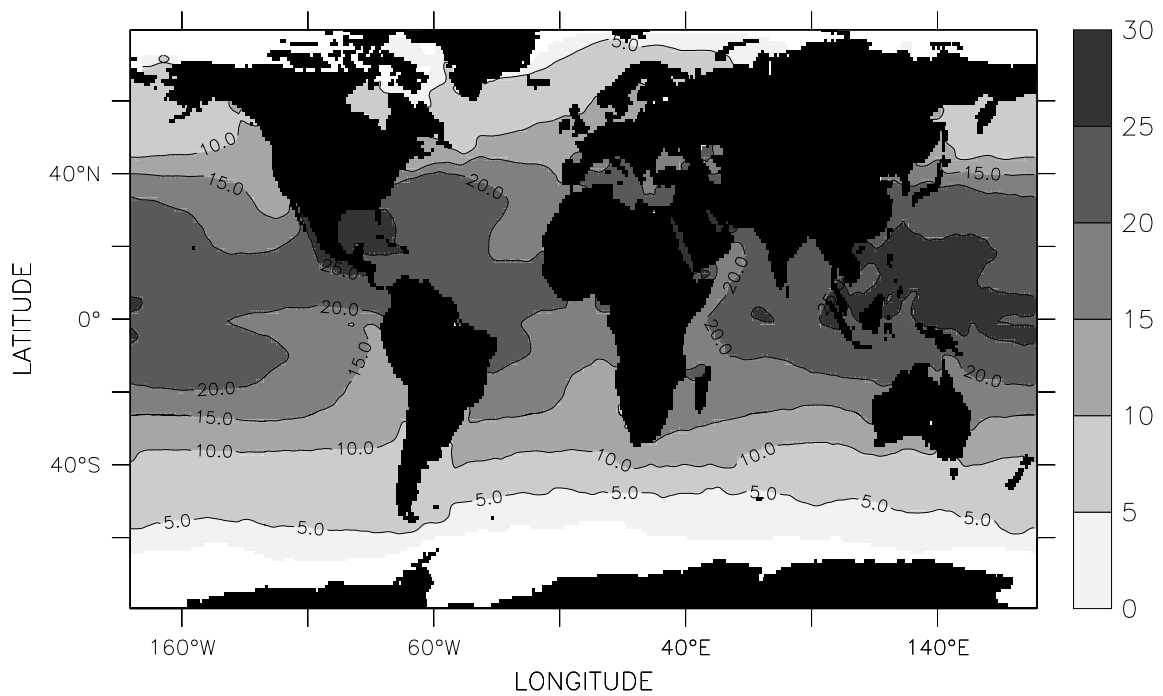
Fig.III.25 Surface Humidity (g/kg), August
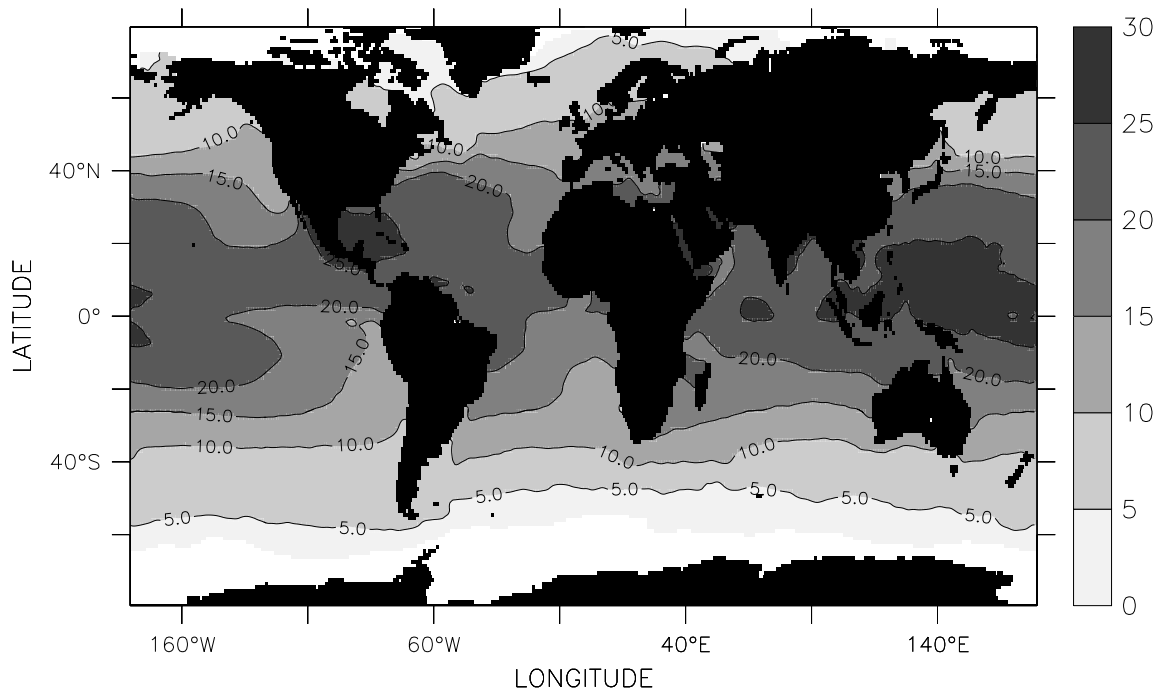
Fig.III.26 Surface Humidity (g/kg), September
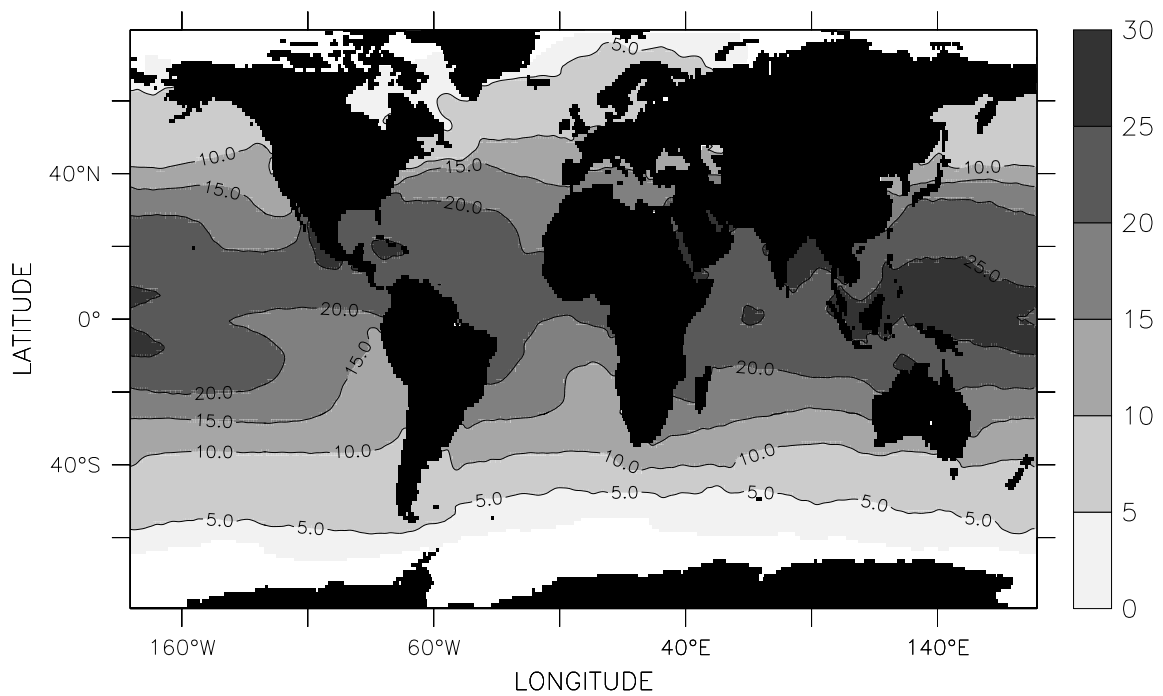
Fig.III.27 Surface Humidity (g/kg), October
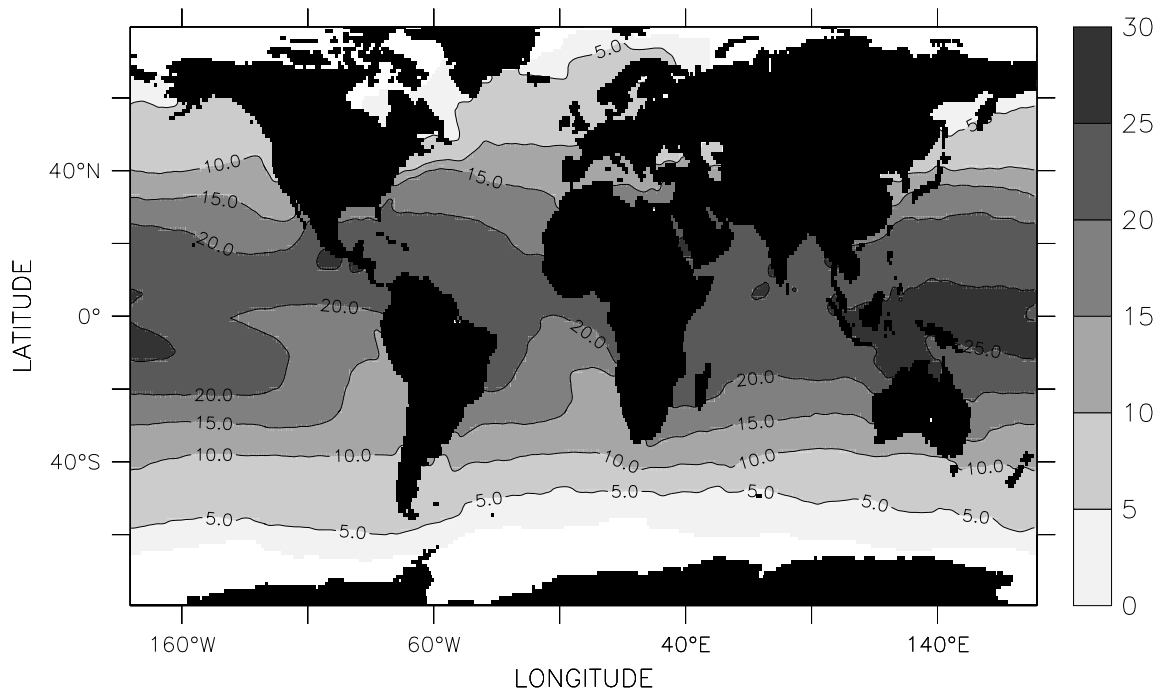
Fig.III.28 Surface Humidity (g/kg), November
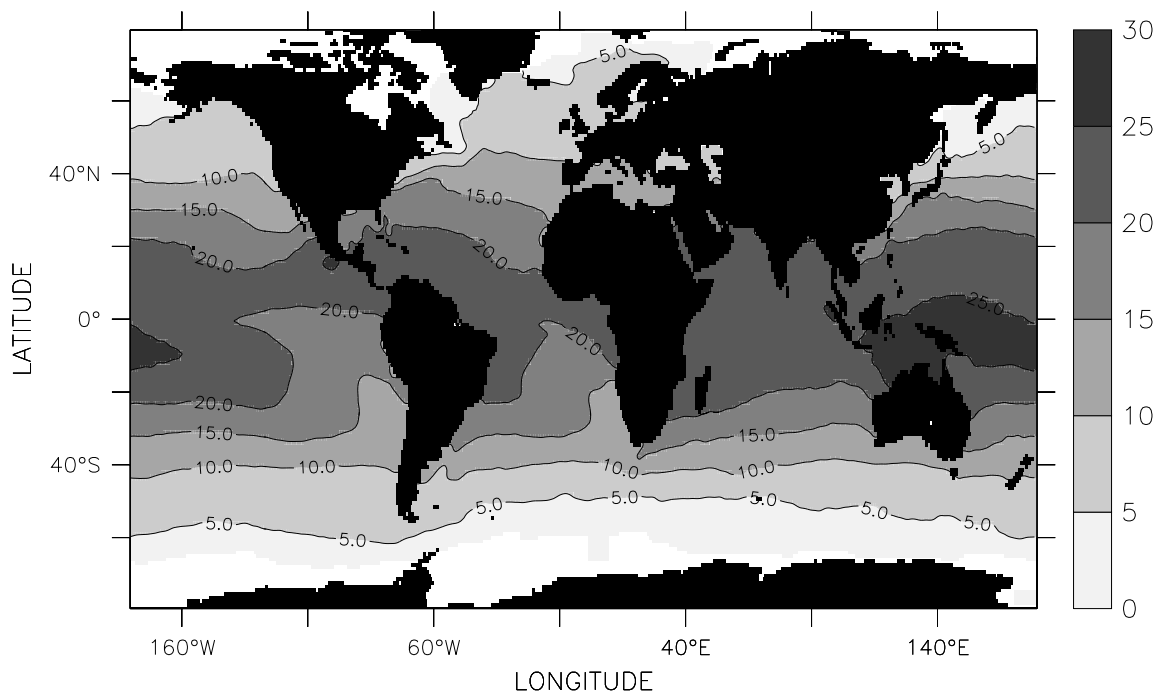
Fig.III.29 Surface Humidity (g/kg), December
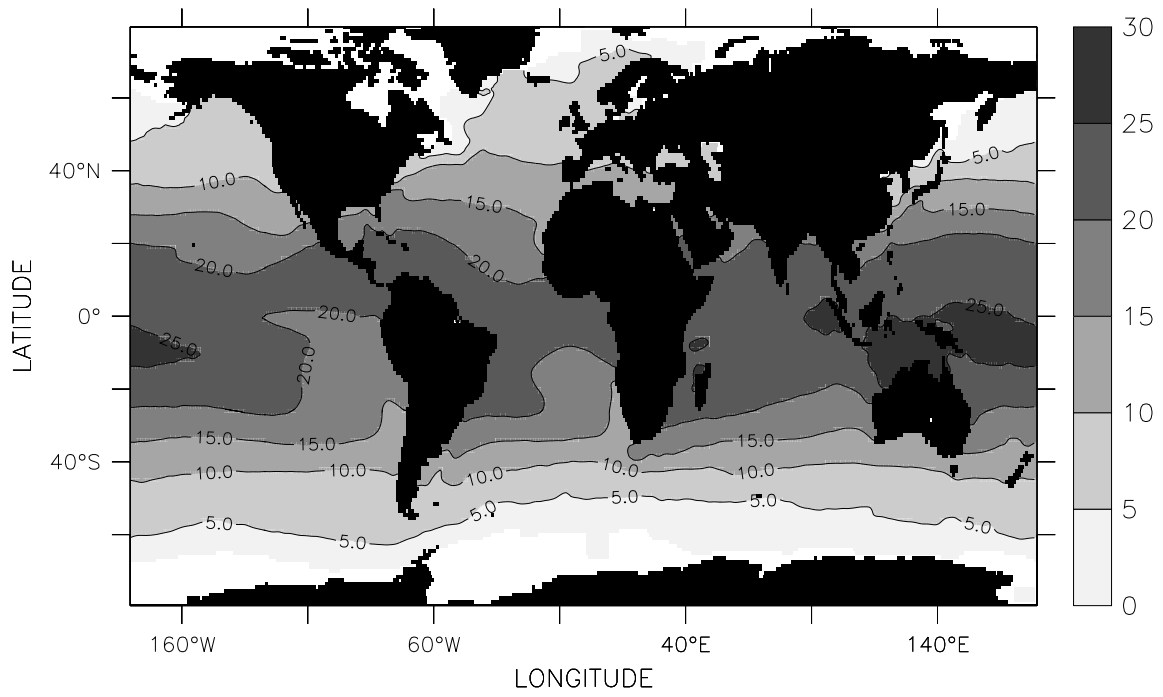
Fig.III.30 Surface Humidity (g/kg), DJF
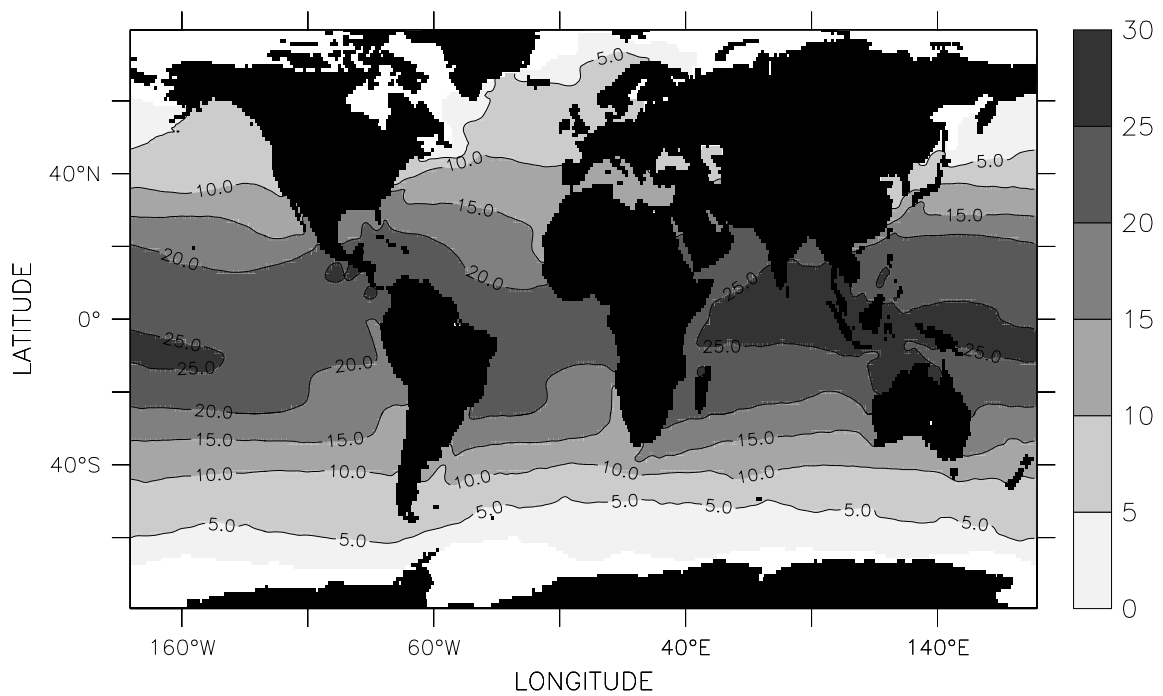
Fig.III.31 Surface Humidity (g/kg), MAM
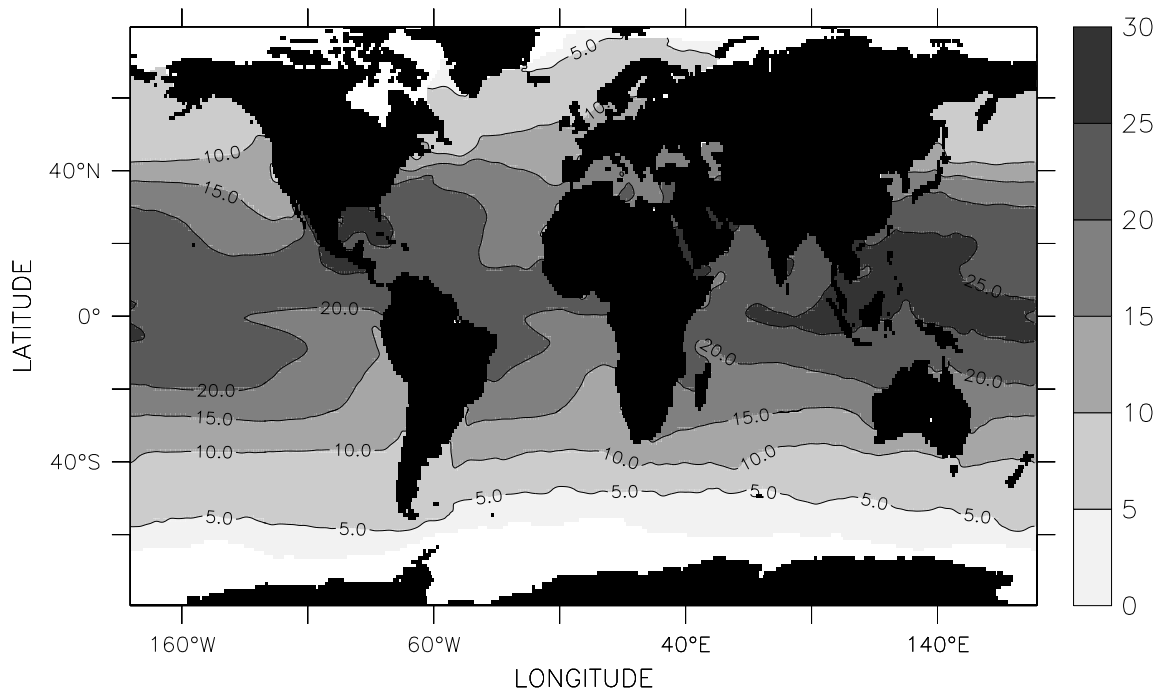
Fig.III.32 Surface Humidity (g/kg), JJA
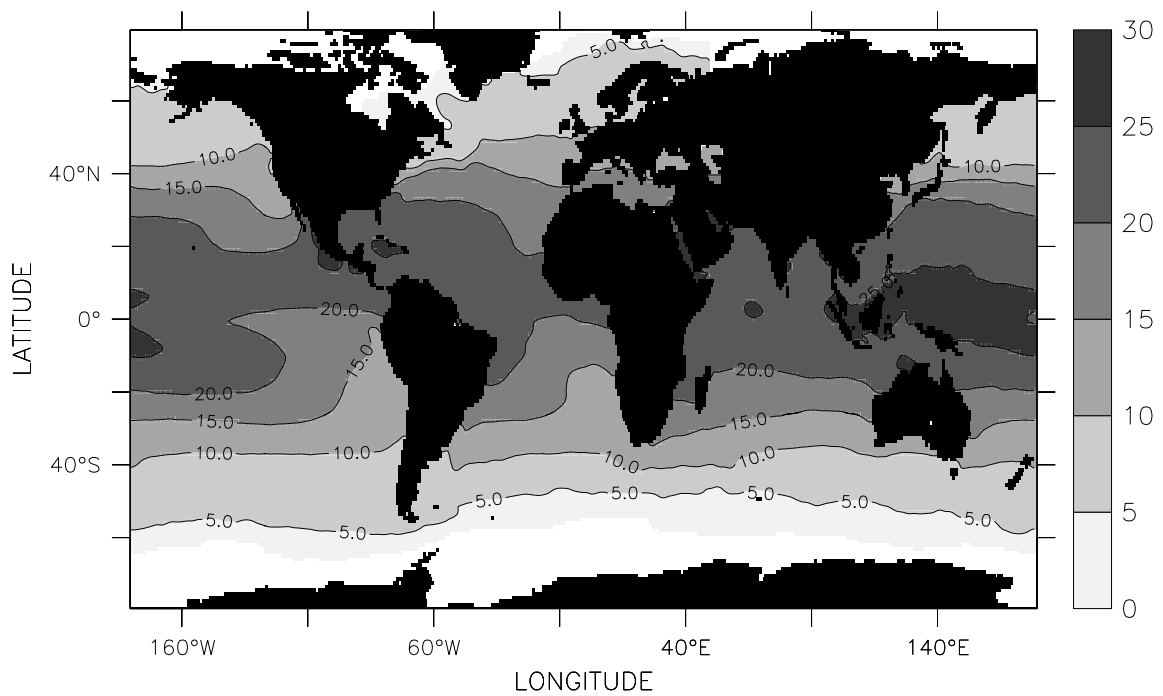
Fig.III.33 Surface Humidity (g/kg), SON
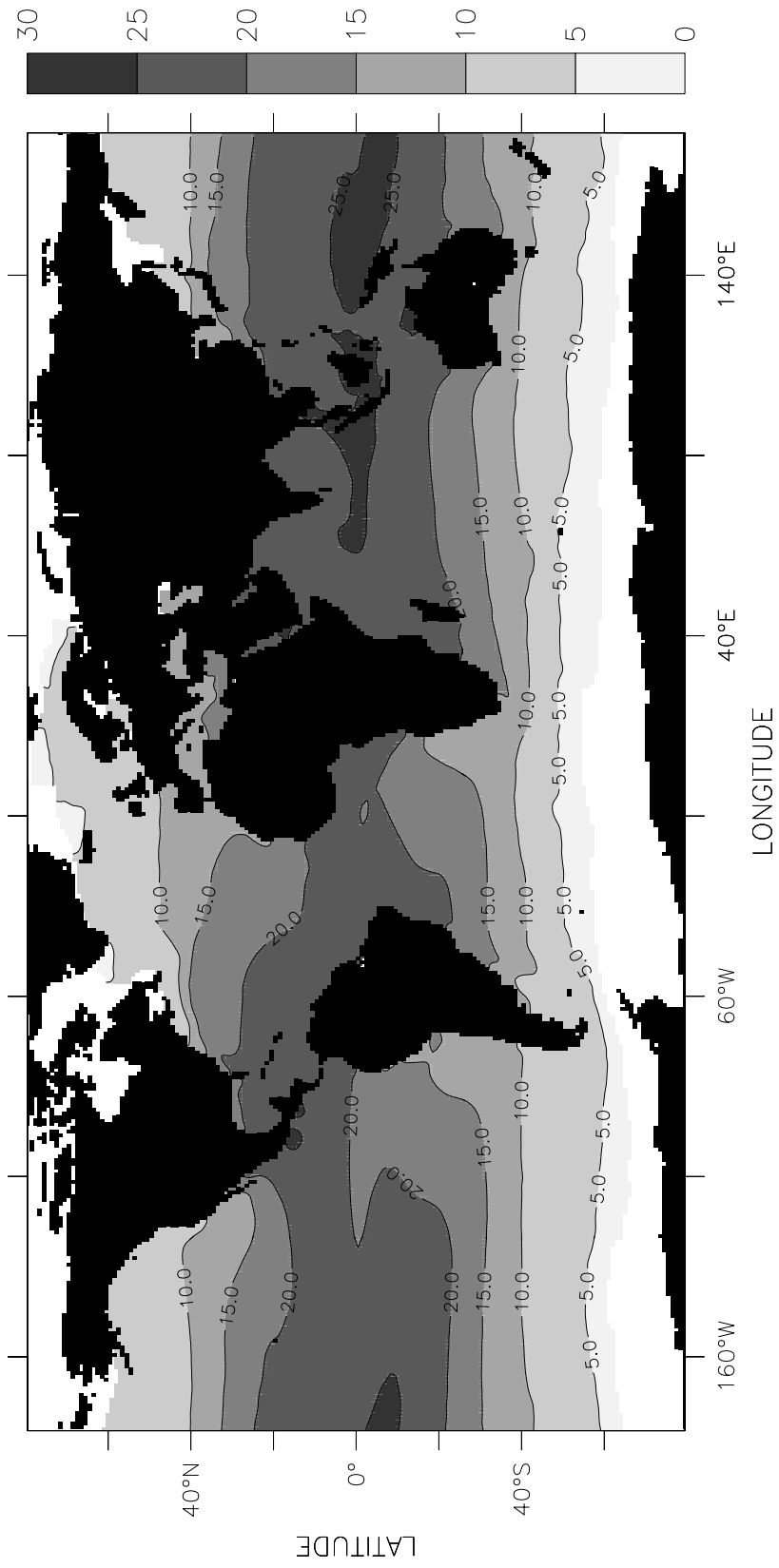
Fig.III.34 Surface Humidity (g/kg), Annual
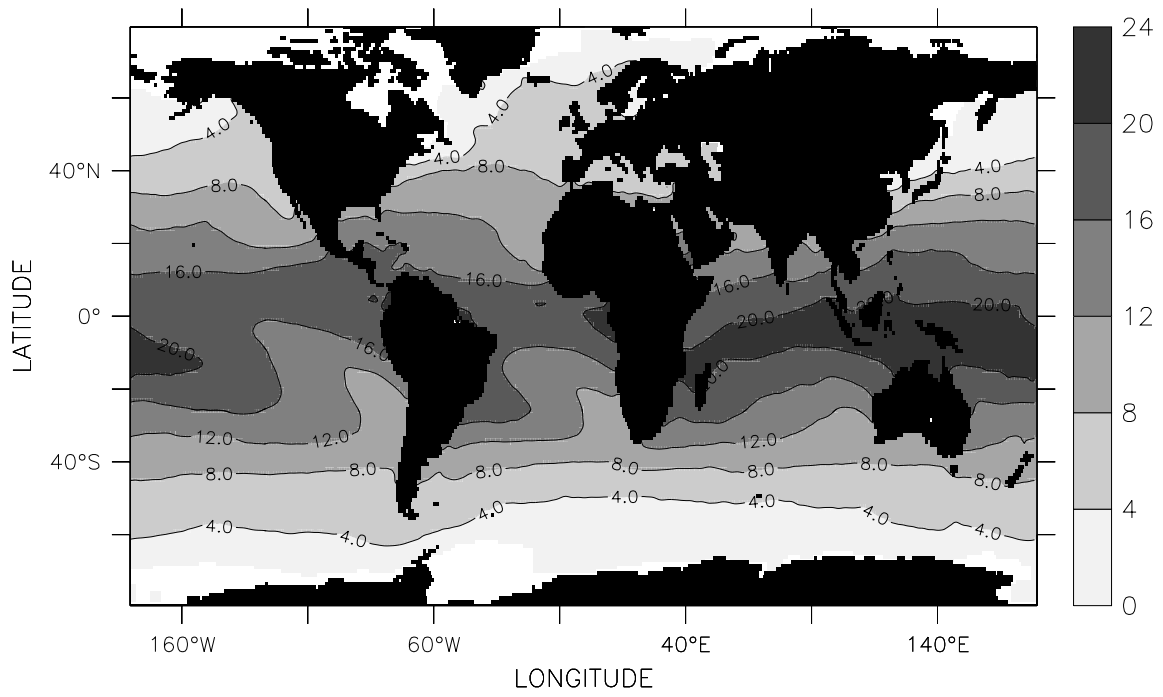
Fig.III.35 Air Humidity (g/kg), January
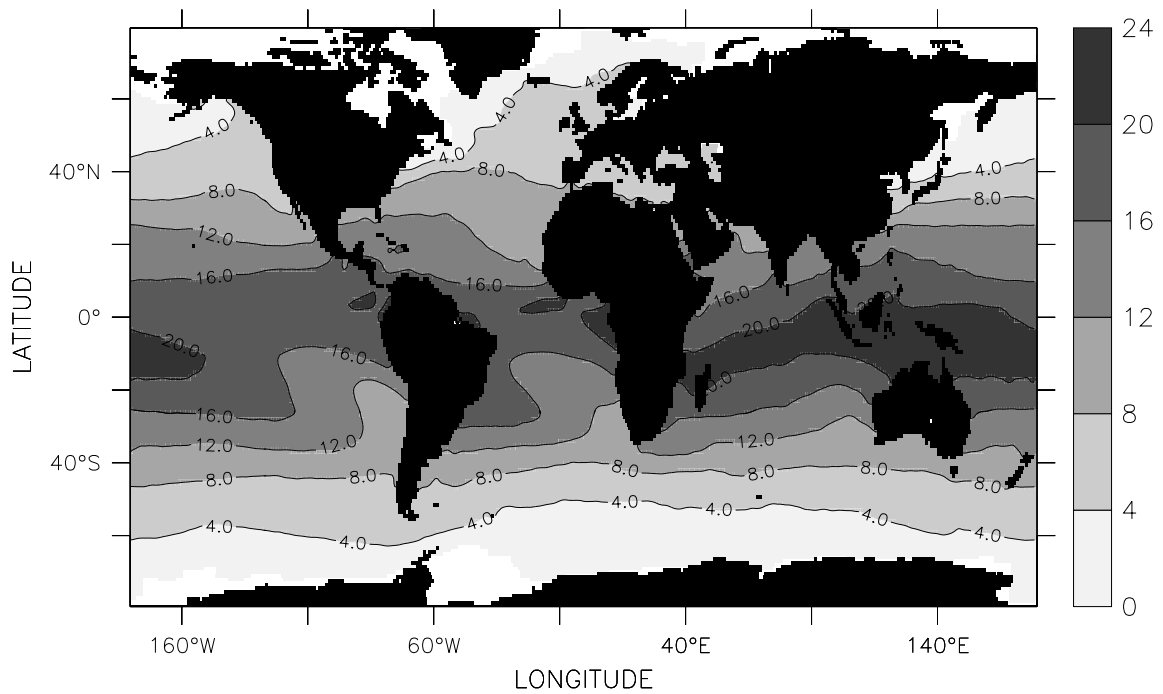
Fig.III.36 Air Humidity (g/kg), February
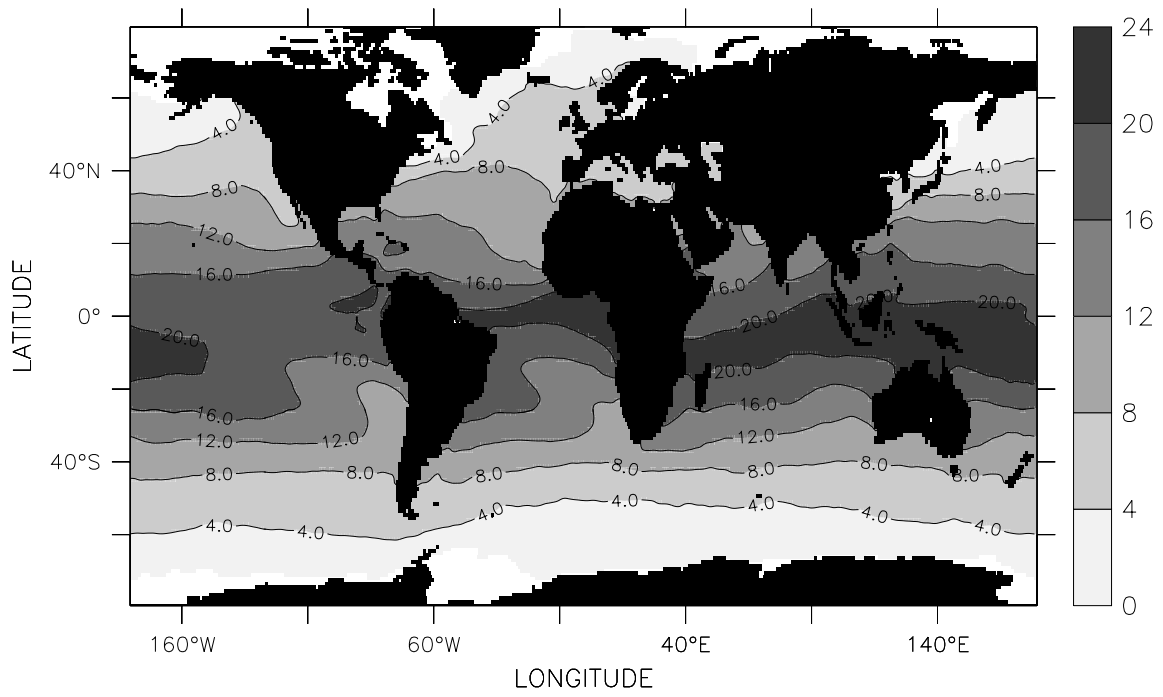
Fig.III.37 Air Humidity (g/kg), March
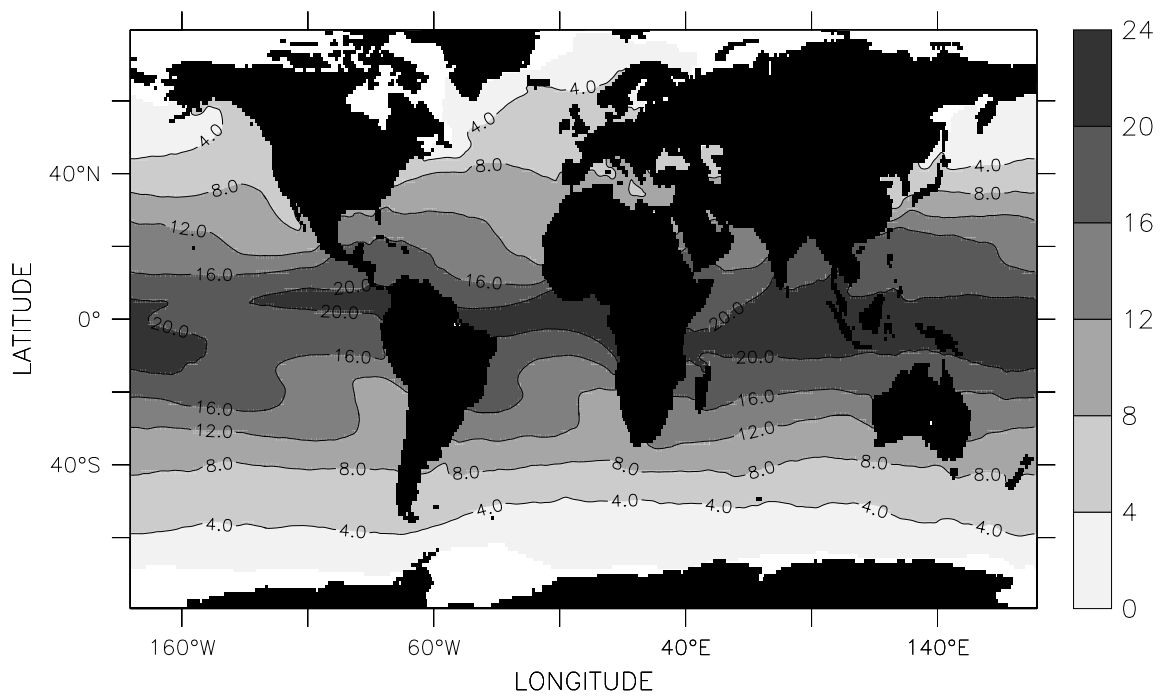
Fig.III.38 Air Humidity (g/kg), April
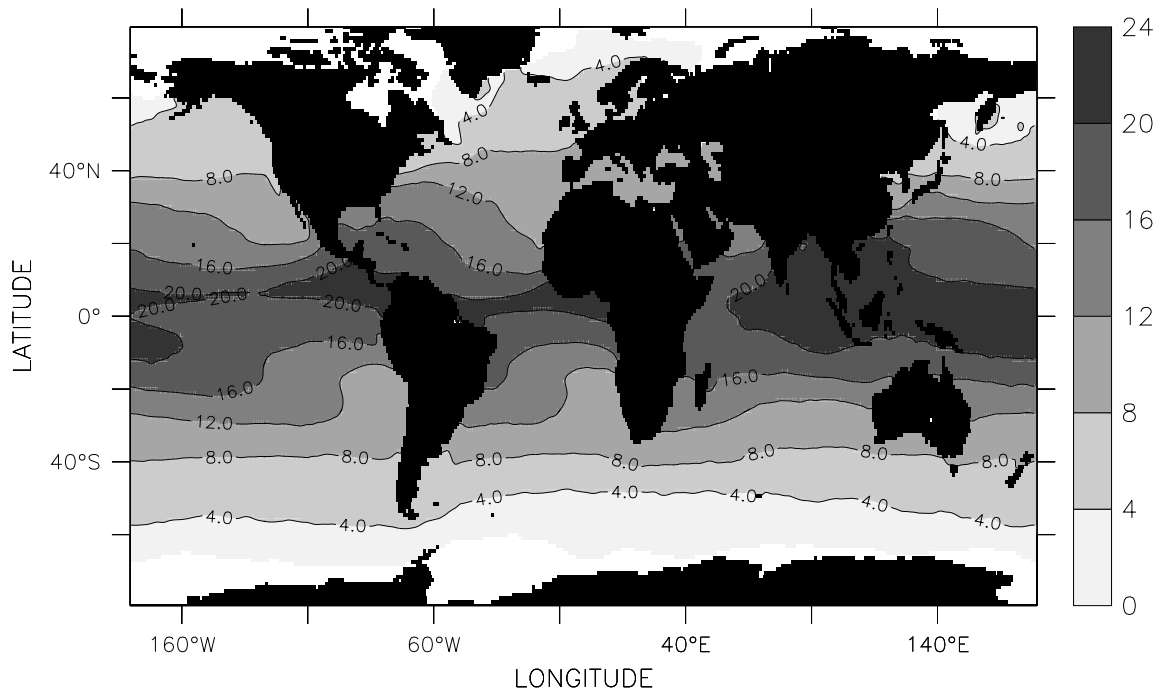
Fig.III.39 Air Humidity (g/kg), May
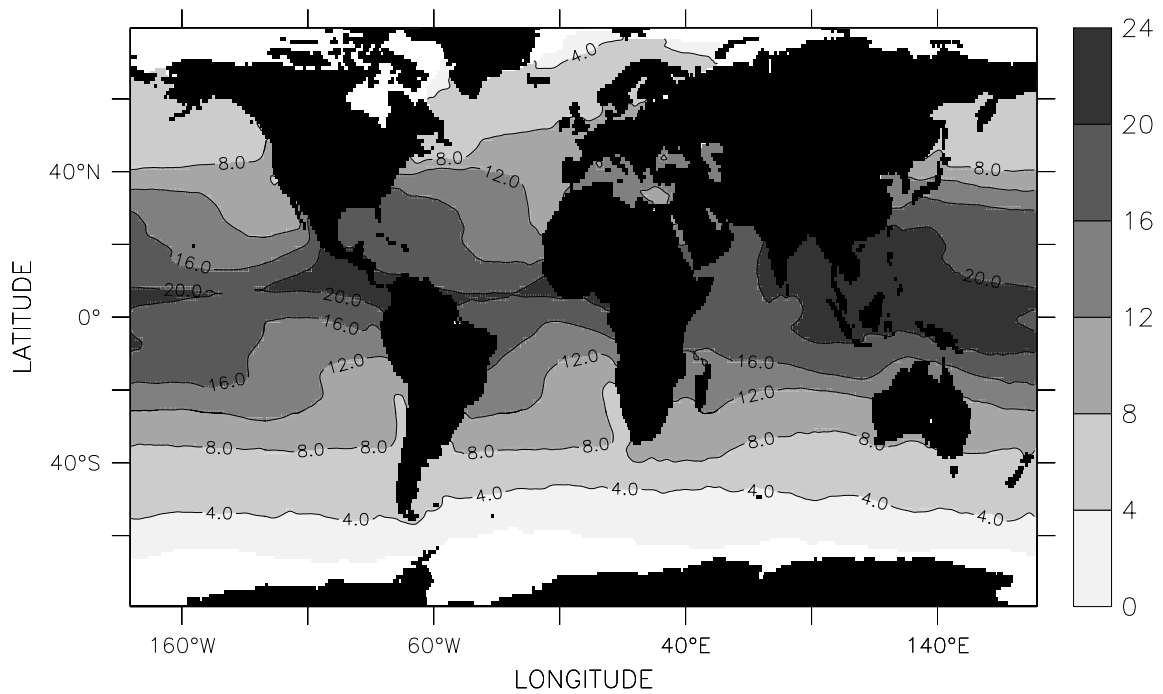
Fig.III.40 Air Humidity (g/kg), June
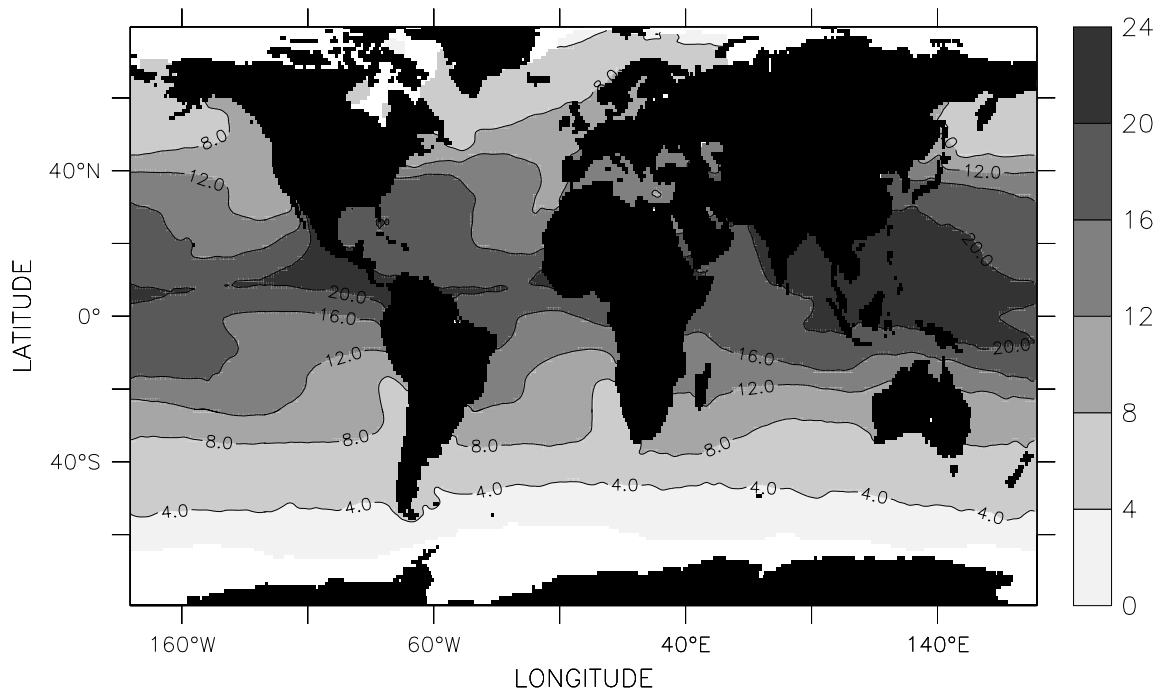
Fig.III.41 Air Humidity (g/kg), July
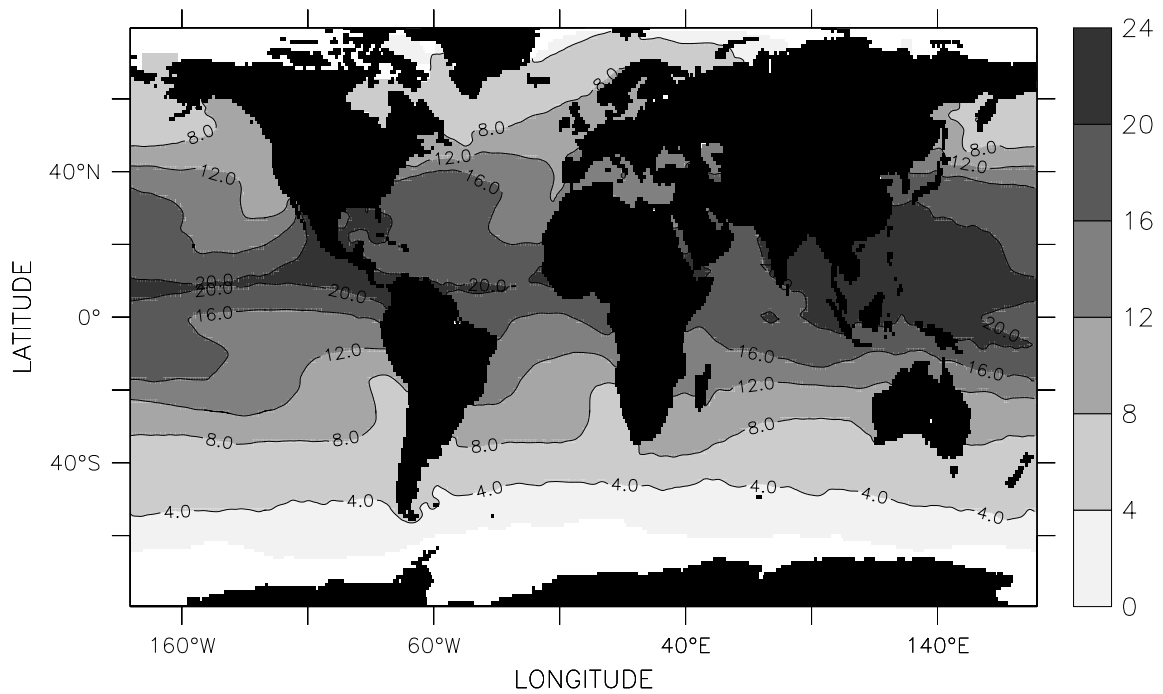
Fig.III.42 Air Humidity (g/kg), August
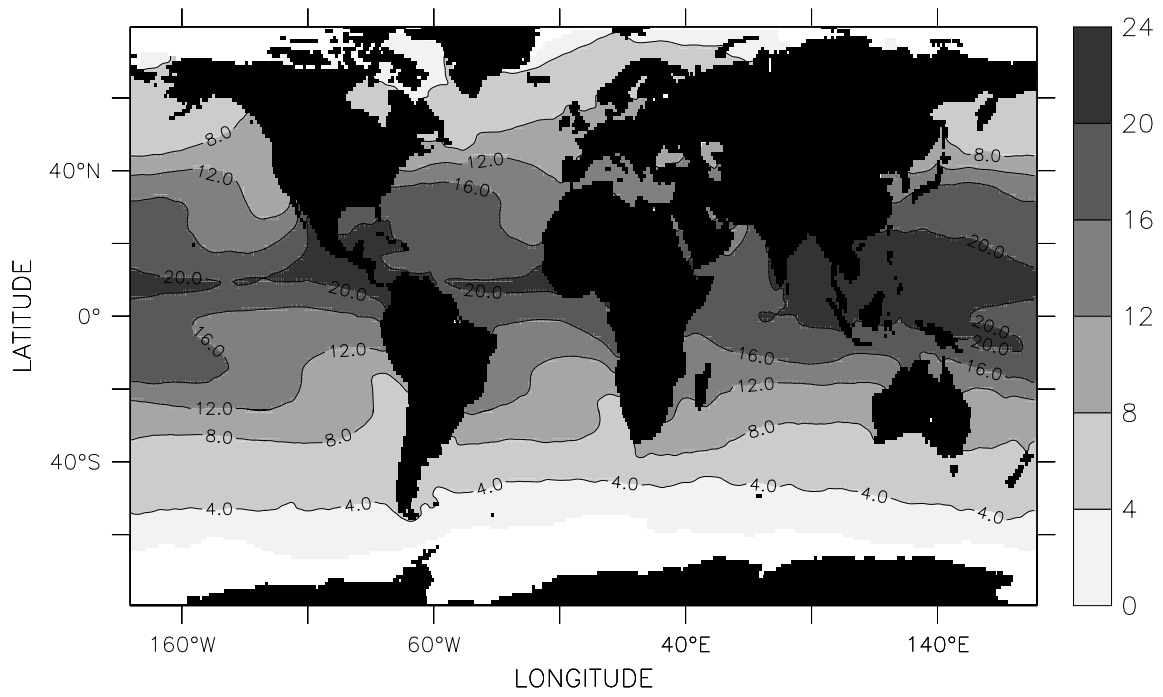
Fig.III.43 Air Humidity (g/kg), September
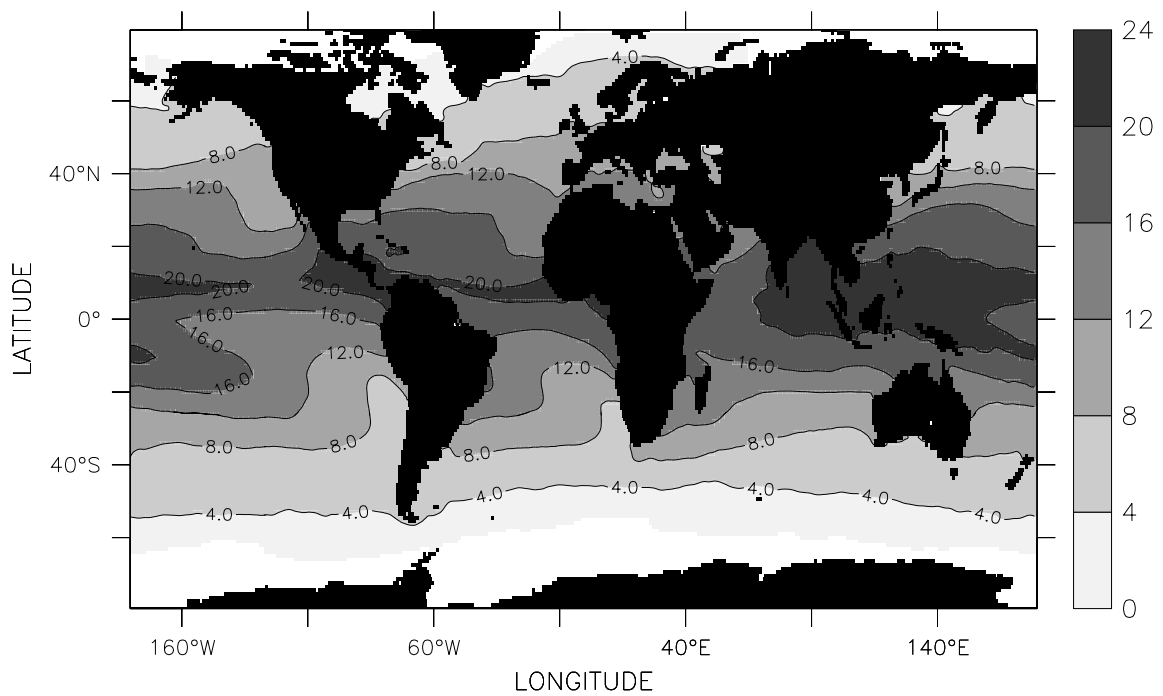
Fig.III.44 Air Humidity (g/kg), October
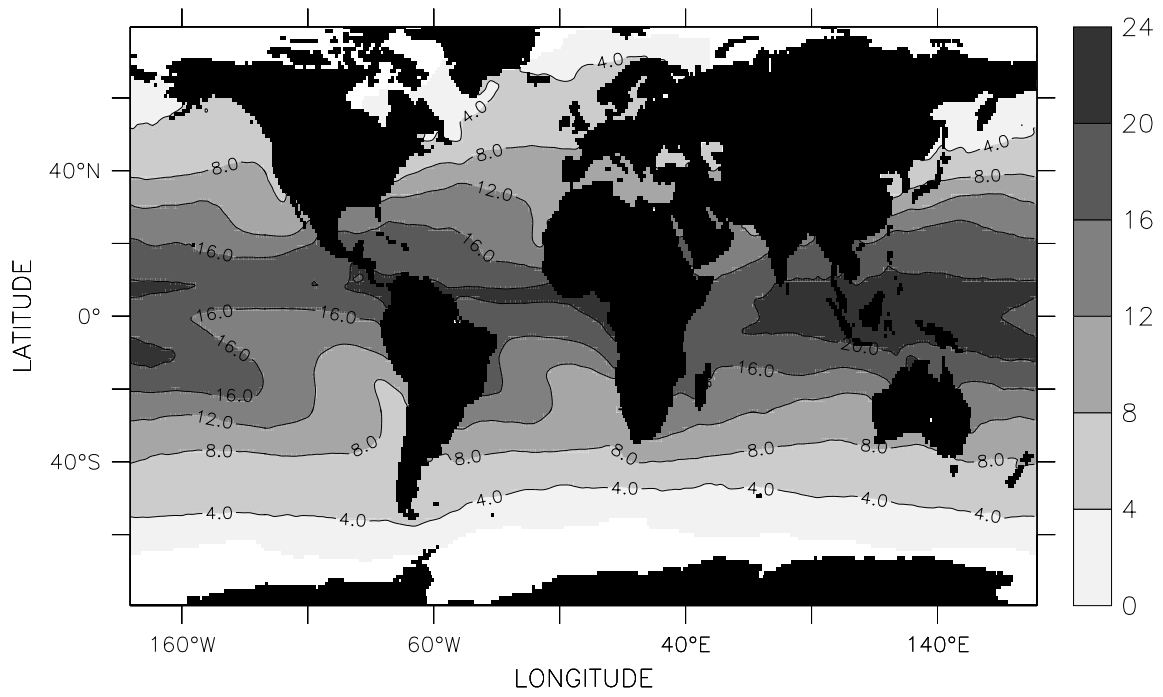
Fig.III.45 Air Humidity (g/kg), November
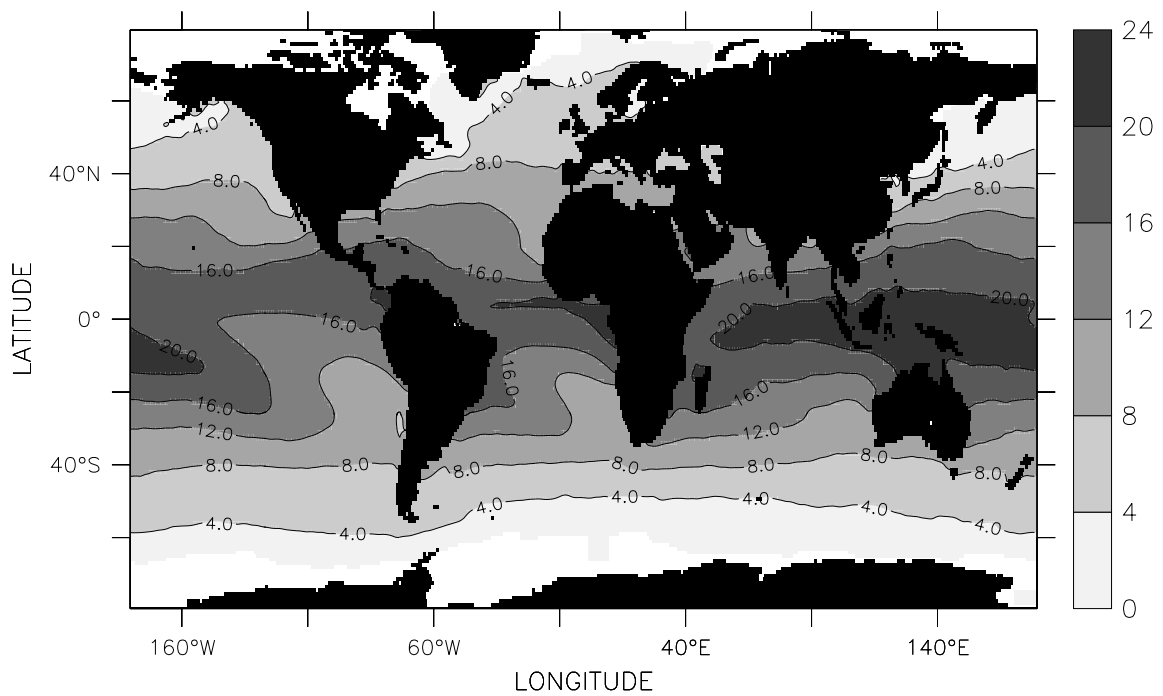
Fig.III.46 Air Humidity (g/kg), December
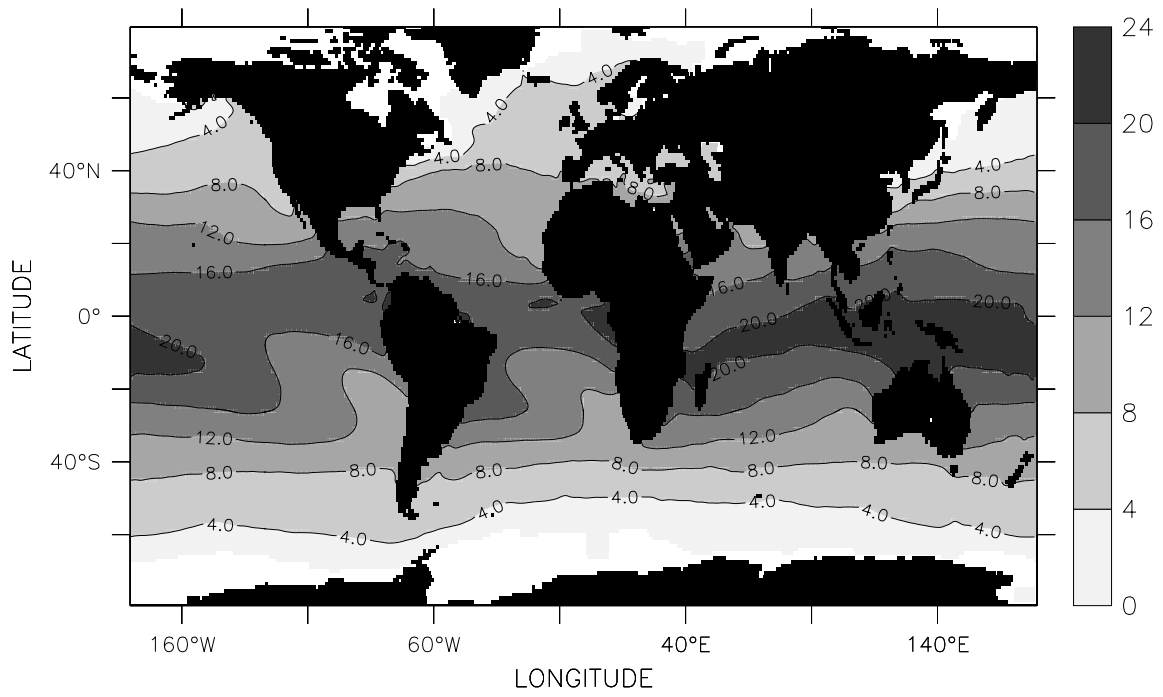
Fig.III.47 Air Humidity (g/kg), DJF
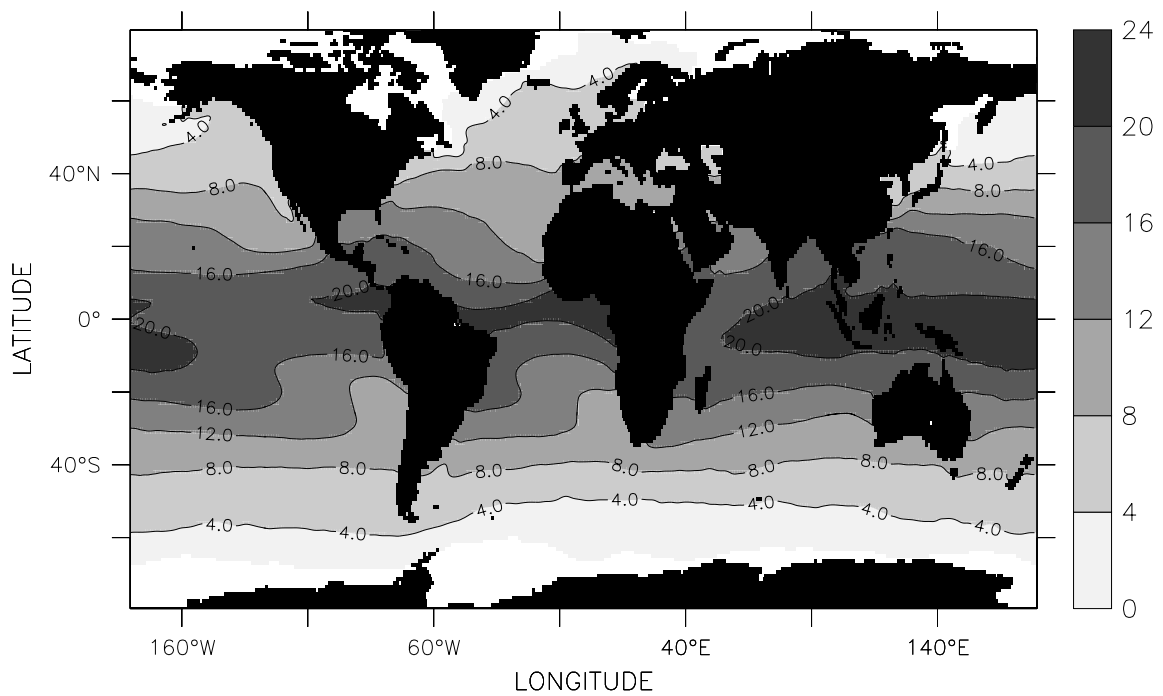
Fig.III.48 Air Humidity (g/kg), MAM
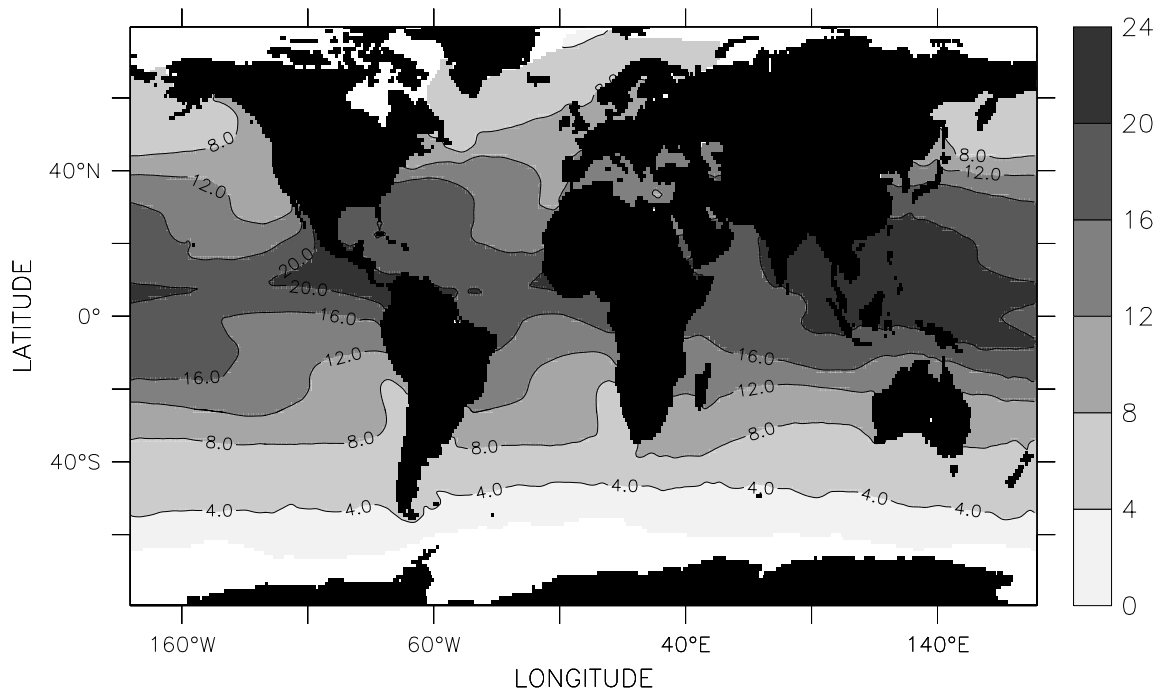
Fig.III.49 Air Humidity (g/kg), JJA
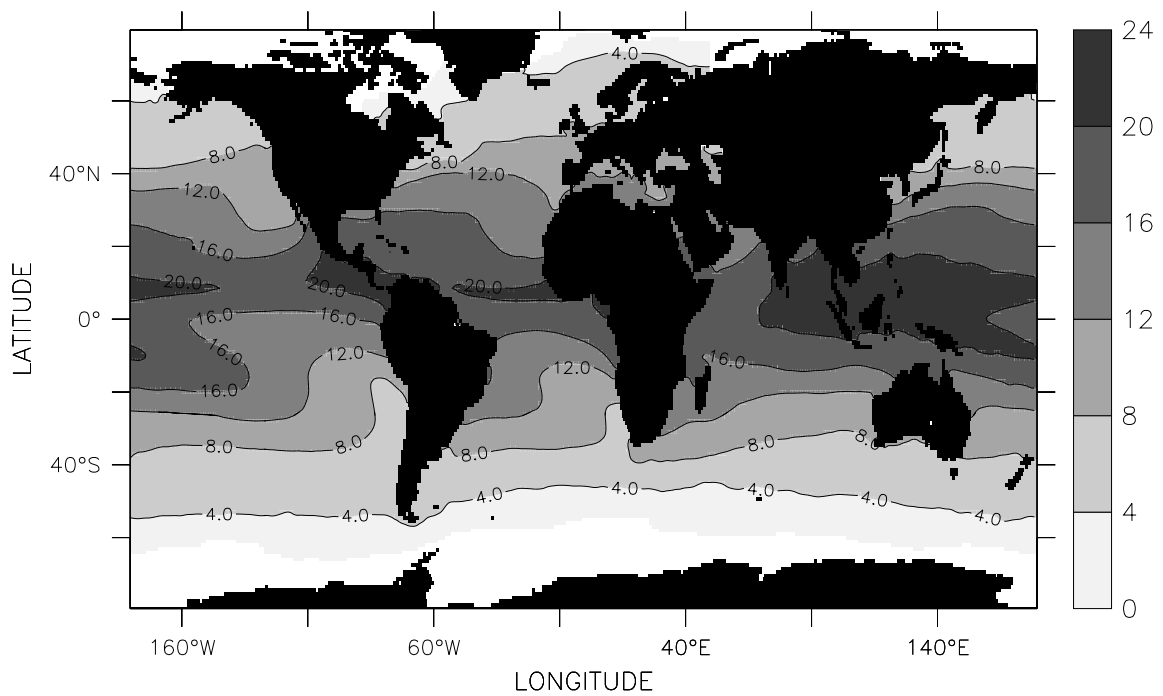
Fig.III.50 Air Humidity (g/kg), SON

40
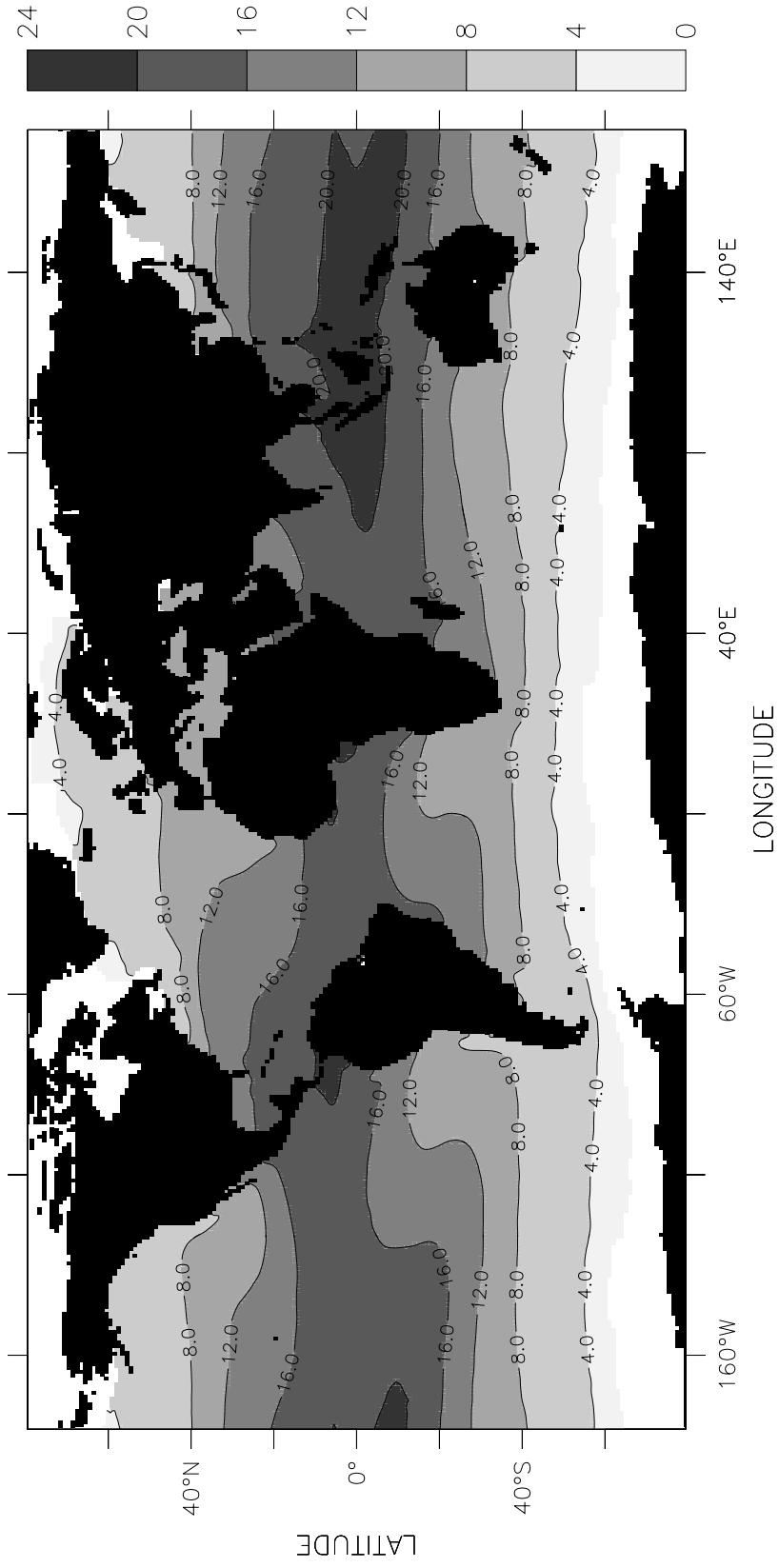
Fig.III.51 Air Humidity (g/kg), Annual
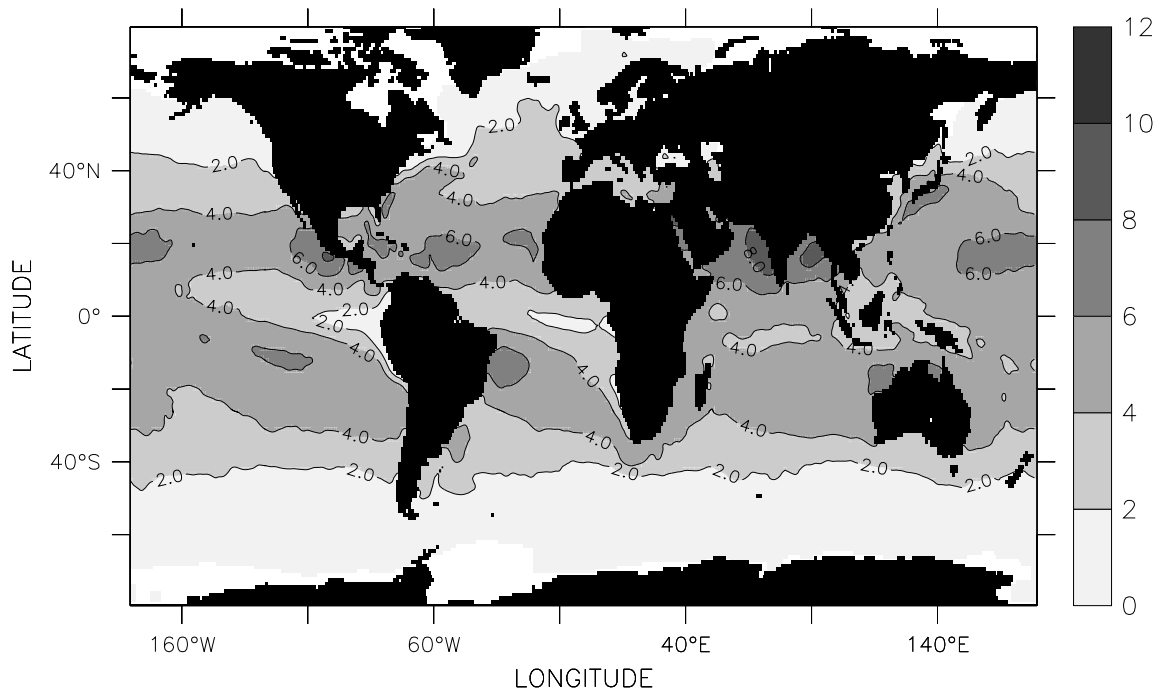
Fig.III.52 Humidity Difference (g/kg), January
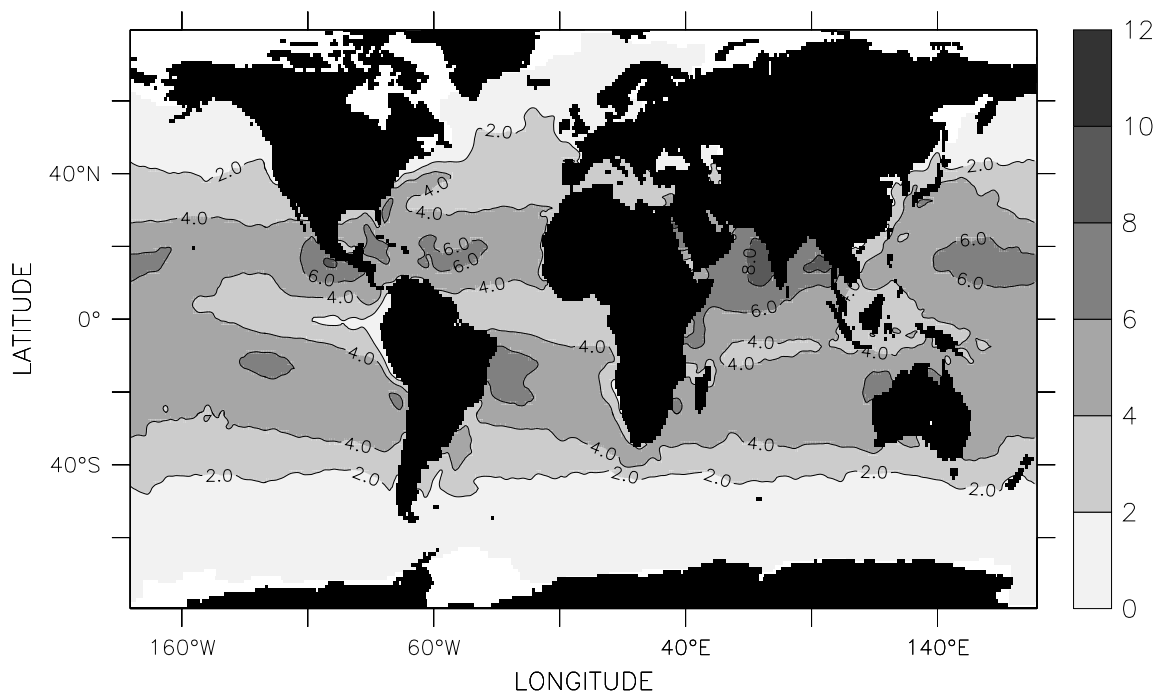
Fig.III.53 Humidity Difference (g/kg), February
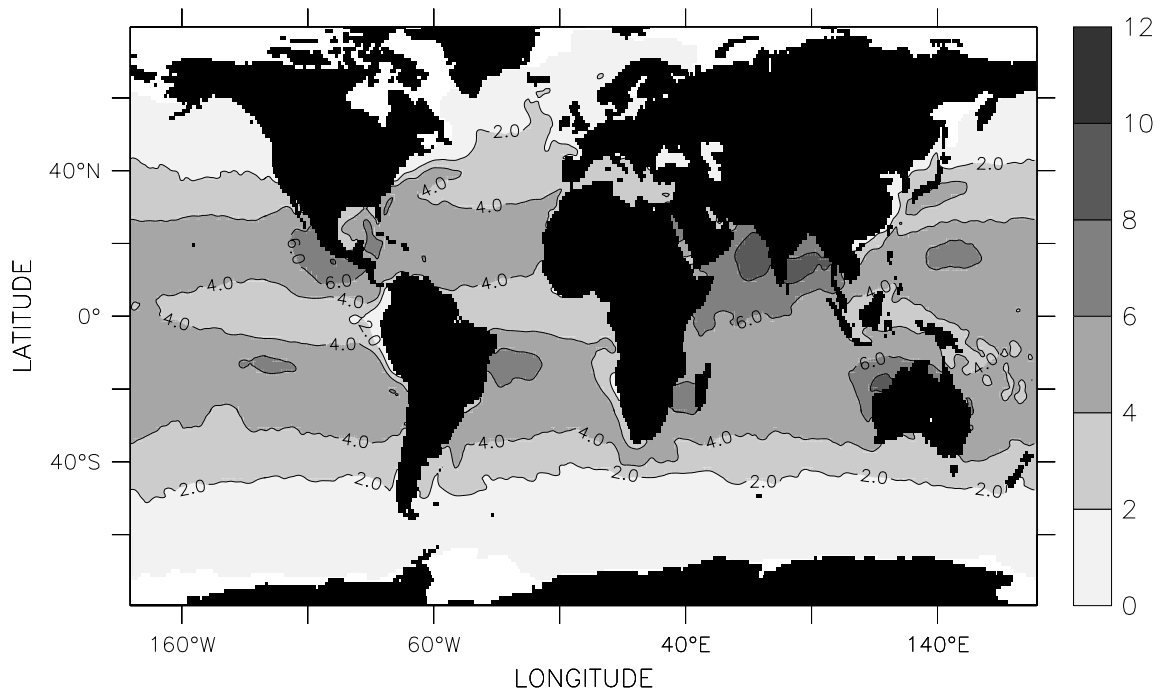
Fig.III.54 Humidity Difference (g/kg), March
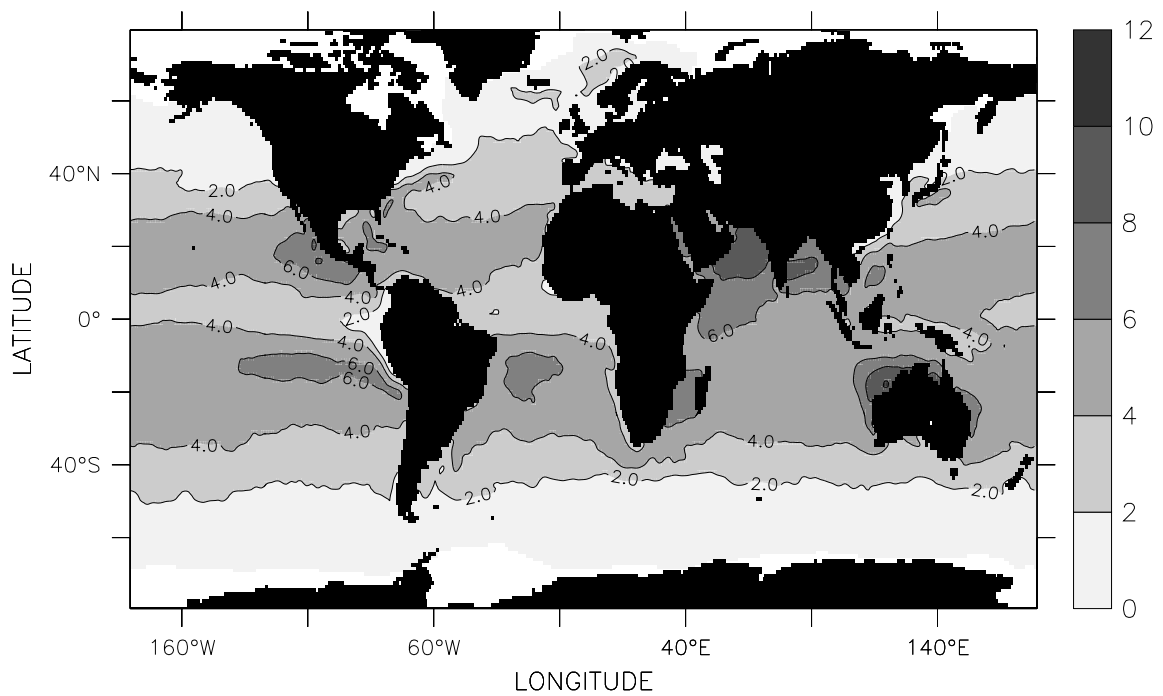
Fig.III.55 Humidity Difference (g/kg), April
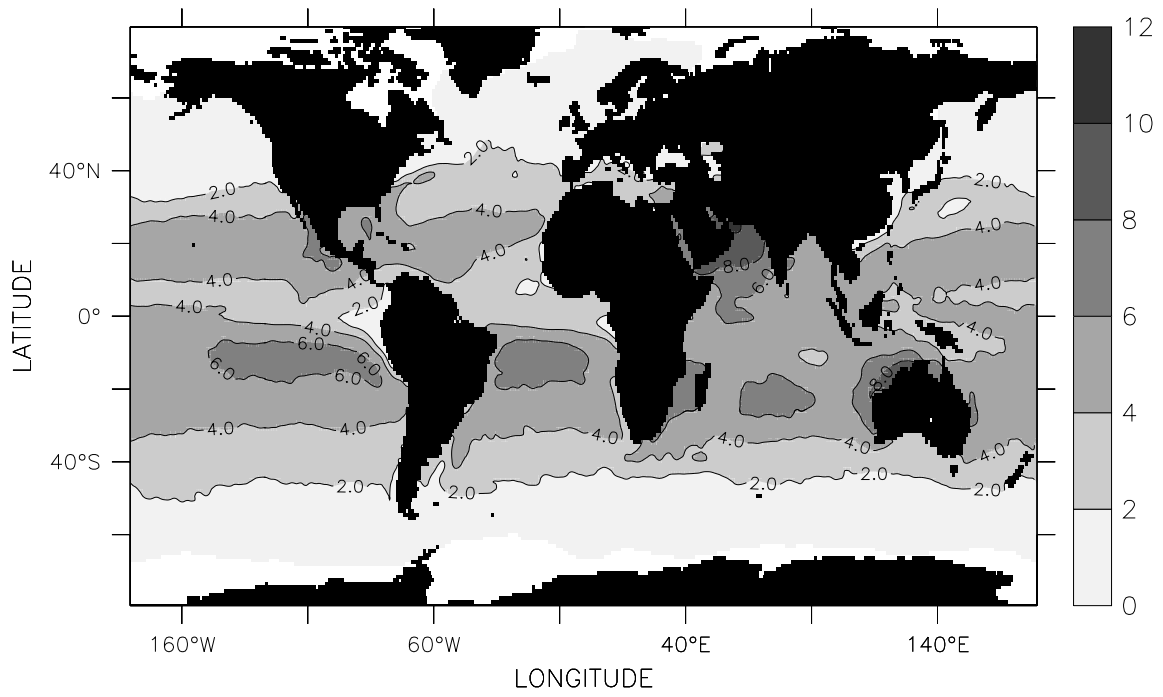
Fig.III.56 Humidity Difference (g/kg), May
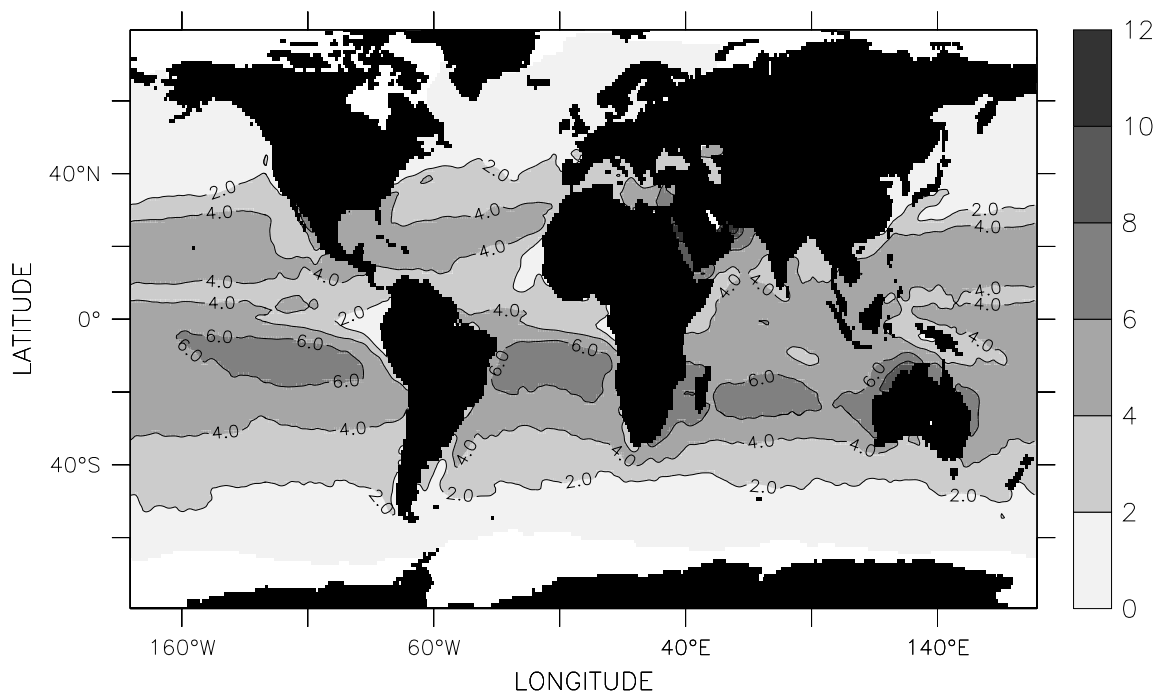
Fig.III.57 Humidity Difference (g/kg), June

44
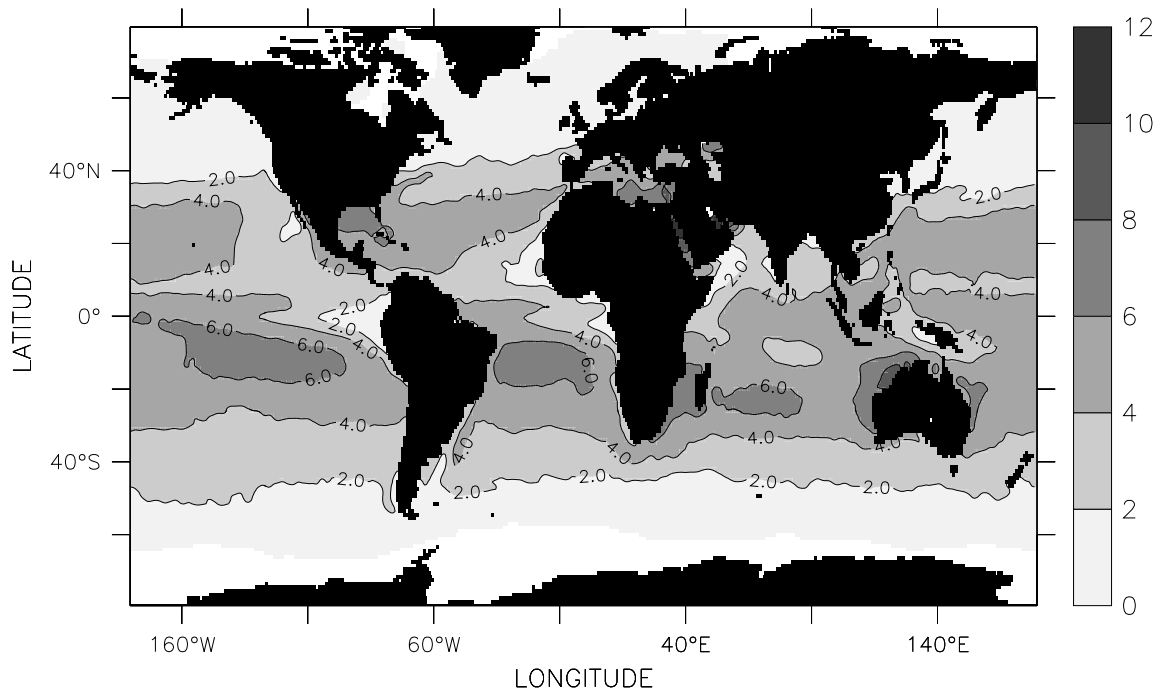
Fig.III.58 Humidity Difference (g/kg), July
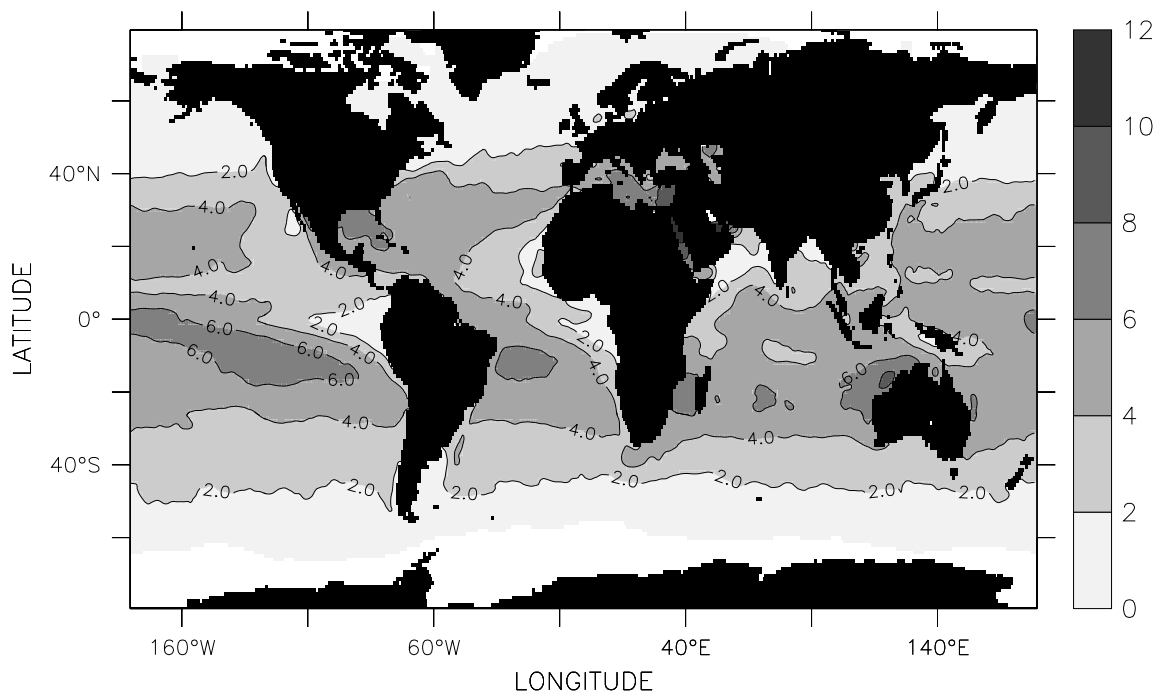
Fig.III.59 Humidity Difference (g/kg), August
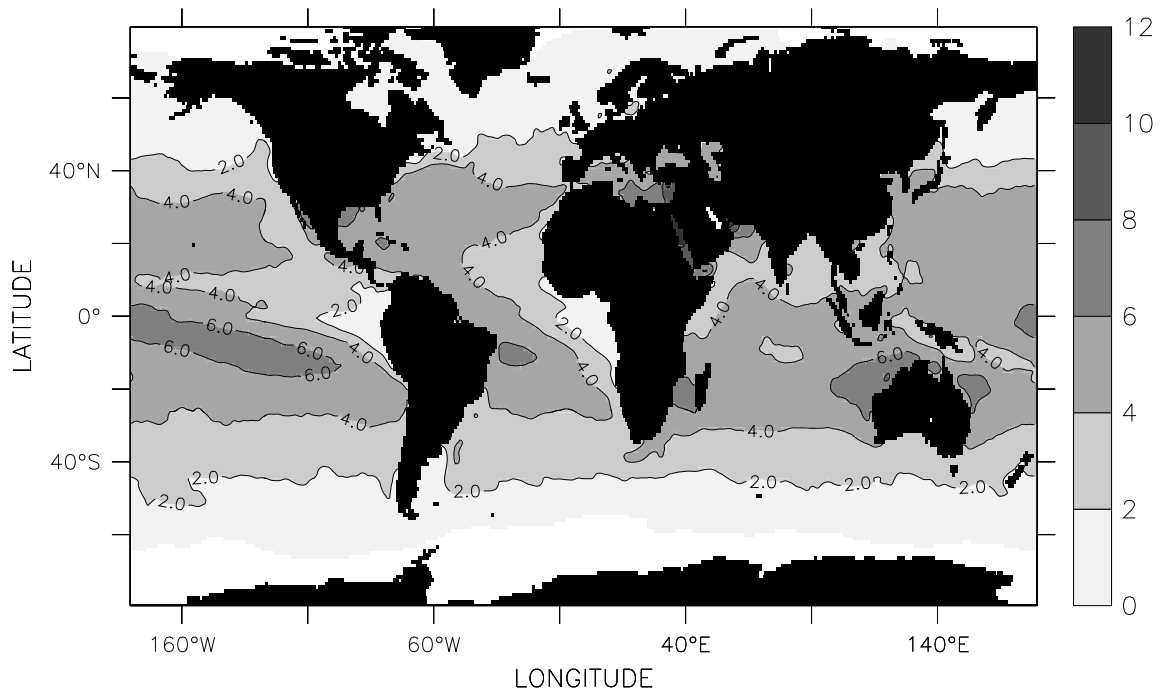
Fig.III.60 Humidity Difference (g/kg), September
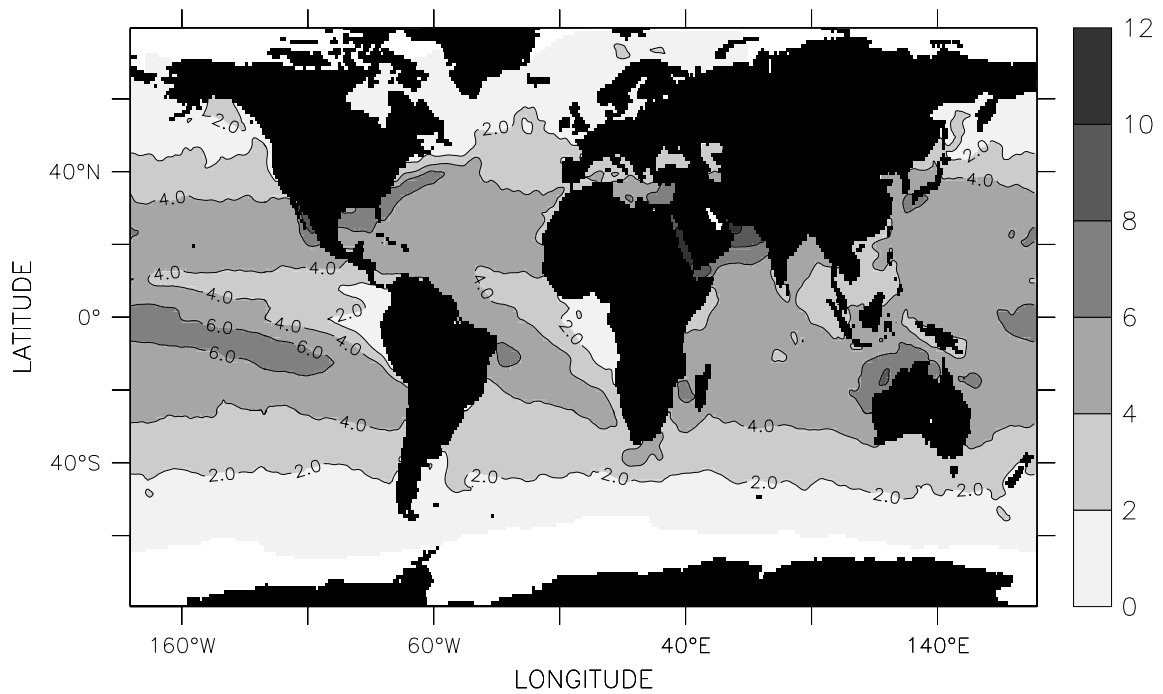
Fig.III.61 Humidity Difference (g/kg), October
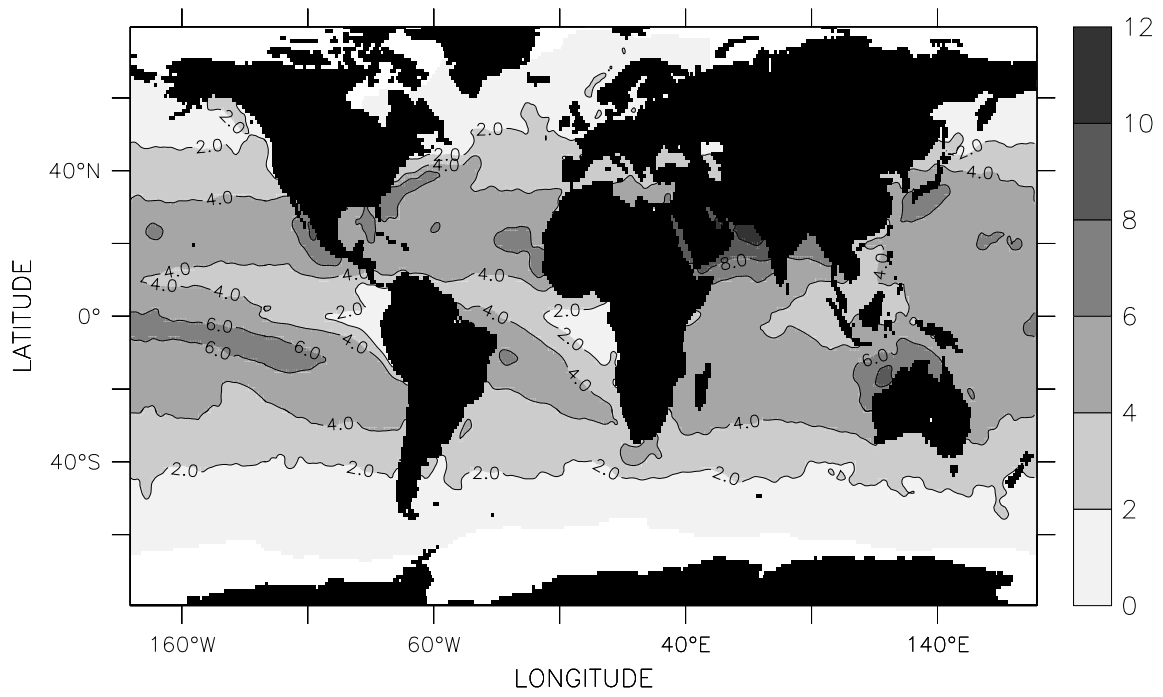
Fig.III.62 Humidity Difference (g/kg), November
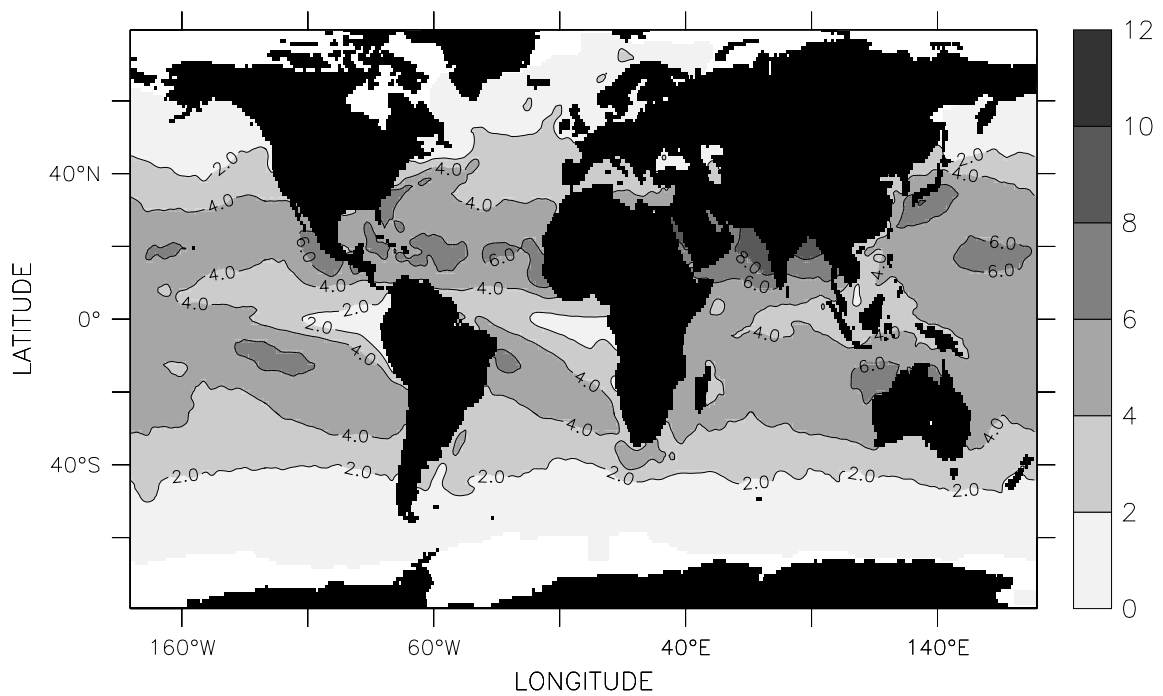
Fig.III.63 Humidity Difference (g/kg), December
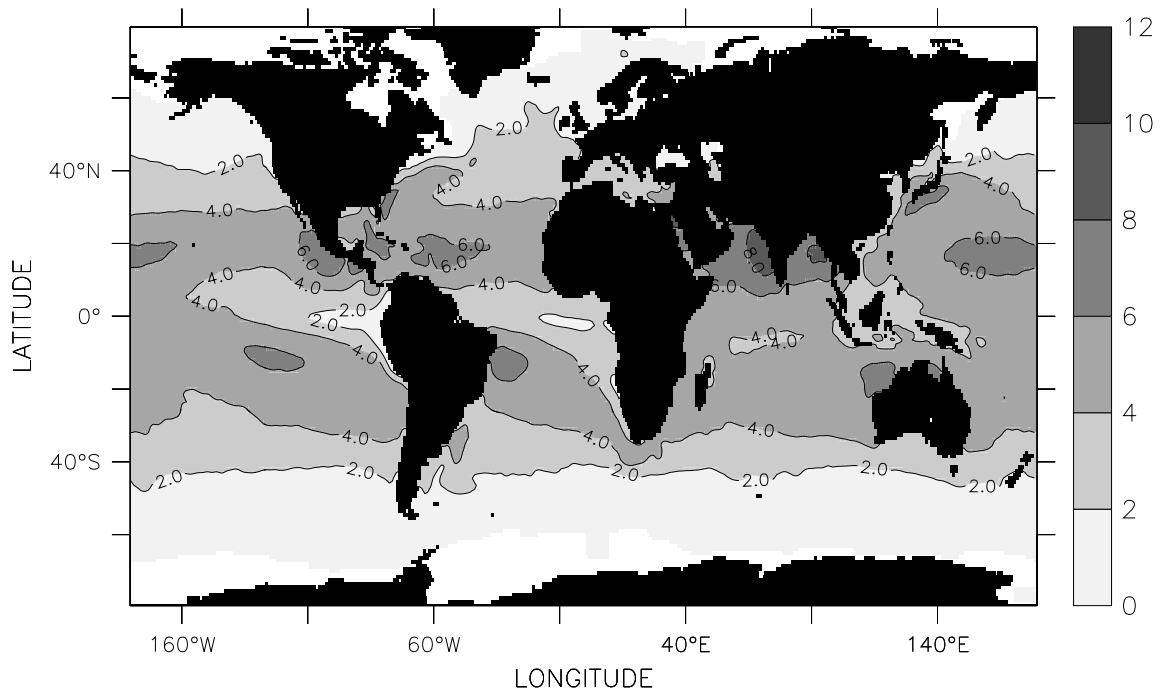
Fig.III.64 Humidity Difference (g/kg), DJF
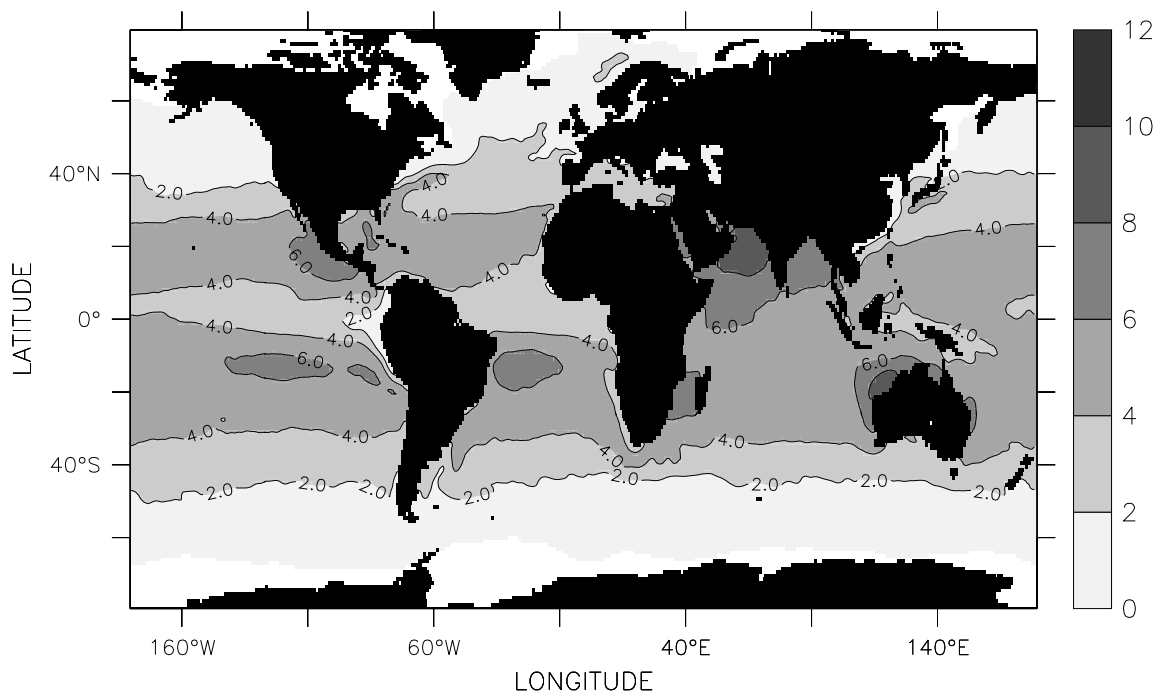
Fig.III.65 Humidity Difference (g/kg), MAM
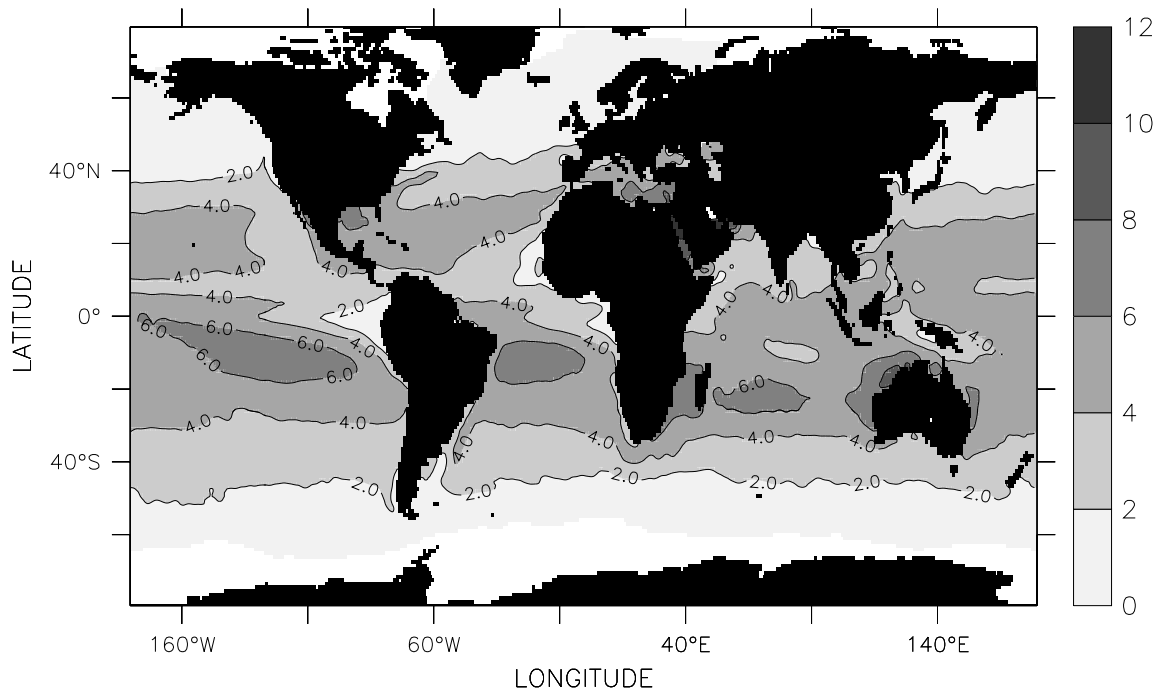
Fig.III.66 Humidity Difference (g/kg), JJA
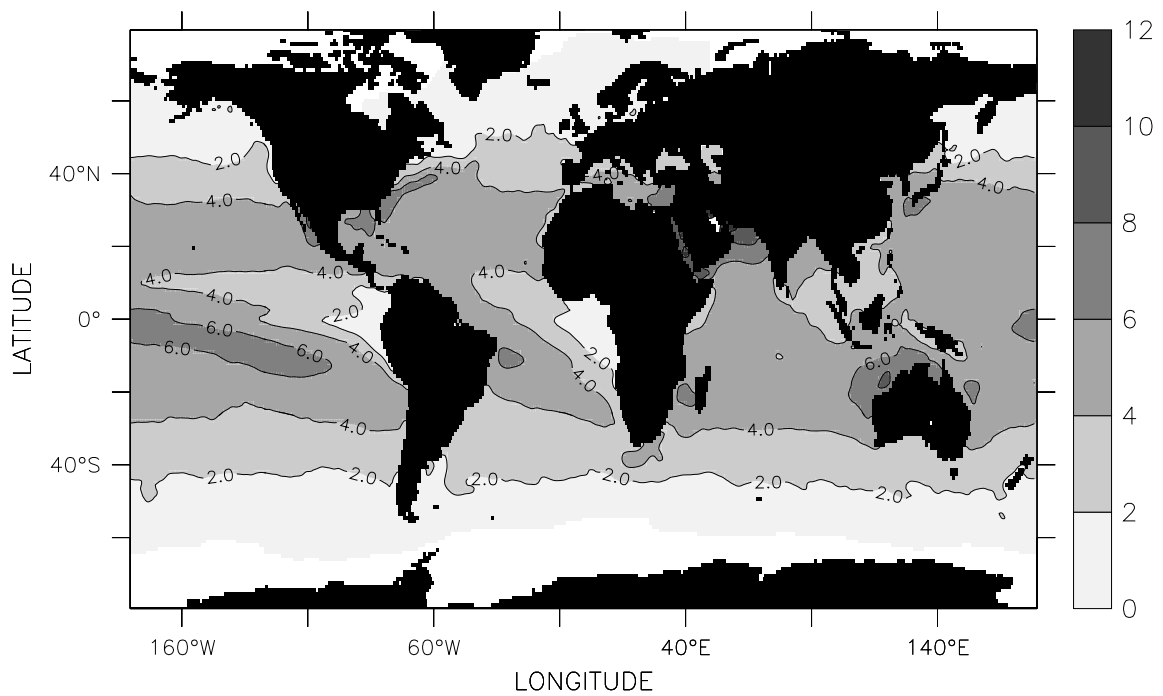
Fig.III.67 Humidity Difference (g/kg), SON
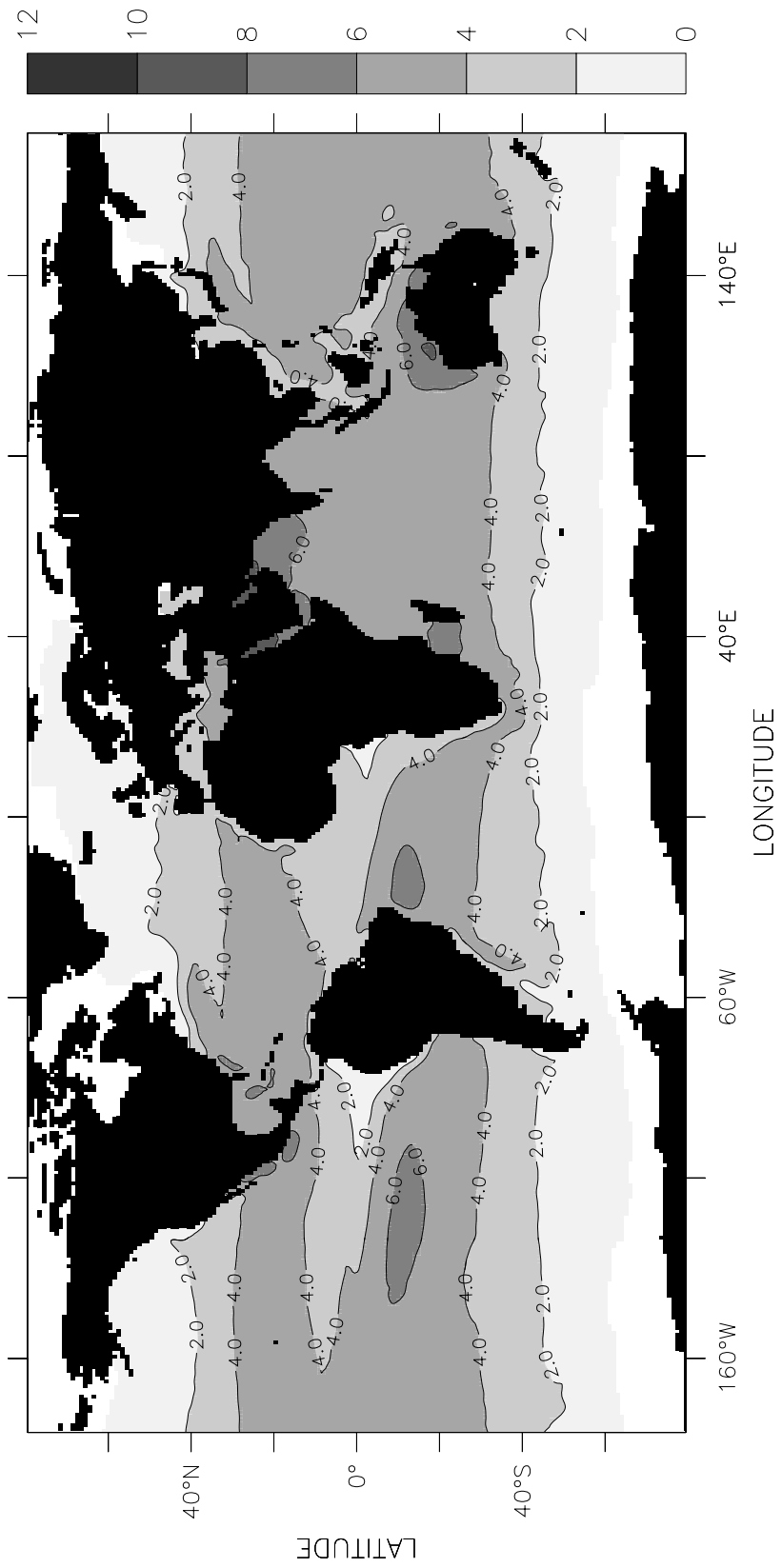
Fig.III.68 Humidity Difference (g/kg), Annual
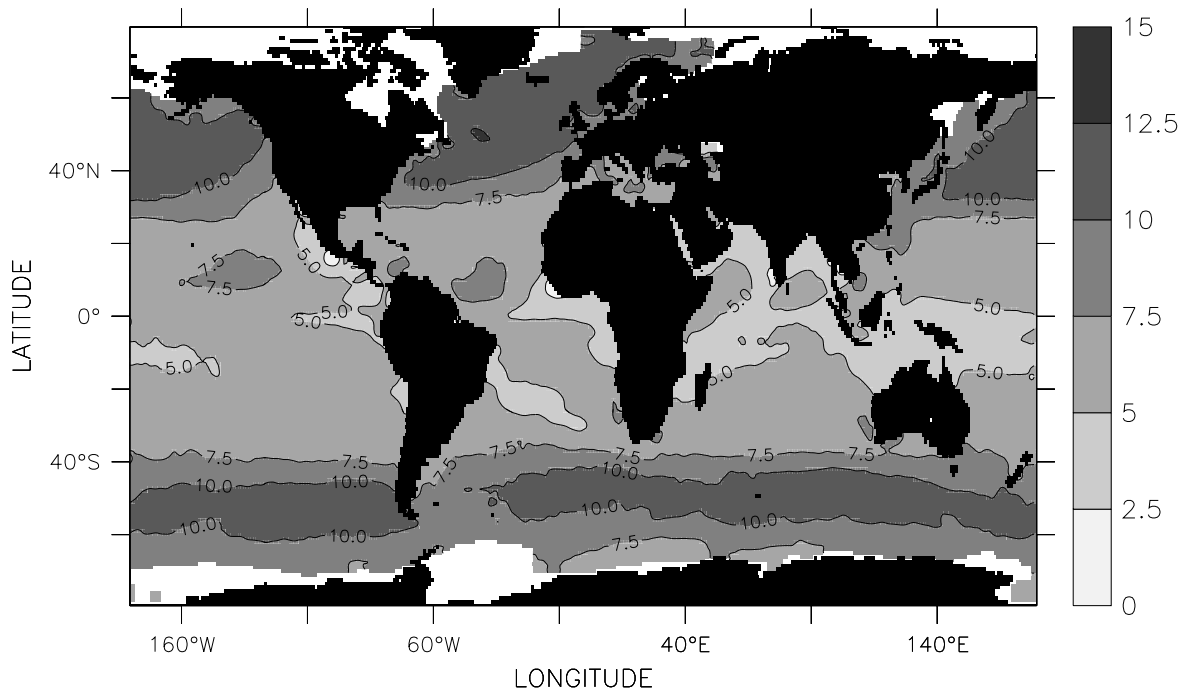
Fig.III.69 Wind Speed (m/s), January
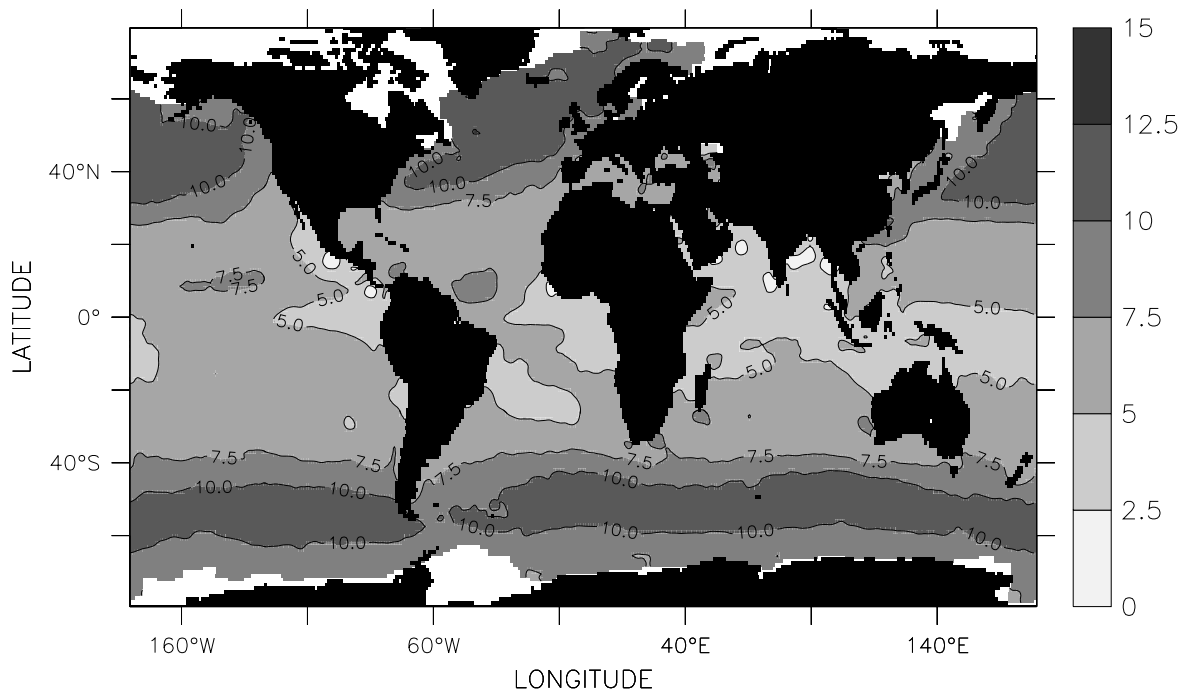
Fig.III.70 Wind Speed (m/s), February
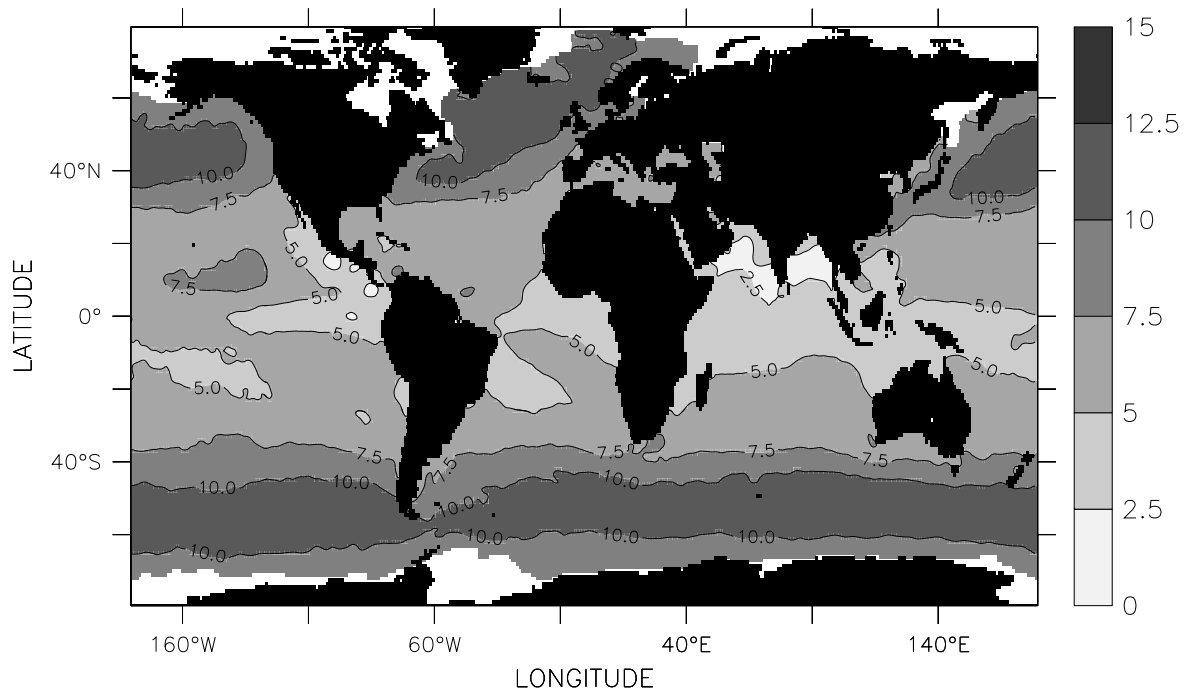
Fig.III.71 Wind Speed (m/s), March
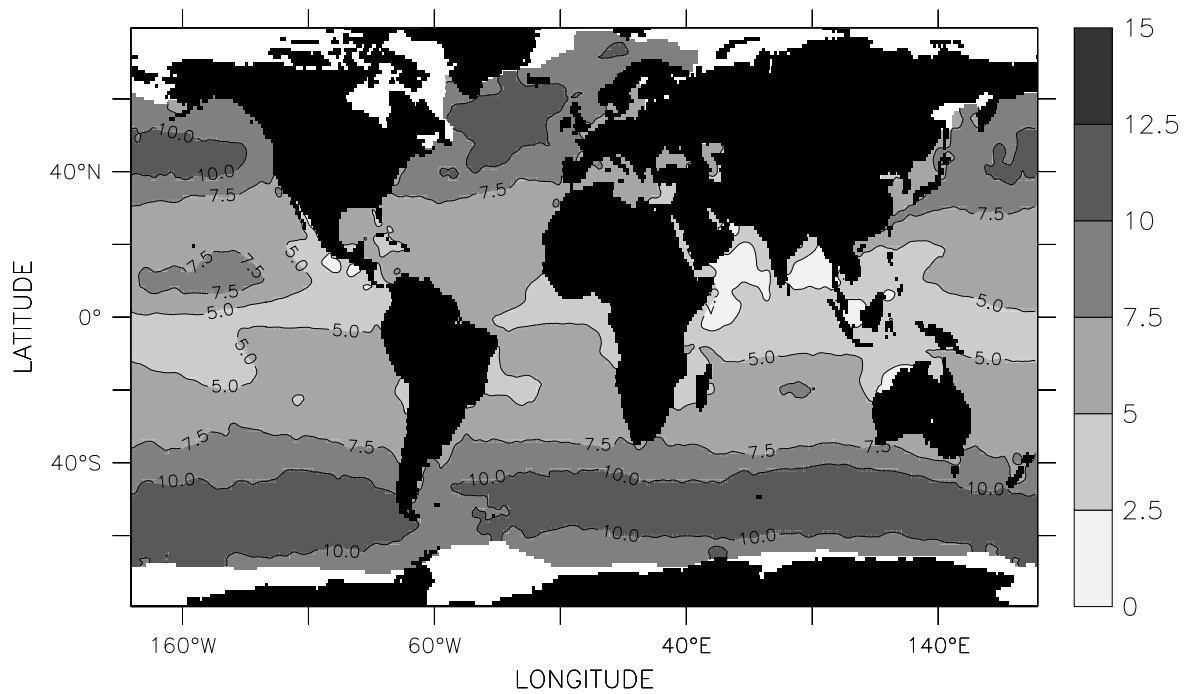
Fig.III.72 Wind Speed (m/s), April
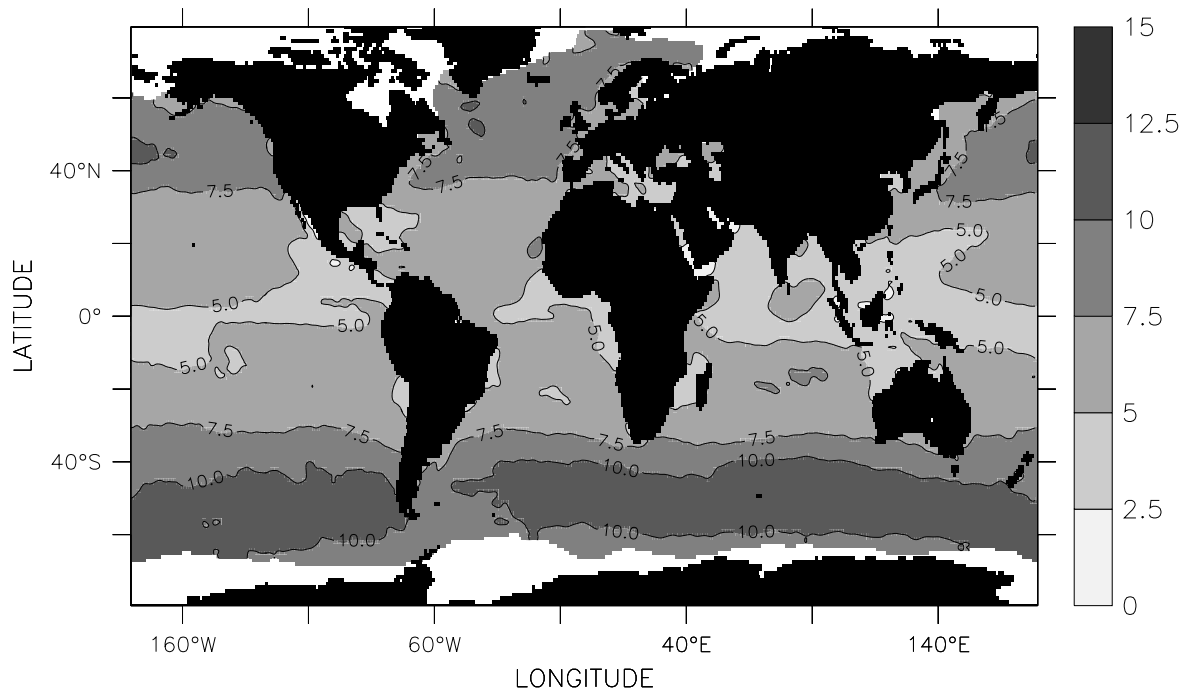
Fig.III.73 Wind Speed (m/s), May
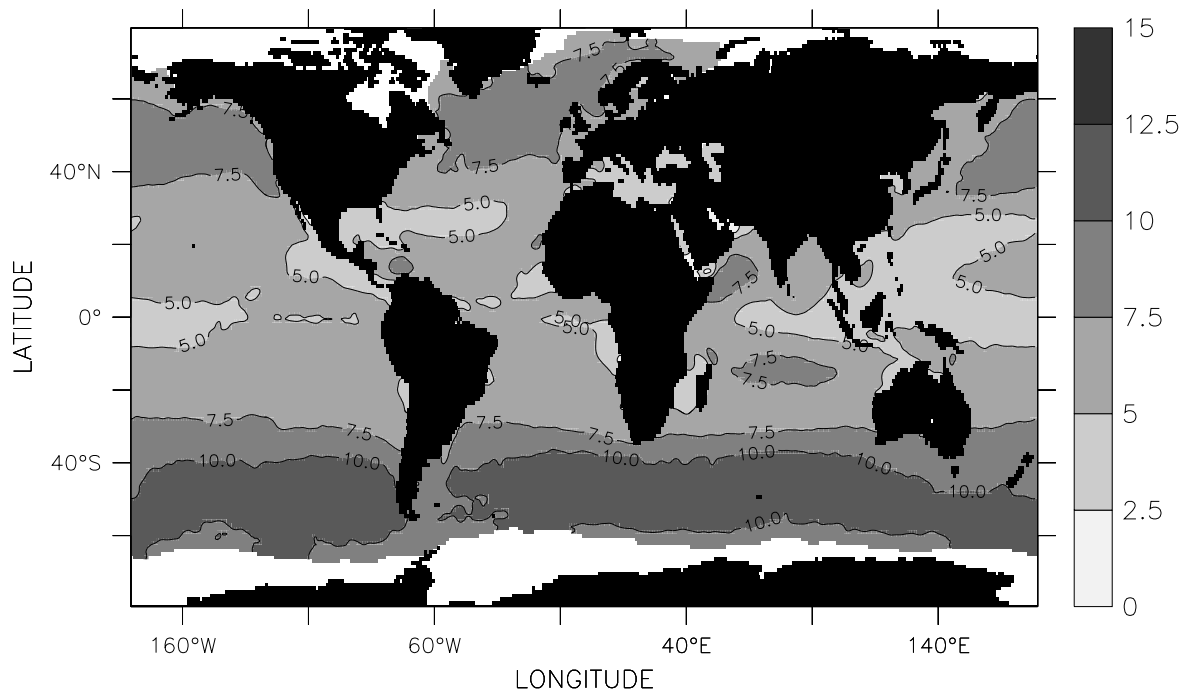
Fig.III.74 Wind Speed (m/s), June

53
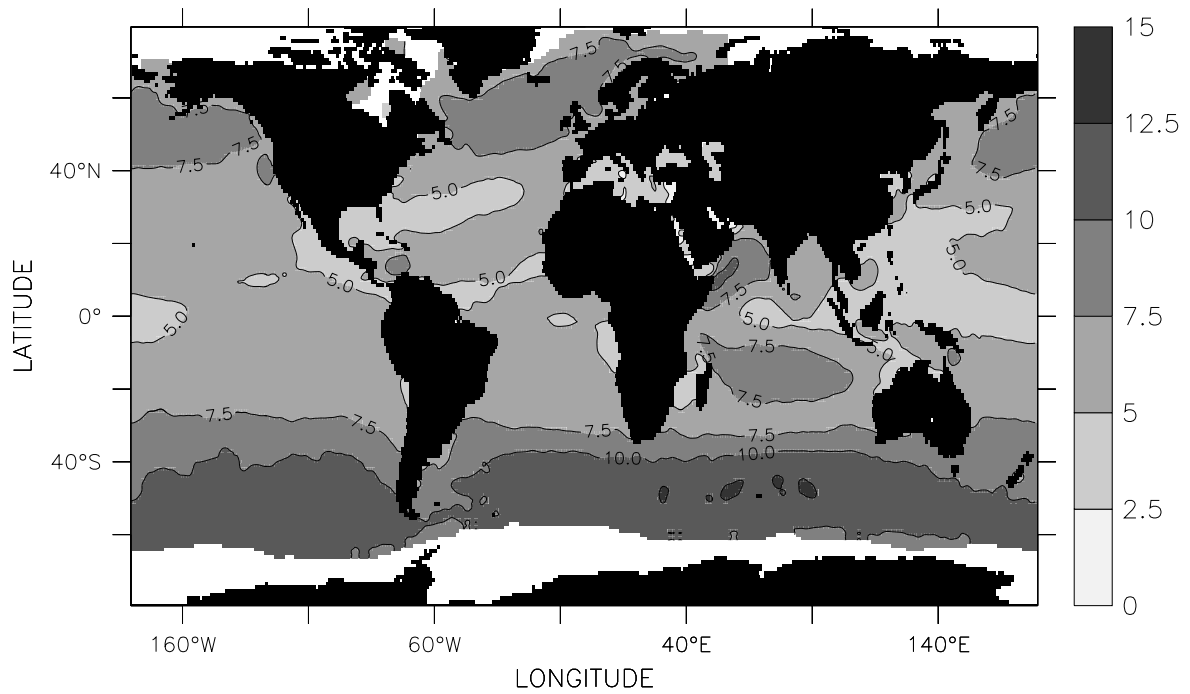
Fig.III.75 Wind Speed (m/s), July
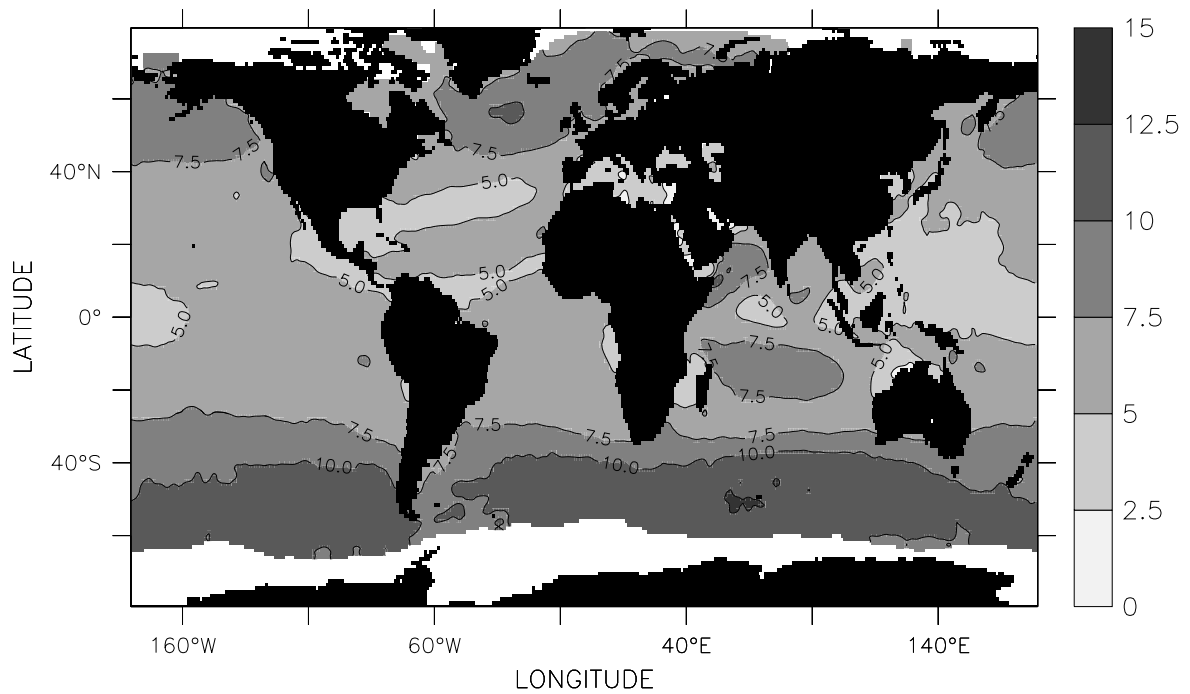
Fig.III.76 Wind Speed (m/s), August
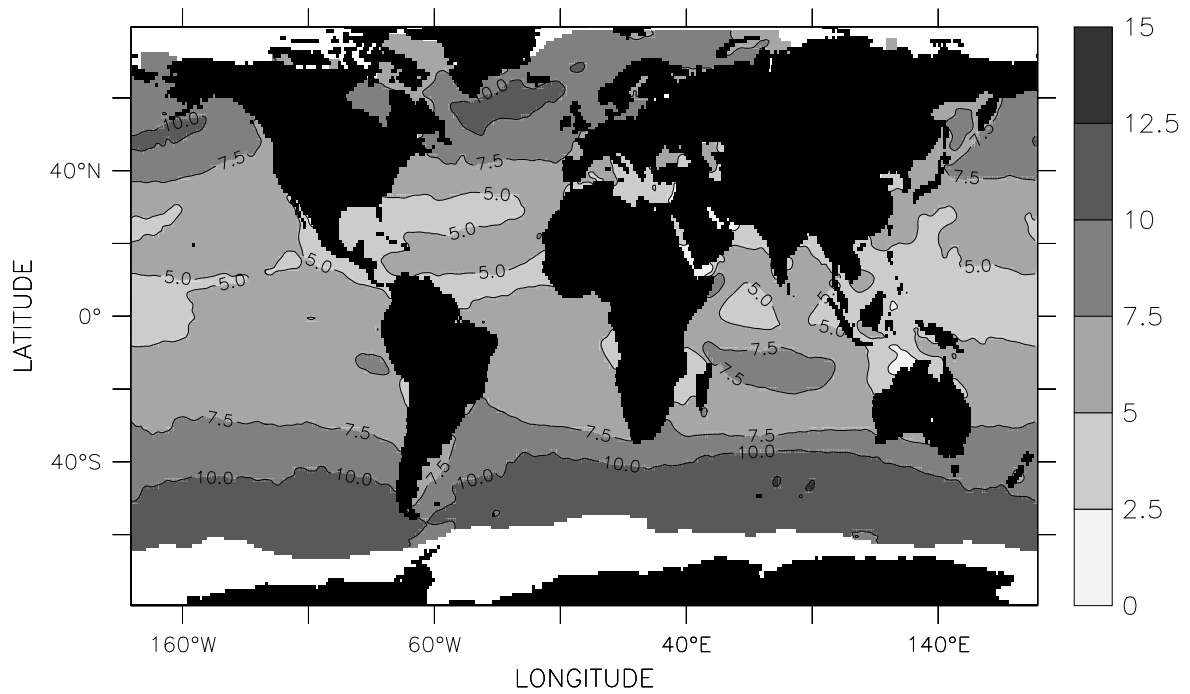
Fig.III.77 Wind Speed (m/s), September
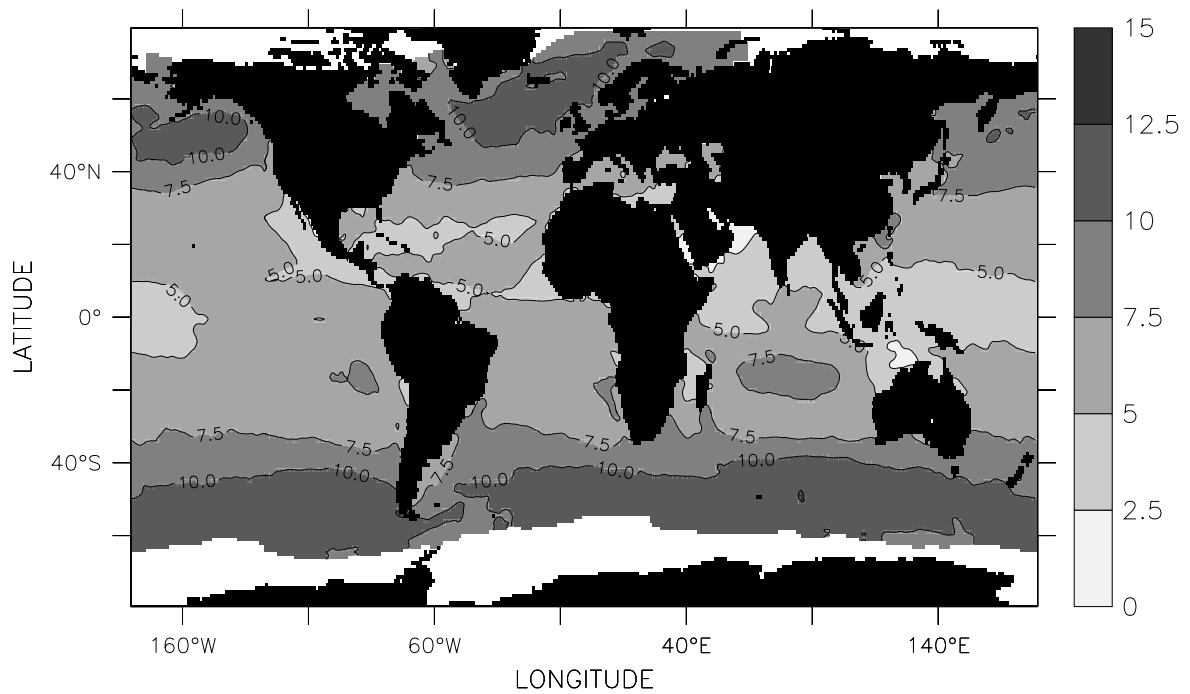
Fig.III.78 Wind Speed (m/s), October
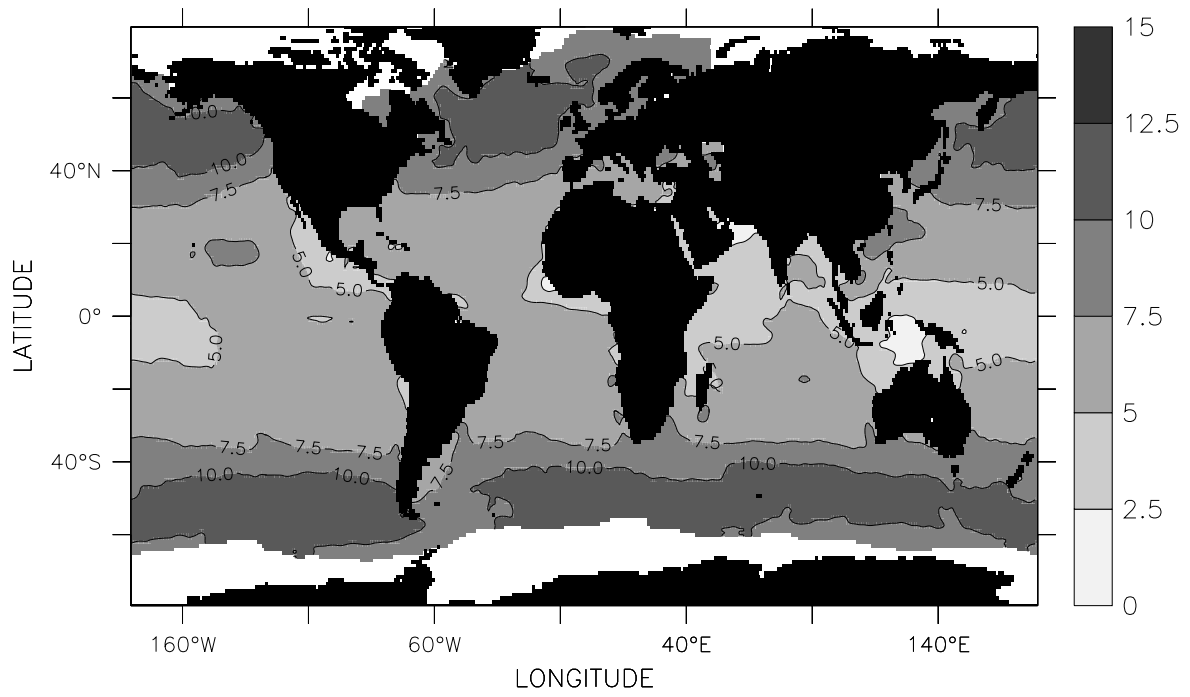
Fig.III.79 Wind Speed (m/s), November
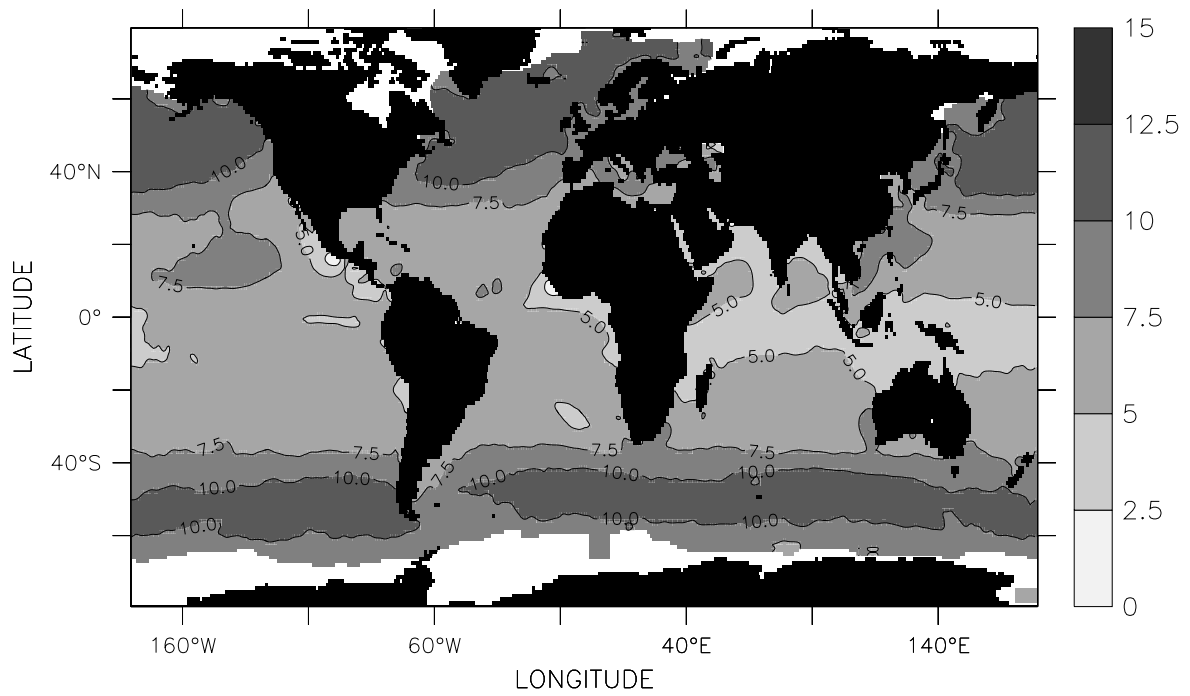
Fig.III.80 Wind Speed (m/s), December
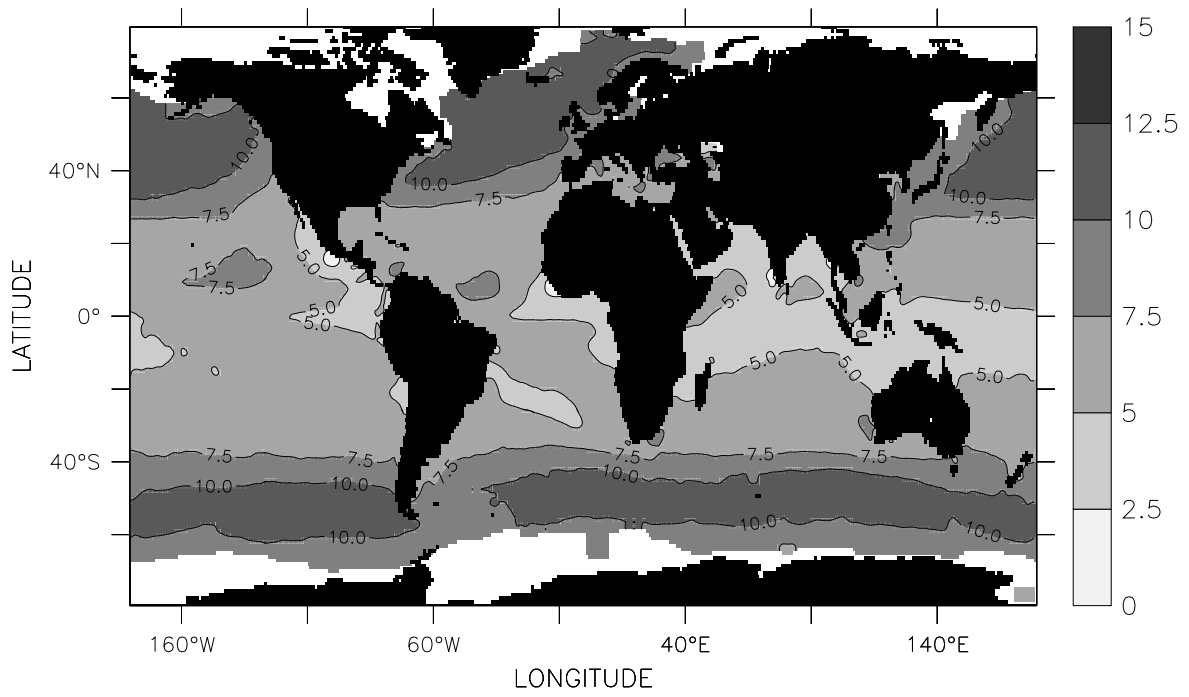
Fig.III.81 Wind Speed (m/s), DJF
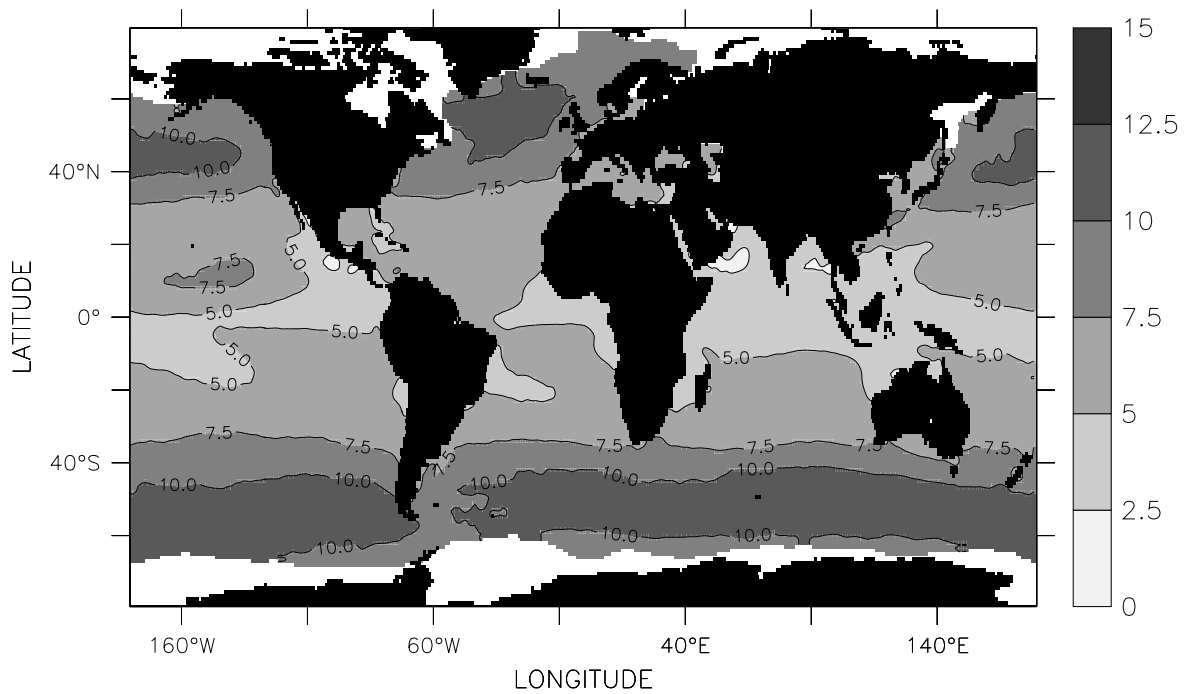
Fig.III.82 Wind Speed (m/s), MAM
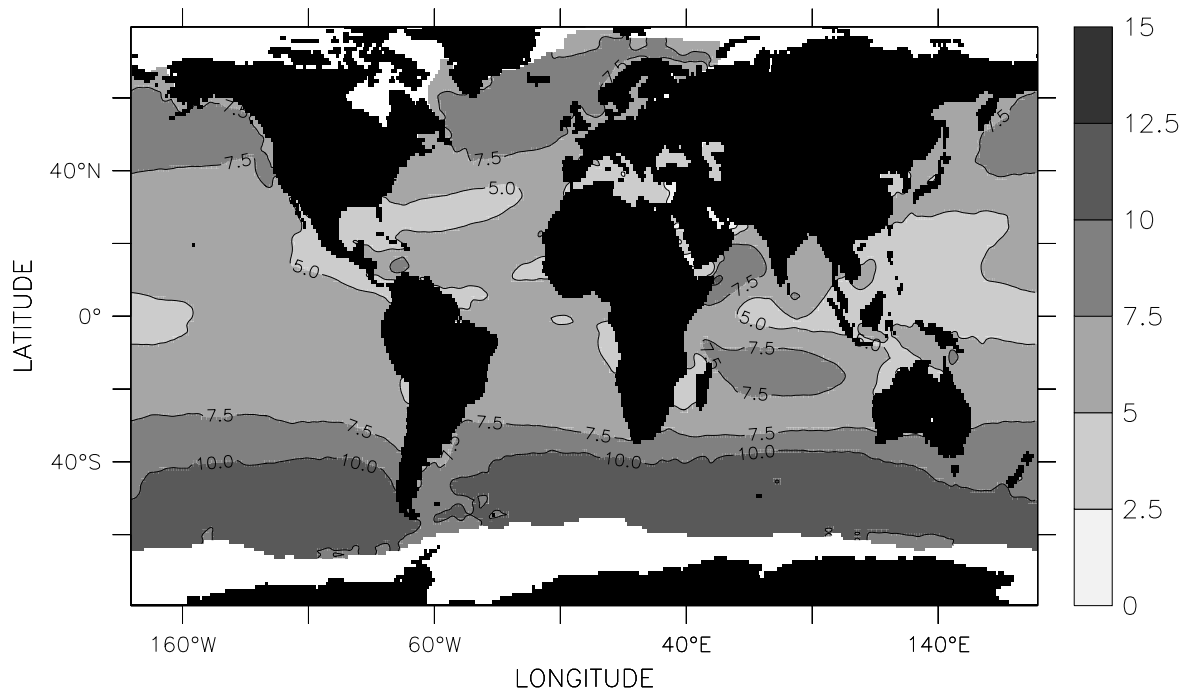
Fig.III.83 Wind Speed (m/s), JJA
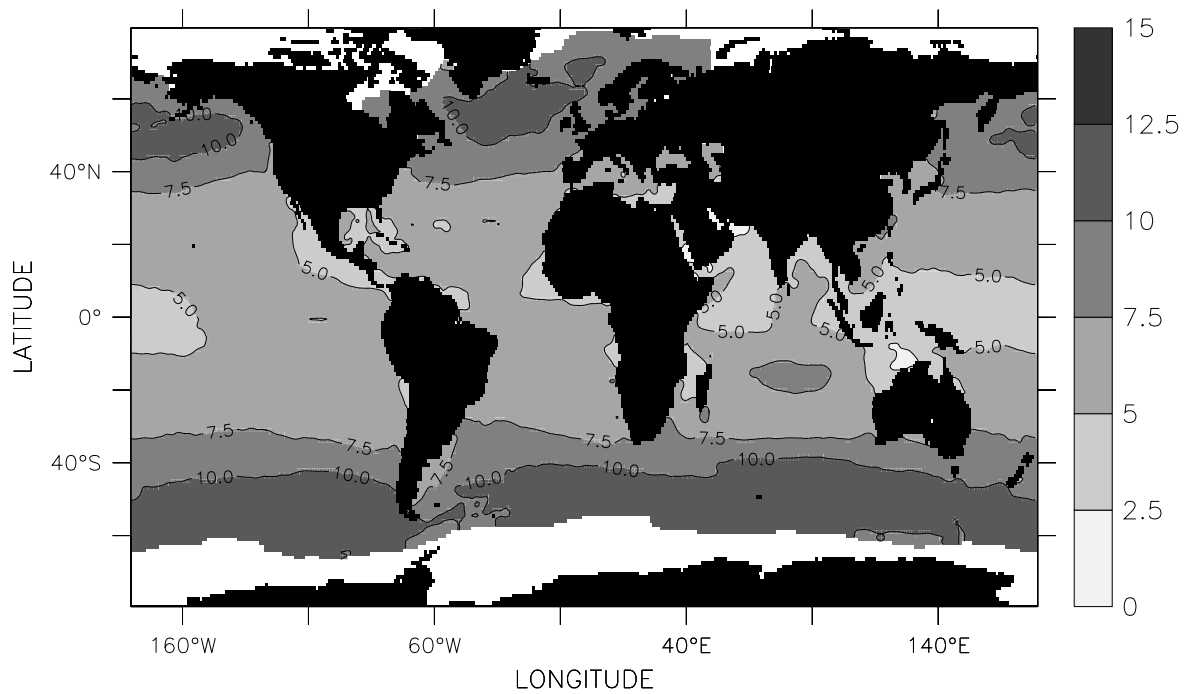
Fig.III.84 Wind Speed (m/s), SON
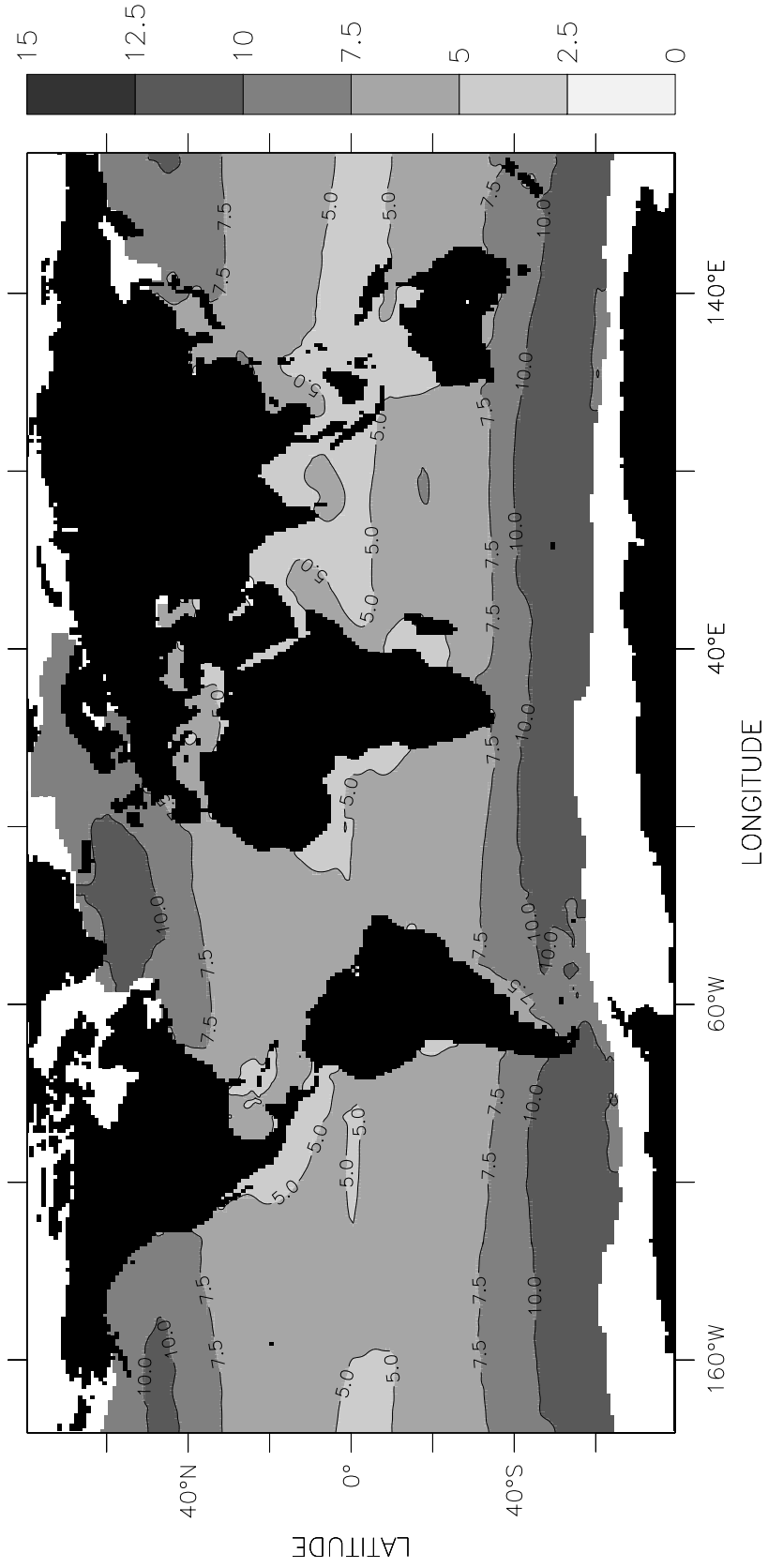
Fig.III.85 Wind Speed (m/s), Annual
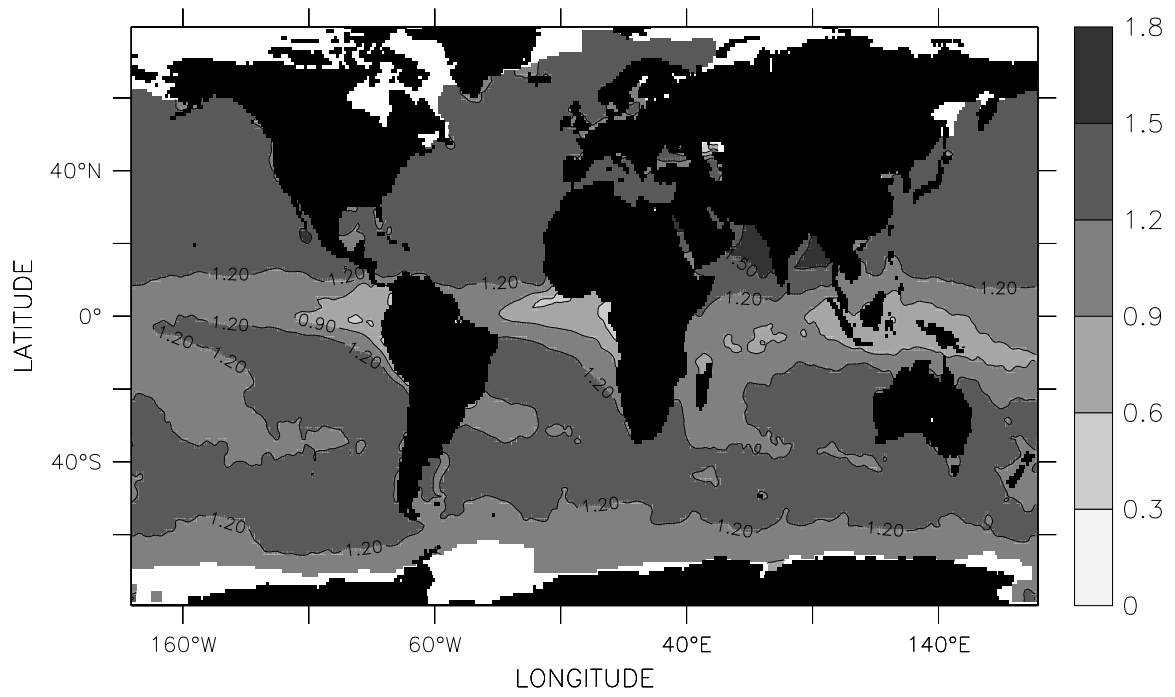
Fig.III.86 Dalton Number ($*10^{-3}$), January
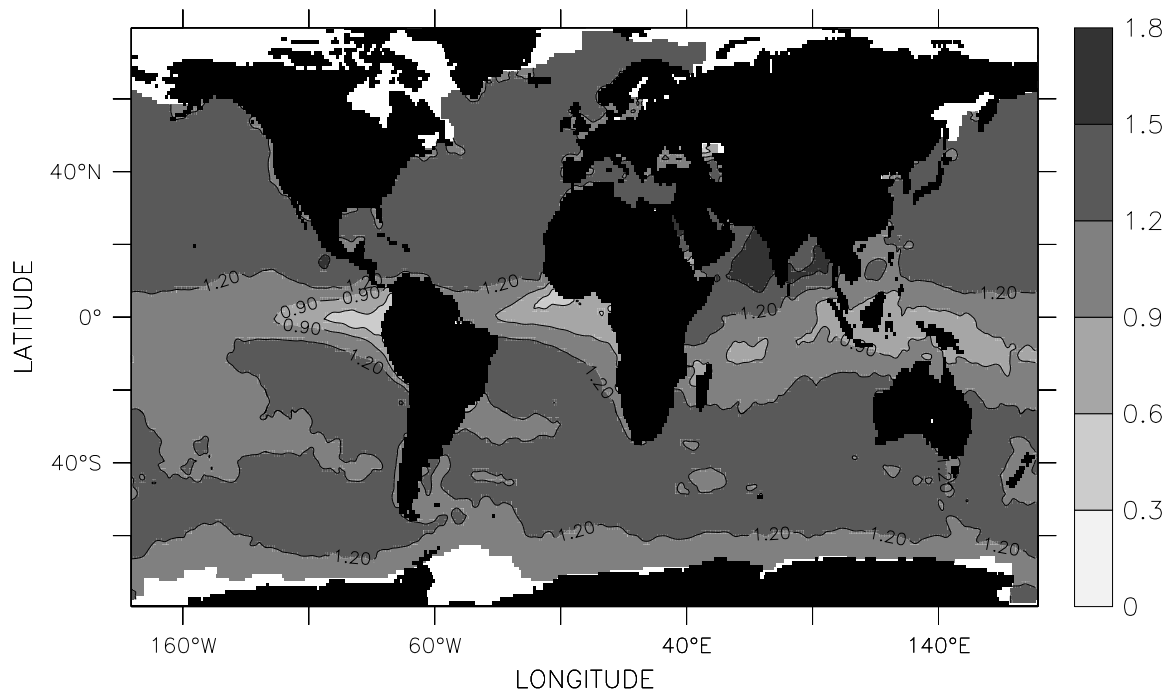
Fig.III.87 Dalton Number ($*10^{-3}$), February
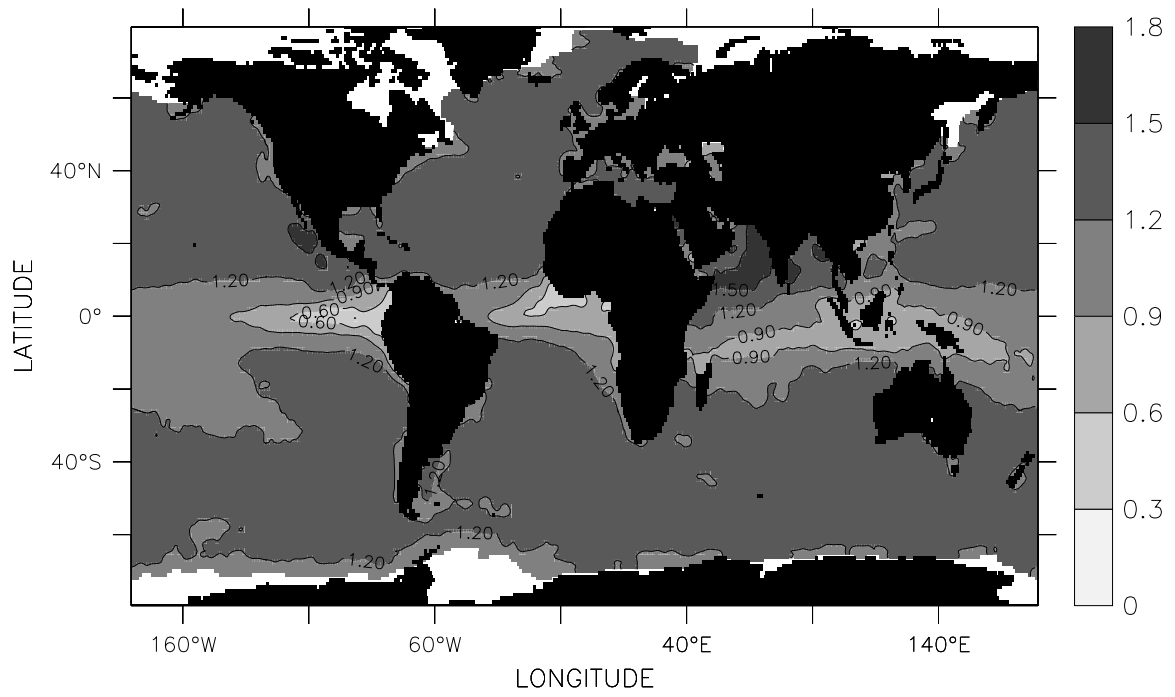
Fig.III.88 Dalton Number $(*10^{-3})$, March
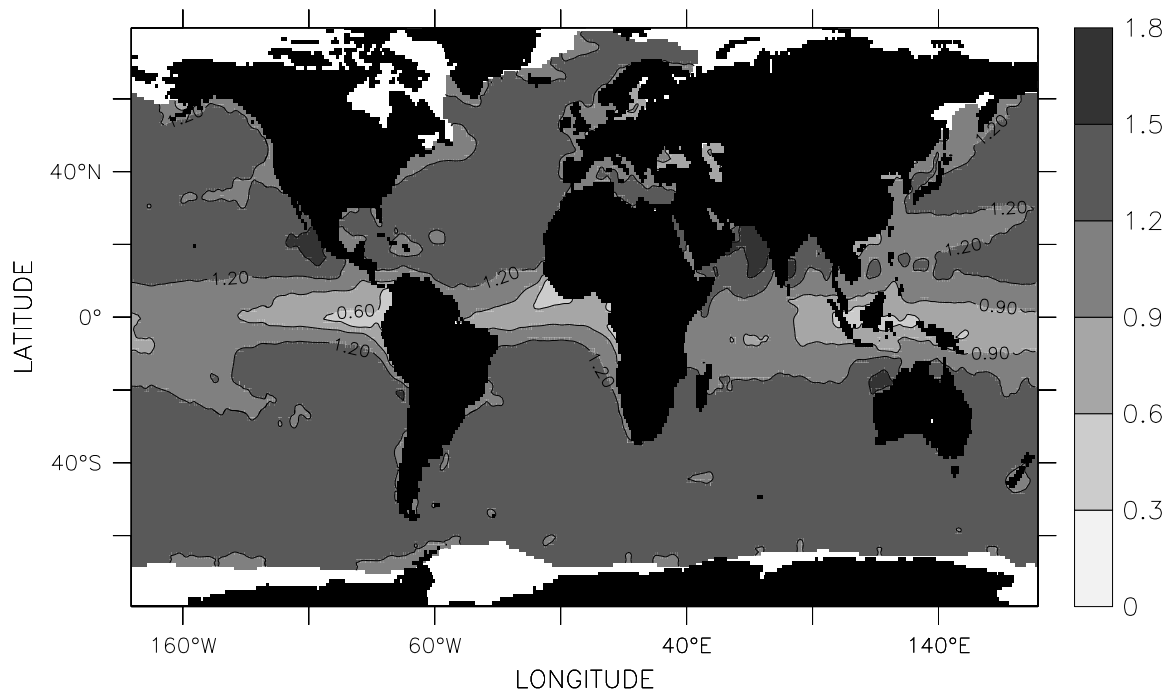
Fig.III.89 Dalton Number $(*10^{-3})$, April
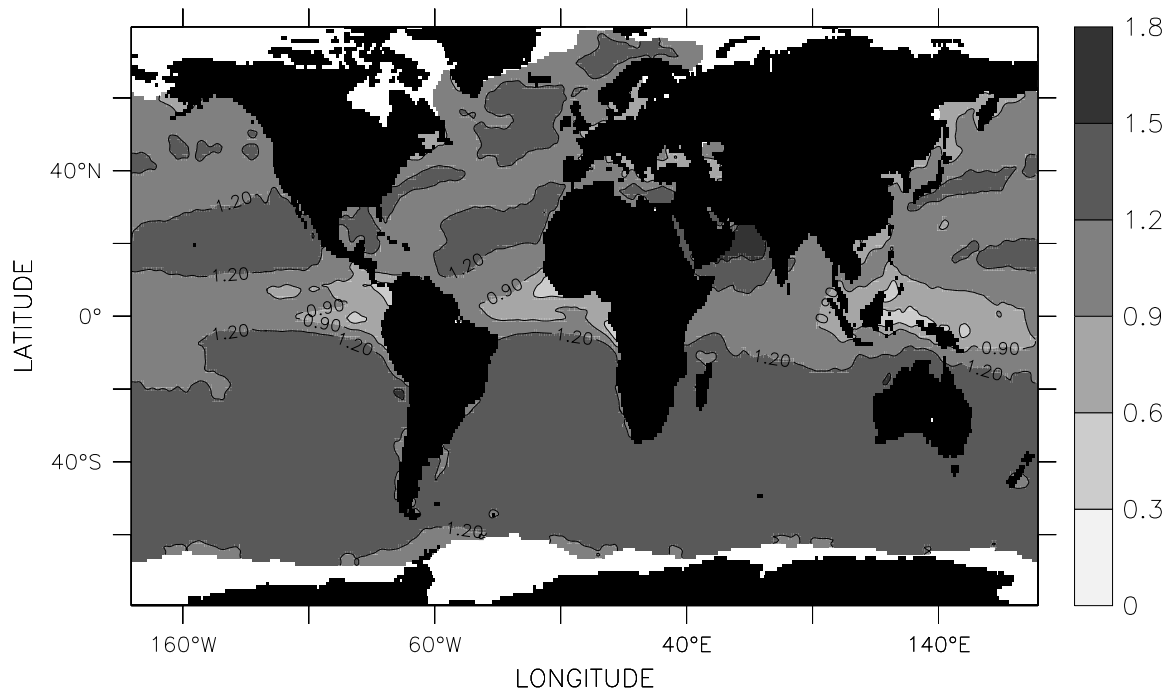
Fig.III.90 Dalton Number ($*10^{-3}$), May
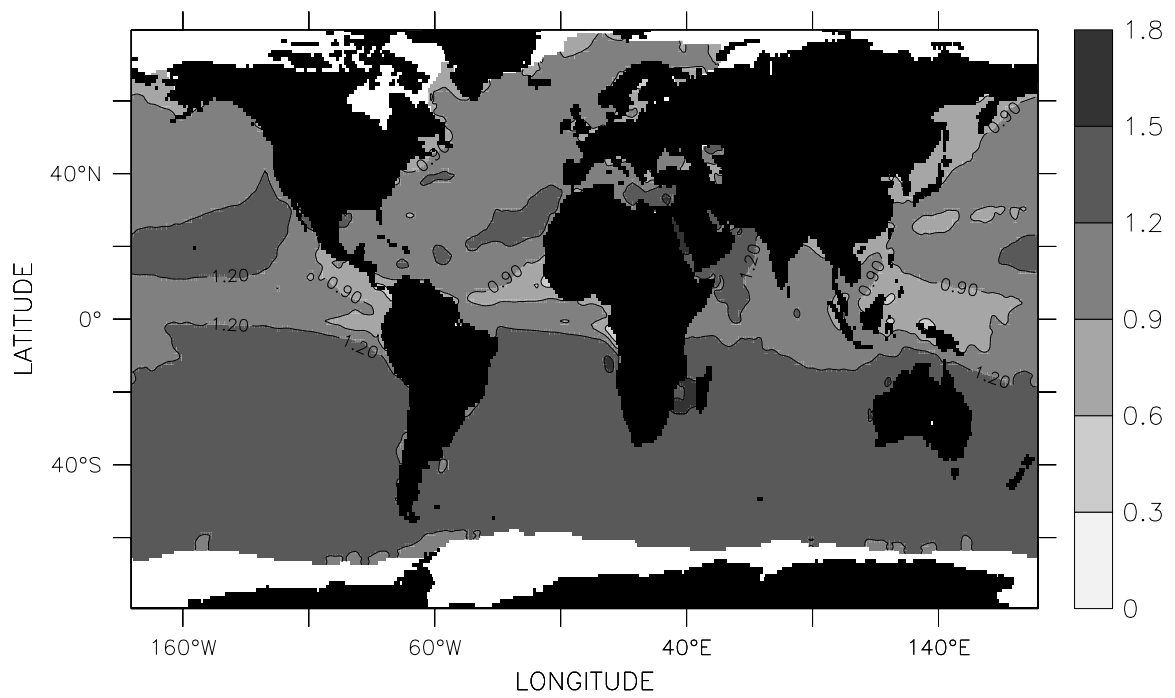
Fig.III.91 Dalton Number ($*10^{-3}$), June
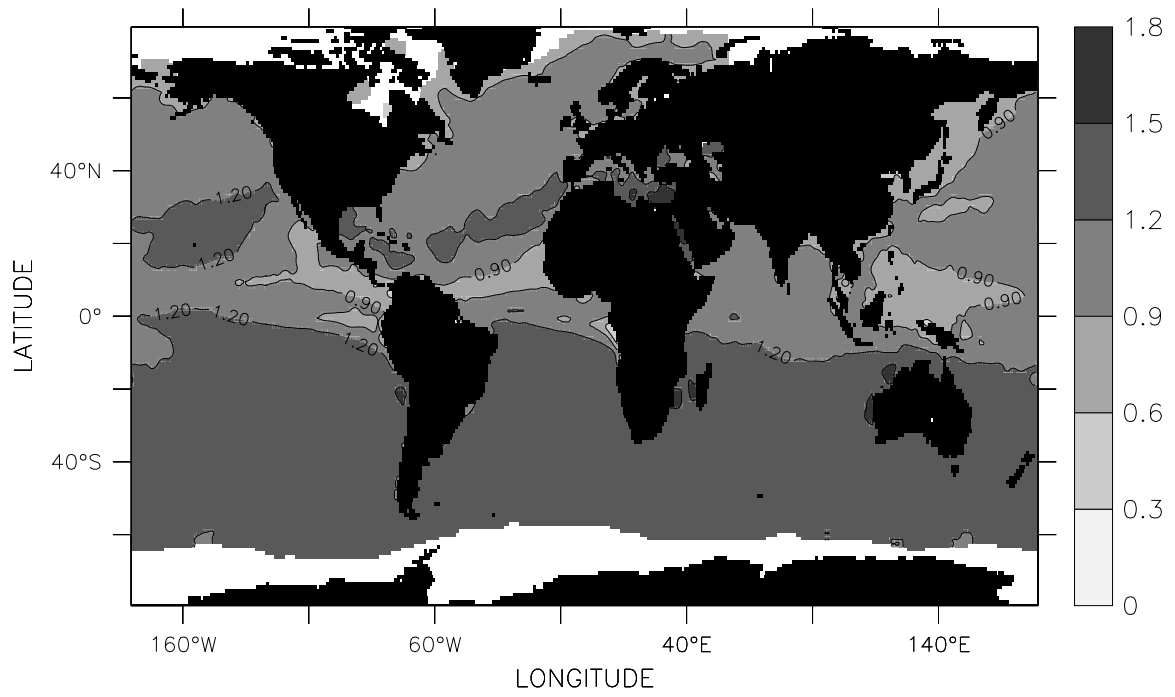
Fig.III.92 Dalton Number ($*10^{-3}$), July
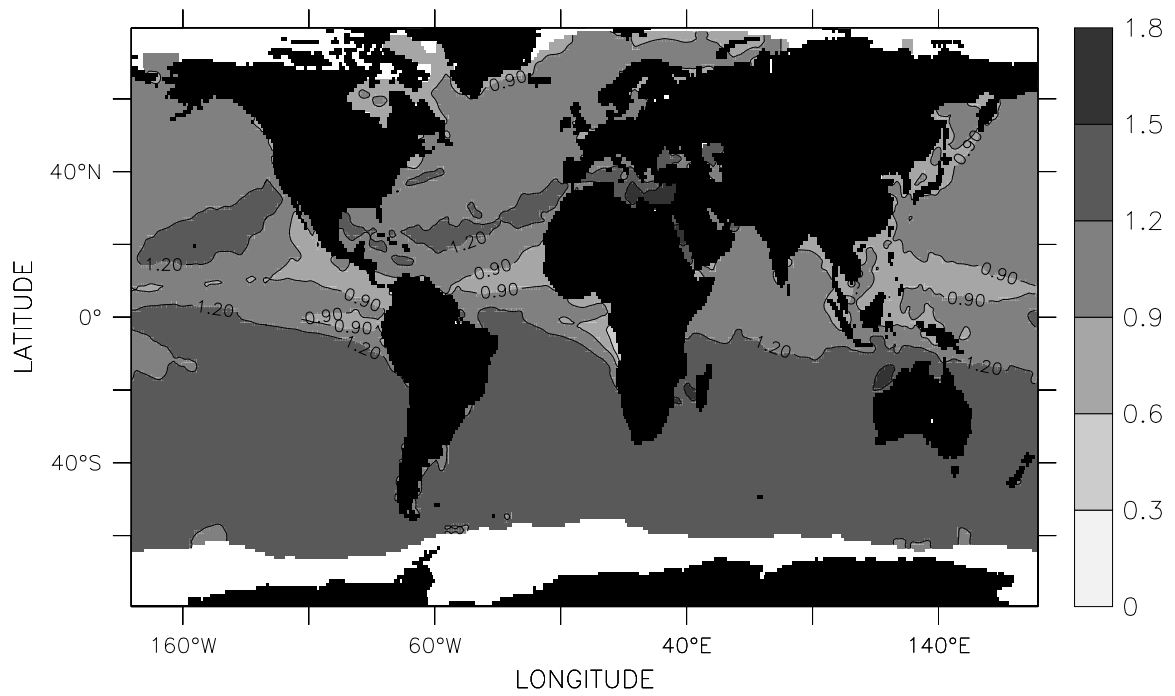
Fig.III.93 Dalton Number ($*10^{-3}$), August
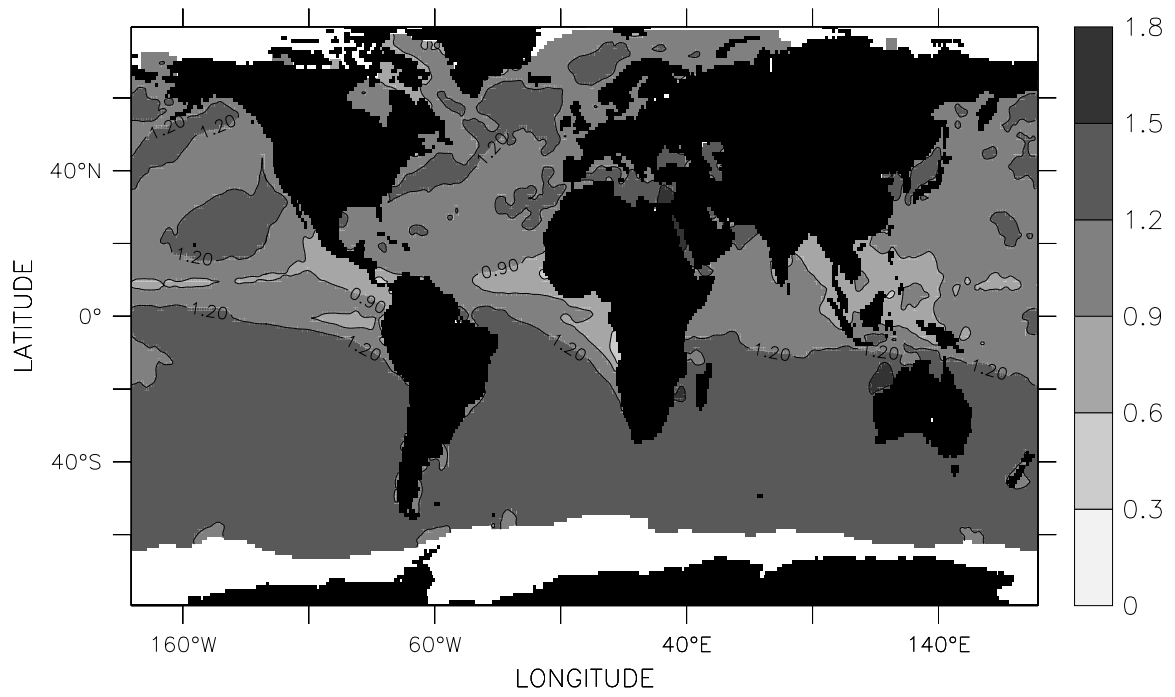
Fig.III.94 Dalton Number ($*10^{-3}$), September
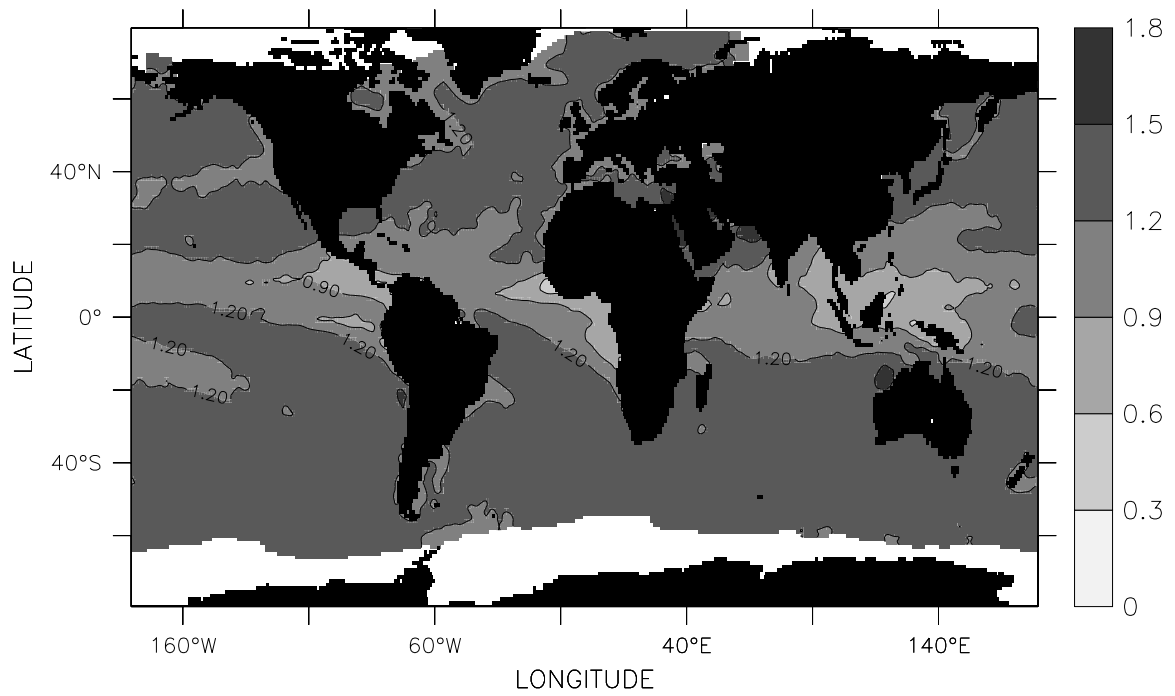
Fig.III.95 Dalton Number ($*10^{-3}$), October
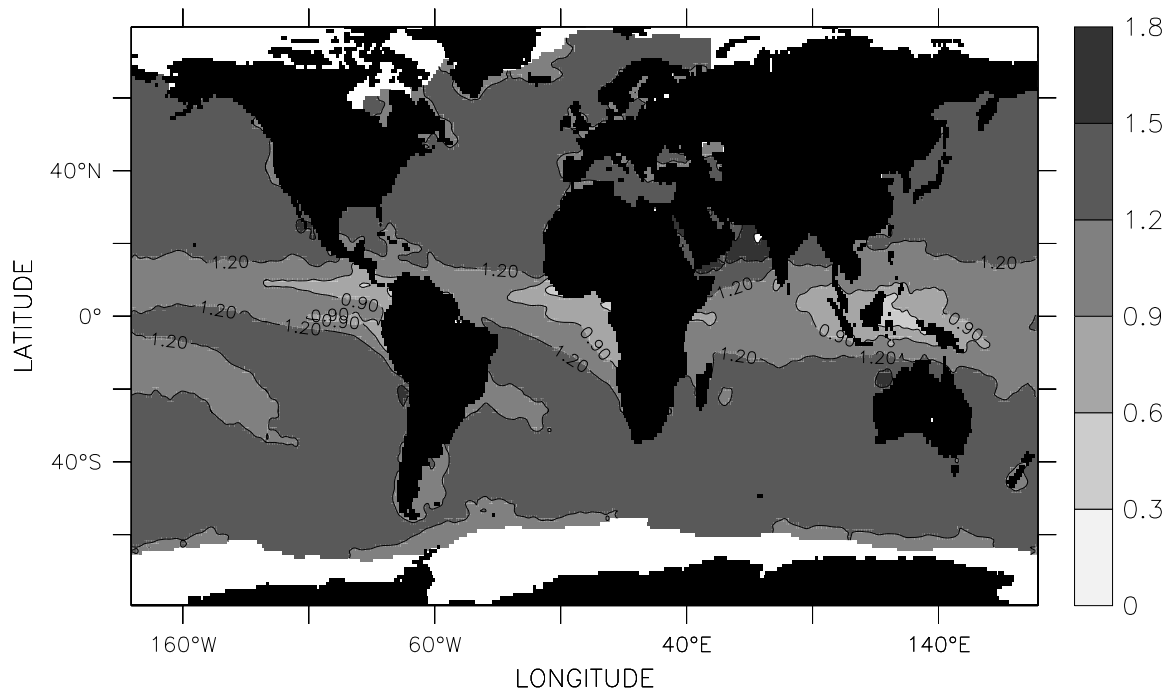
Fig.III.96 Dalton Number ($*10^{-3}$), November
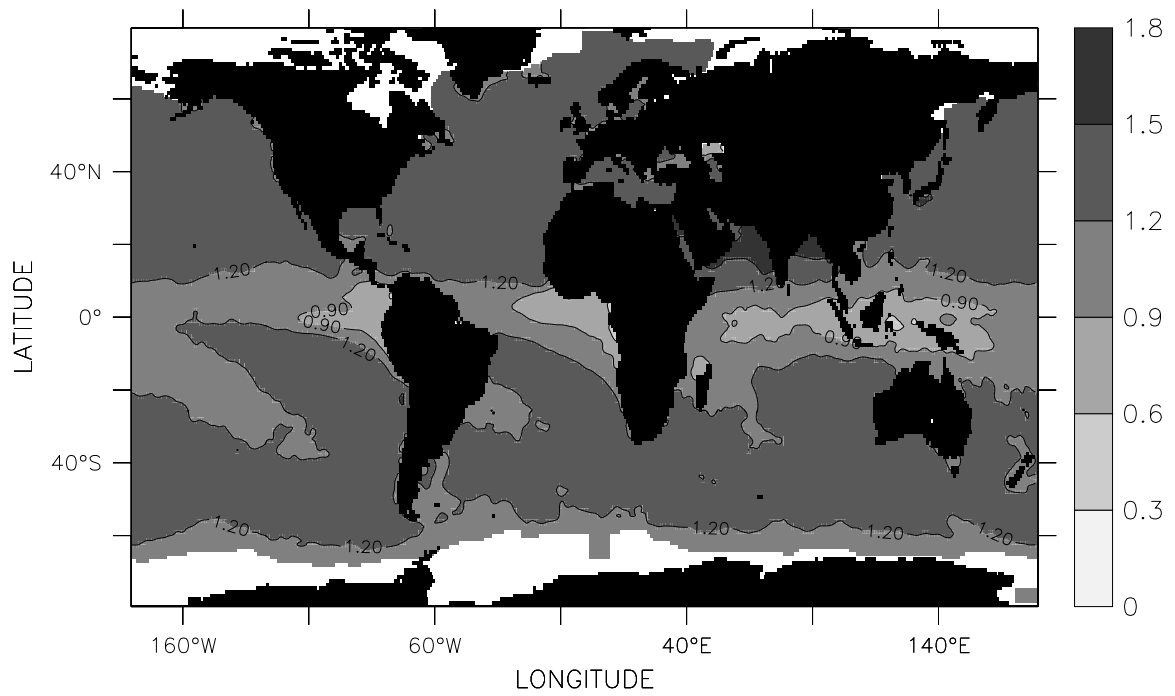
Fig.III.97 Dalton Number ($*10^{-3}$), December

65
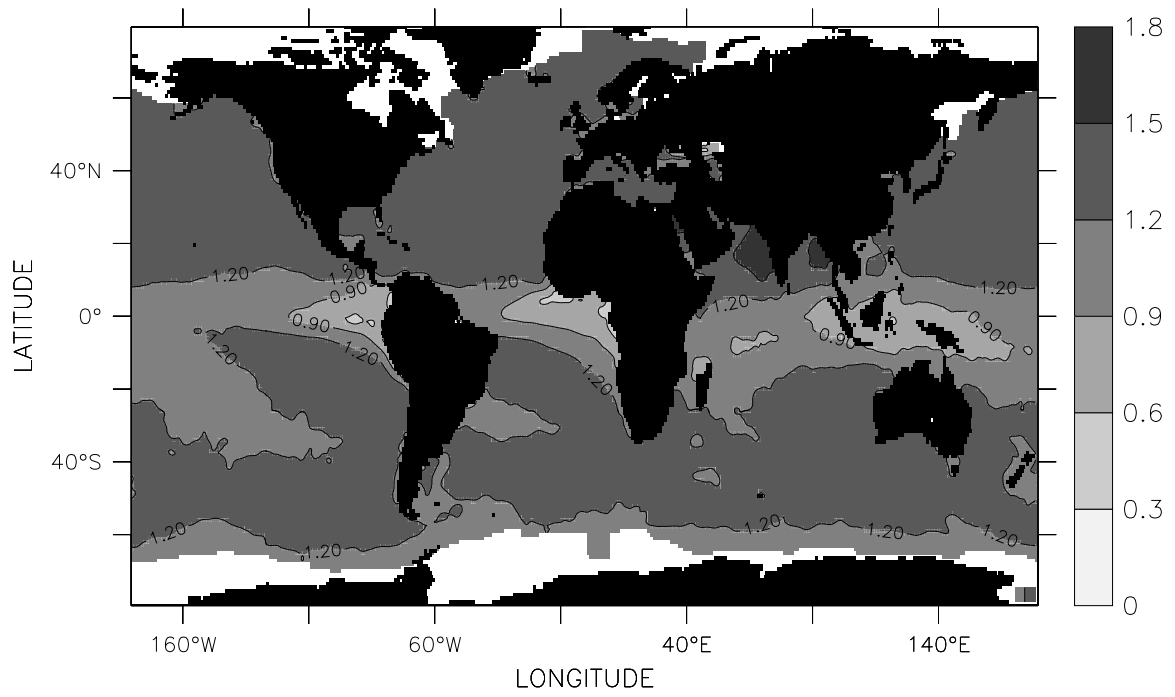
Fig.III.98 Dalton Number ($*10^{-3}$), DJF
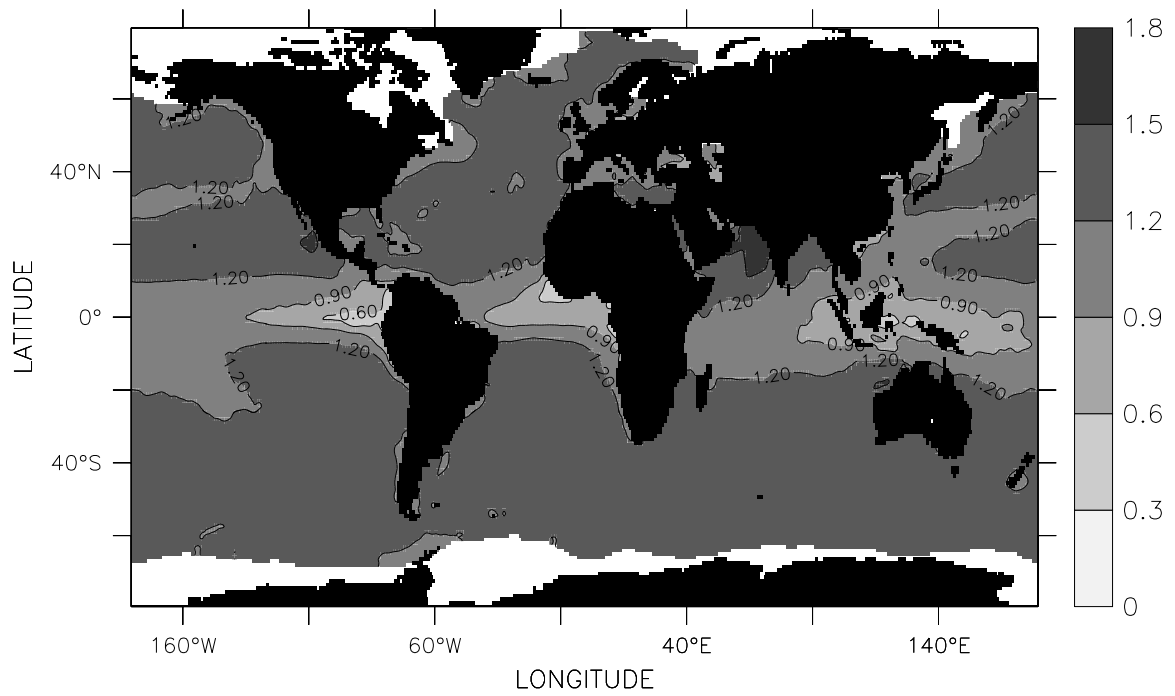
Fig.III.99 Dalton Number ($*10^{-3}$), MAM
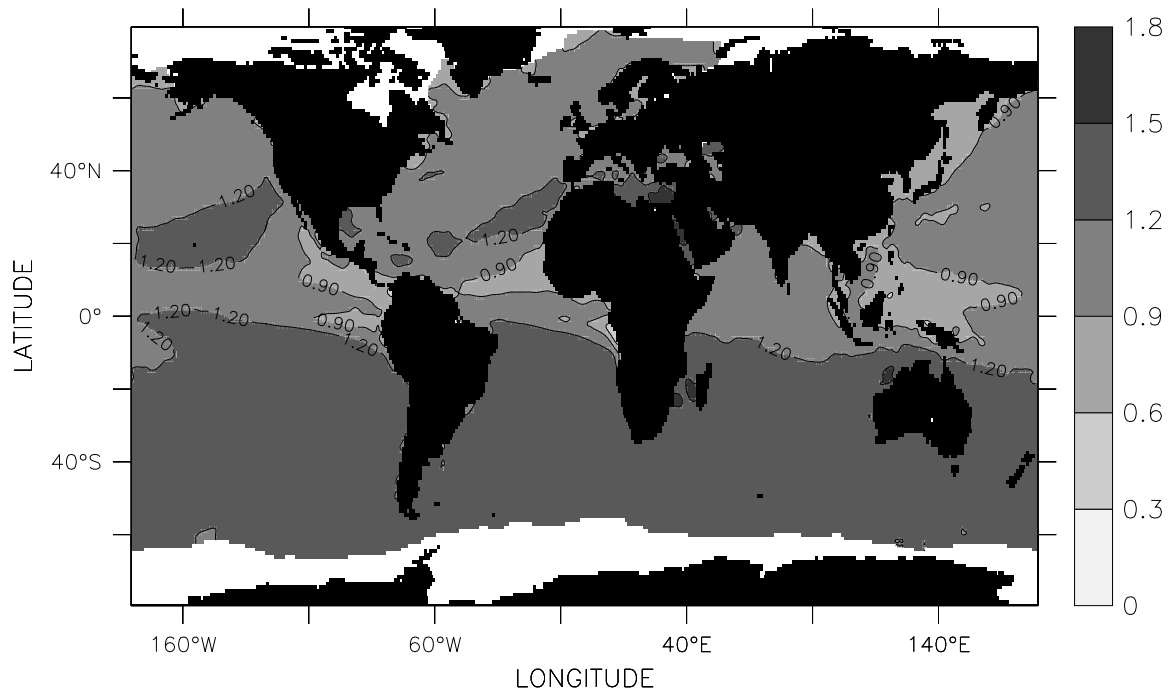
Fig.III.100 Dalton Number (*10^{-3}), JJA
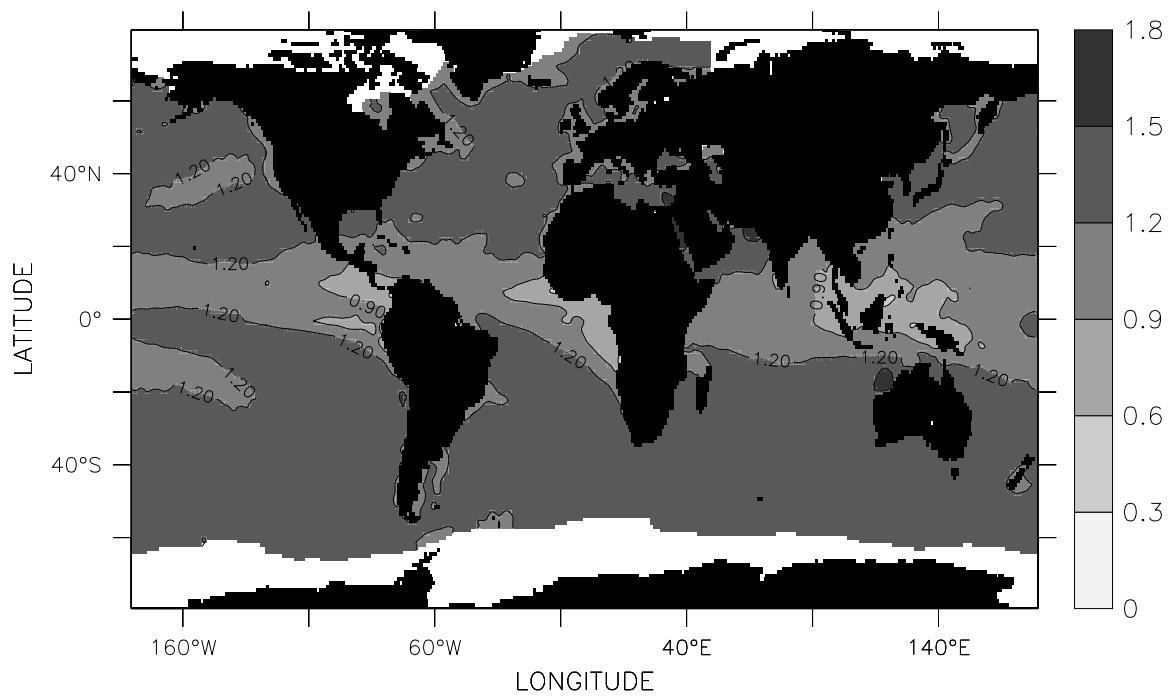
Fig.III.101 Dalton Number (*10^{-3}), SON
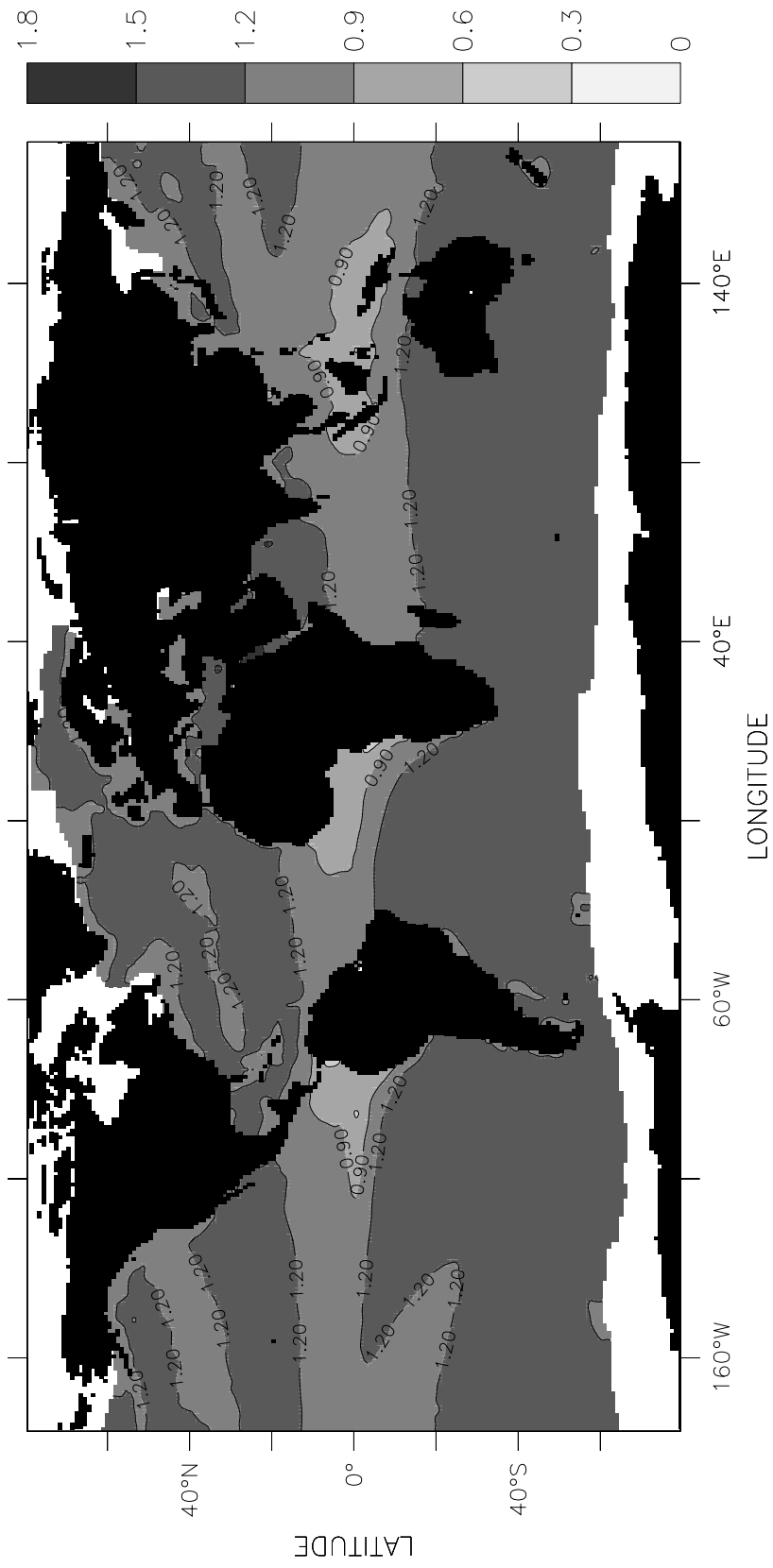
Fig.III.102 Dalton Number ($*10^{-3}$), Annual

Chapter IV   Air Sea Fluxes

The surface heat budget of the oceans is an integral part of the general circulation of the atmosphere. The heating of the atmosphere largely occurs by the transfer of sensible and latent heat from the oceans to the atmosphere in the subtropical regions as well as the mid- to high latitude regions in winter. The longwave radiational flux also plays an equally important role. In this chapter, we present the latent and sensible heat fluxes as well as the longwave net radiation.

IV.1. Latent Heat Flux (Figures IV.1 to IV.17)

The latent heat flux (*LHF*) is the major source of energy for the atmosphere. The latent heat flux is a function of wind speed, difference in humidity and the atmospheric stability. The regions of maximum *LHF* values are seen in the Kuroshio and Gulf Stream regions during the winter months (Figures IV.1, 2, and 12). The regions of the lowest *LHF* values are found in the eastern equatorial Pacific and equatorial Atlantic during the winter and spring (Figures IV.13 and 14). During summer season the minimum *LHF* values are observed in the northern parts of the Atlantic and the Pacific (Figure IV.15). During autumn, the minimum is observed along the south American and southwestern African coasts (Figure IV.16). On an annual scale, *LHF* is higher in the southern Indian Ocean as compared to the northern and it is the major source of moisture for the summer monsoon rainfall over the Indian subcontinent.

IV.2. Sensible Heat Flux (Figures IV.18 to IV.34)

The sensible heat flux (*SHF*) distribution follows to a certain extent broadly that of the sea surface temperature and the sea-air temperature difference. The *SHF* can be positive and negative. Positive values point to a heat flux from the ocean to the atmosphere and negative values to a heat flux from the atmosphere into the ocean. The negative values of *SHF*, in general occur over the major upwelling zones of the global oceans. During the winter season, we observe large areas of positive *SHF* at high northern latitudes off the eastern parts of the continents, as the cold air advected from the continents flows over the warm currents of Kuroshio and Gulf Stream from November till March. This feature then disappears in April (Figures IV. 18 to 29). During the summer season (Figure IV.32), the maximum values are observed in the southern oceans, especially in the southern Indian Ocean. During the summer period, the entire northern Indian ocean looses heat to the atmosphere, with the region off the Somalia coast experiencing the maximum heat loss (-20 to –40 Wm^{-2}). Please note, that we have used 80 percent relative humidity to derive the air temperature from the measured atmospheric specific humidity, which may lead to systematic errors in the sensible heat flux. Therefore *SHF* fields must be interpreted with care in areas where the relative humidity strongly deviates from 80%, particularly in the Tropics between 10^oN and 10^oS.

IV.3. Longwave Net Radiation (Figures IV.35 to IV.51)

The longwave net radiation flux (*LWR*) is another important energy source for the atmosphere after the *LHF* flux. It is dependent upon the sea surface and air temperature as well as the near-surface air humidity. The lowest values occur usually over the cloudy regions such as the Inter Tropical Convergence Zones (ITCZ). This strong variation in the *LWR* can be clearly seen in the Arabian Sea and Bay of Bengal, where the maximum values of 100-140 Wm^{-2} drops drastically with the progress of the ITCZ into the northern Indian Ocean to 0-40 Wm^{-2} in the monsoon months when the ITCZ merges with the monsoon trough over the Indian subcontinent (Figures IV.35 to 43). The *LWR* then gradually increases with the withdrawal of the summer monsoon (i.e from October to January, Figures IV.44 to 46). On an annual scale (Figure IV.51), the lowest values are observed in the southern Pacific and Atlantic oceans just south of the equator.
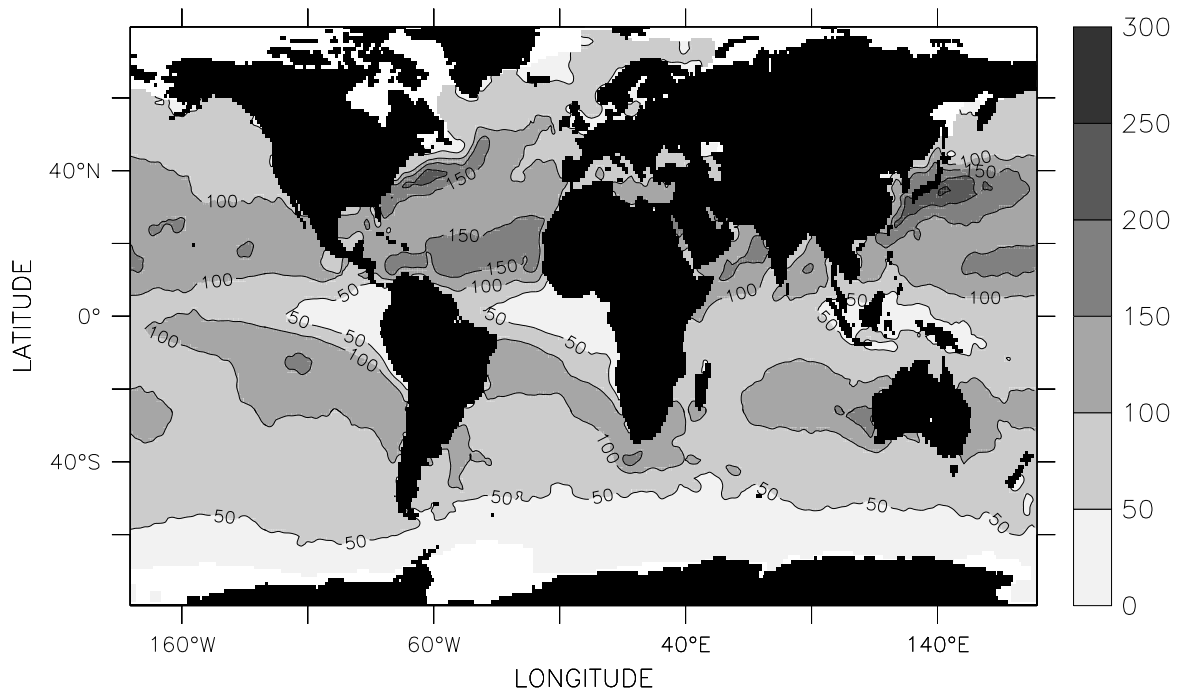
Fig.IV.1 Latent Heat Flux (W/m^2), January
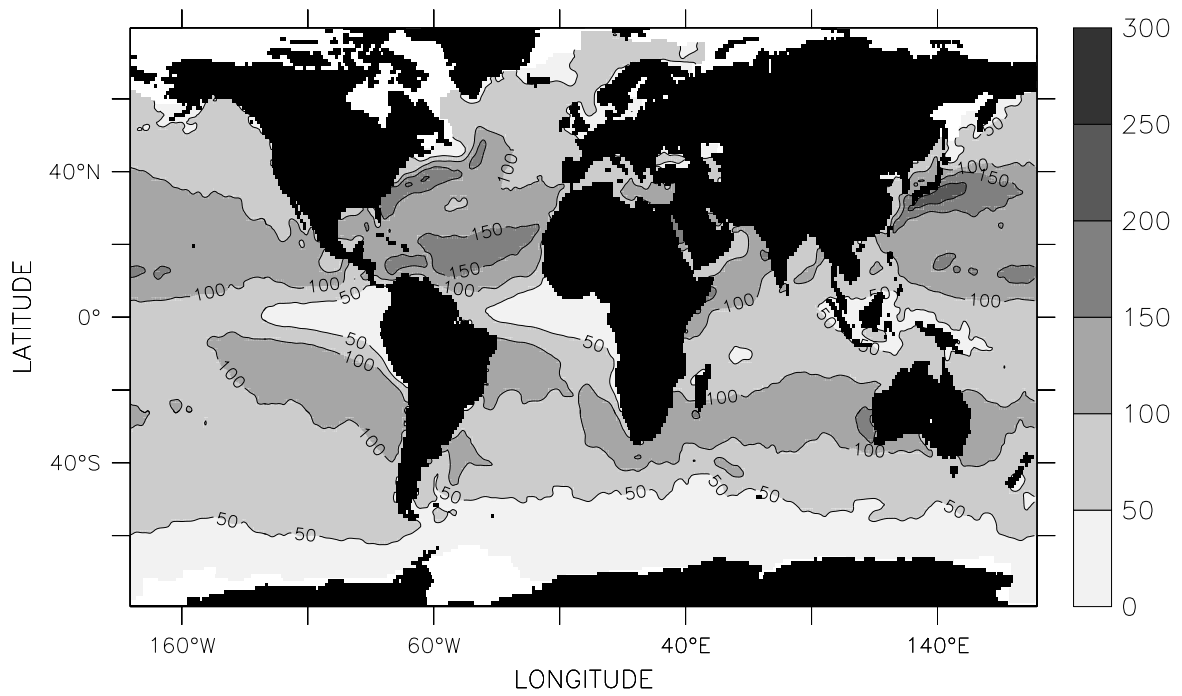
Fig.IV.2 Latent Heat Flux (W/m^2), February
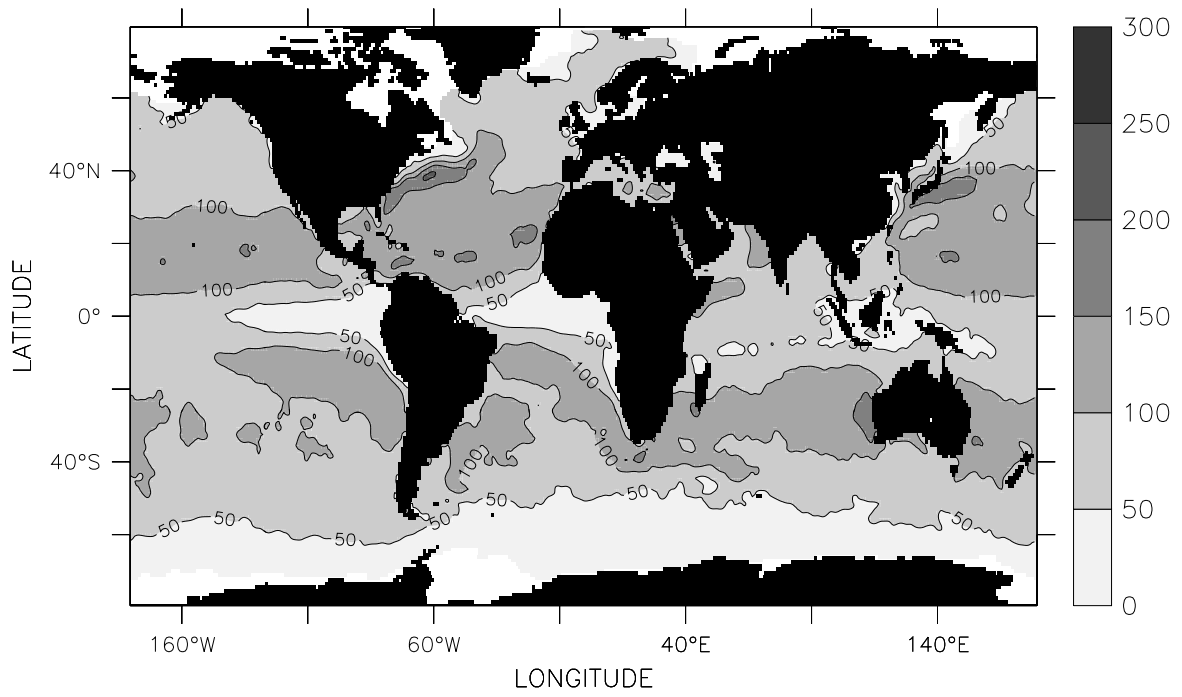
Fig.IV.3 Latent Heat Flux (W/m^2), March
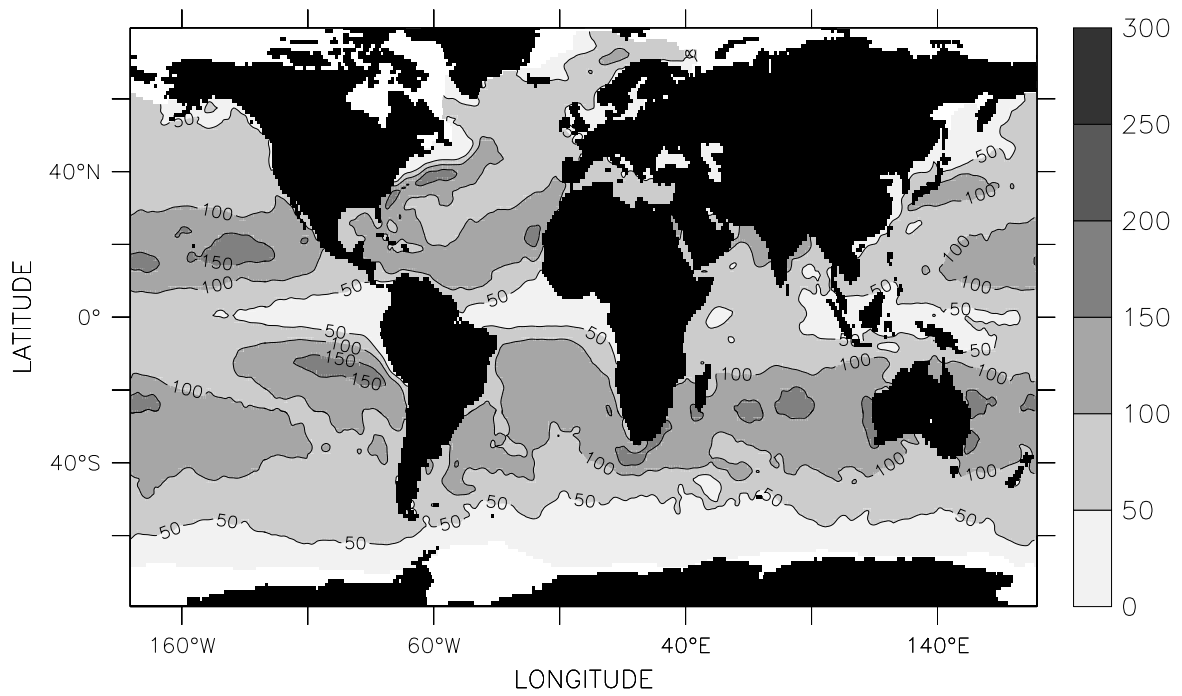
Fig.IV.4 Latent Heat Flux (W/m^2), April
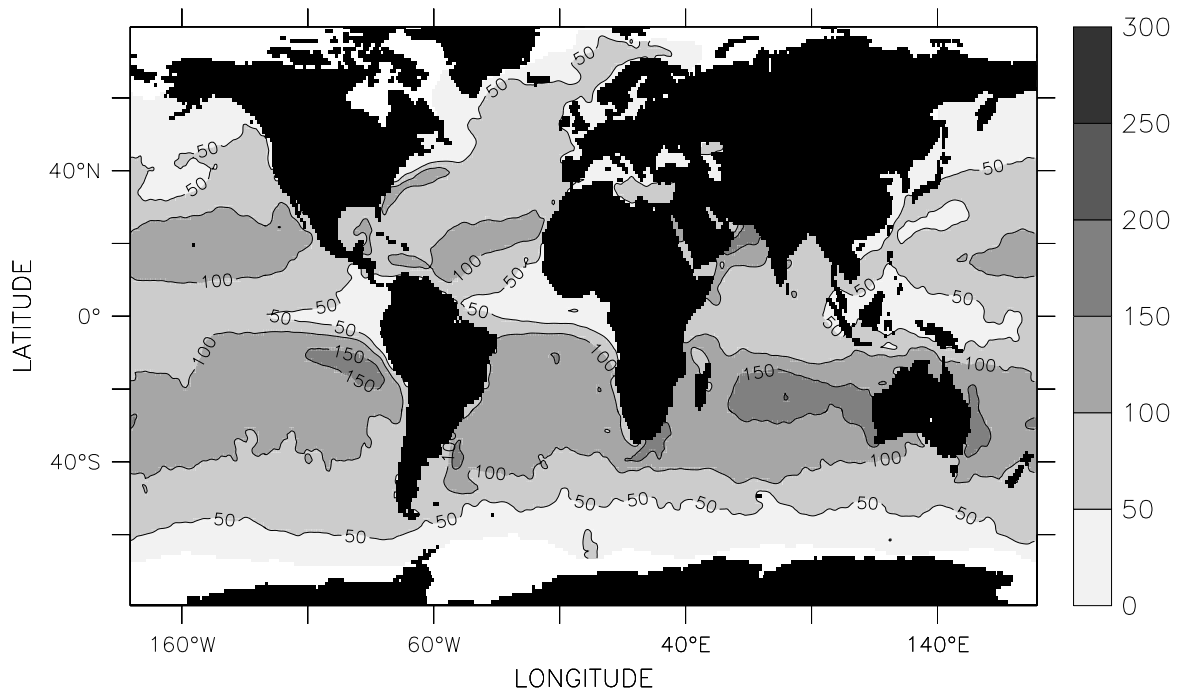
Fig.IV.5 Latent Heat Flux (W/m^2), May
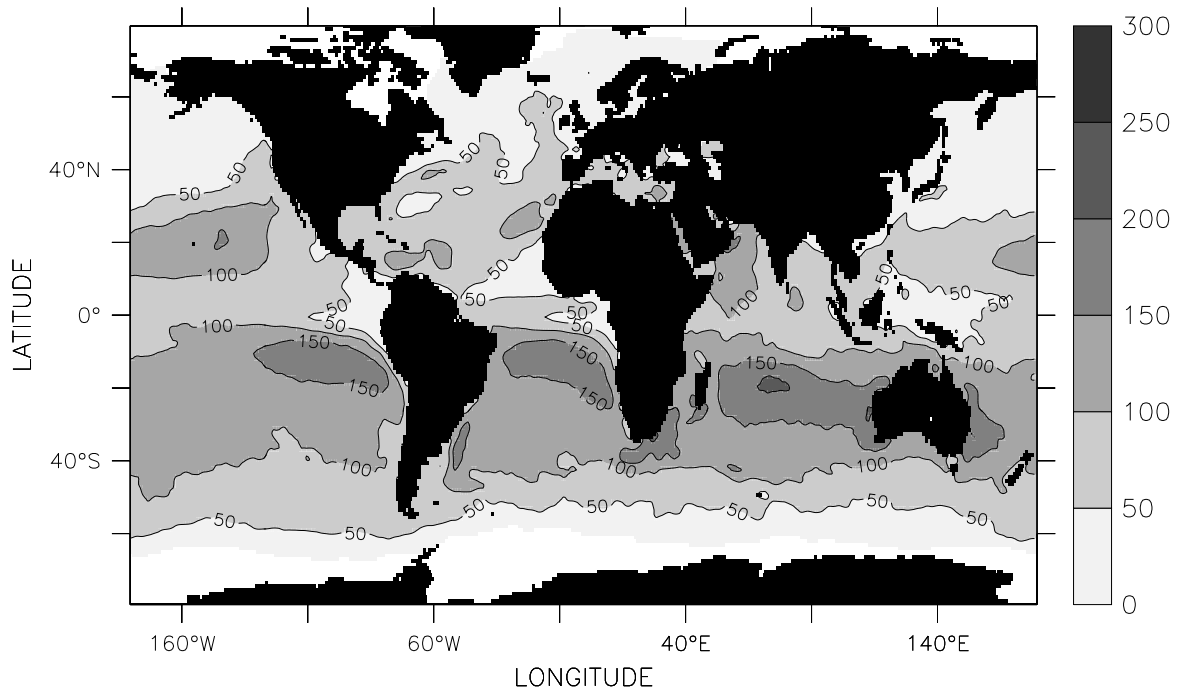
Fig.IV.6 Latent Heat Flux (W/m^2), June
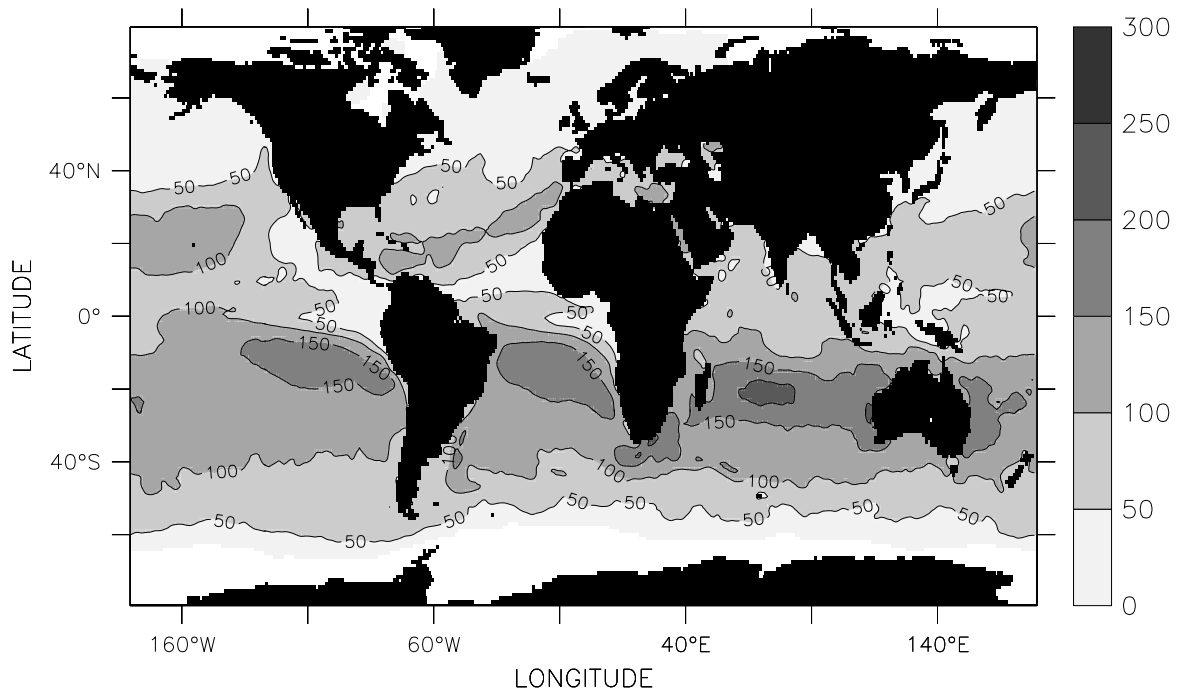
Fig.IV.7 Latent Heat Flux (W/m^2), July
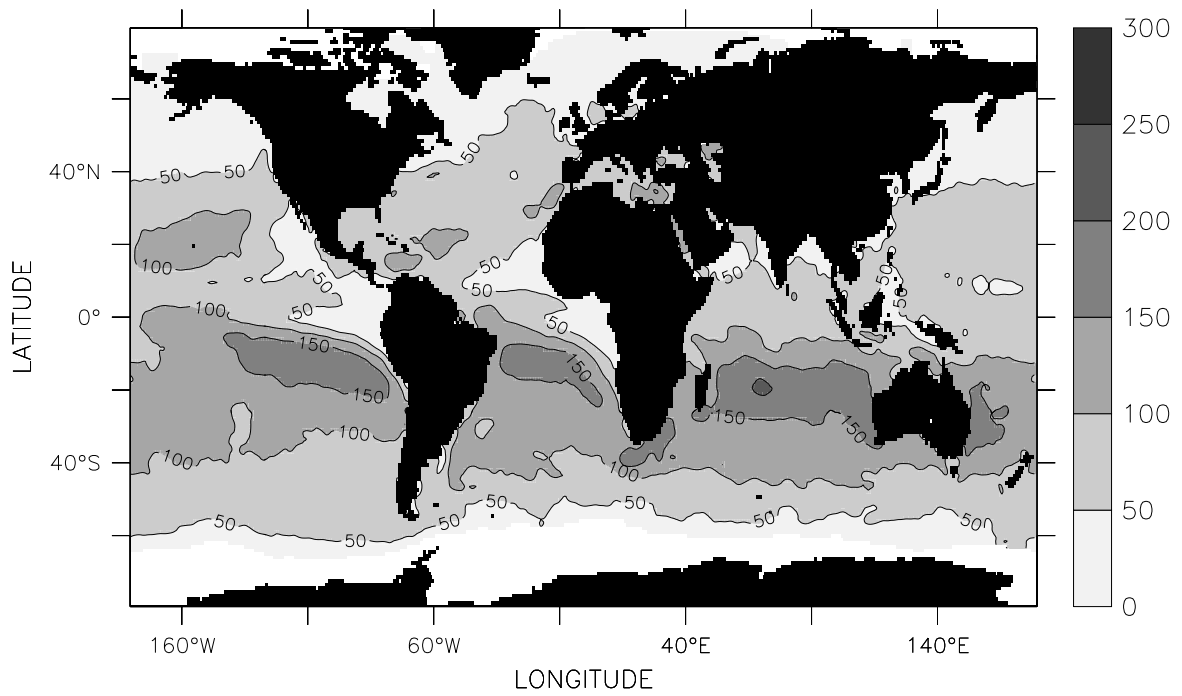
Fig.IV.8 Latent Heat Flux (W/m^2), August
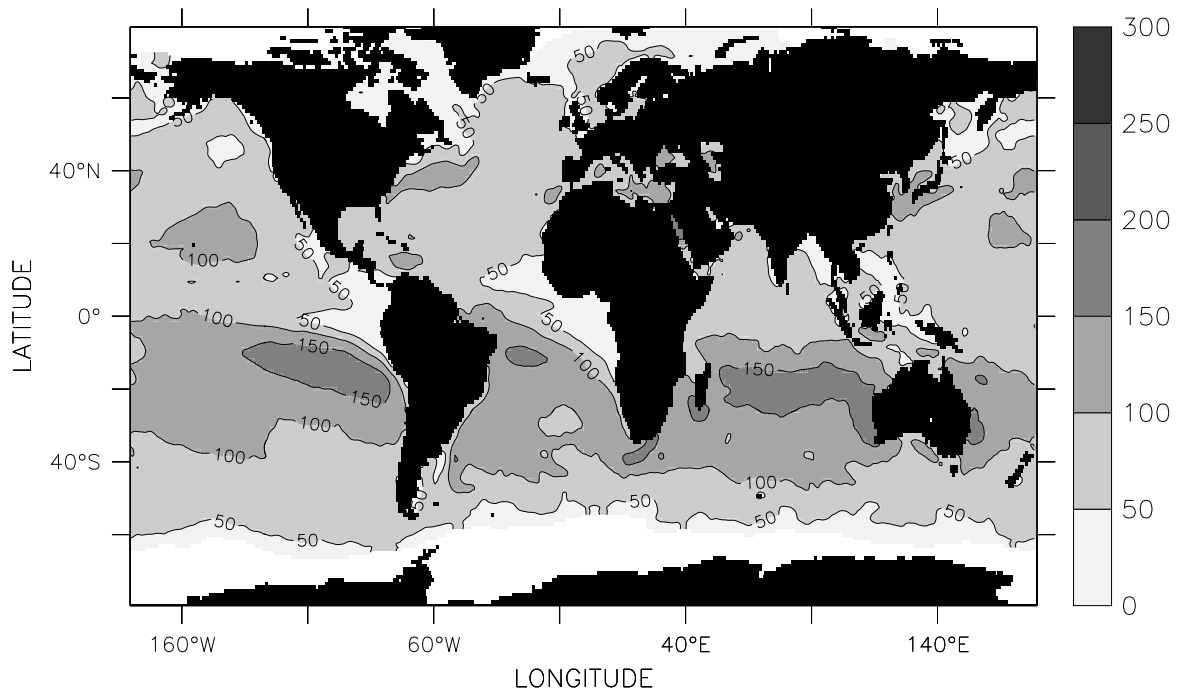
Fig.IV.9 Latent Heat Flux (W/m^2), September
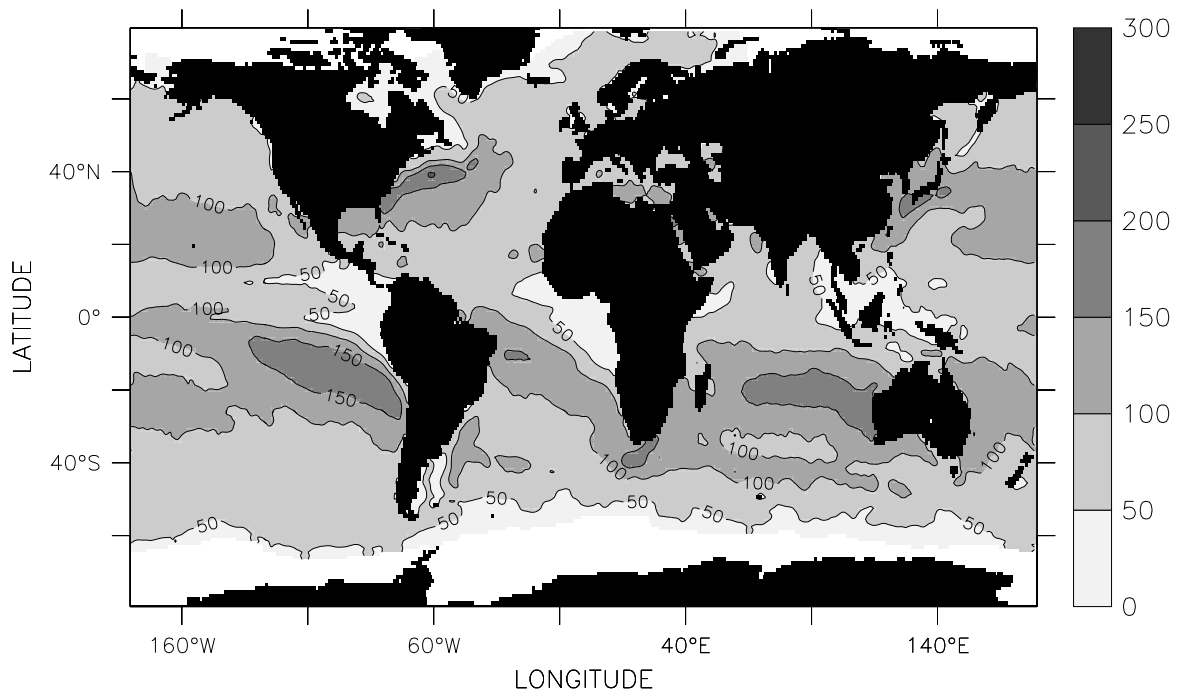
Fig.IV.10 Latent Heat Flux (W/m^2), October

75
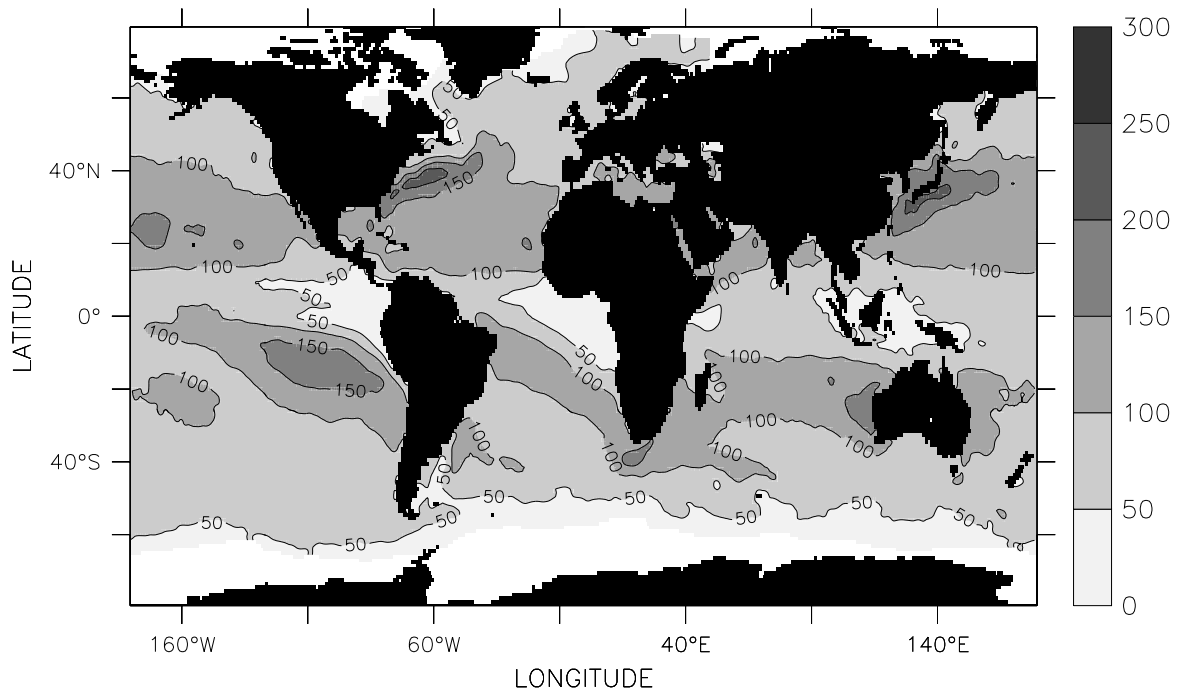
Fig.IV.11 Latent Heat Flux (W/m^2), November
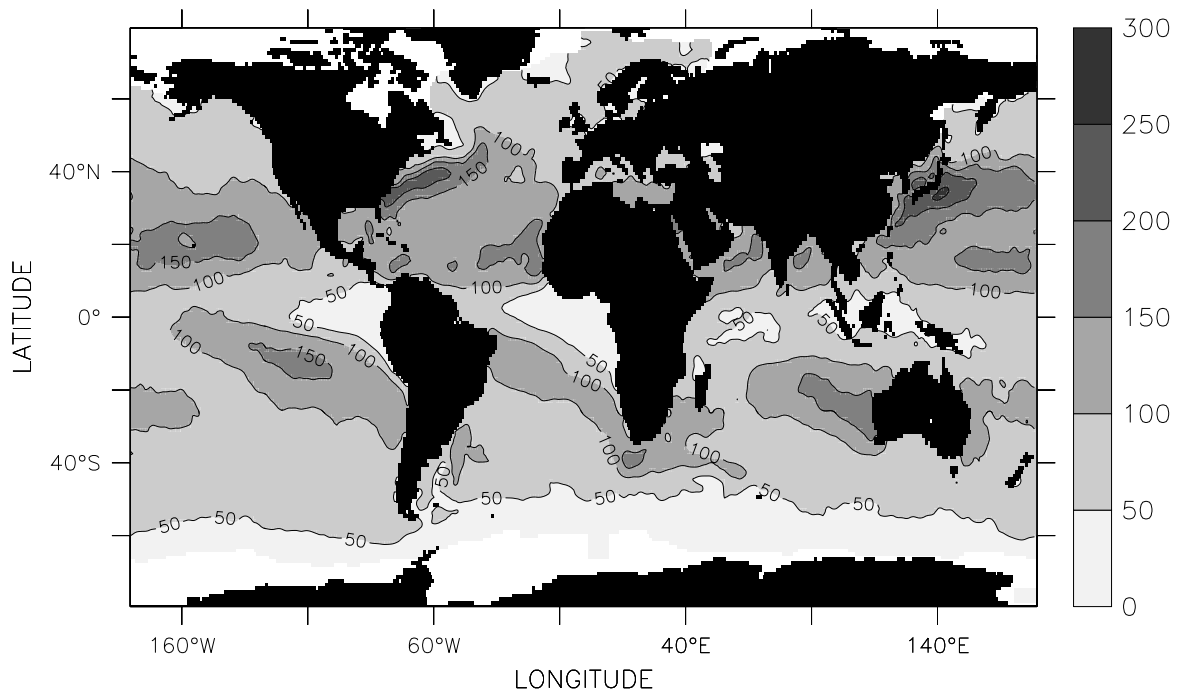
Fig.IV.12 Latent Heat Flux (W/m^2), December
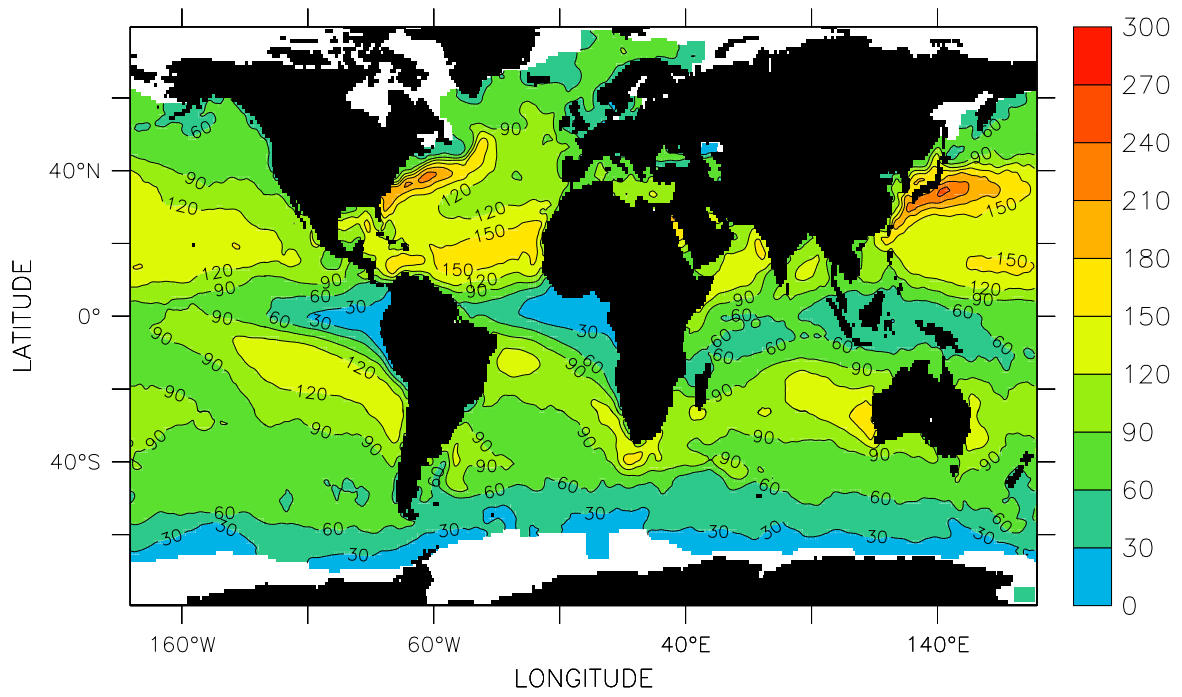
Fig.IV.13 Latent Heat Flux (W/m^2), DJF
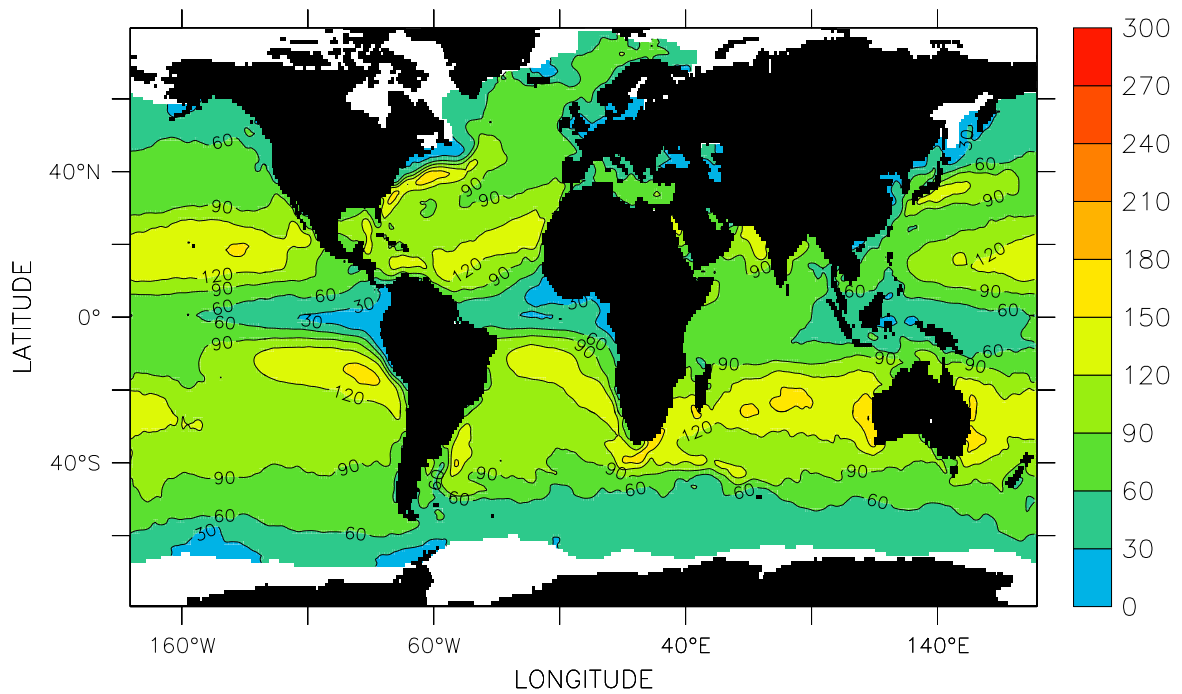
Fig.IV.14 Latent Heat Flux (W/m^2), MAM
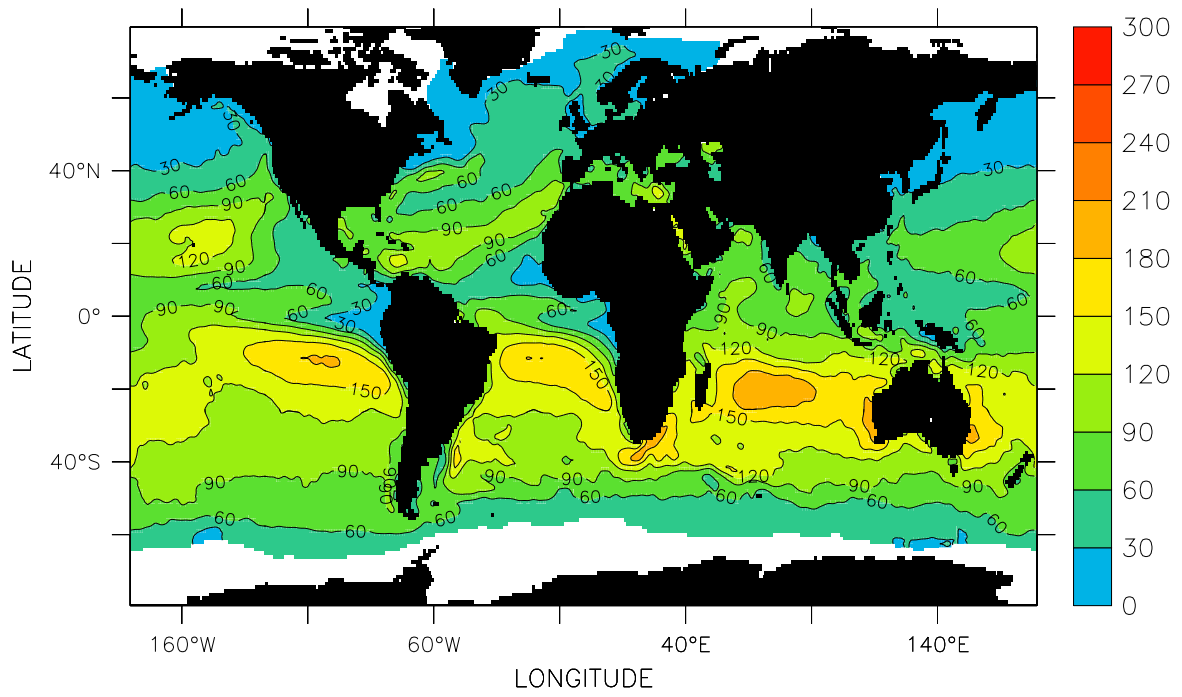
Fig.IV.15 Latent Heat Flux (W/m^2), JJA
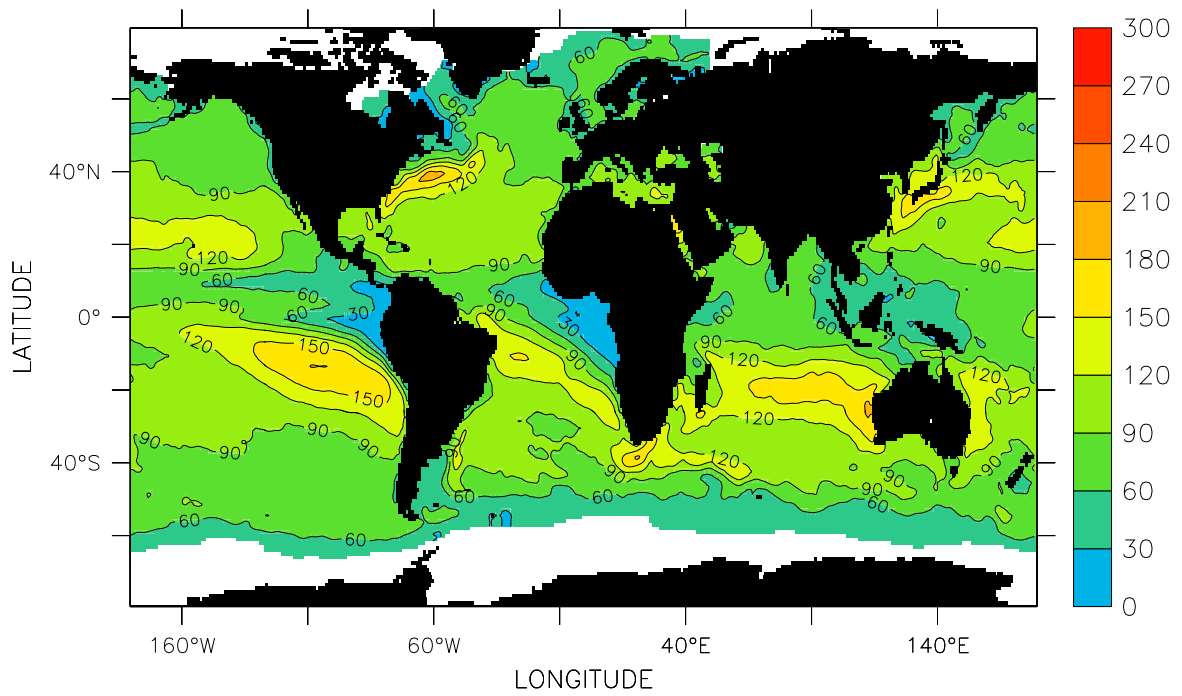
Fig.IV.16 Latent Heat Flux (W/m^2), SON
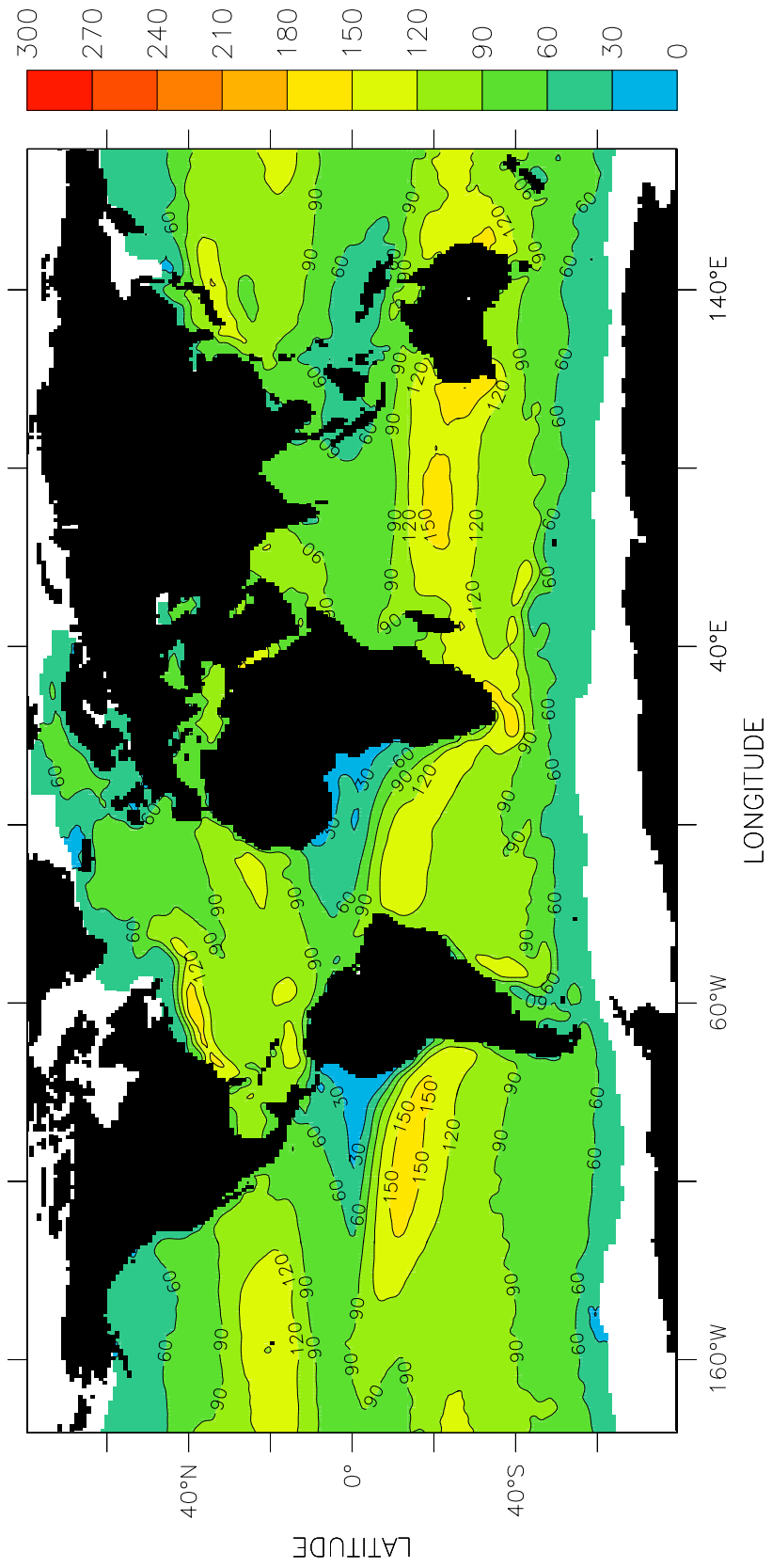
Fig.IV.17 Latent Heat Flux (W/m²), Annual
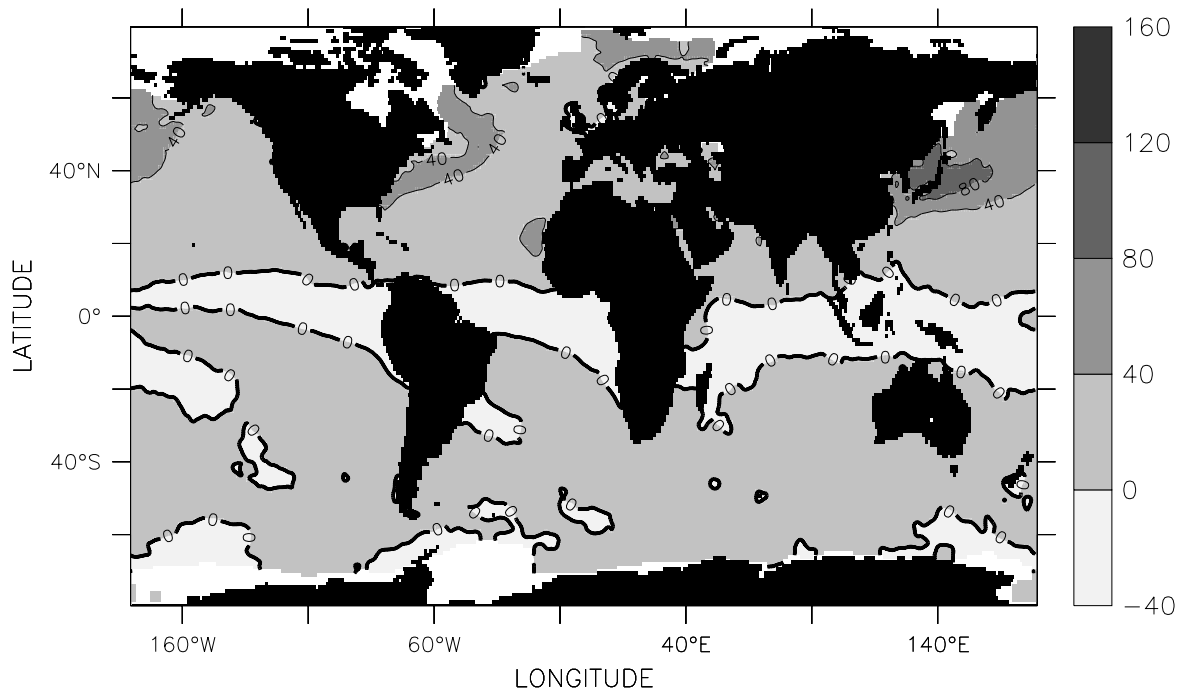
Fig.IV.18 Sensible Heat Flux (W/m^2), January
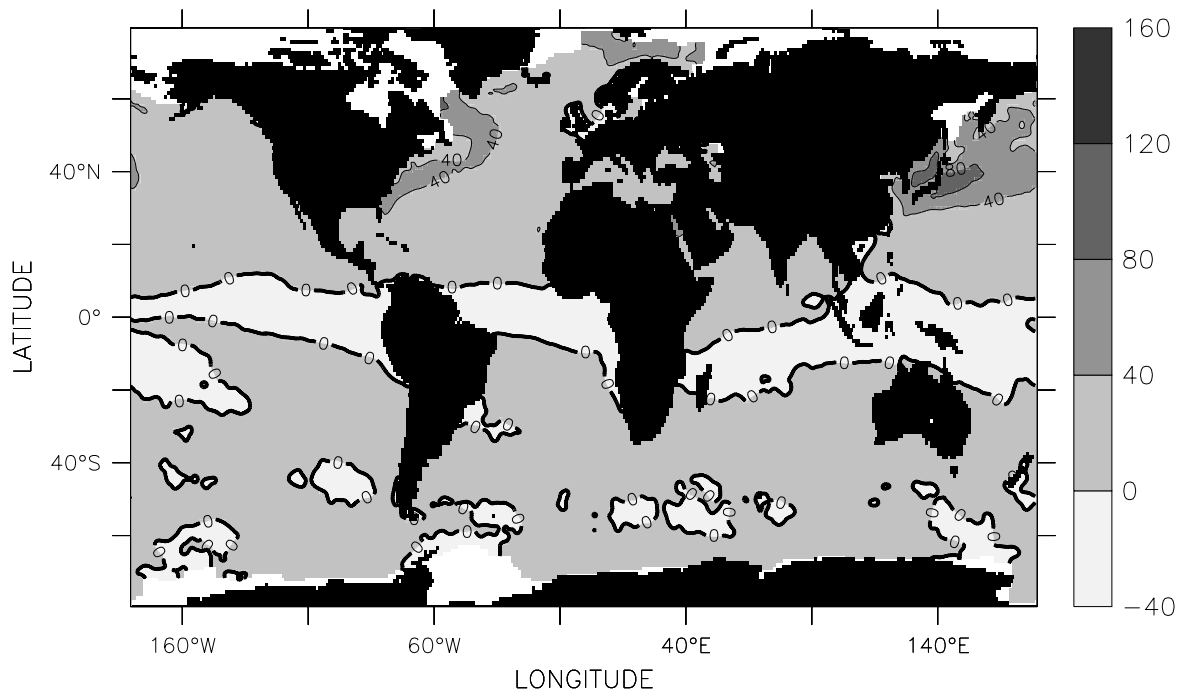
Fig.IV.19 Sensible Heat Flux (W/m^2), February
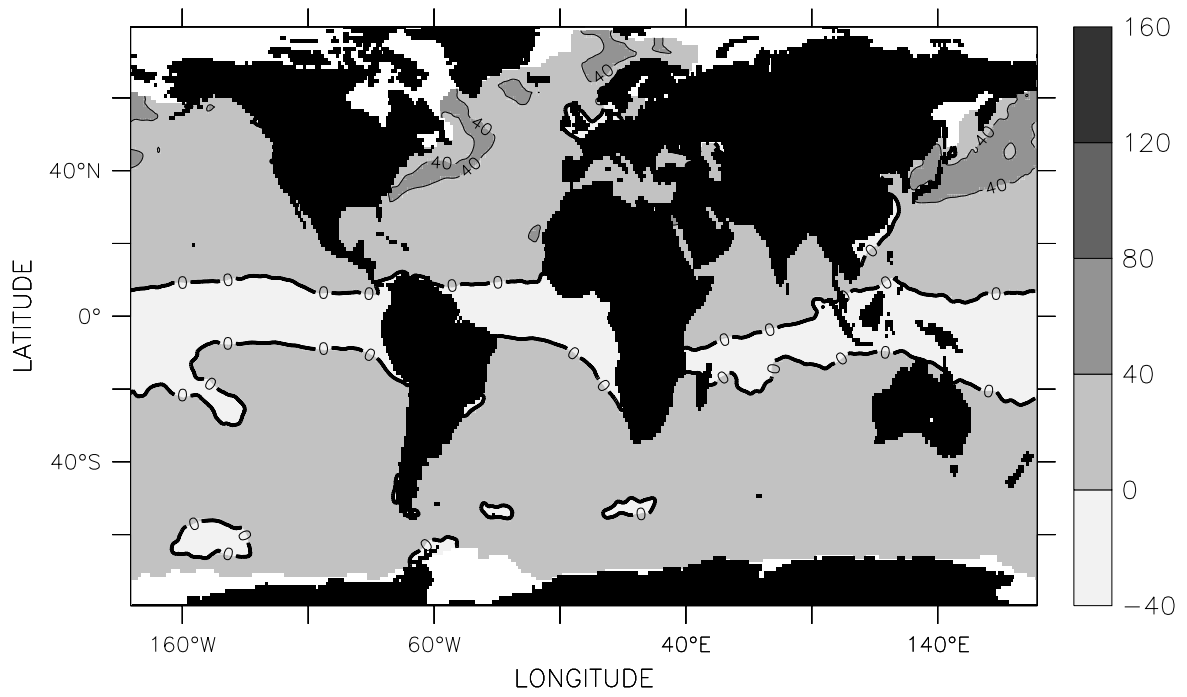
Fig.IV.20 Sensible Heat Flux (W/m^2), March
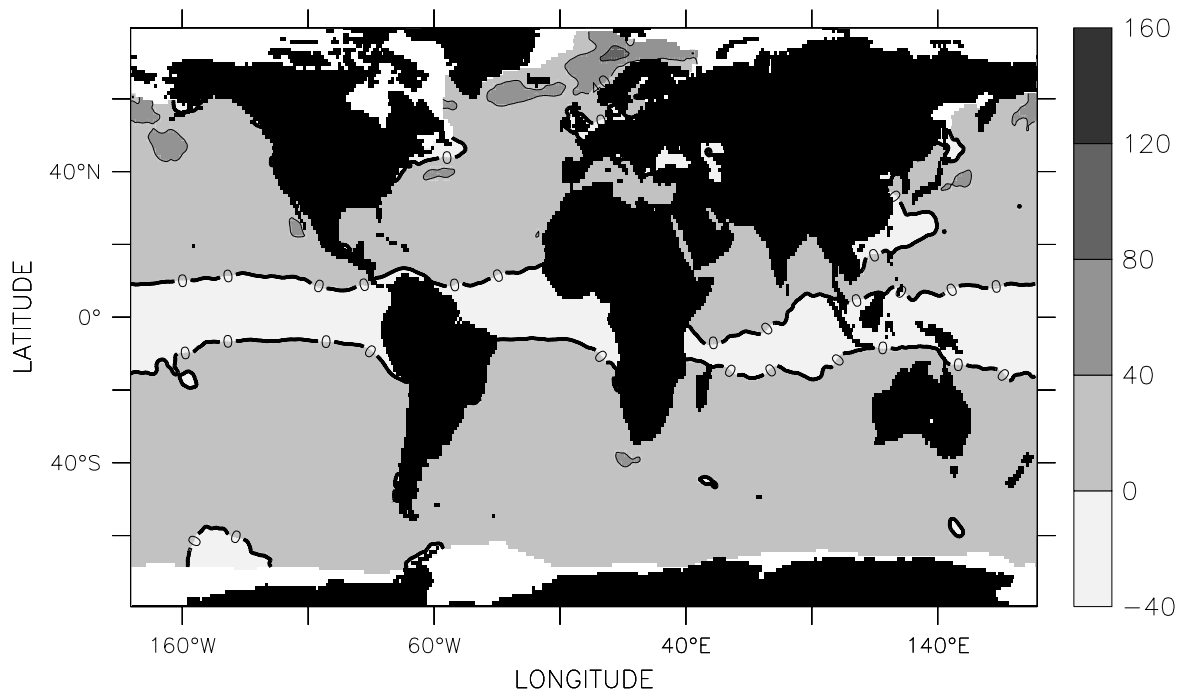
Fig.IV.21 Sensible Heat Flux (W/m^2), April

81
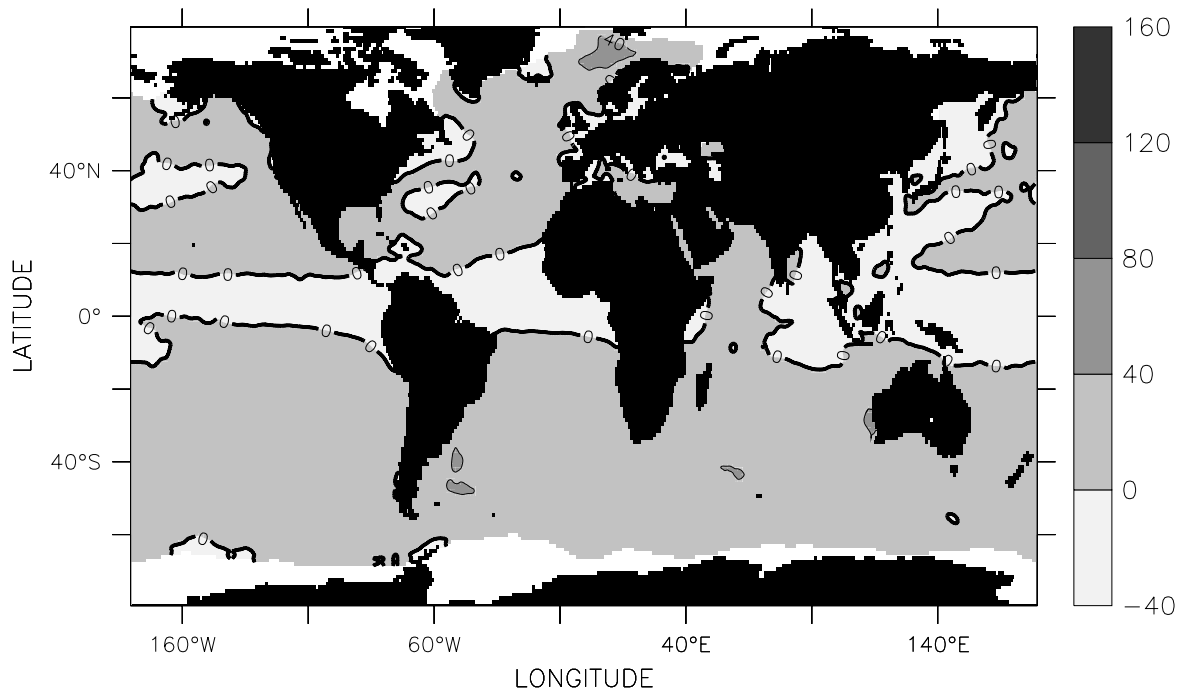
Fig.IV.22 Sensible Heat Flux (W/m^2), May
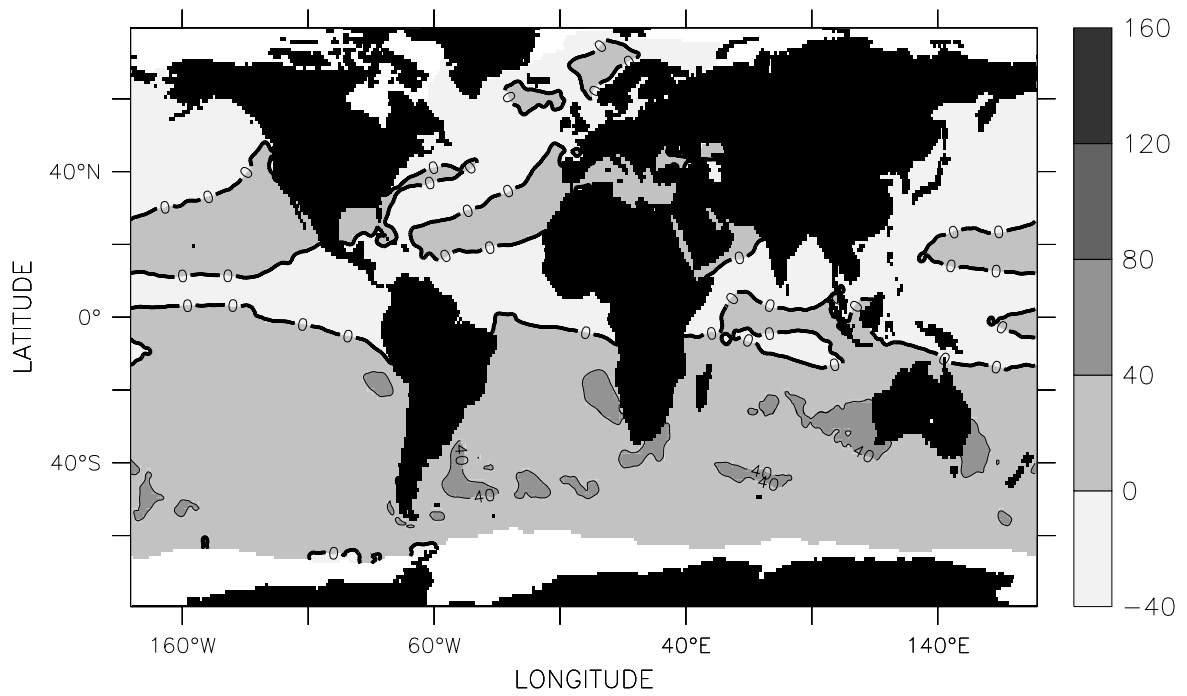
Fig.IV.23 Sensible Heat Flux (W/m^2), June
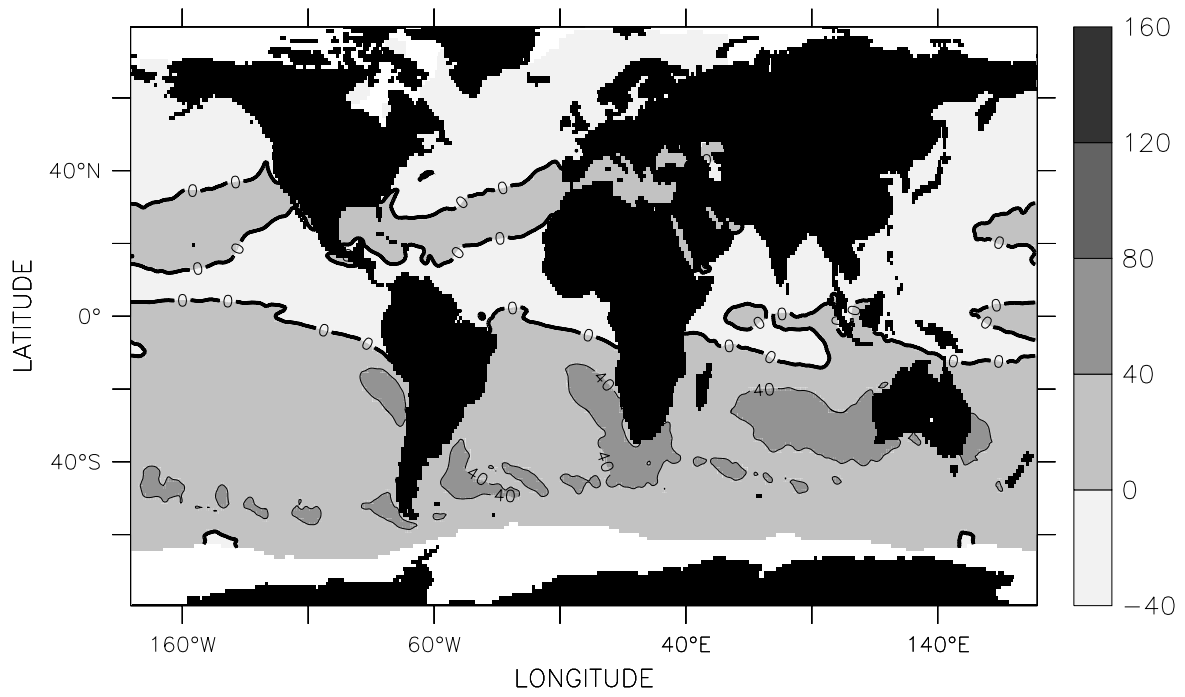
Fig.IV.24 Sensible Heat Flux (W/m^2), July
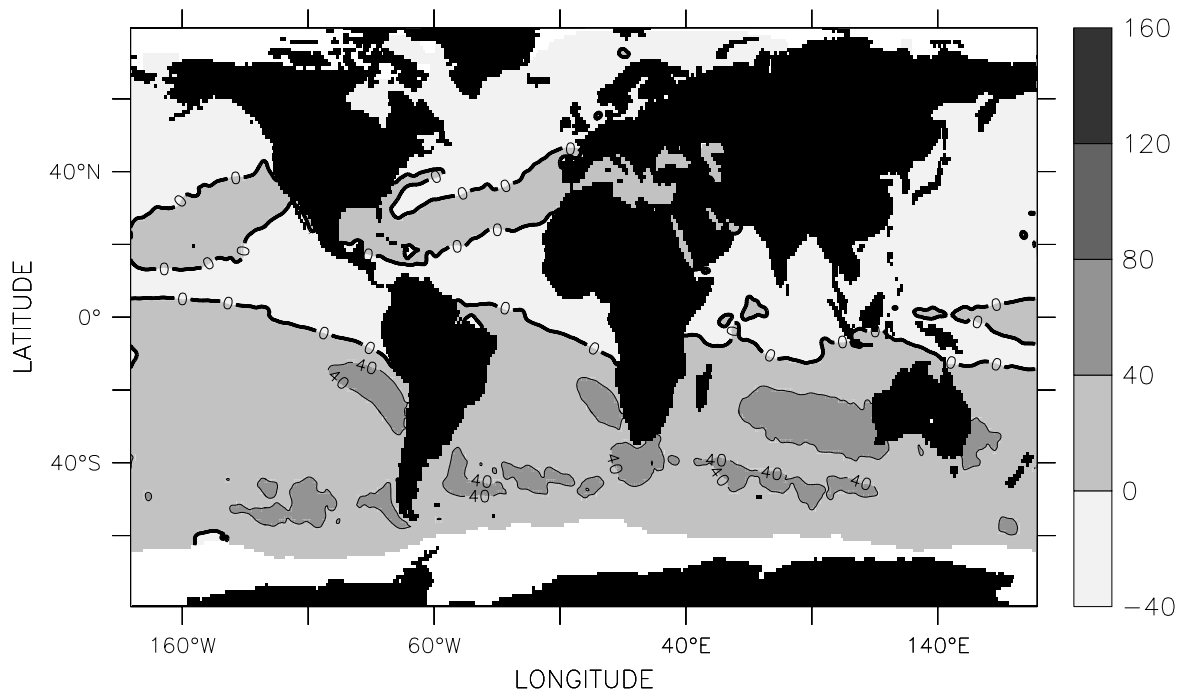
Fig.IV.25 Sensible Heat Flux (W/m^2), August
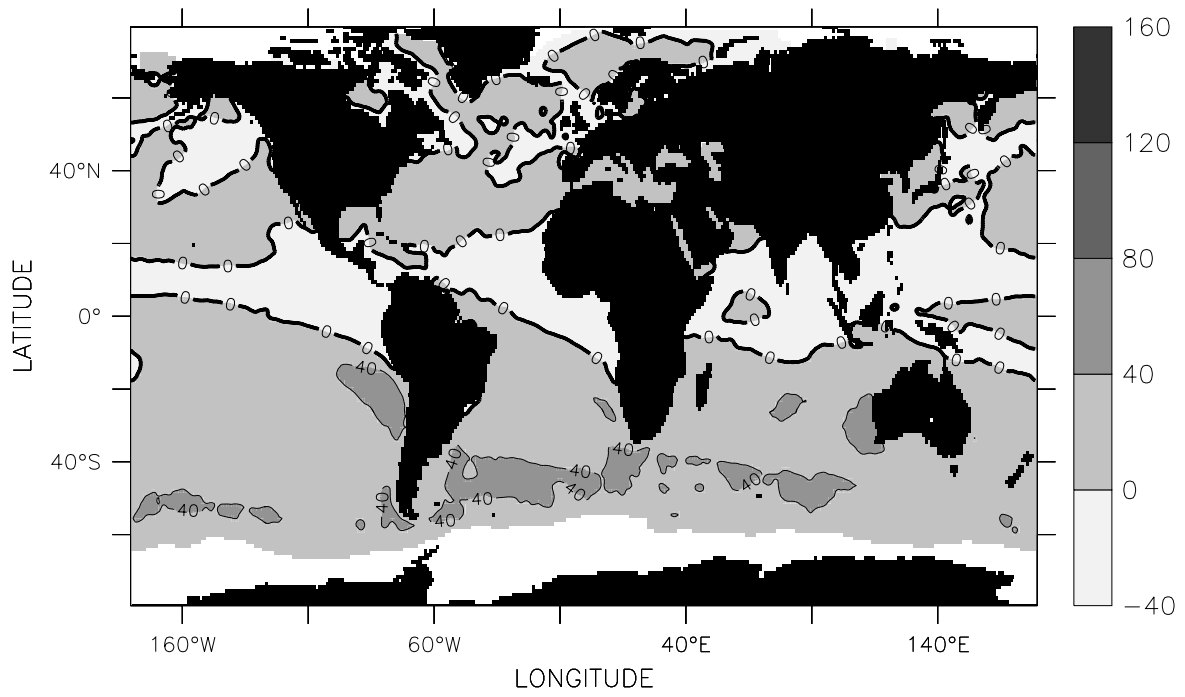
Fig.IV.26 Sensible Heat Flux (W/m^2), September
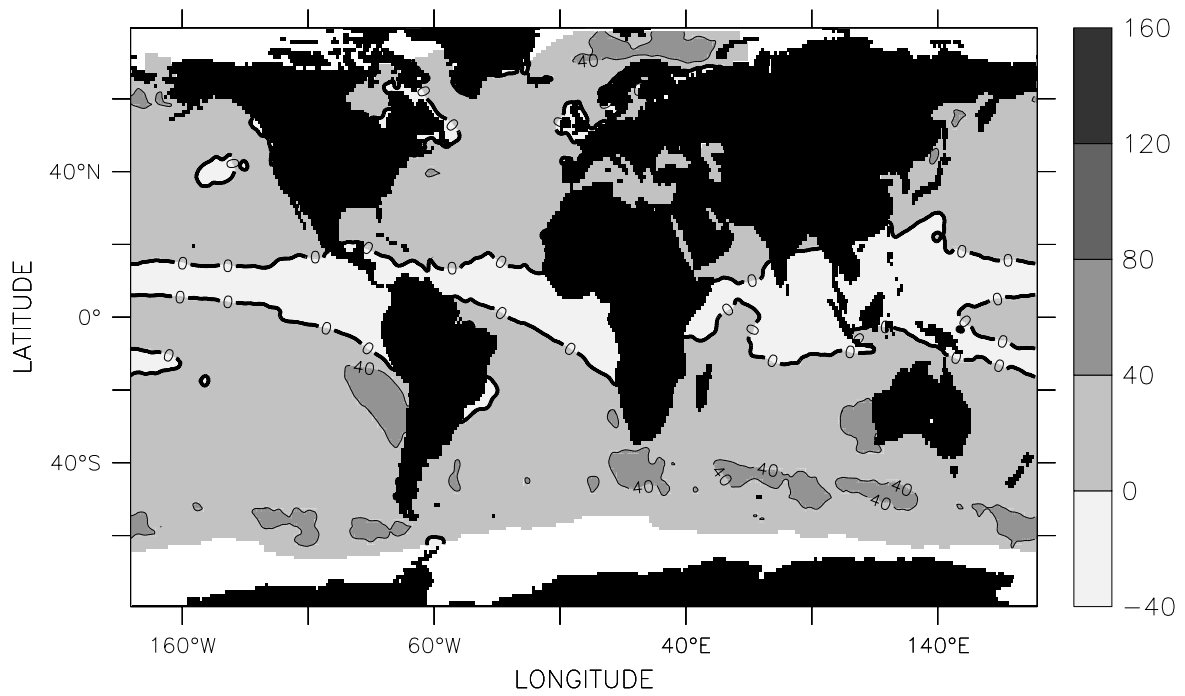
Fig.IV.27 Sensible Heat Flux (W/m^2), October
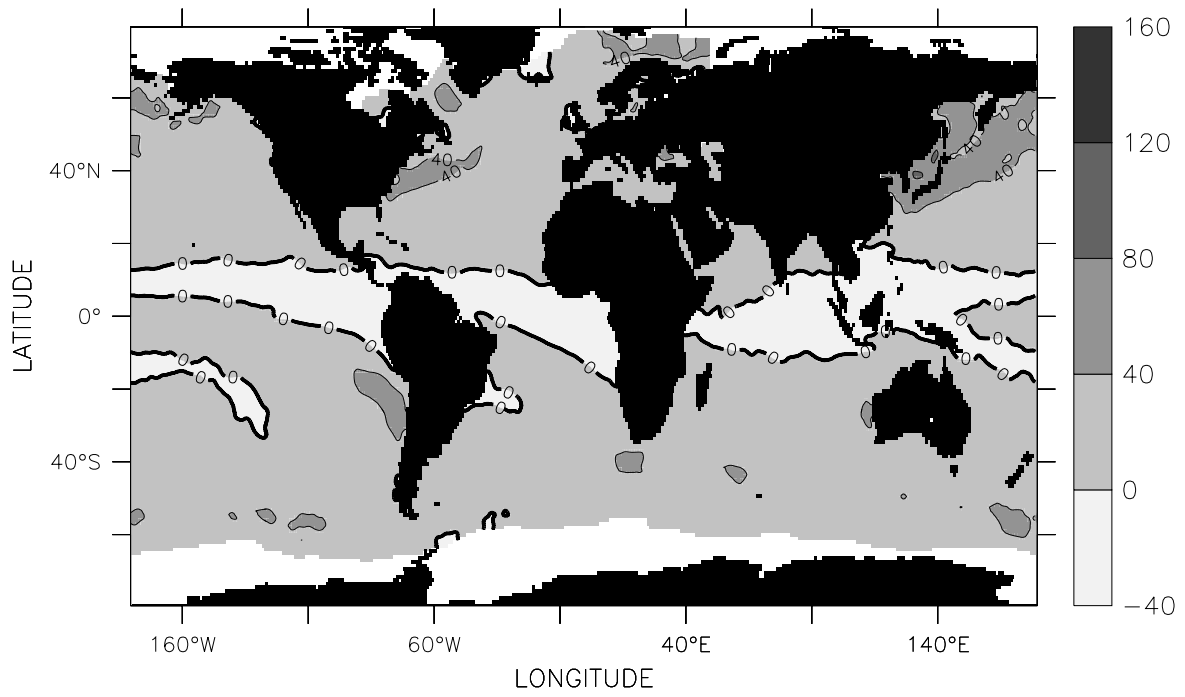
Fig.IV.28 Sensible Heat Flux (W/m^2), November
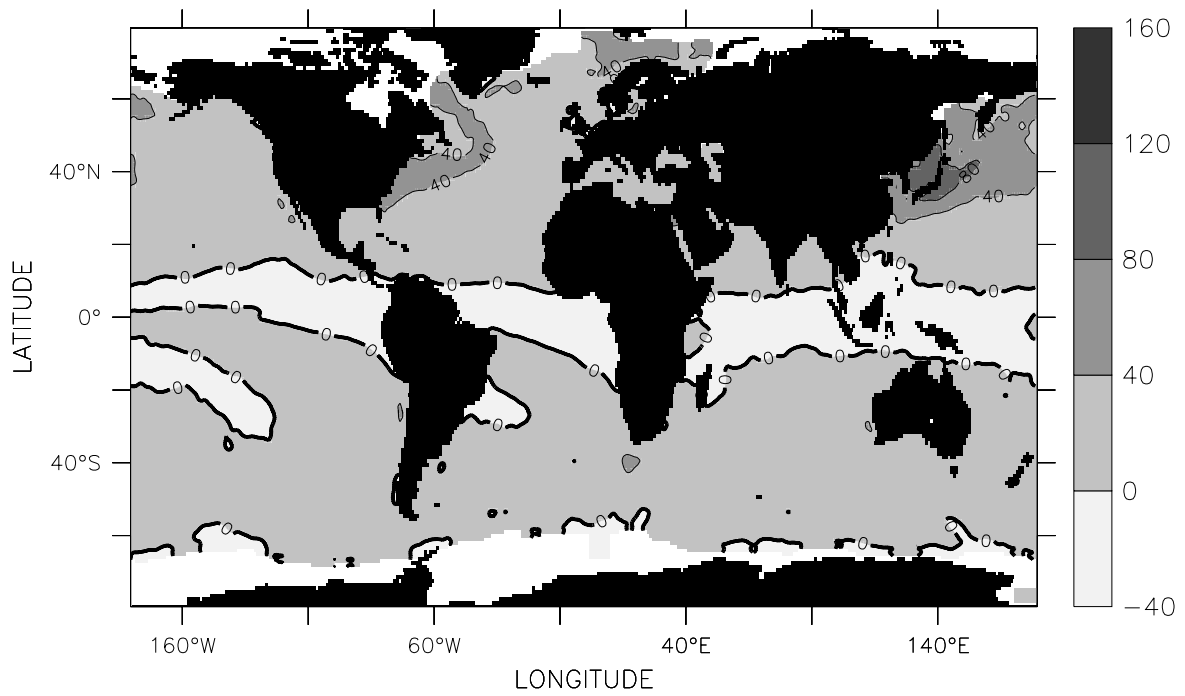
Fig.IV.29 Sensible Heat Flux (W/m^2), December
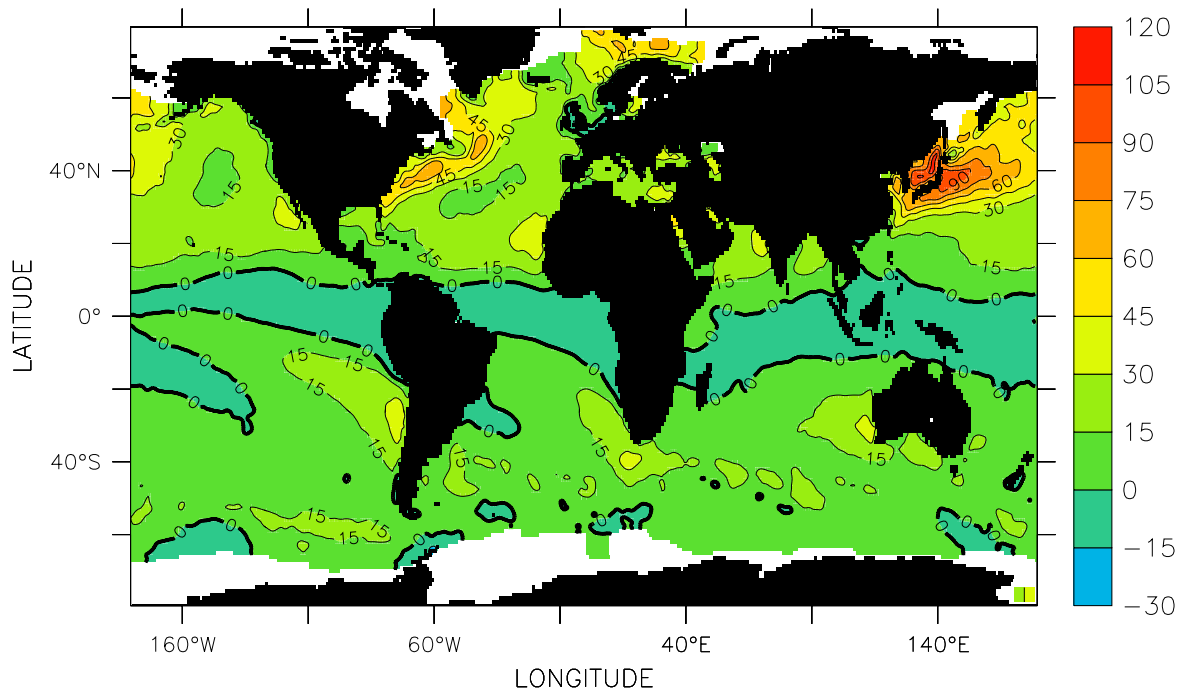
Fig.IV.30 Sensible Heat Flux (W/m^2), DJF
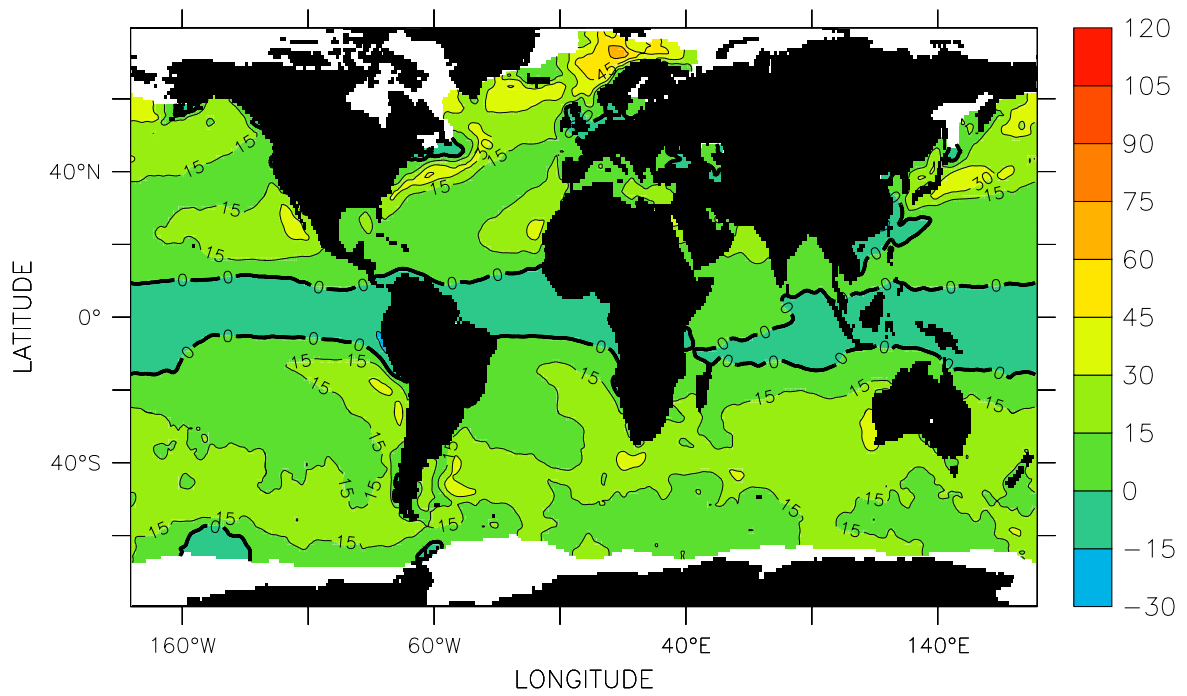
Fig.IV.31 Sensible Heat Flux (W/m^2), MAM
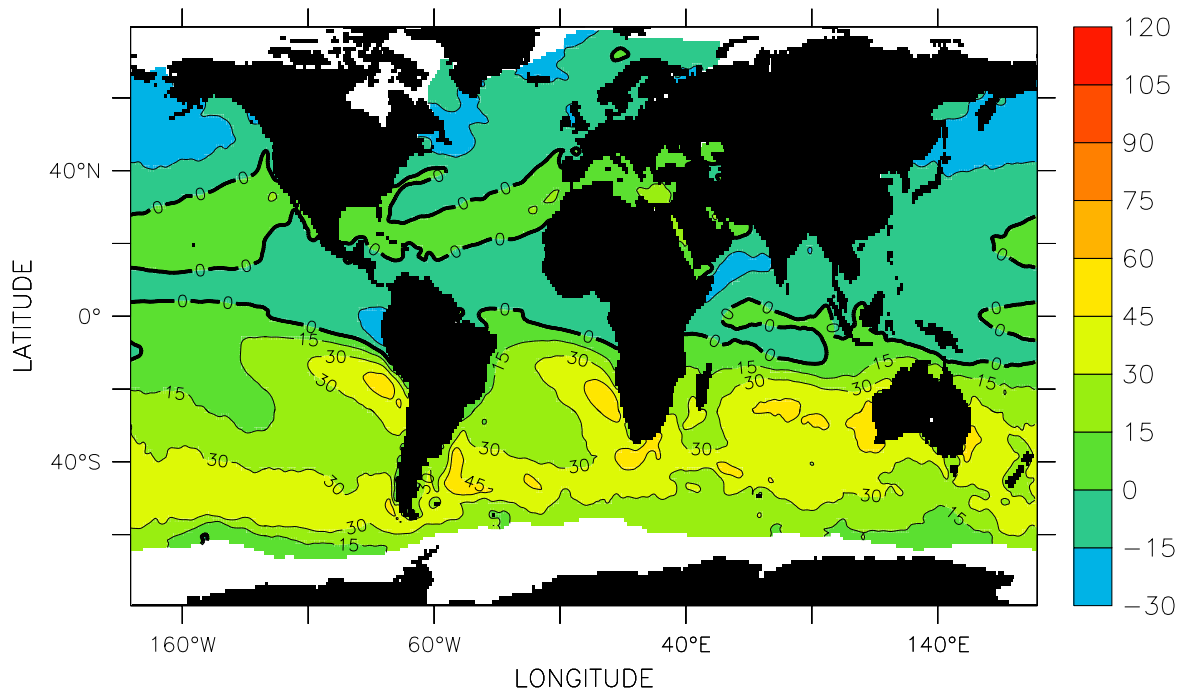
Fig.IV.32 Sensible Heat Flux (W/m^2), JJA
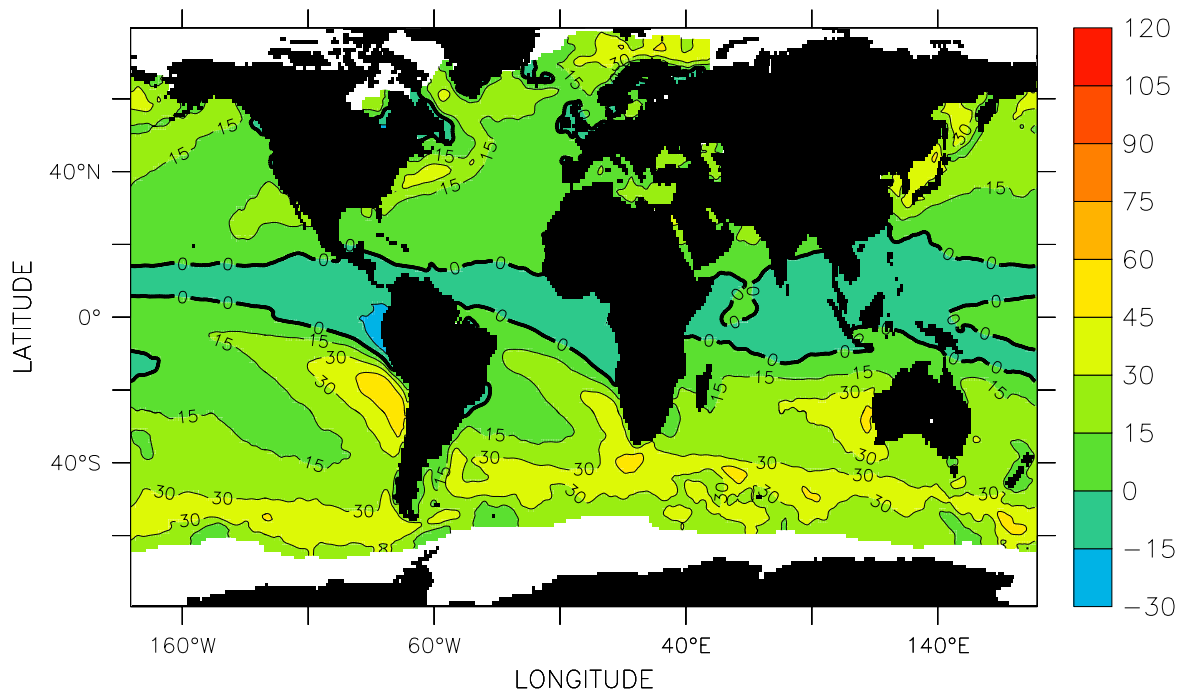
Fig.IV.33 Sensible Heat Flux (W/m^2), SON
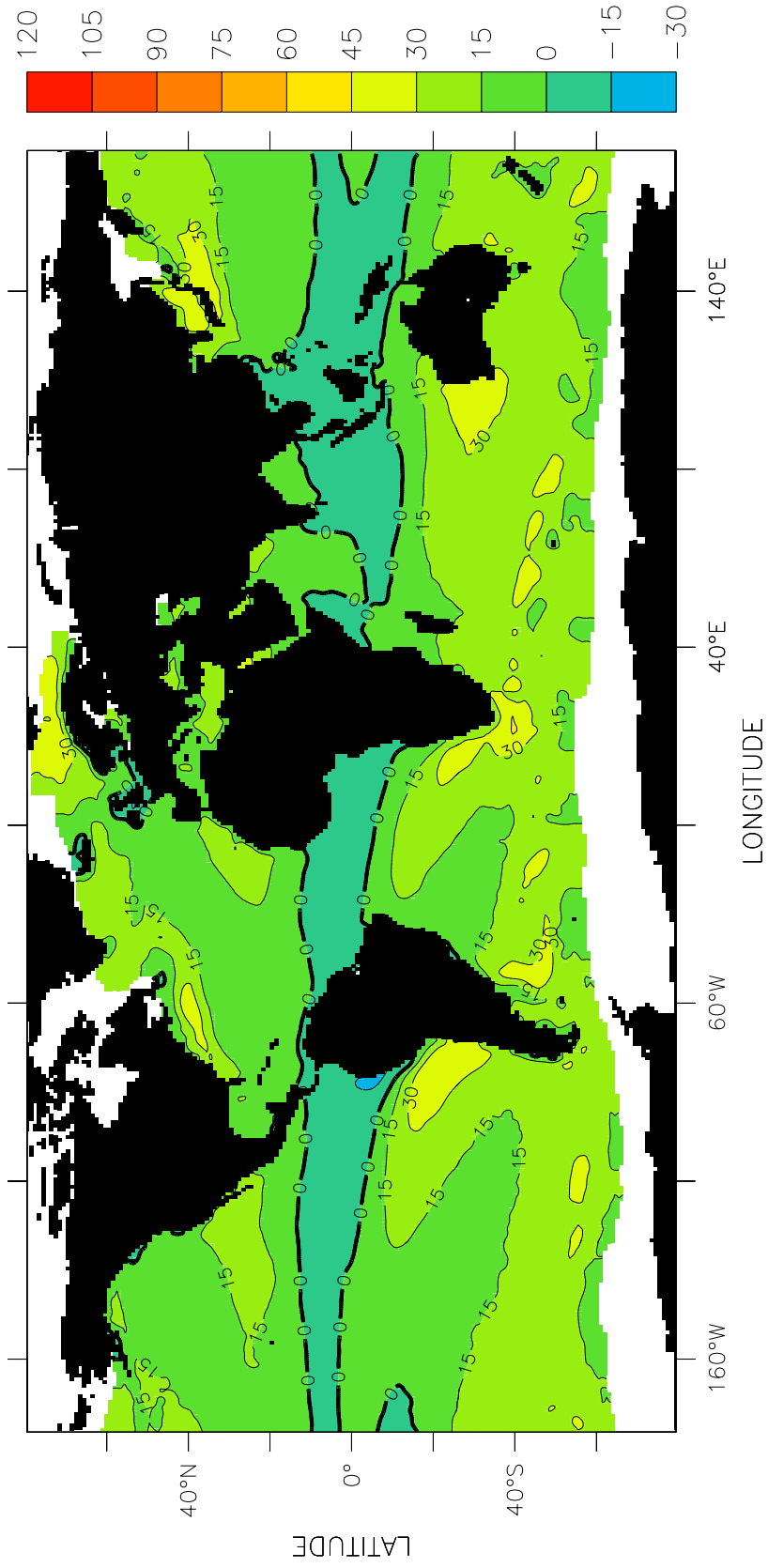
Fig.IV.34 Sensible Heat Flux (W/m^2), Annual
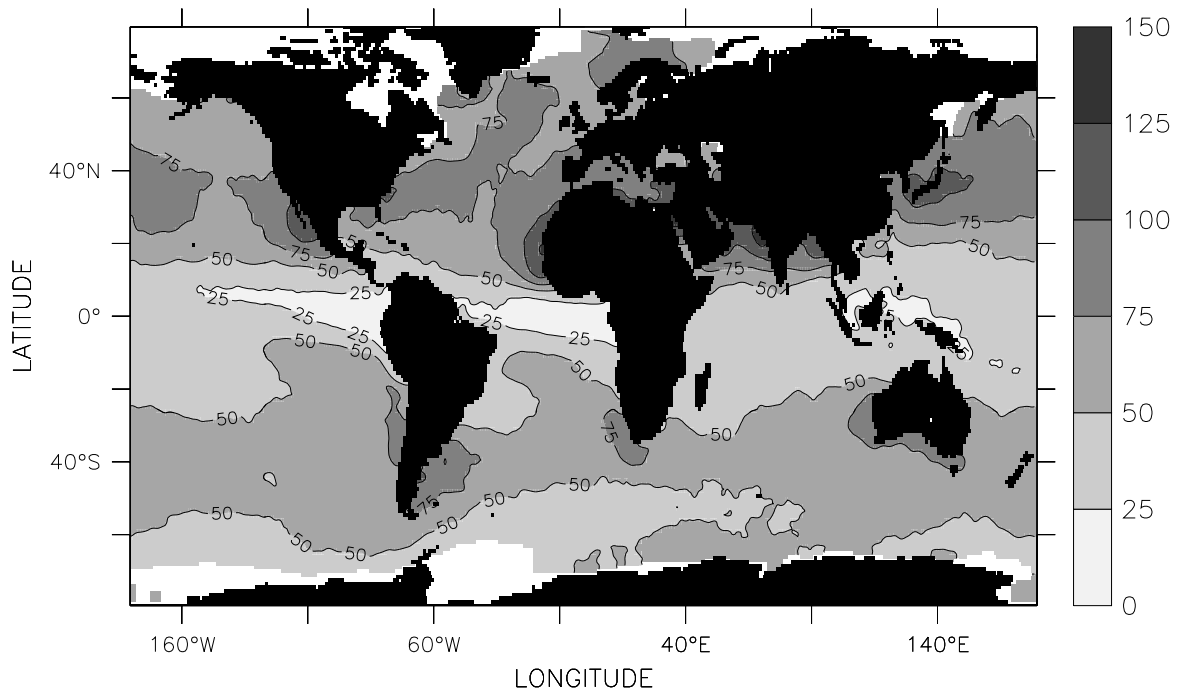
Fig.IV.35 Longwave Net Radiation (W/m^2), January
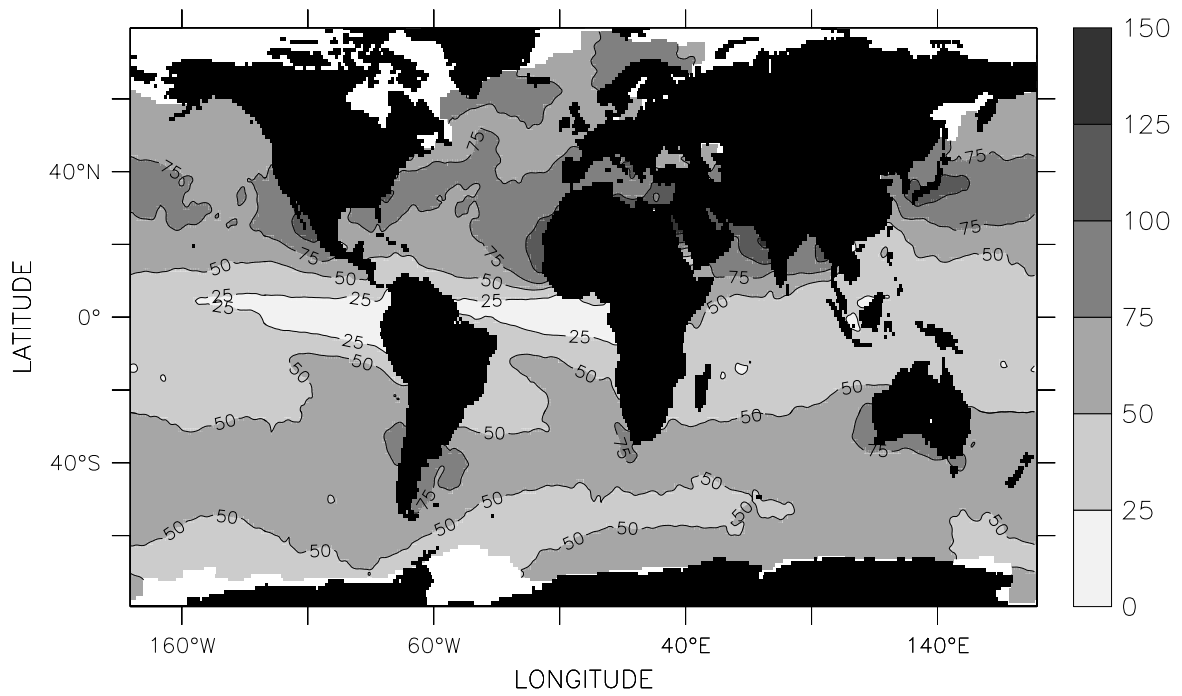
Fig.IV.36 Longwave Net Radiation (W/m^2), February
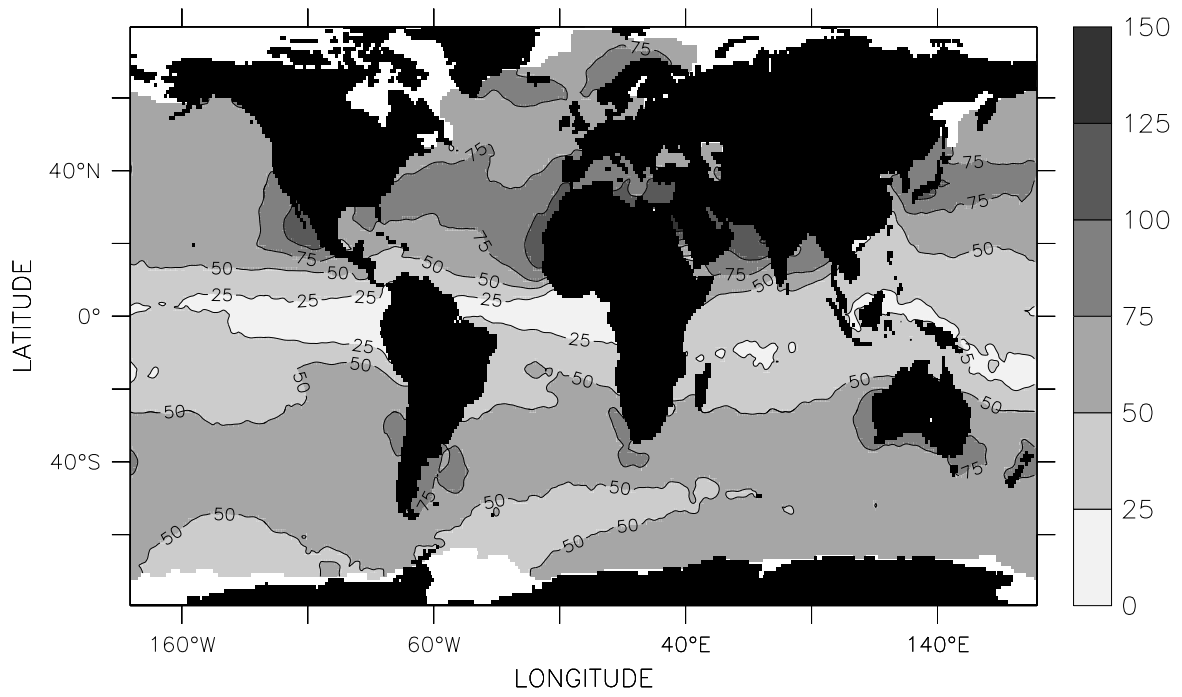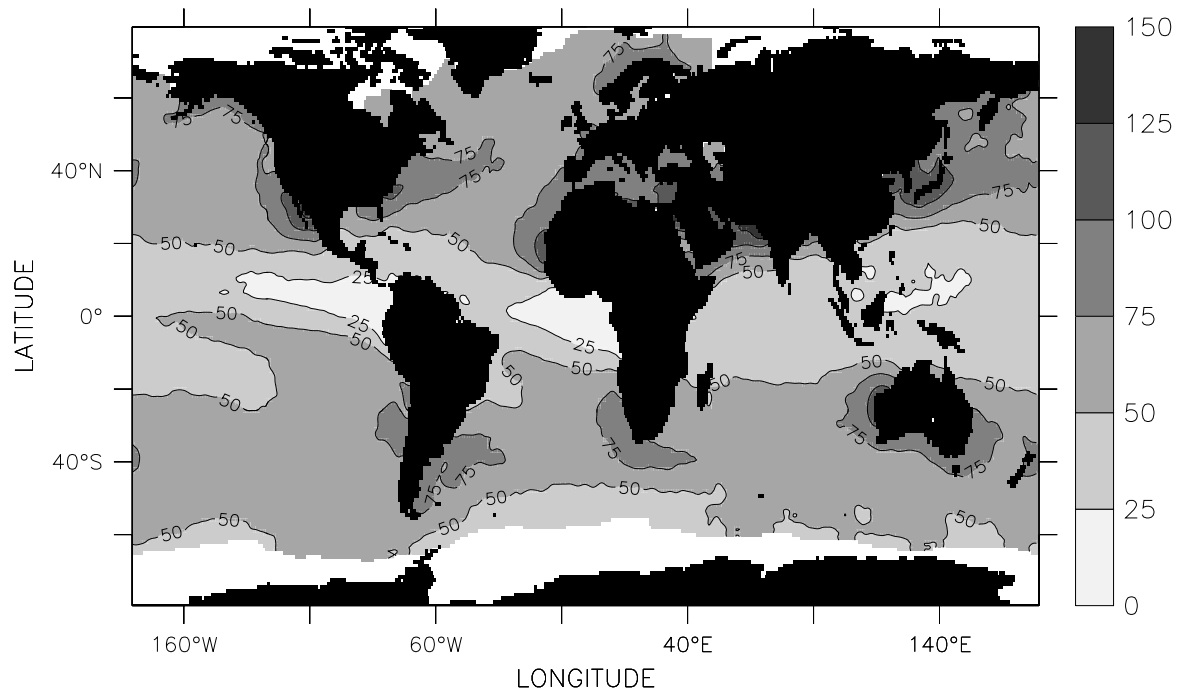
Fig.IV.37 Longwave Net Radiation (W/m^2), March
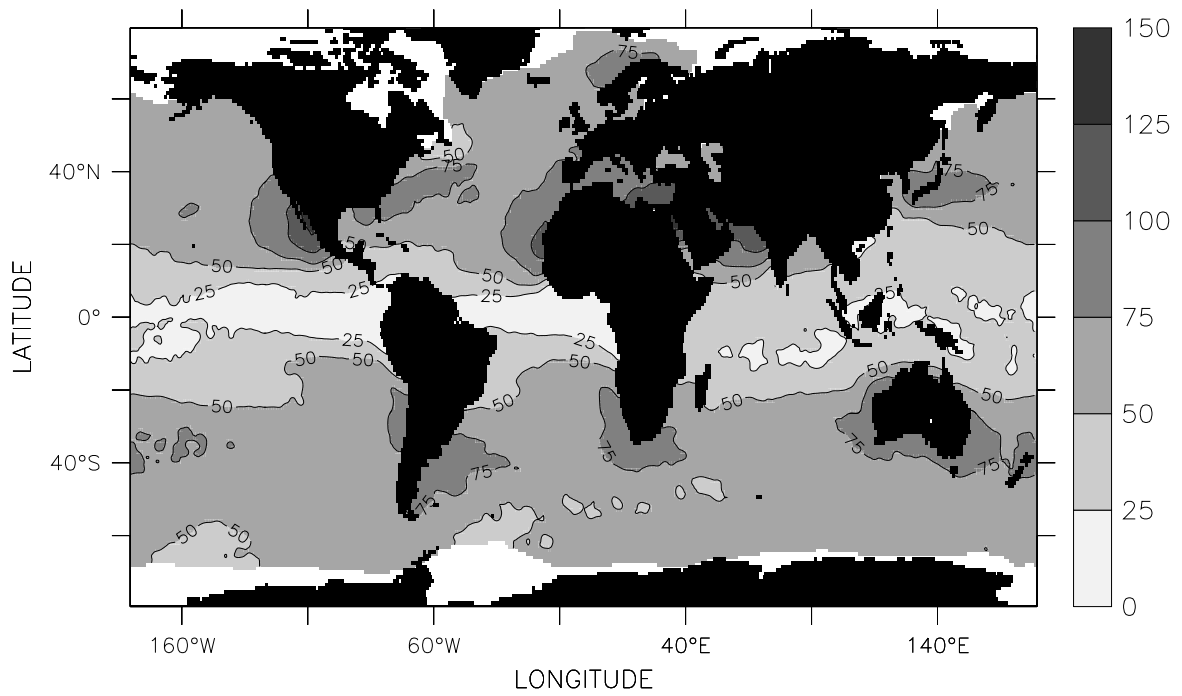
Fig.IV.38 Longwave Net Radiation (W/m^2), April
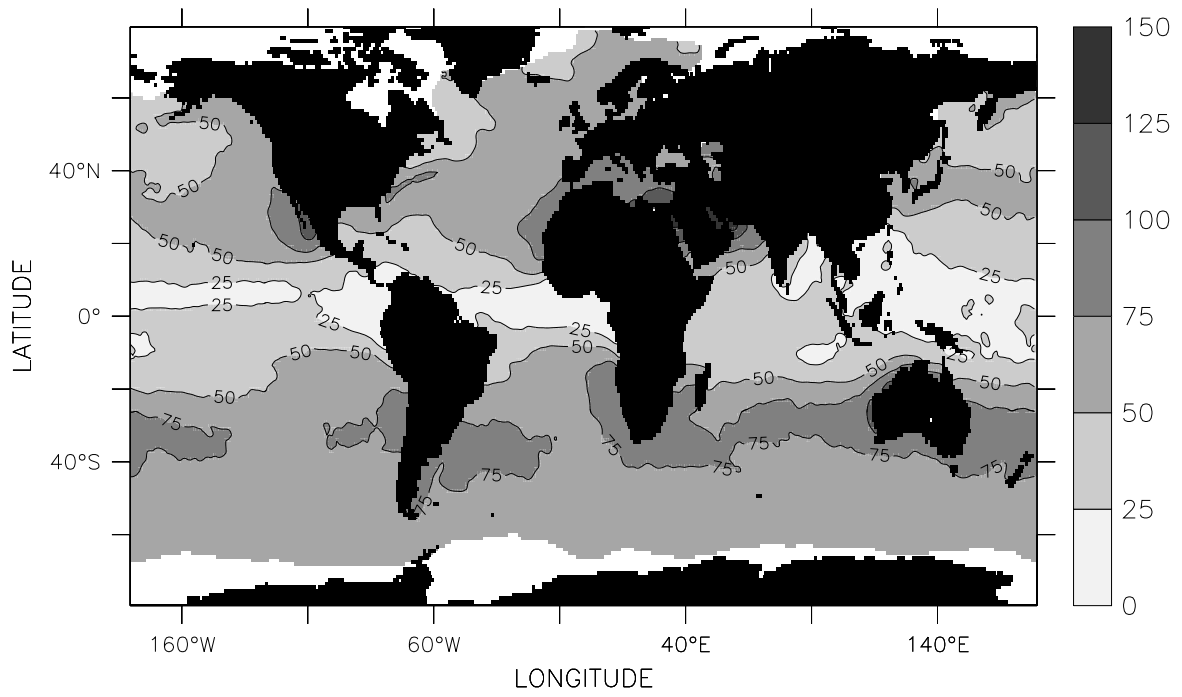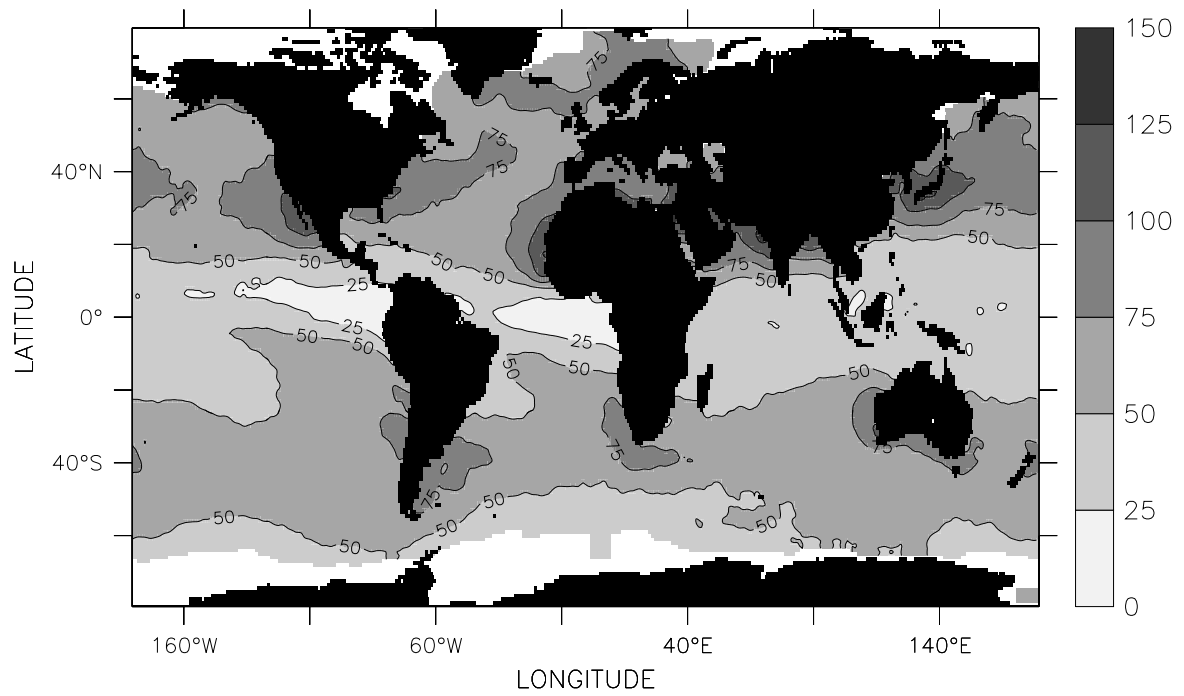
Fig.IV.39 Longwave Net Radiation (W/m^2), May
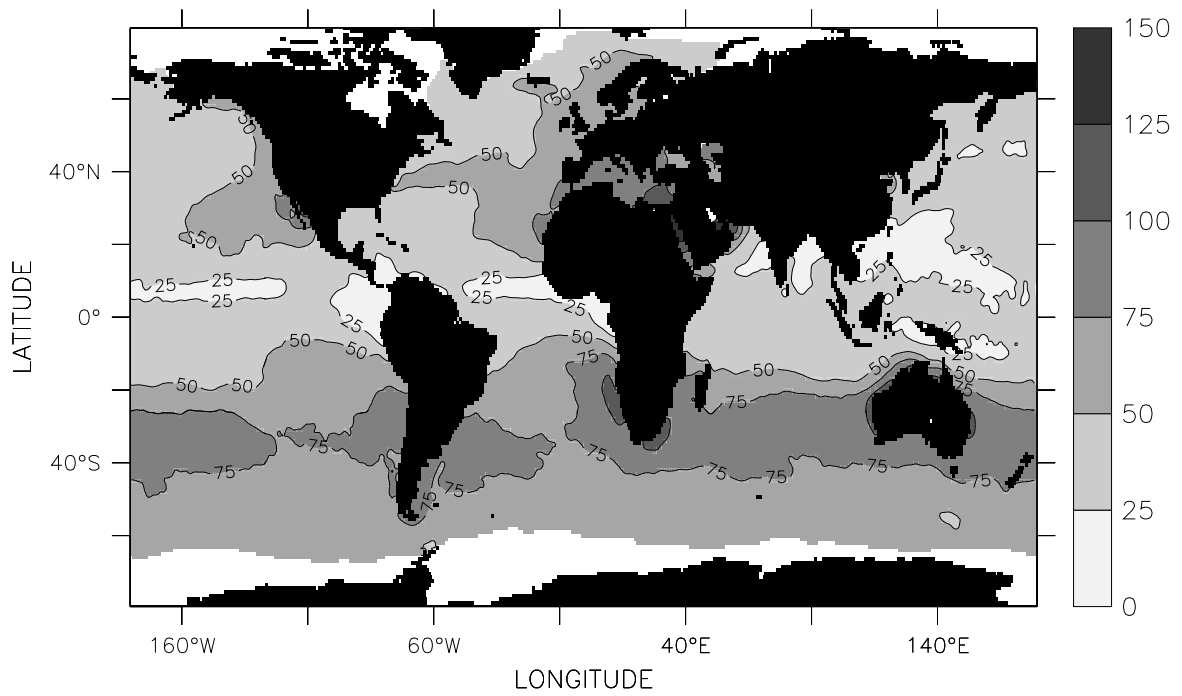
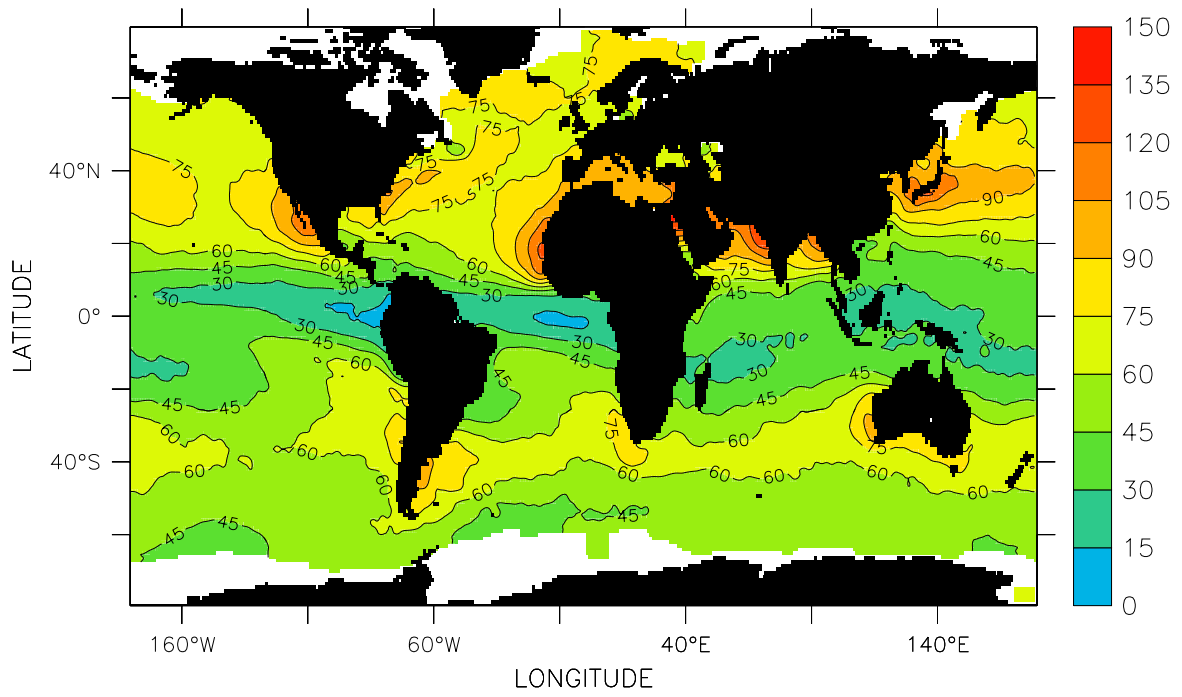

Fig.IV.40 Longwave Net Radiation (W/m^2), June

91
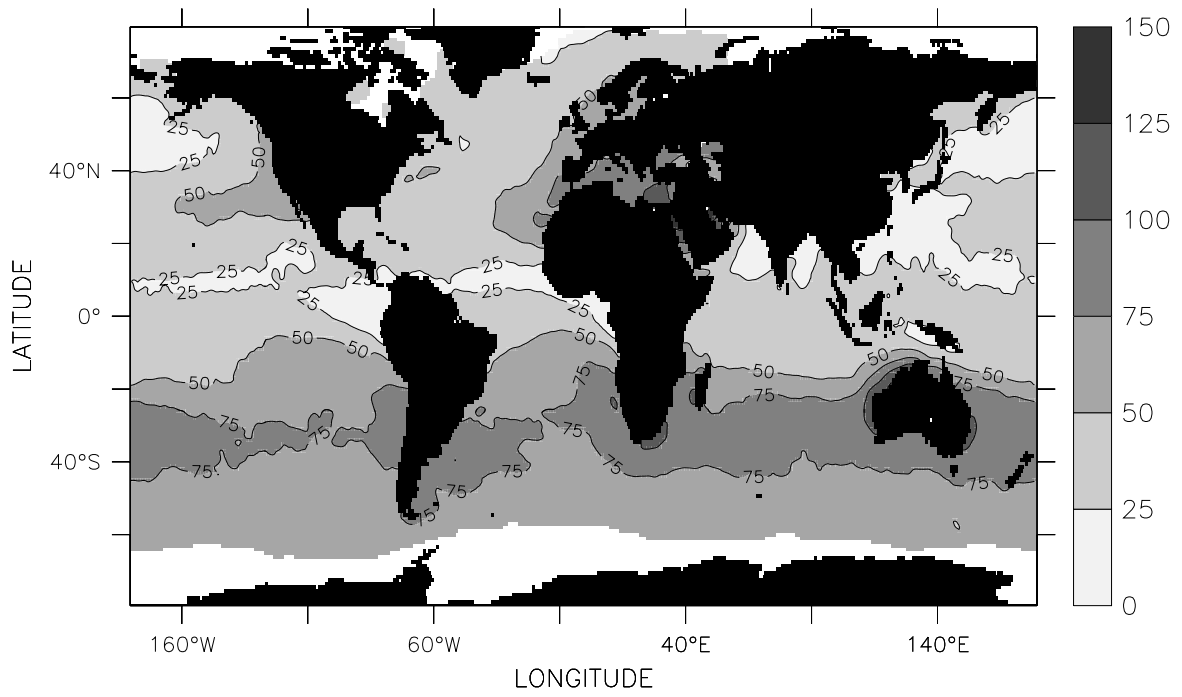
Fig.IV.41 Longwave Net Radiation (W/m²), July
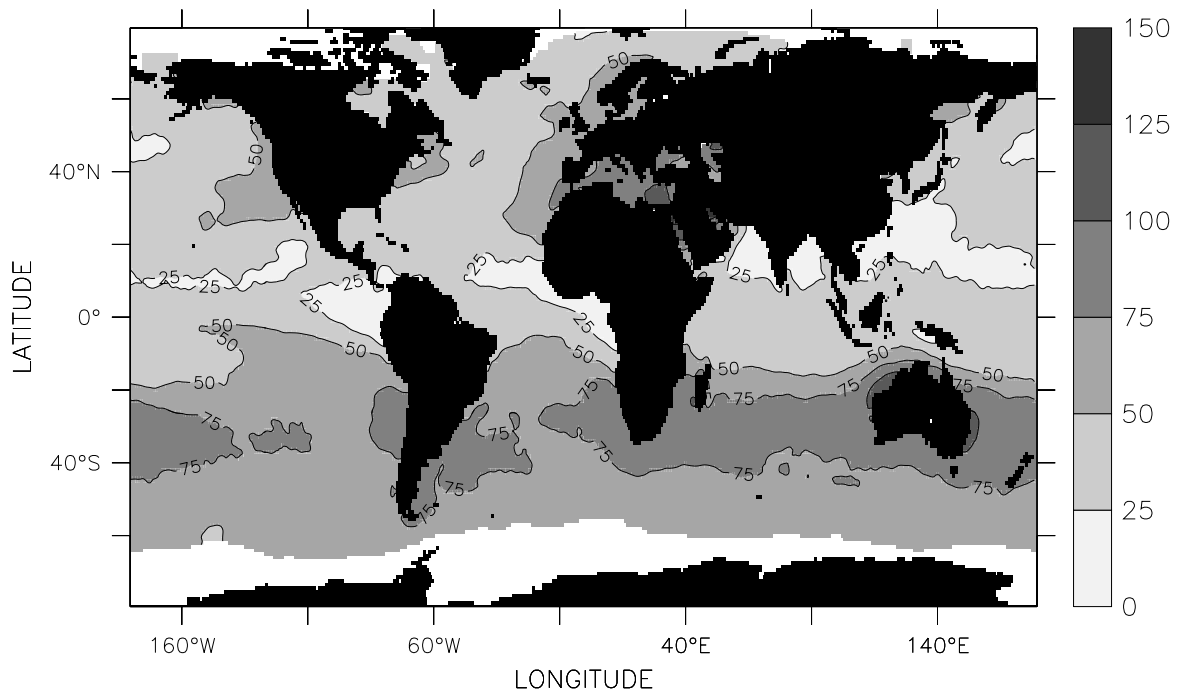
Fig.IV.42 Longwave Net Radiation (W/m²), August
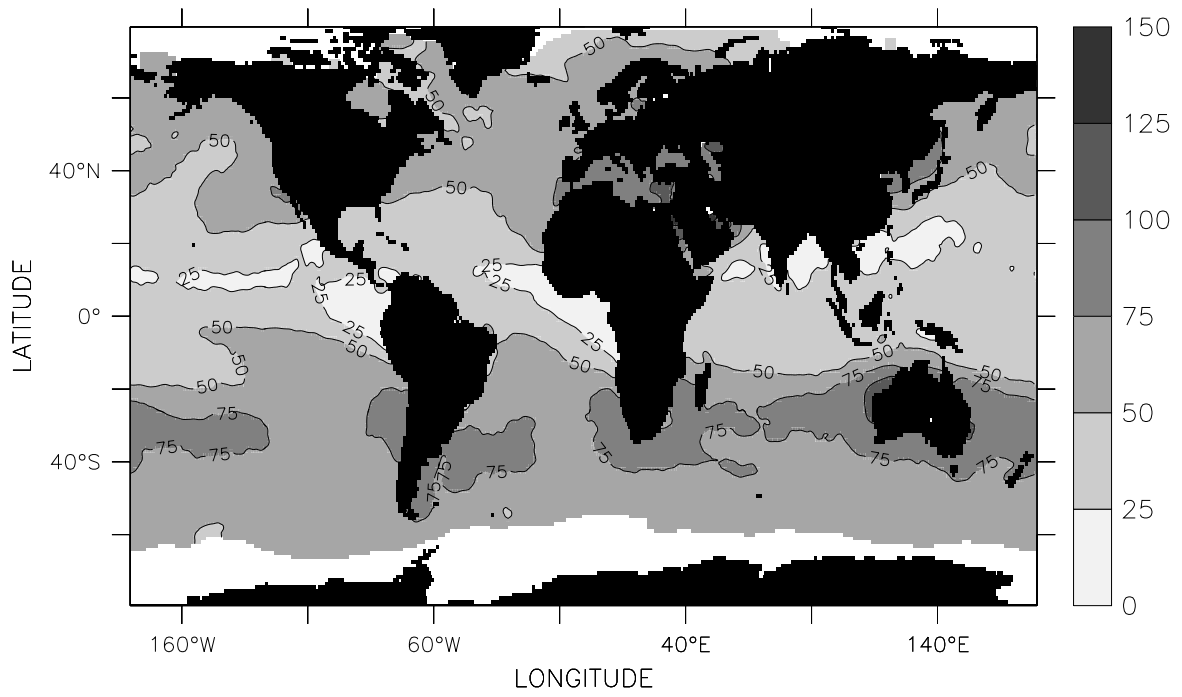
Fig.IV.43 Longwave Net Radiation (W/m^2), September
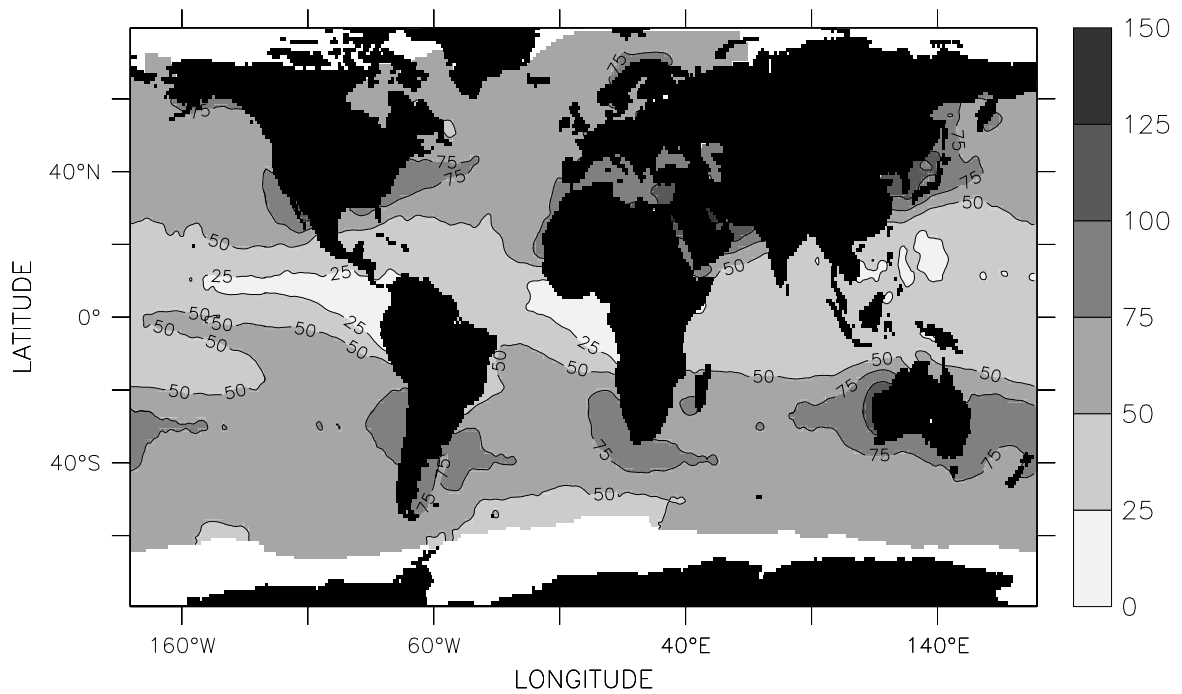
Fig.IV.44 Longwave Net Radiation (W/m^2), October

Fig.IV.45 Longwave Net Radiation (W/m^2), November

Fig.IV.46 Longwave Net Radiation (W/m^2), December
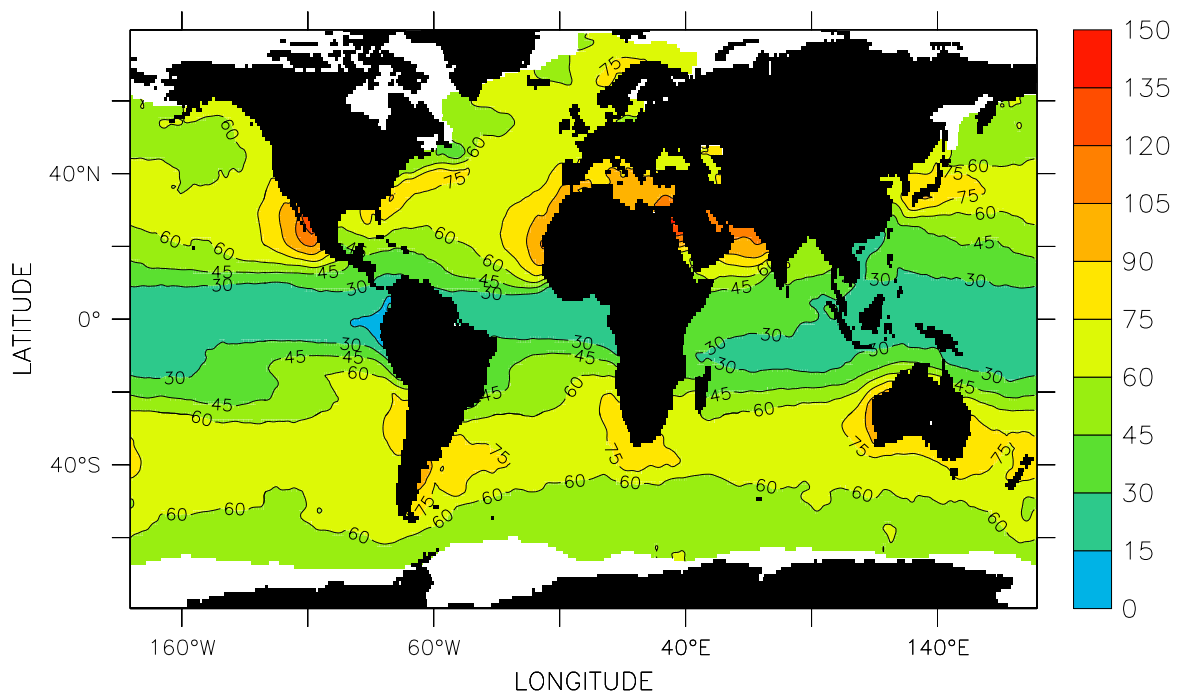
94

Fig.IV.47 Longwave Net Radiation (W/m^2), DJF
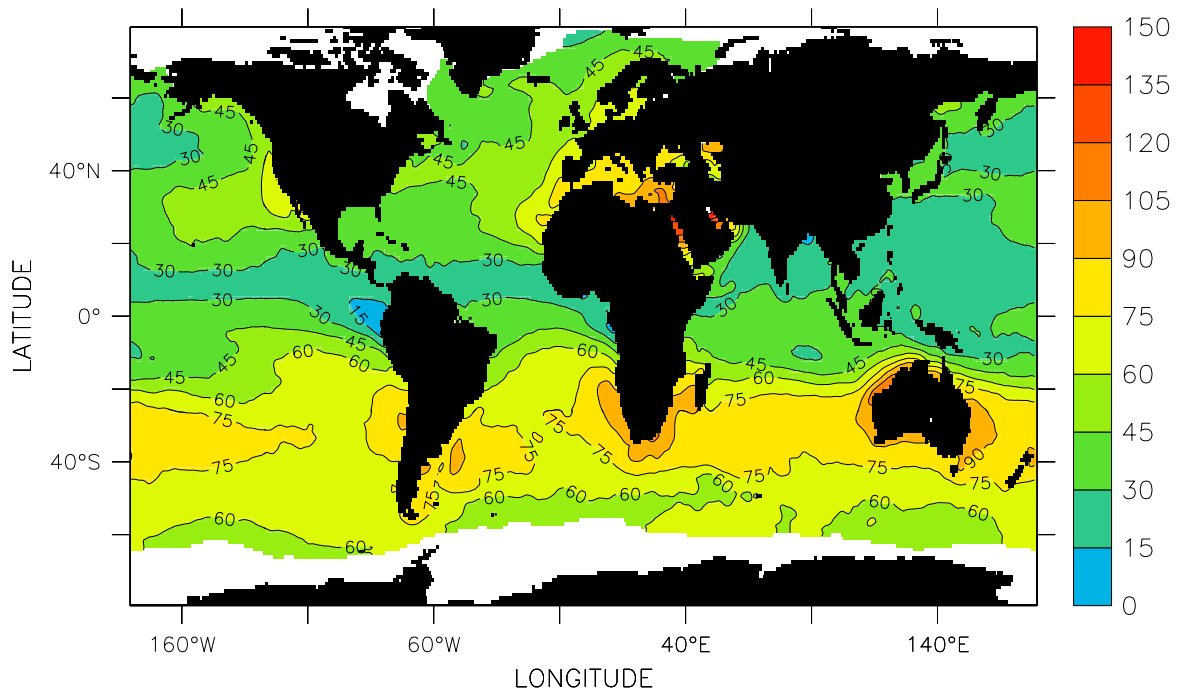

Fig.IV.48 Longwave Net Radiation (W/m^2), MAM

Fig.IV.49 Longwave Net Radiation (W/m^2), JJA
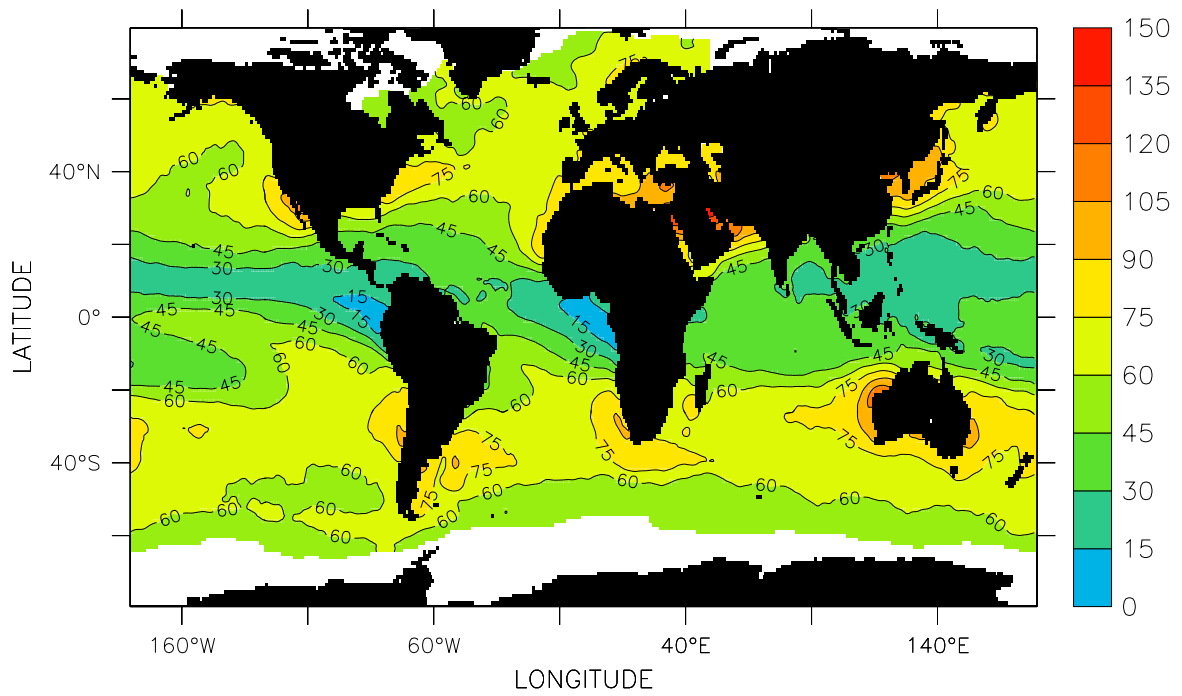

Fig.IV.50 Longwave Net Radiation (W/m^2), SON
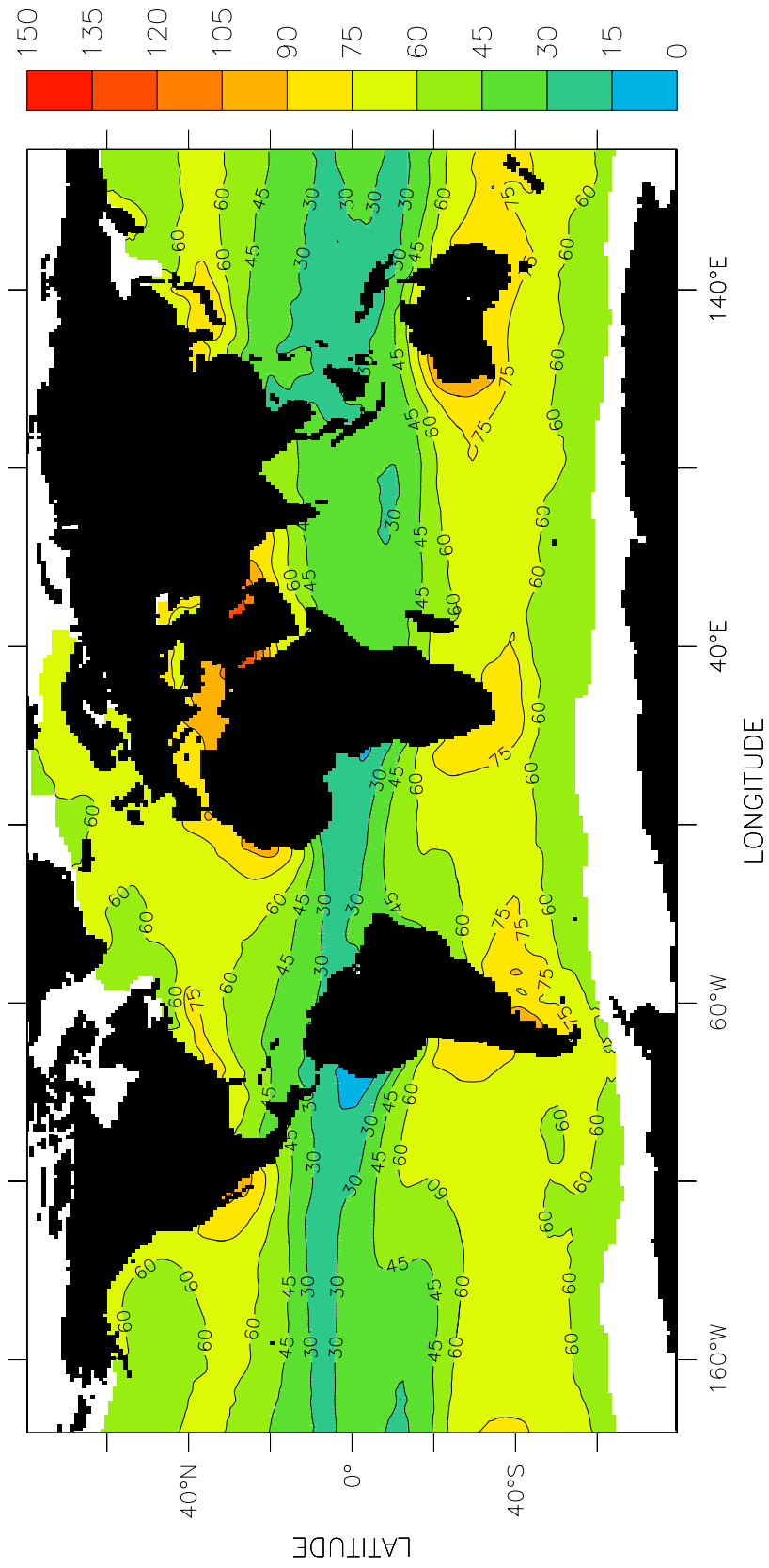
96

Fig.IV.51 Longwave Net Radiation (W/m^2), Annual

Chapter V   Hydrological Cycle

The hydrological cycle parameters evaporation, precipitation and freshwater flux show significant variations both on monthly and seasonal scale.

V.1. Evaporation (Figures V.1 to V.17)

The evaporation maps are very similar to the LHF maps with the maximum values up to 9 mm d^{-1} observed over the Kuroshio and Gulf Stream regions in winter (Figures V.1,2 and 12 as well as 13) and the minimum values below 1 mm/d seen in the eastern equatorial Pacific and Atlantic during all months. Large areas with high evaporation rates of 5-6 mm d^{-1} are found in the main trade wind belts between about 10° and $40^o \times \times$ latitude both on the northern and southern hemisphere. These high evaporation regions are known as the major source of the global hydrological cycle. Whereas during winter and spring the maximum extent and the highest values are found north of the equator (Figure V.13,14), maximum evaporation is observed in the southern Indian, Atlantic and Pacific Ocean during summer and autumn (Figure V.15,16).

V.2. Precipitation (Figures V.18 to V.34)

The global precipitation pattern (Figures V.18 to 29) is dominated by a strong band of precipitation girdling the globe just north of the equator. This is the region where the northern and southern Hadley circulation cells meet, forming a region of strong surface convergence known as the Intertropical Convergence Zone (ITCZ). There the maximum precipitation on an annual scale exceeds 6 mm d^{-1}. Another convergence zone in the western tropical Pacific is known as the South Pacific Convergence Zone (SPCZ). This region is somewhat broader with precipitation values similar to the ITCZ and it extends from the region of Indonesia and the Philippines southeast across the southern Pacific. With the onset of the summer monsoon, the ITCZ, which was earlier located in the southern Indian Ocean shifts to its northernmost location and merges with the Monsoon trough giving rise to copious rainfall over the Indian subcontinent and the adjacent seas, namely the Arabian Sea and Bay of Bengal (Figures V.22 to 26).

On an annual scale (Figure V.34) the region off the Indonesian islands receive the maximum rainfall of more than 10 mm d^{-1}. Outside the two convergence zones, precipitation rates are significantly lower, with the exception of two regions. Precipitation rates are quite high over the Gulf Stream and Kuroshio region, too. During the period November to March values are found to be as high as in the ITCZ. This feature has not been recognized in any earlier climatology.

In tropical and subtropical latitudes, between about 15° and 40° in the northern hemisphere and between 5° and 30° in the southern hemisphere, the eastern portions of the Pacific and the Atlantic are regions where precipitation is below 1 mm d^{-1}. In the Indian Ocean, a similar region is found in the southern hemisphere, but in the northern hemisphere the precipitation minimum is found along the eastern coast of Africa and Saudi Arabia during all months with a maximum extent in winter.

V.3. Freshwater Flux (Figures V.35 to V.51)

The patterns of precipitation and evaporation have quite different spatial distributions. Precipitation maxima occur in the global convergence regions, while evaporation maxima occur in regions of high humidity difference and wind speed. As a result the freshwater flux (E-P), which we have computed as the difference of evaporation and precipitation, shows the major features of both the evaporation and precipitation fields (Figures V.35 to 46).

The ITCZ and SPCZ appear prominently as regions of negative freshwater flux. In these regions the freshwater flux from atmosphere to ocean is generally larger than 4 mm d^{-1}. With the exception of the SPCZ, precipitation decreases rapidly with latitude to the north and to the south of the ITCZ, while evaporation remains strong or even increases, causing positive values of the freshwater flux.

The strongest gradients in the freshwater flux fields occur in the boundary regions between the negative values of 4 mm d^{-1} within the ITCZ and the strong positive flux regions to the north and south with values up to 6 mm d^{-1}. Poleward from the evaporation regions the freshwater flux fields again become negative. The evaporation fields generally decrease towards the poles primarily as a result of the decrease in the humidity difference except wintery arctic cold air outbreaks, which lead often to very high evaporation and therefore to positive freshwater fluxes. Although evaporation is quite high, large negative values of E-P can be found in the Gulf Stream and Kuroshio region below -4 mm d^{-1} during the winter due to high precipitation, while in all other months evaporation almost balances precipitation.

An analysis of the freshwater flux on a seasonal scale (Figures V.47 to 50), shows that the eastern parts of the Arabian Sea, the Bay of Bengal and the South China Sea all have negative values of freshwater flux during summer and autumn. Further, on an annual scale (Figure V.51), it can be seen that the eastern equatorial Indian Ocean, the Bay of Bengal, the Kuroshio and the Gulf Stream regions all exhibit negative fluxes. The regions of positive flux are over the northwest Arabian Sea and the southern Indian Ocean south of 20° S. Also the North Atlantic and the South Atlantic exhibit positive fluxes on both sides of the ITCZ.
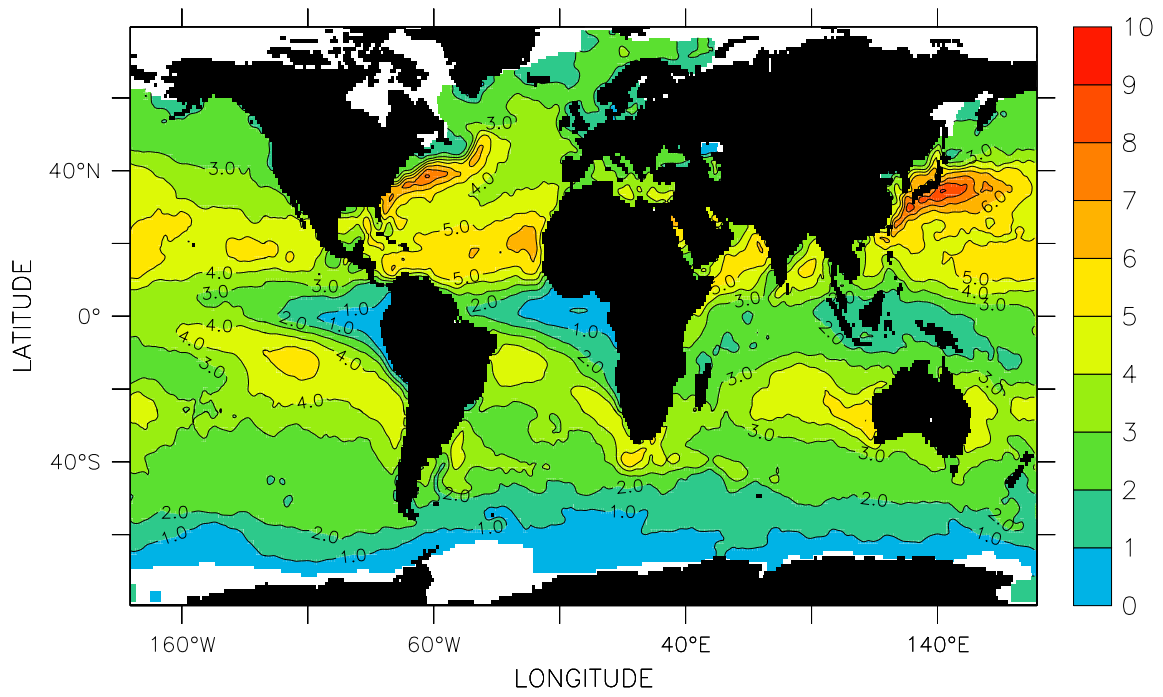
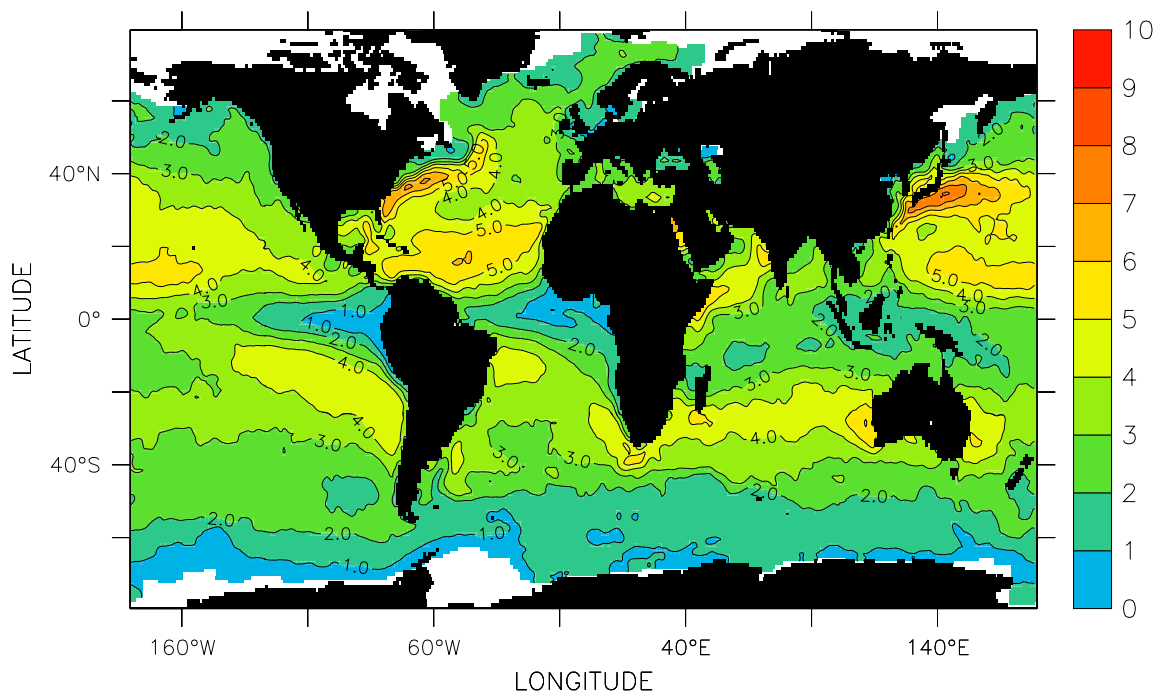Fig.V.1 Evaporation (mm/d), January

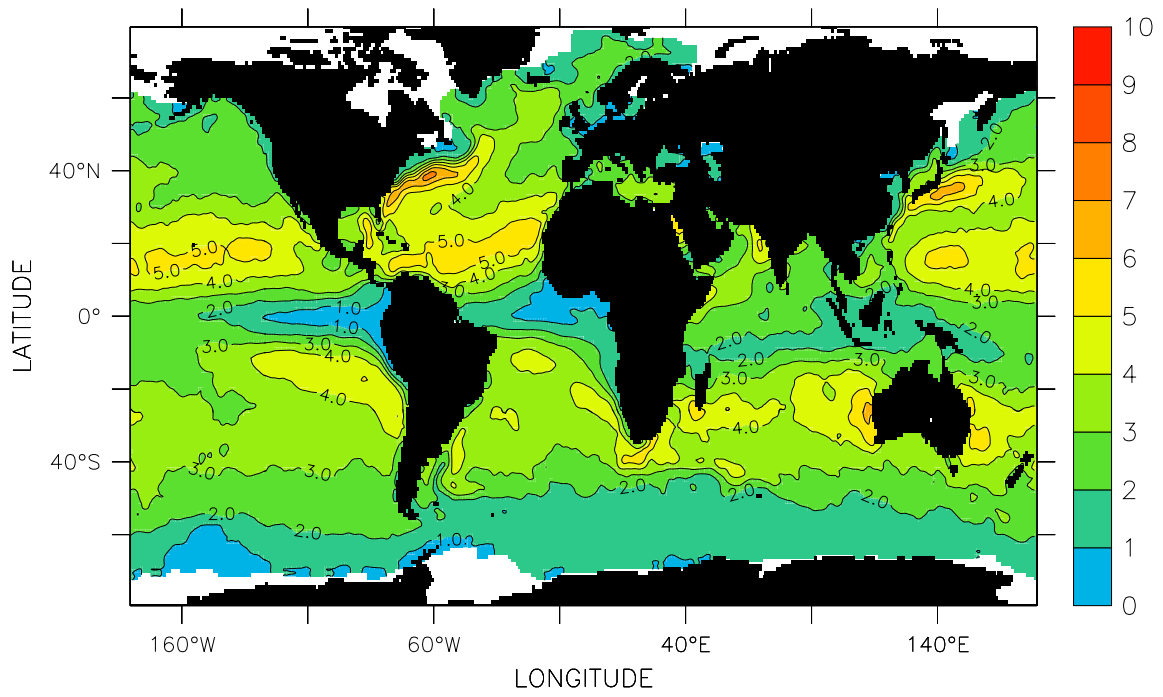Fig.V.2 Evaporation (mm/d), February
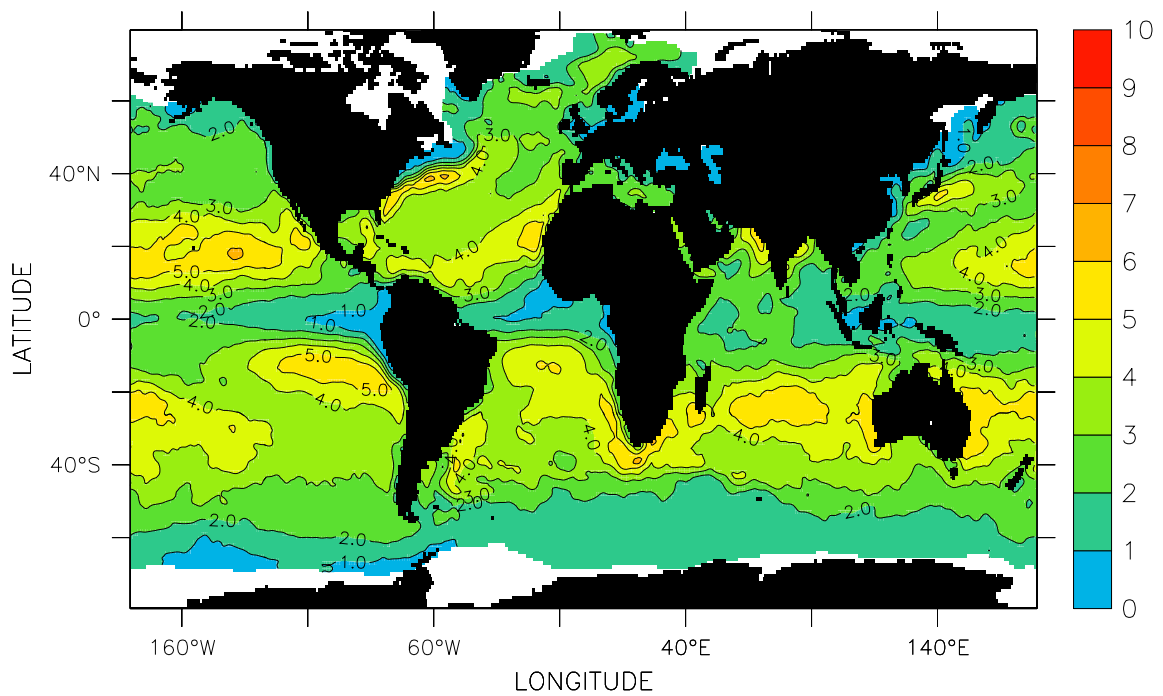
Fig.V.3 Evaporation (mm/d), March
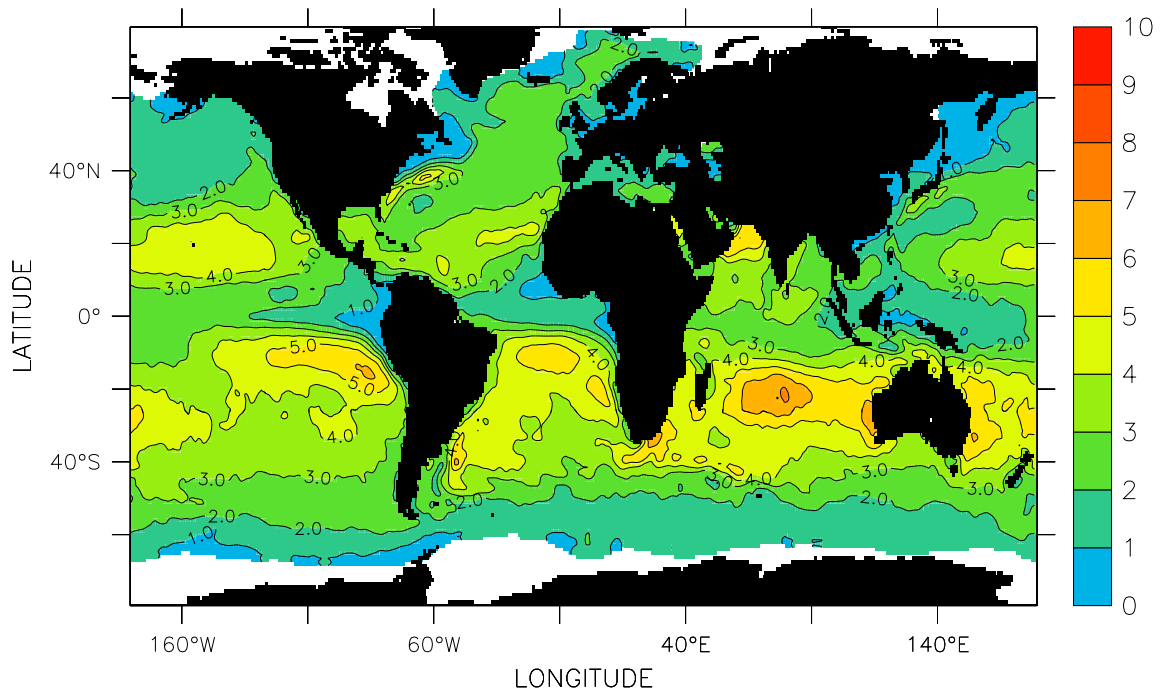

Fig.V.4 Evaporation (mm/d), April
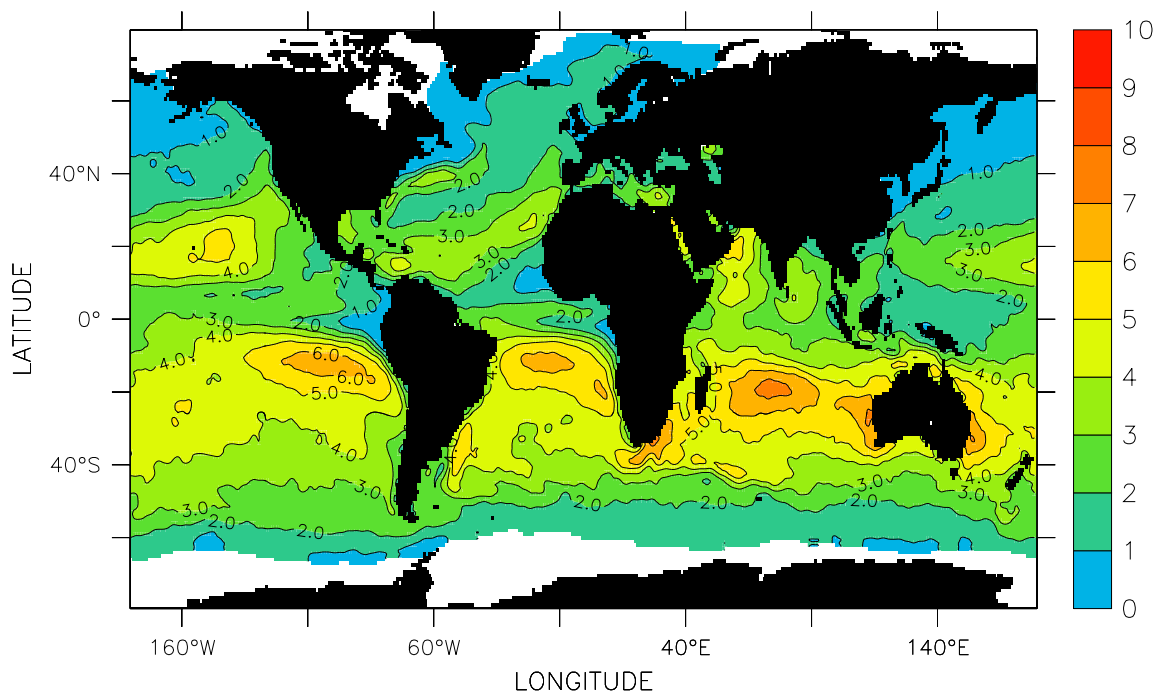
Fig.V.5 Evaporation (mm/d), May

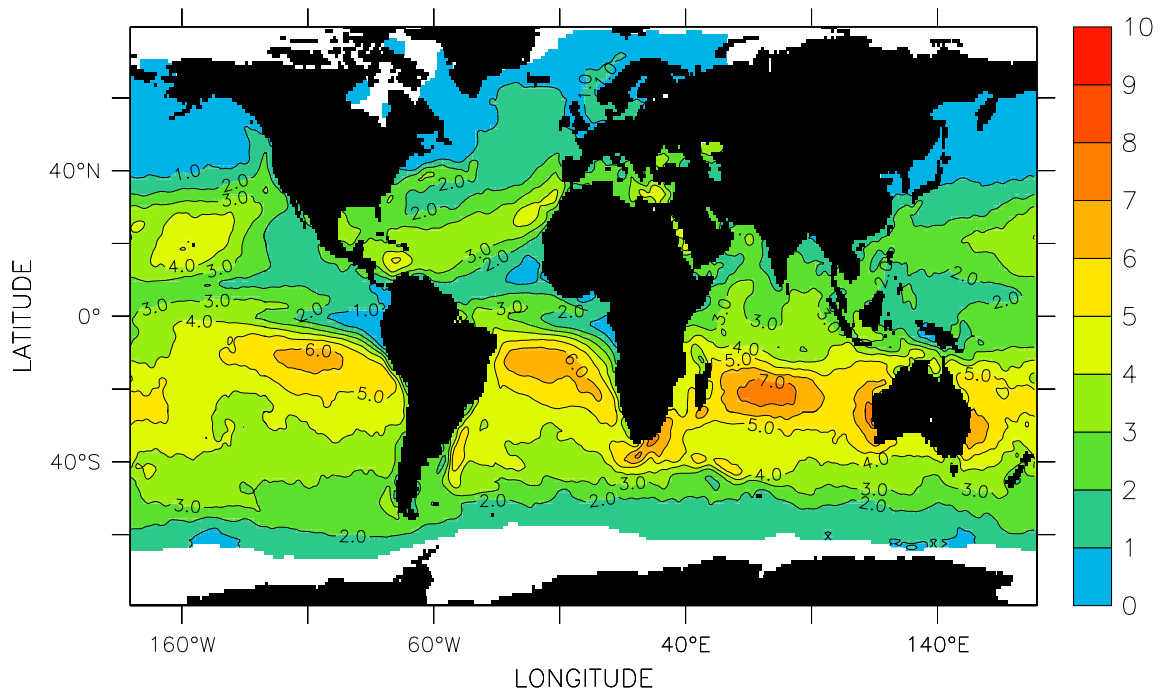Fig.V.6 Evaporation (mm/d), June

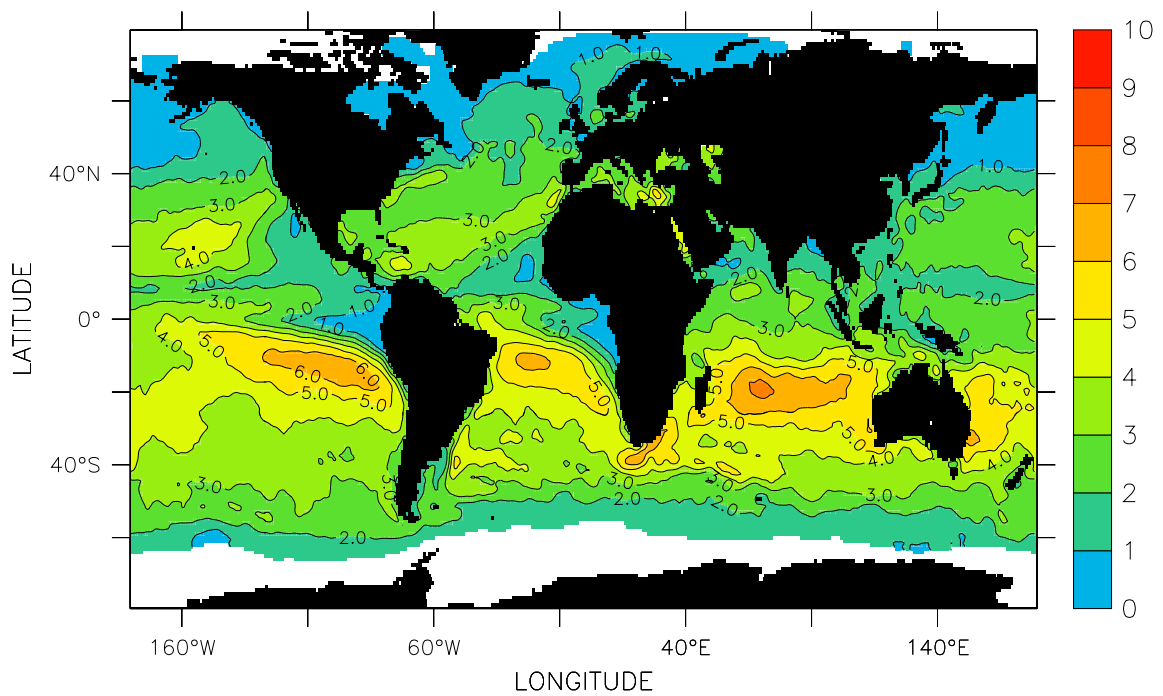Fig.V.7 Evaporation (mm/d), July
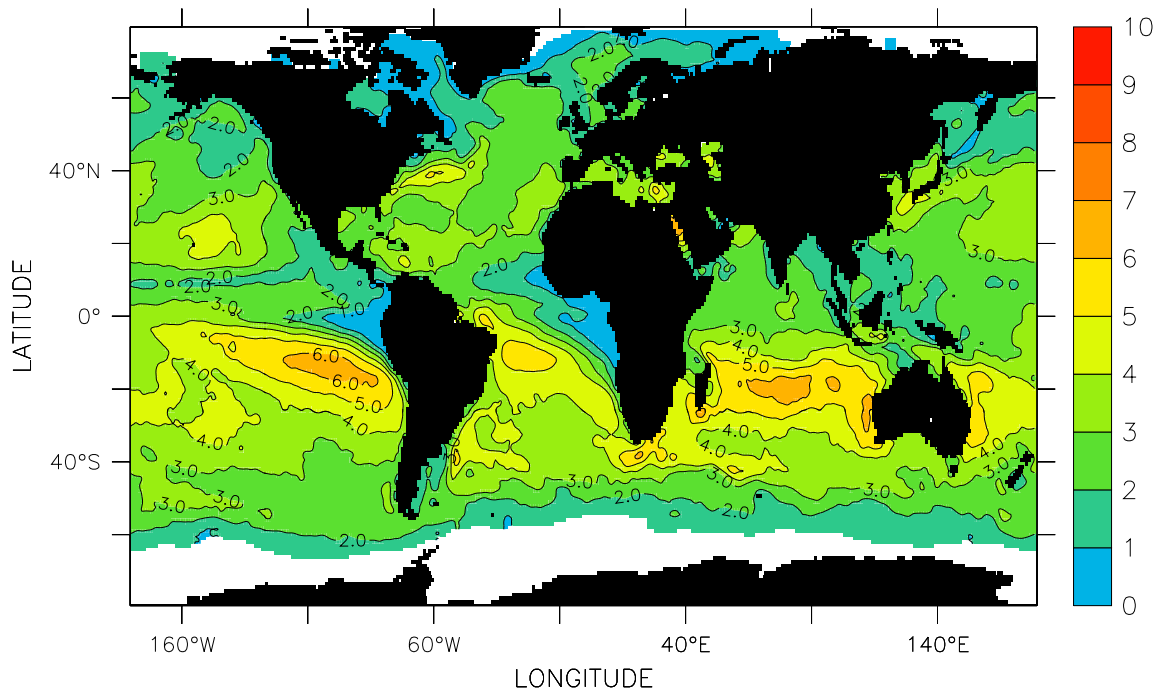

Fig.V.8 Evaporation (mm/d), August
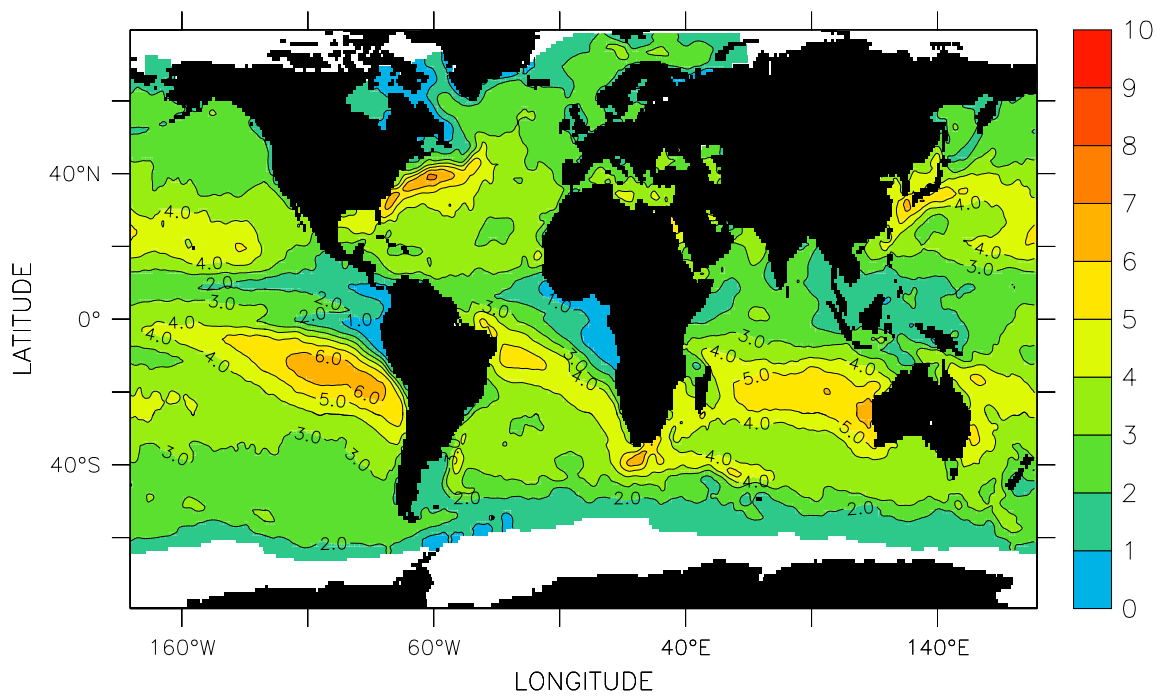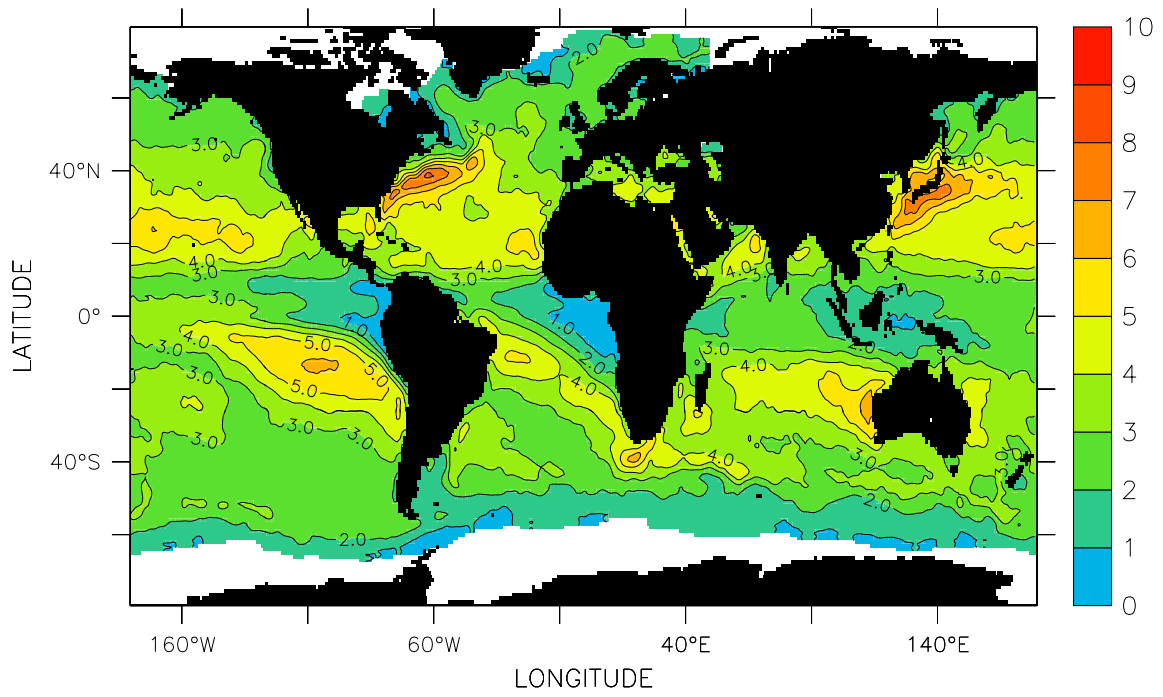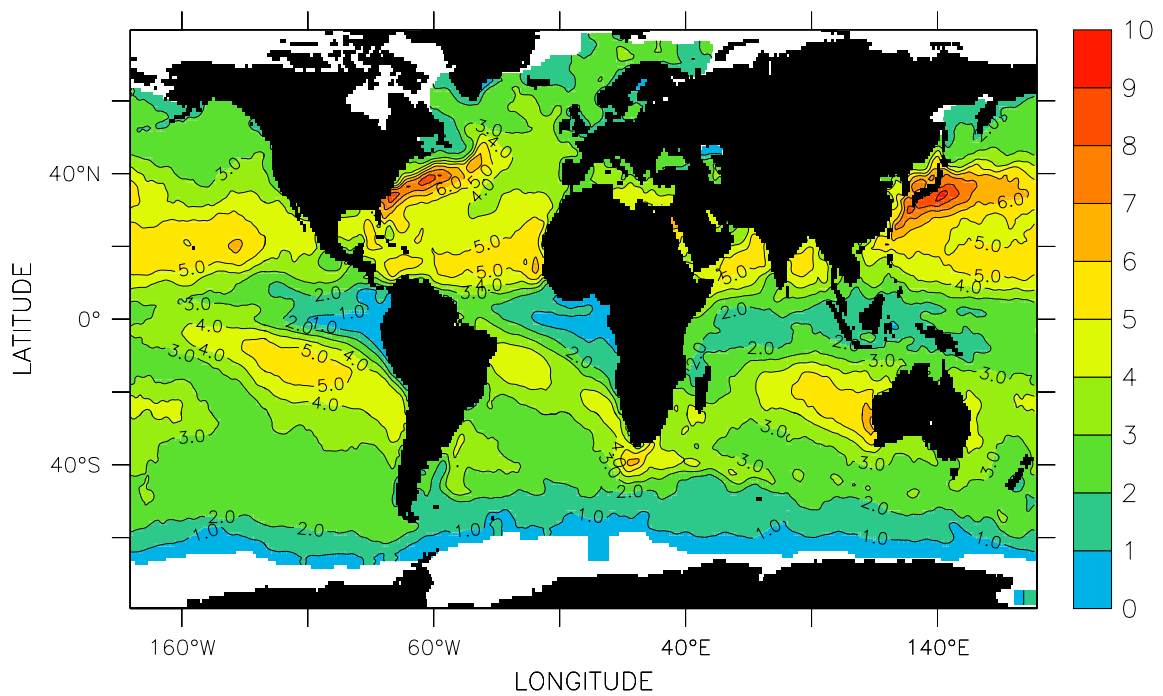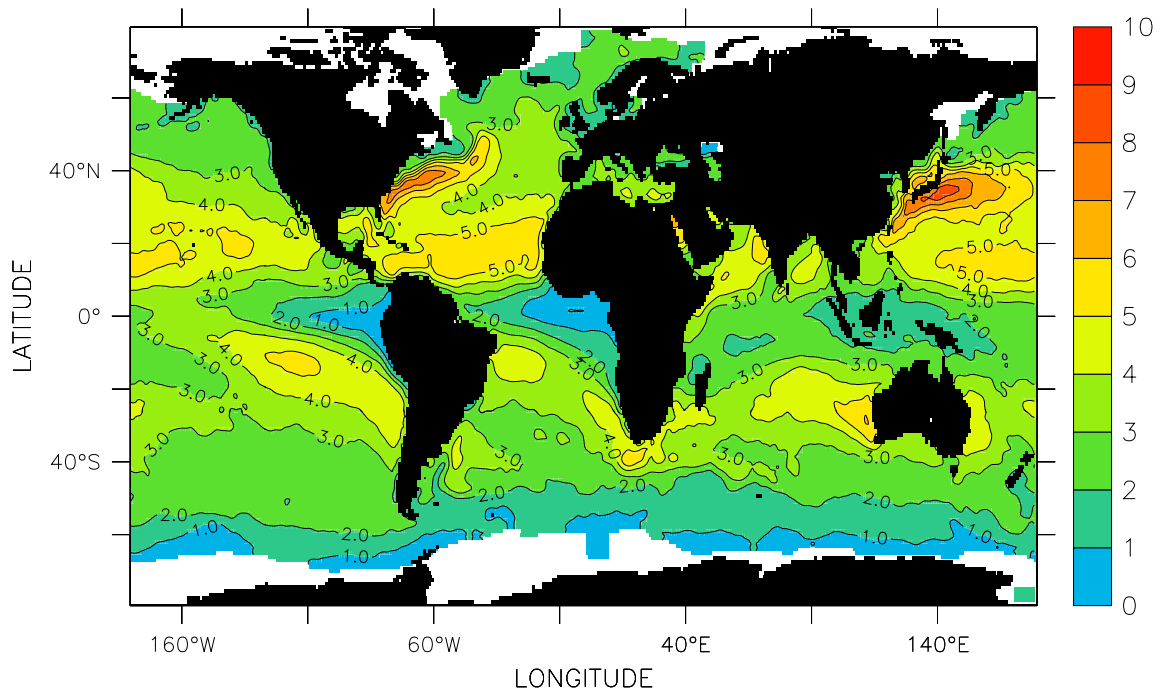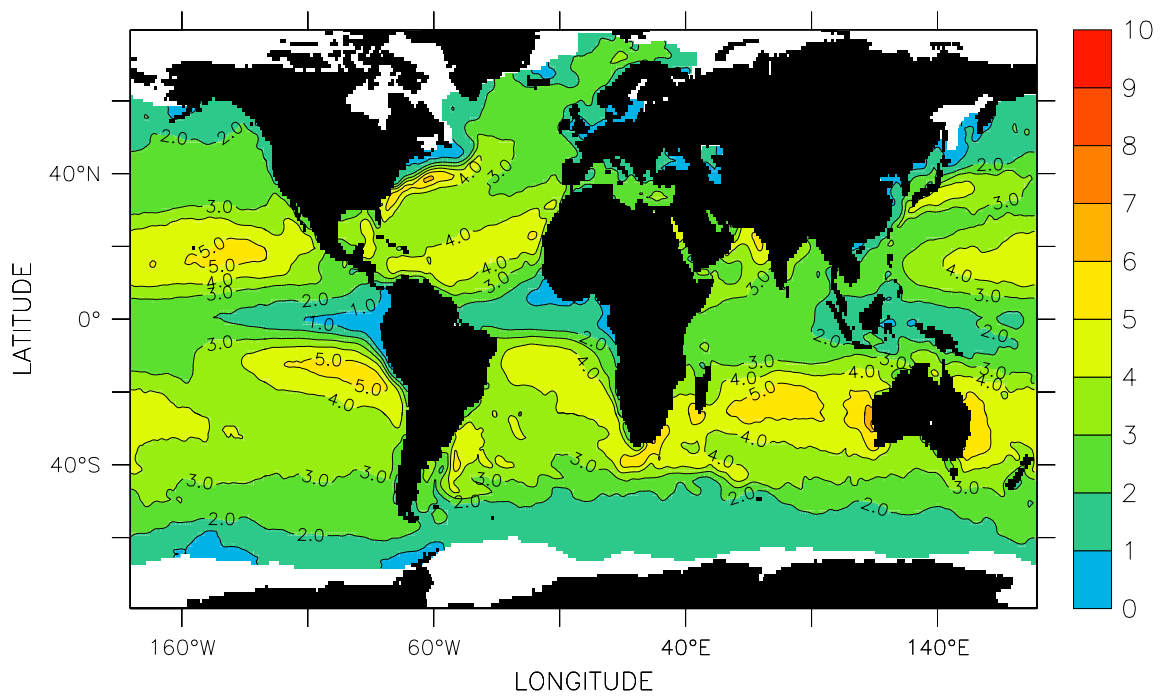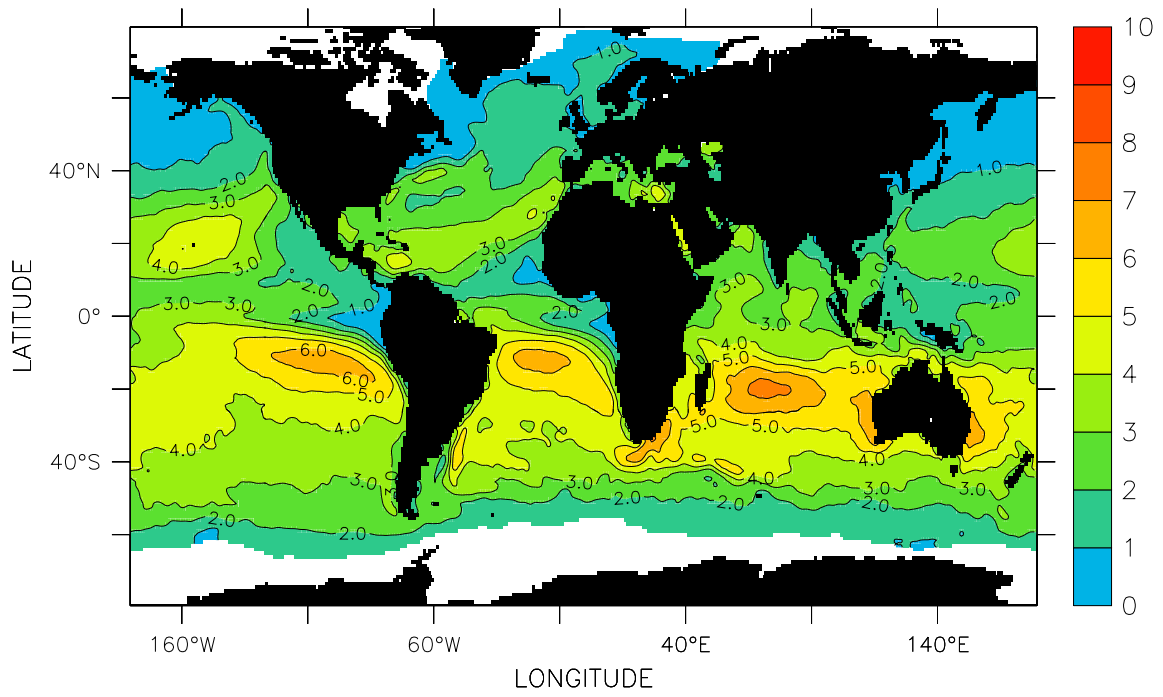
Fig.V.9 Evaporation (mm/d), September

Fig.V.10 Evaporation (mm/d), October

Fig.V.11 Evaporation (mm/d), November

Fig.V.12 Evaporation (mm/d), December

Fig.V.13 Evaporation (mm/d), DJF

Fig.V.14 Evaporation (mm/d), MAM

Fig.V.15 Evaporation (mm/d), JJA
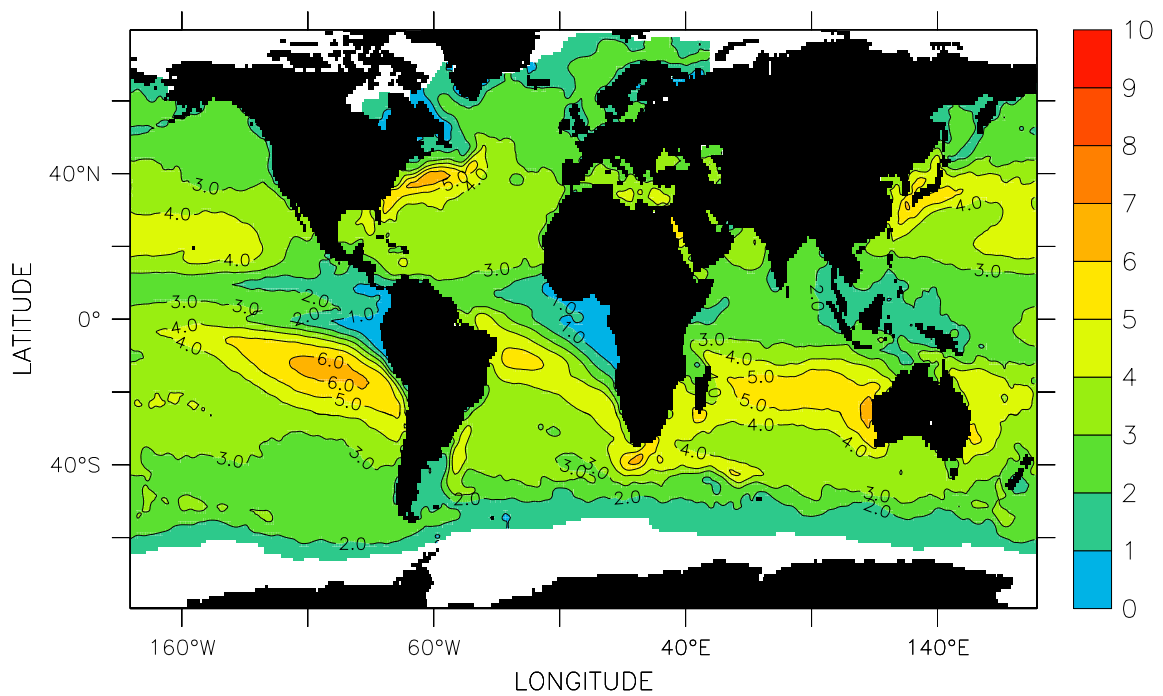
Fig.V.16 Evaporation (mm/d), SON
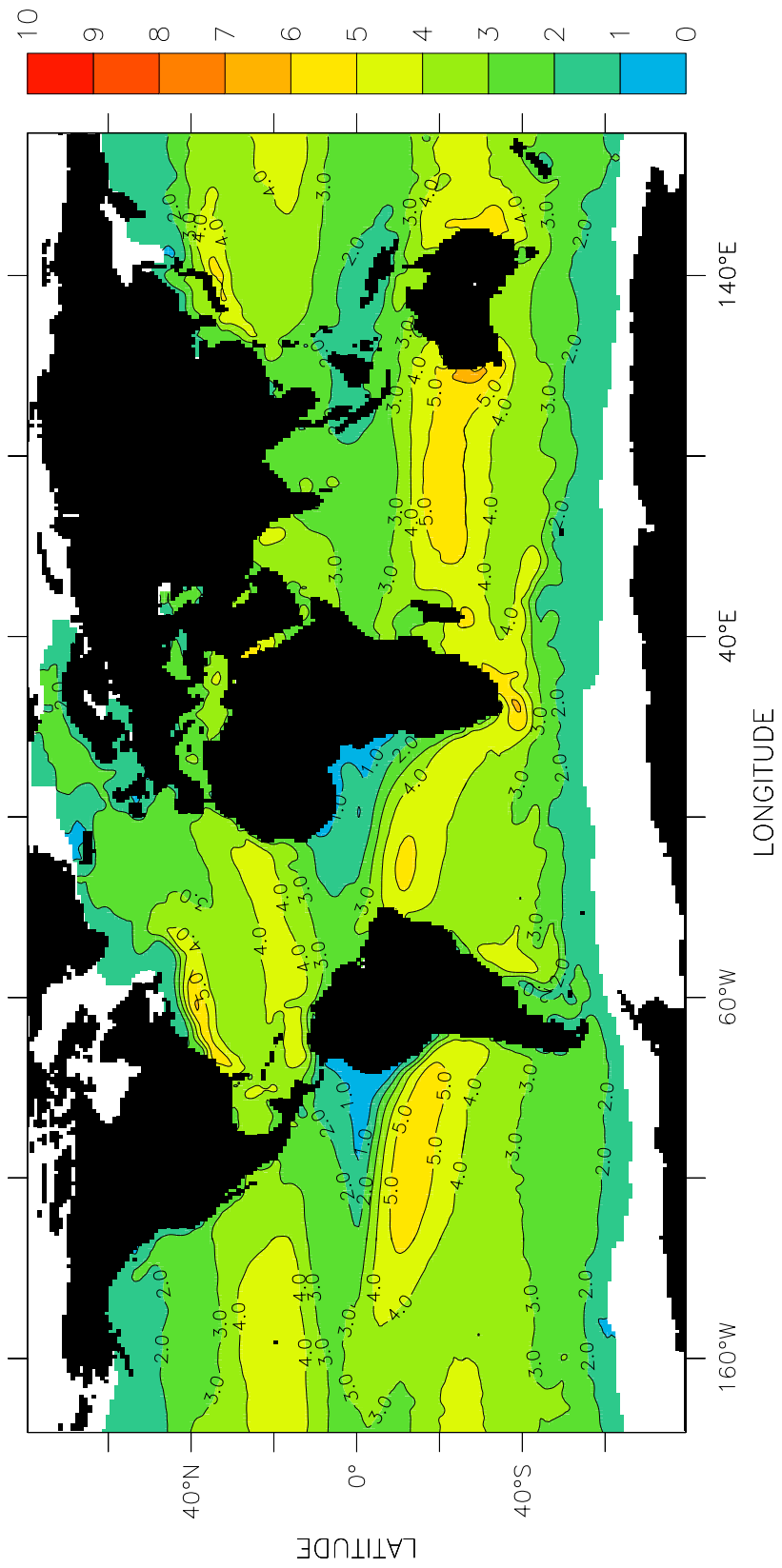
Fig.V.17 Evaporation (mm/d), Annual
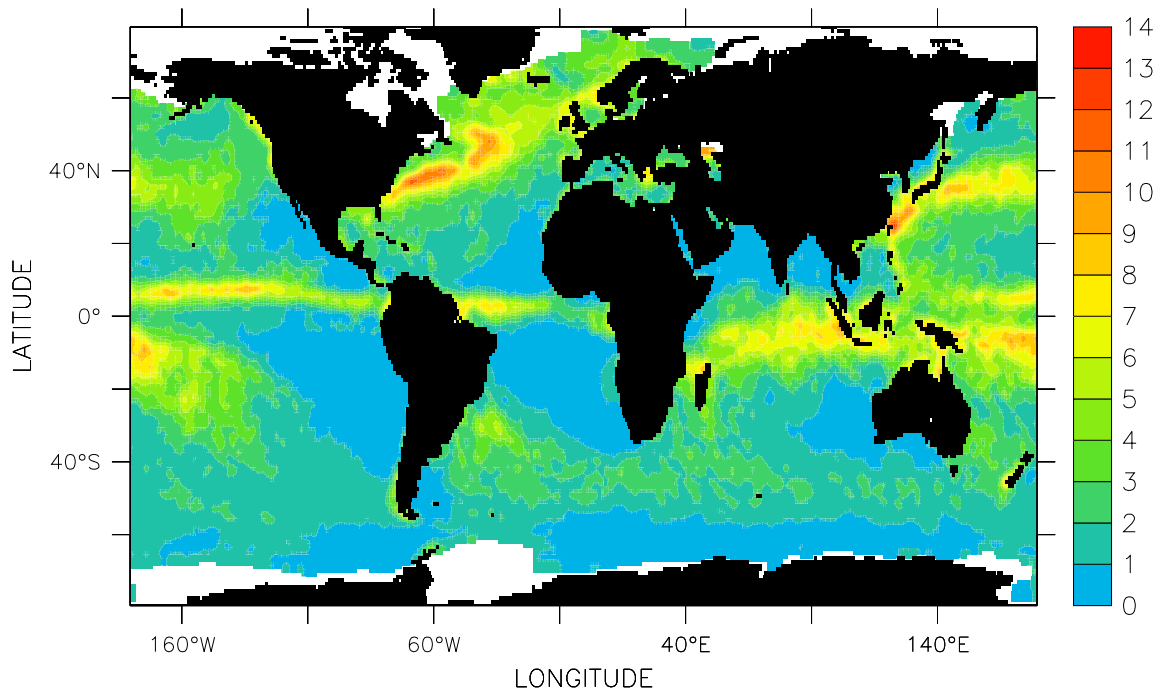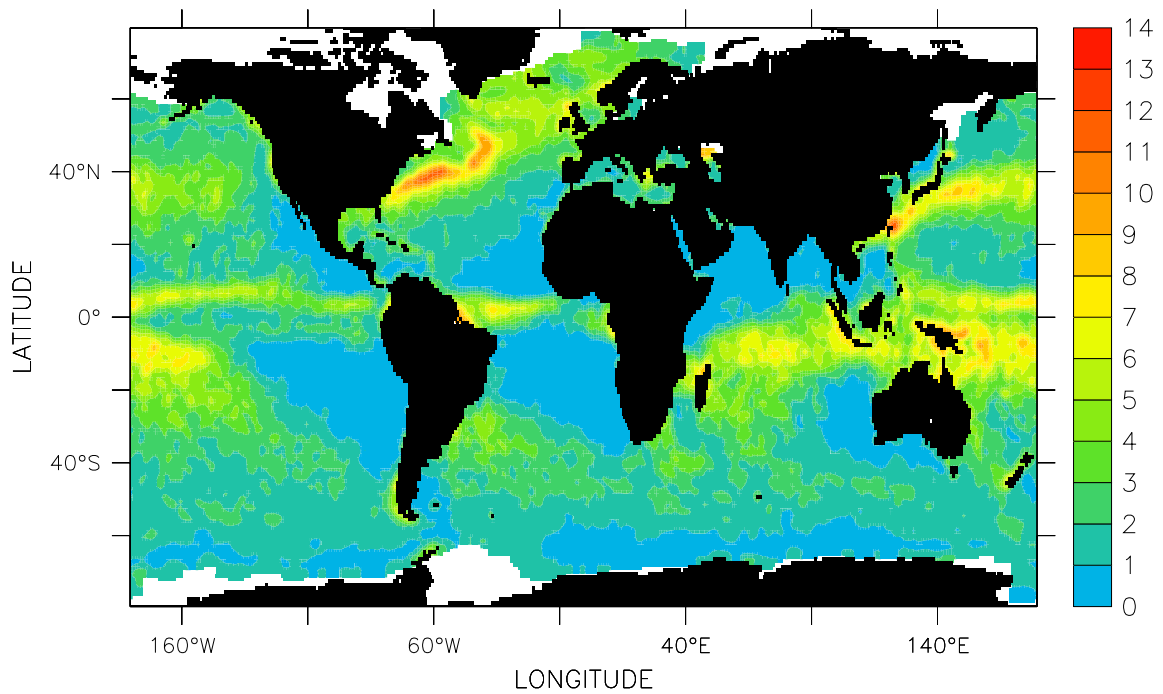
Fig.V.18 Rain Rate (mm/d), January
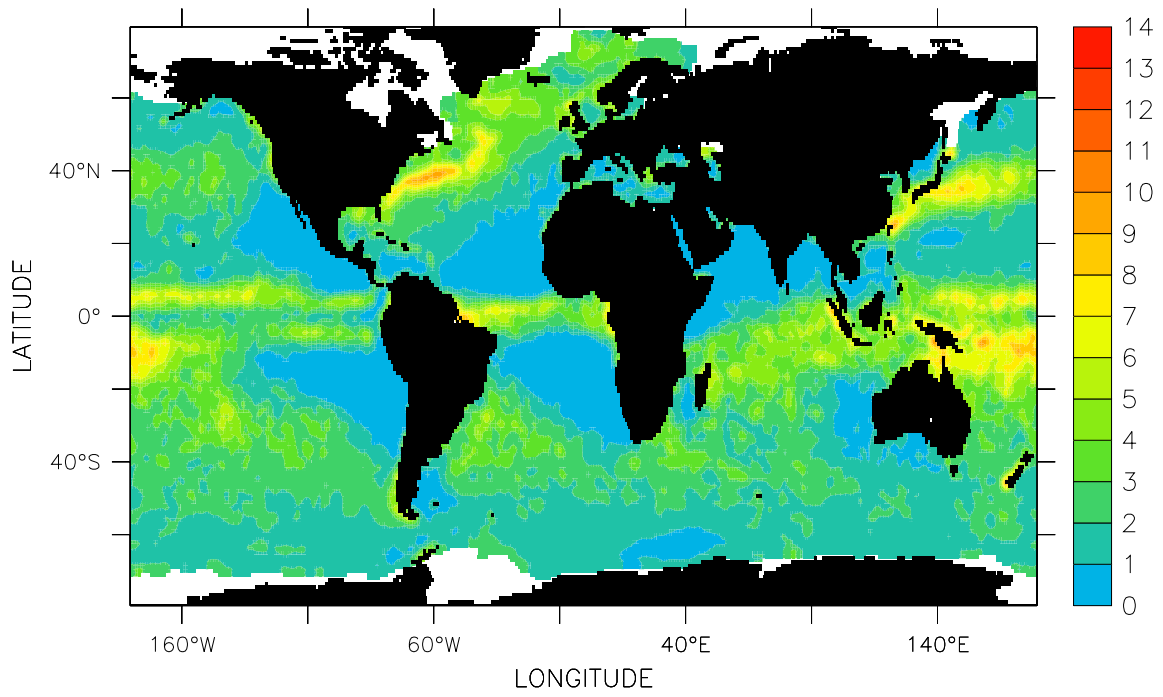

Fig.V.19 Rain Rate (mm/d), February

Fig.V.20 Rain Rate (mm/d), March

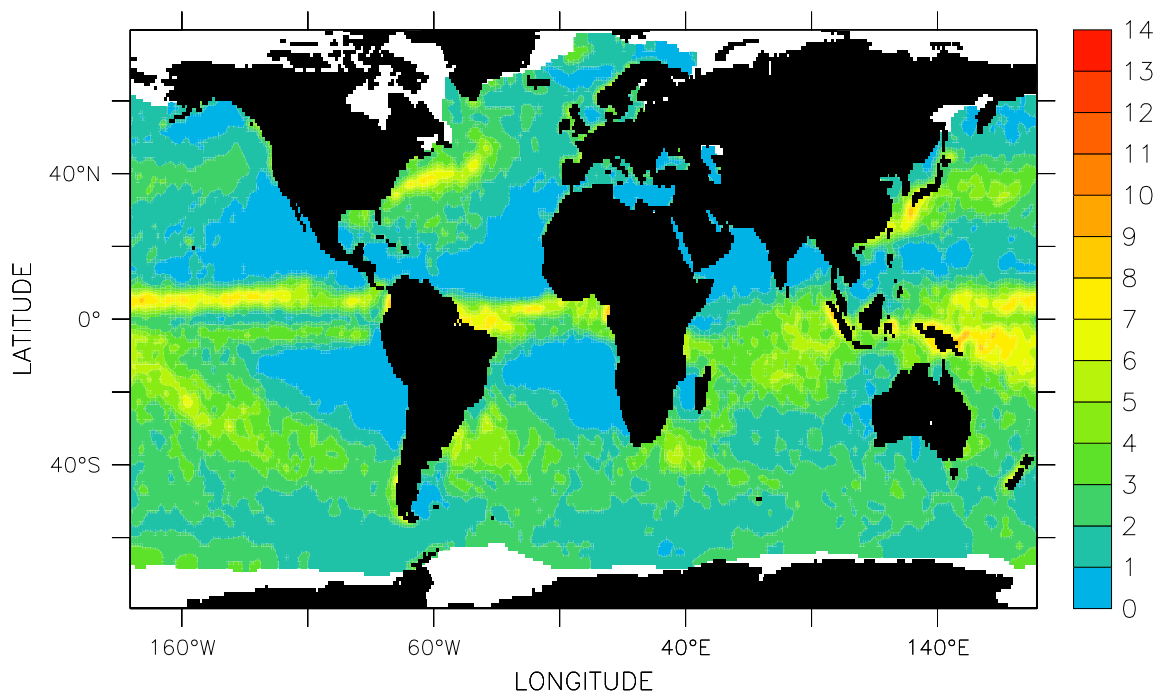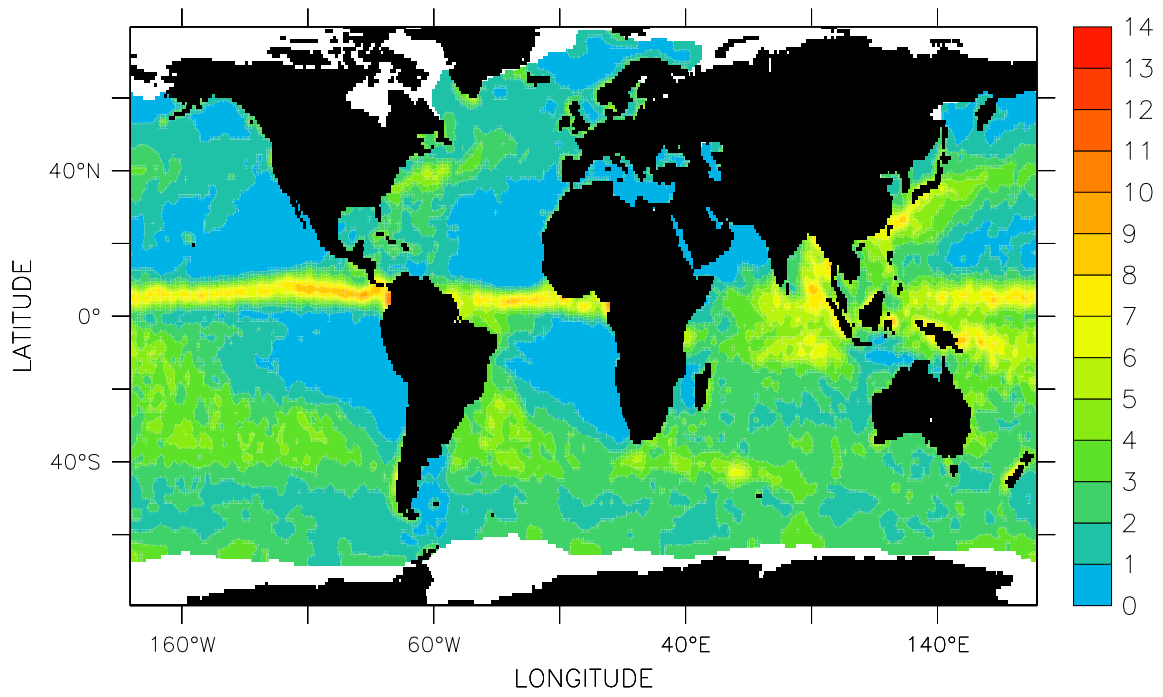Fig.V.21 Rain Rate (mm/d), April
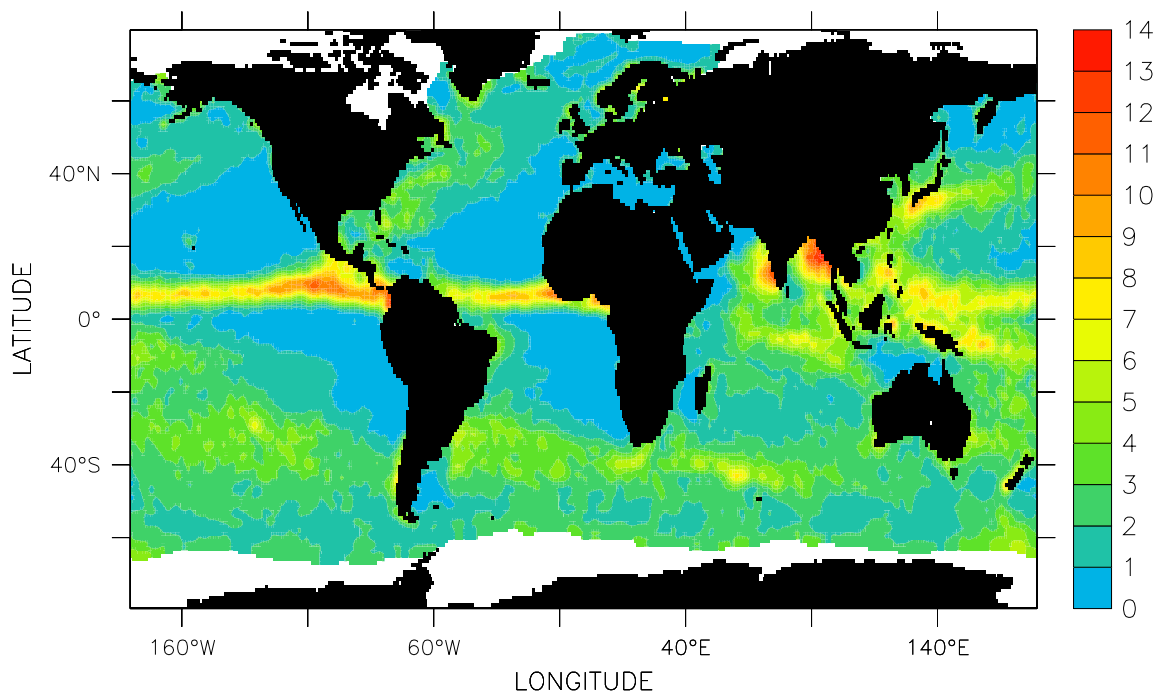
Fig.V.22 Rain Rate (mm/d), May
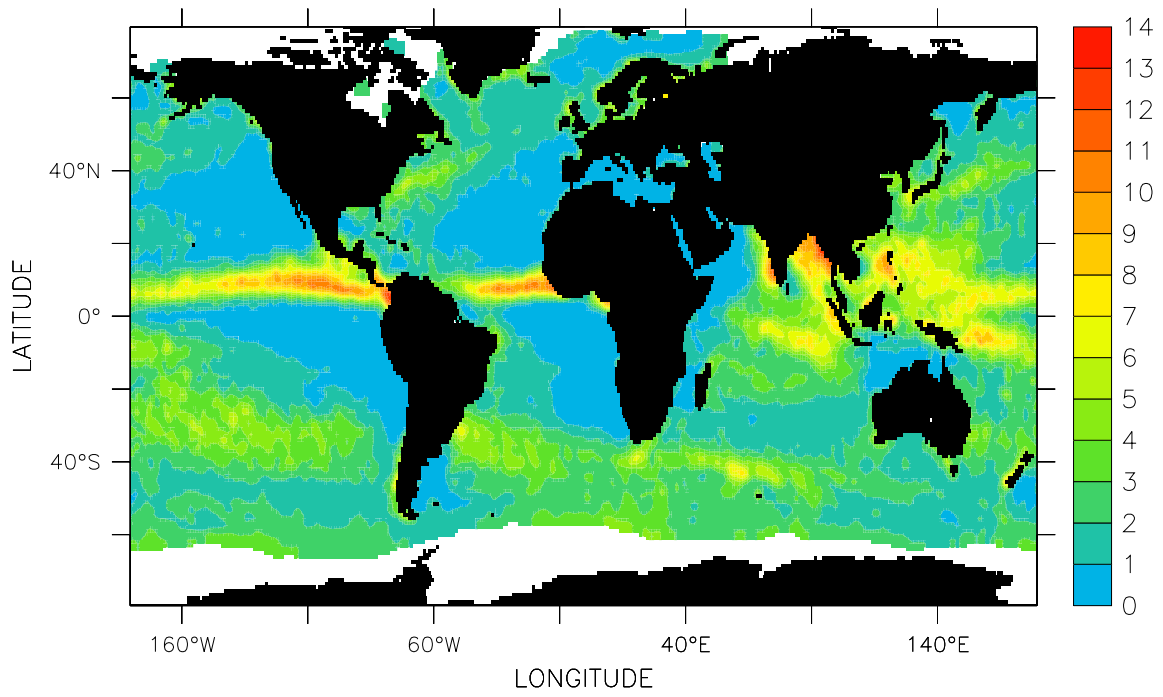

Fig.V.23 Rain Rate (mm/d), June

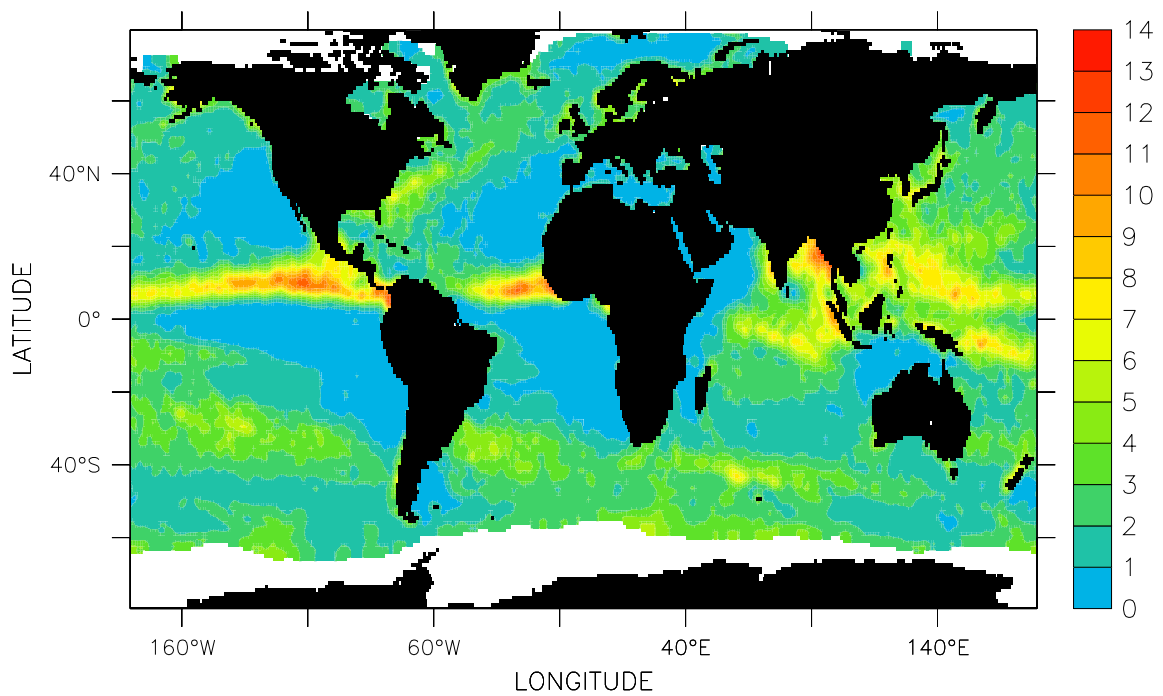Fig.V.24 Rain Rate (mm/d), July
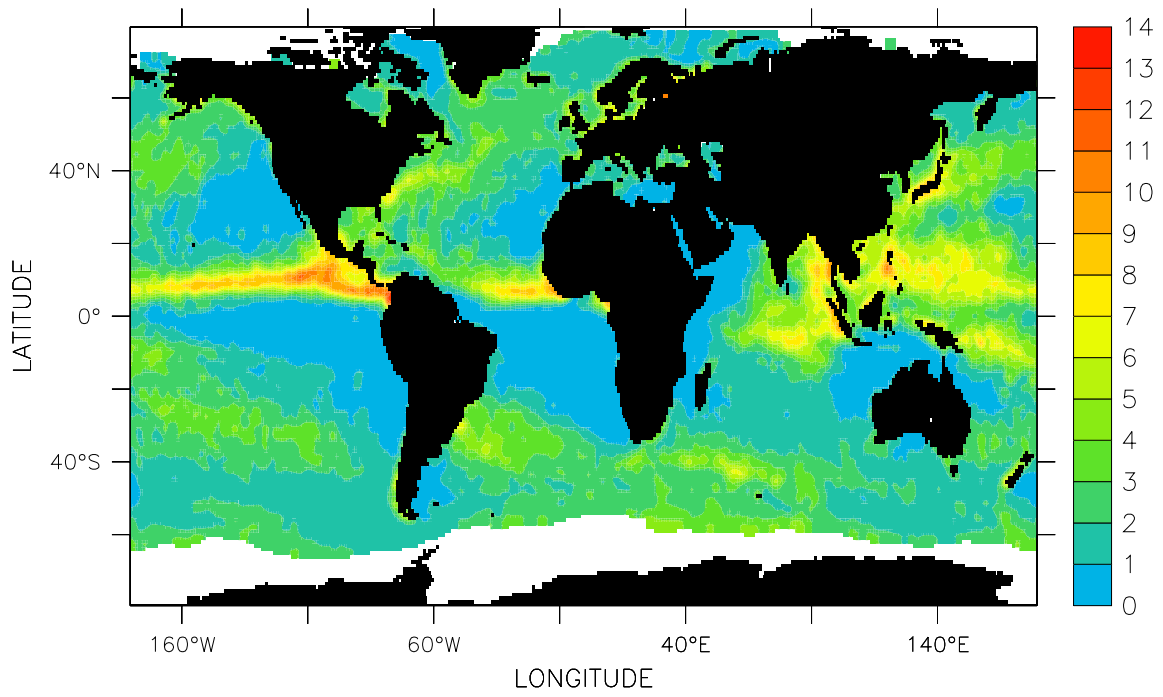

Fig.V.25 Rain Rate (mm/d), August

Fig.V.26 Rain Rate (mm/d), September
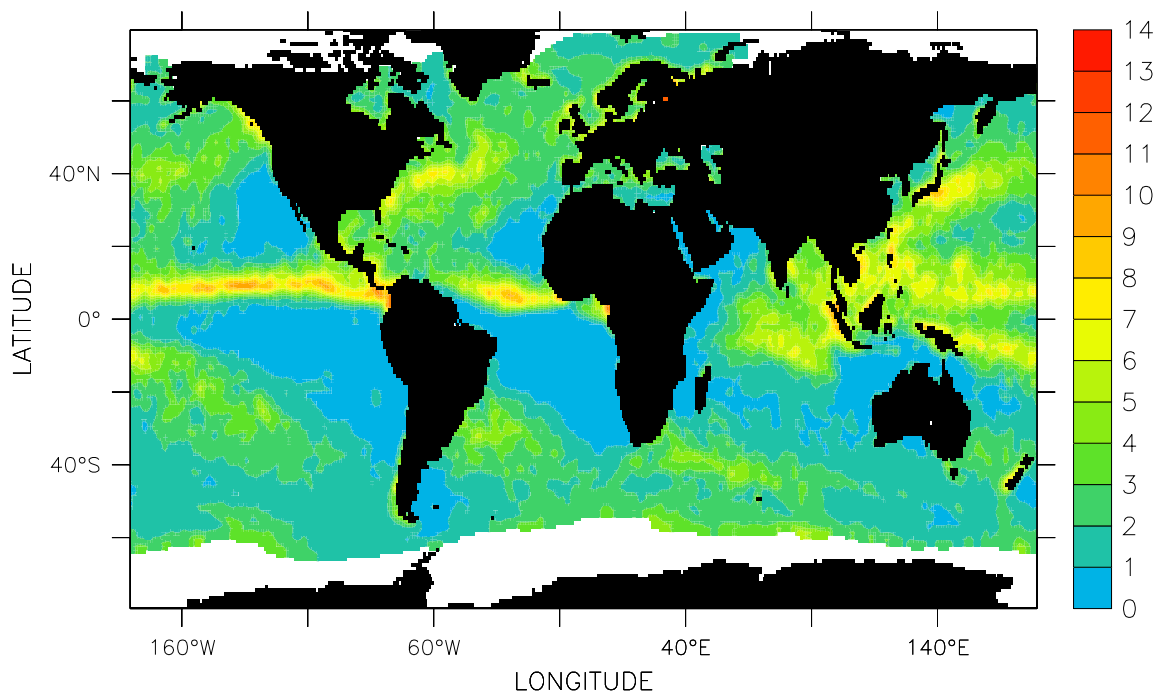
Fig.V.27 Rain Rate (mm/d), October
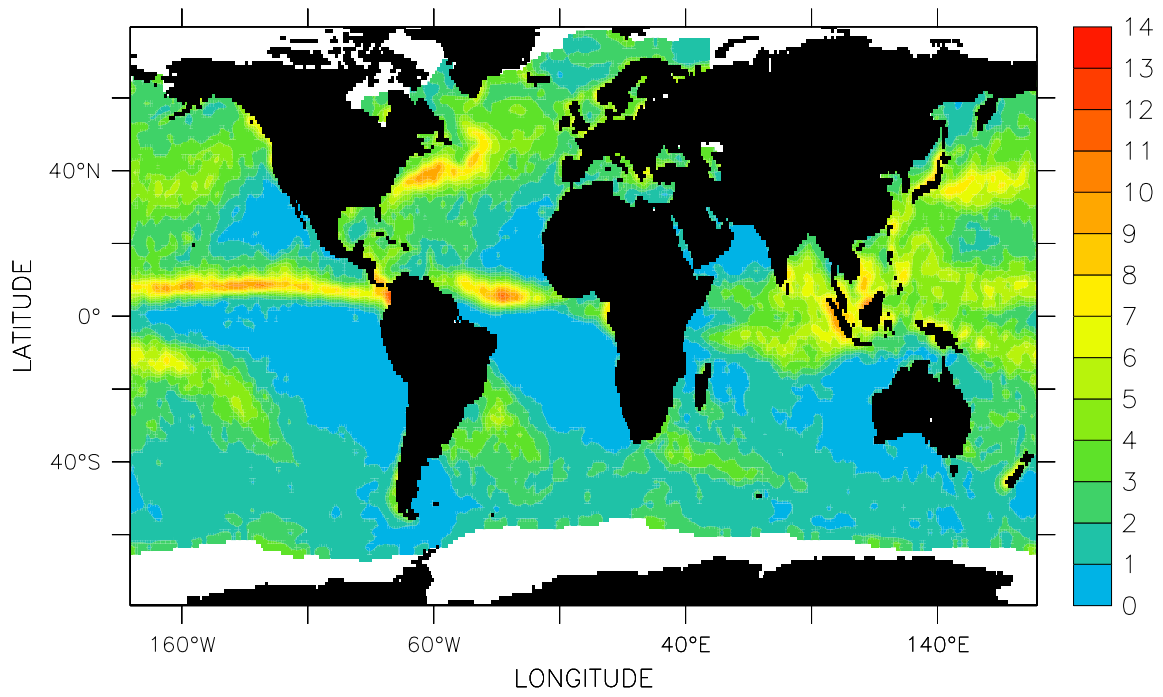
Fig.V.28 Rain Rate (mm/d), November
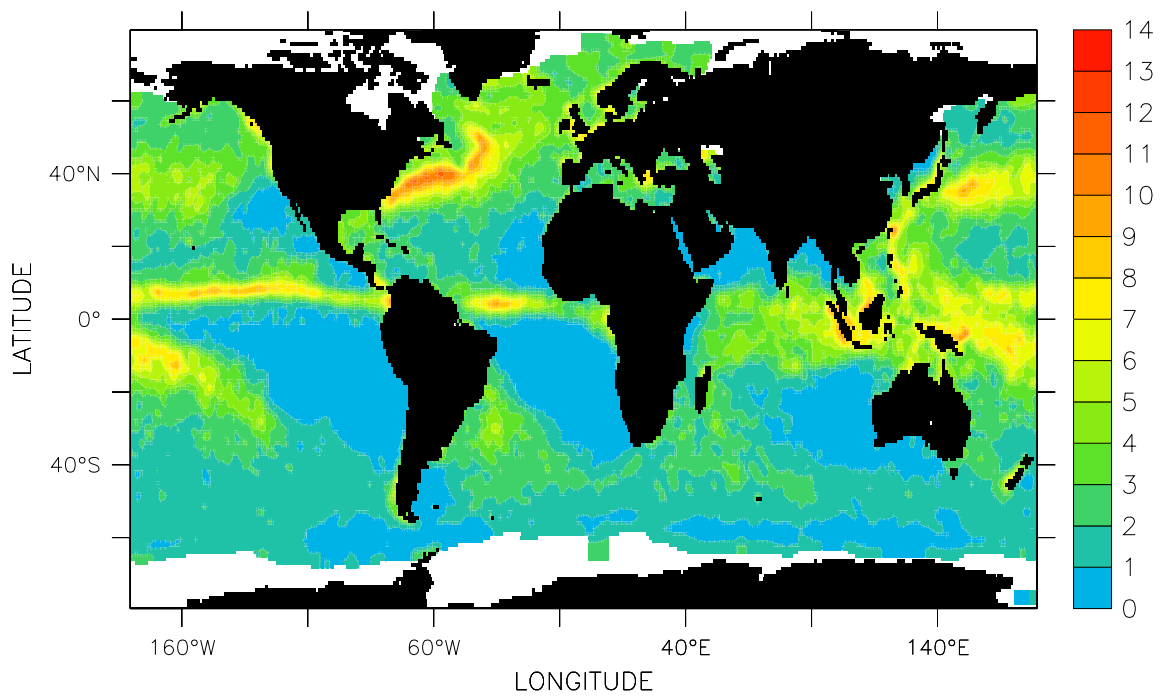
Fig.V.29 Rain Rate (mm/d), December
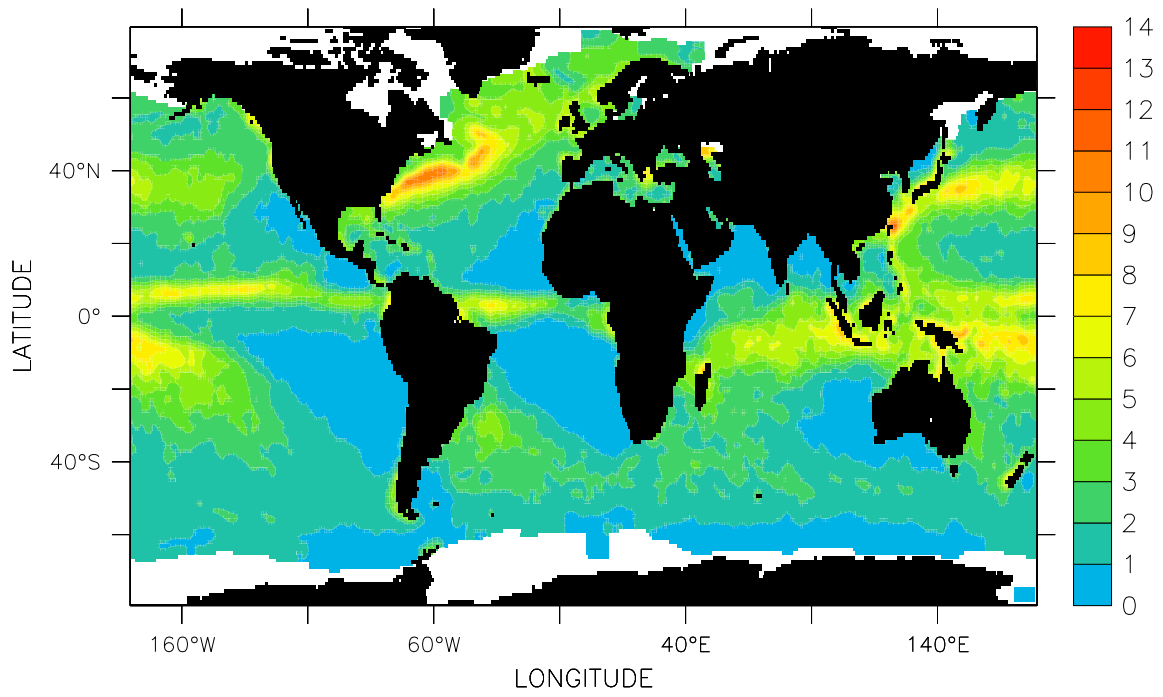
Fig.V.30 Rain Rate (mm/d), DJF
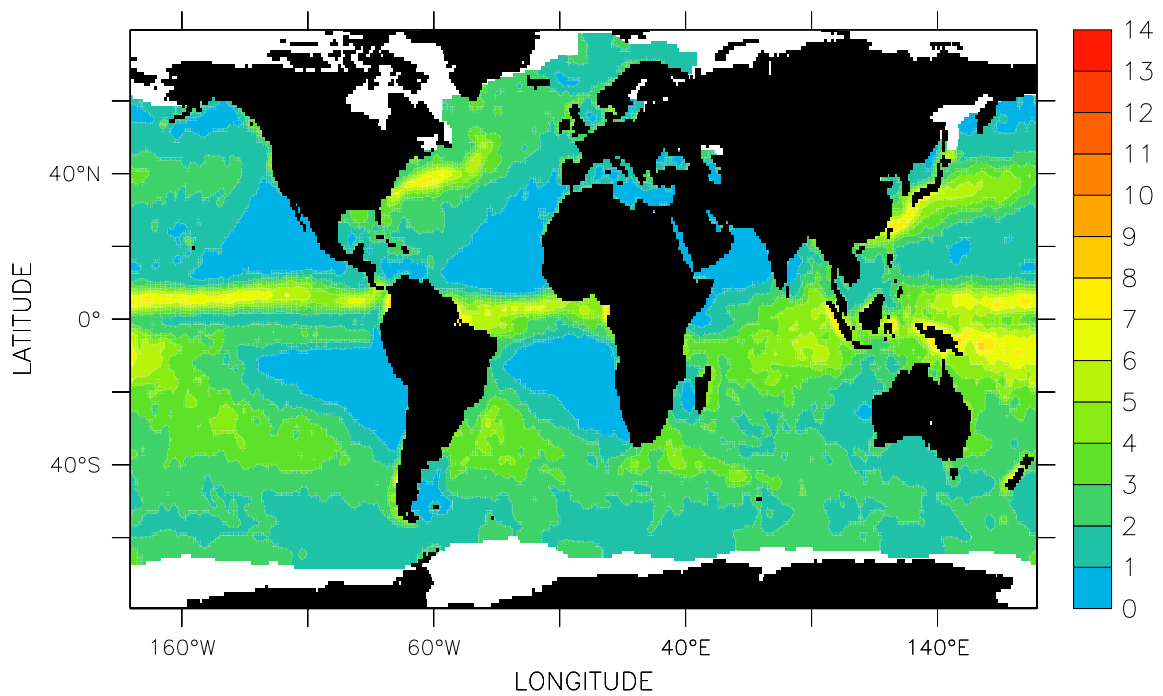
Fig.V.31 Rain Rate (mm/d), MAM
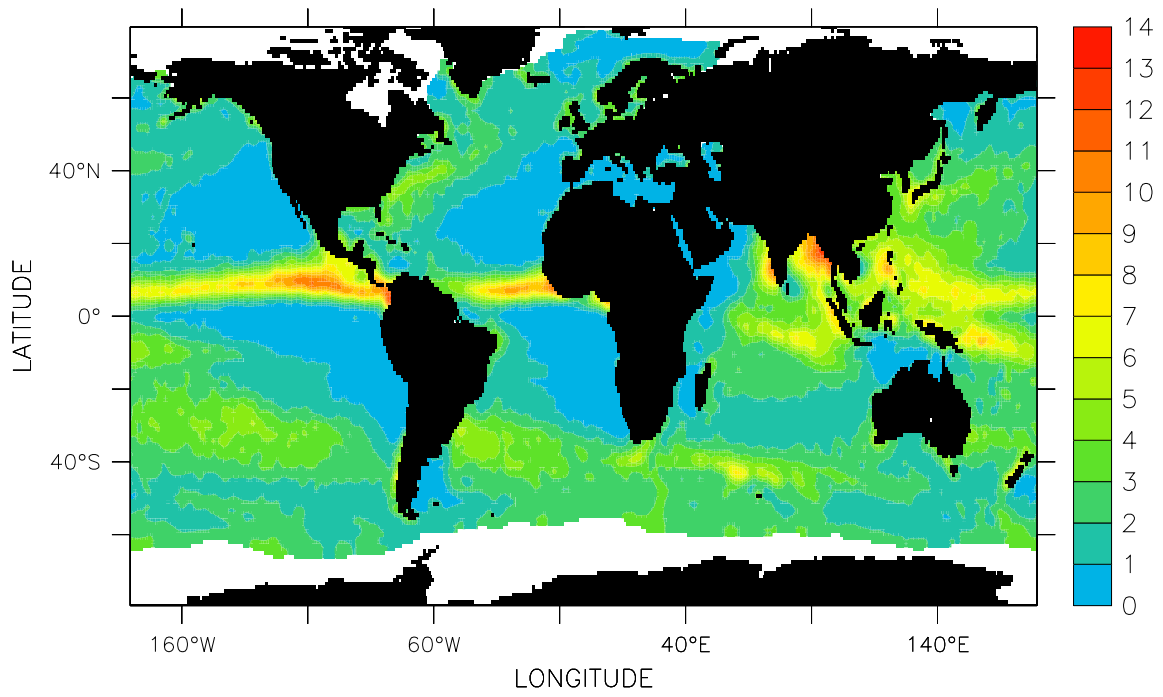
Fig.V.32 Rain Rate (mm/d), JJA
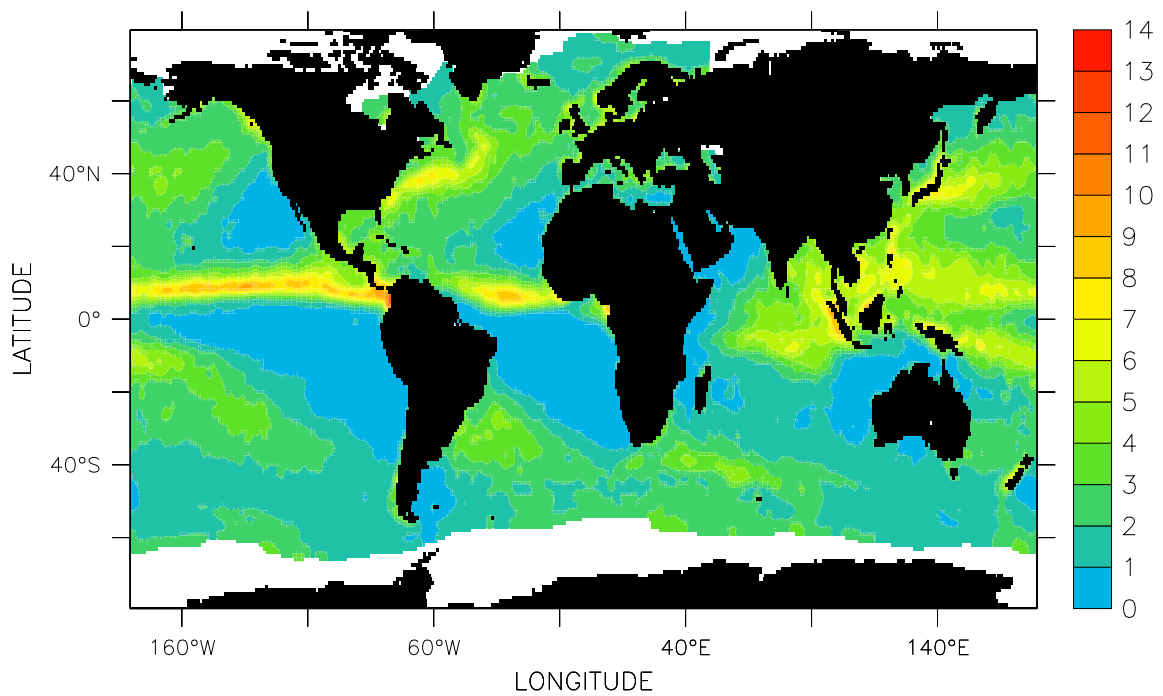
Fig.V.33 Rain Rate (mm/d), SON
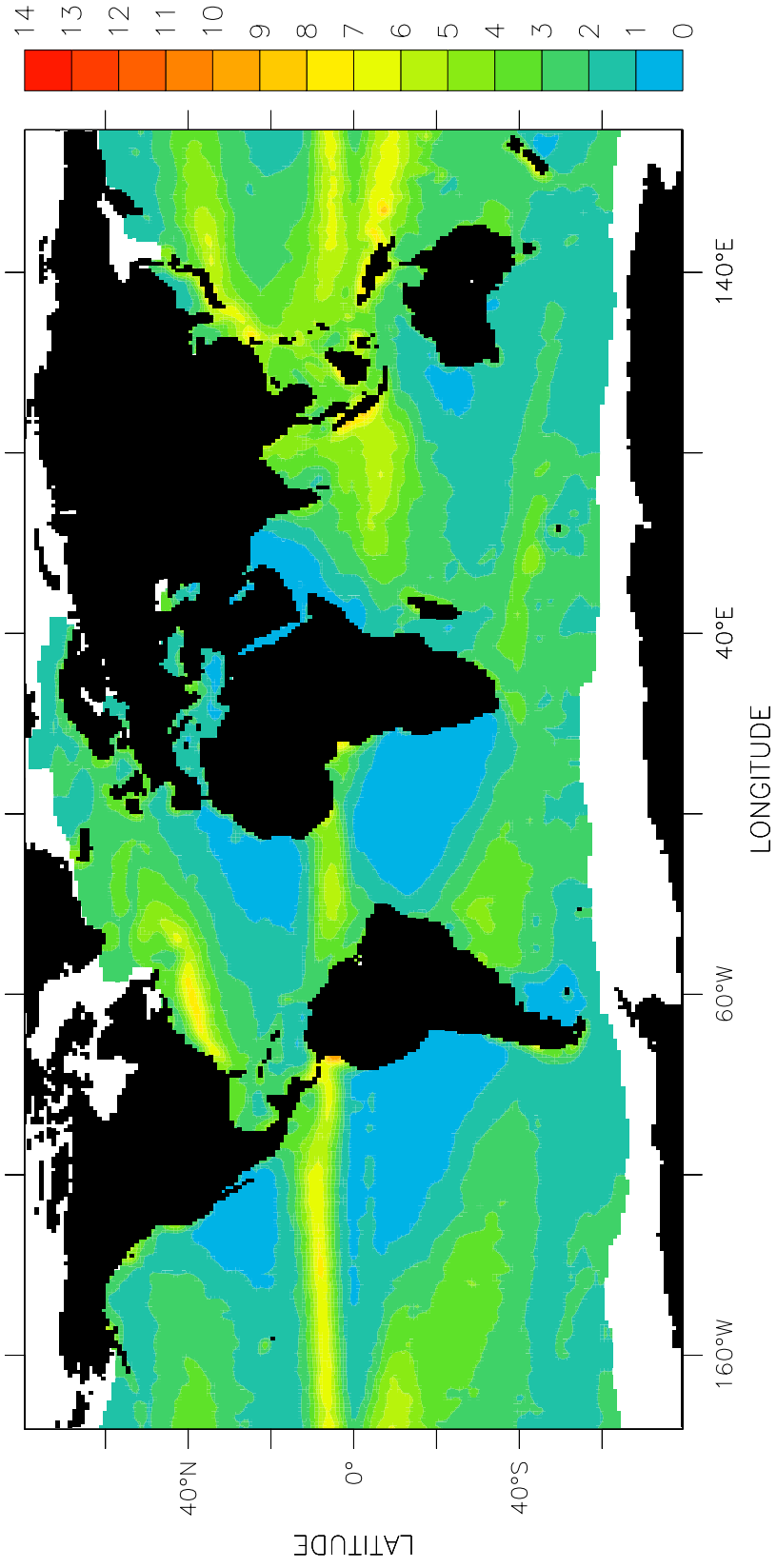
Fig.V.34 Rain Rate (mm/d), Annual
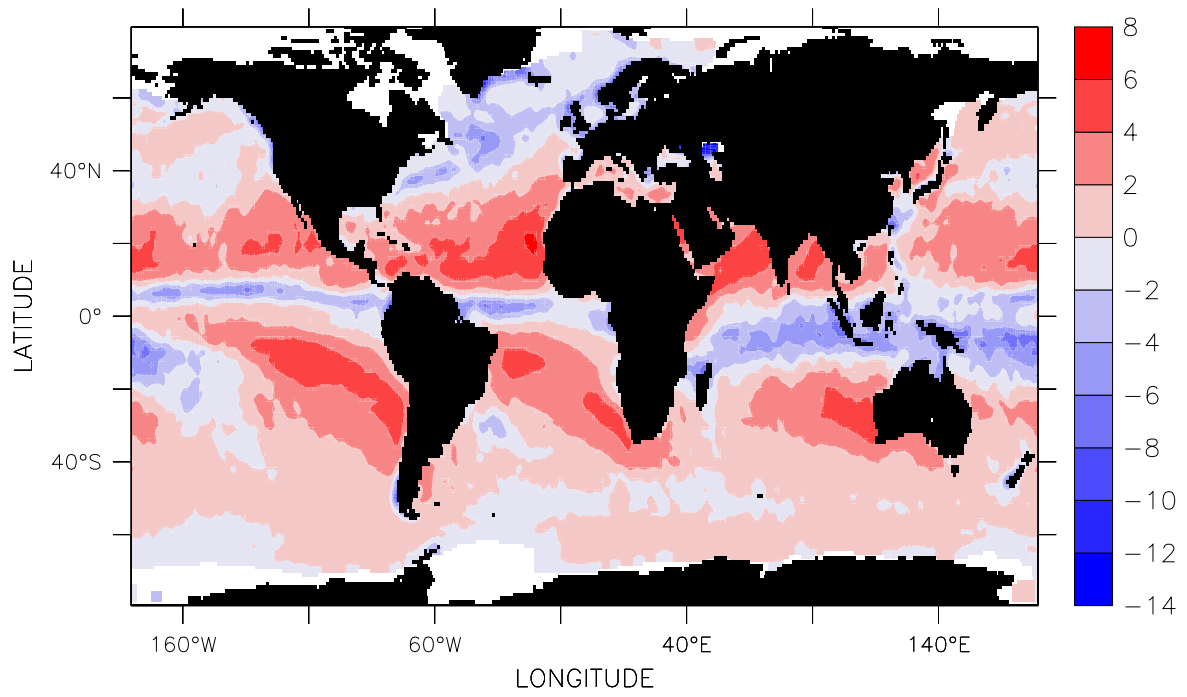
Fig.V.35 Freshwater Flux (mm/d), January
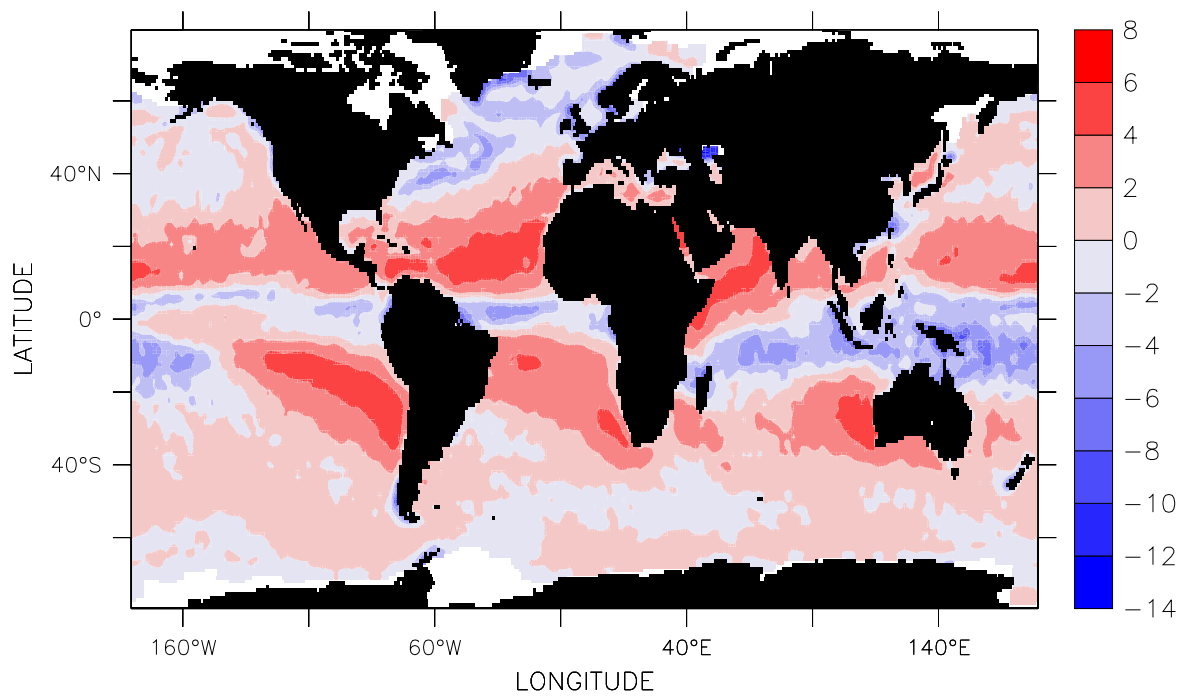
Fig.V.36 Freshwater Flux (mm/d), February
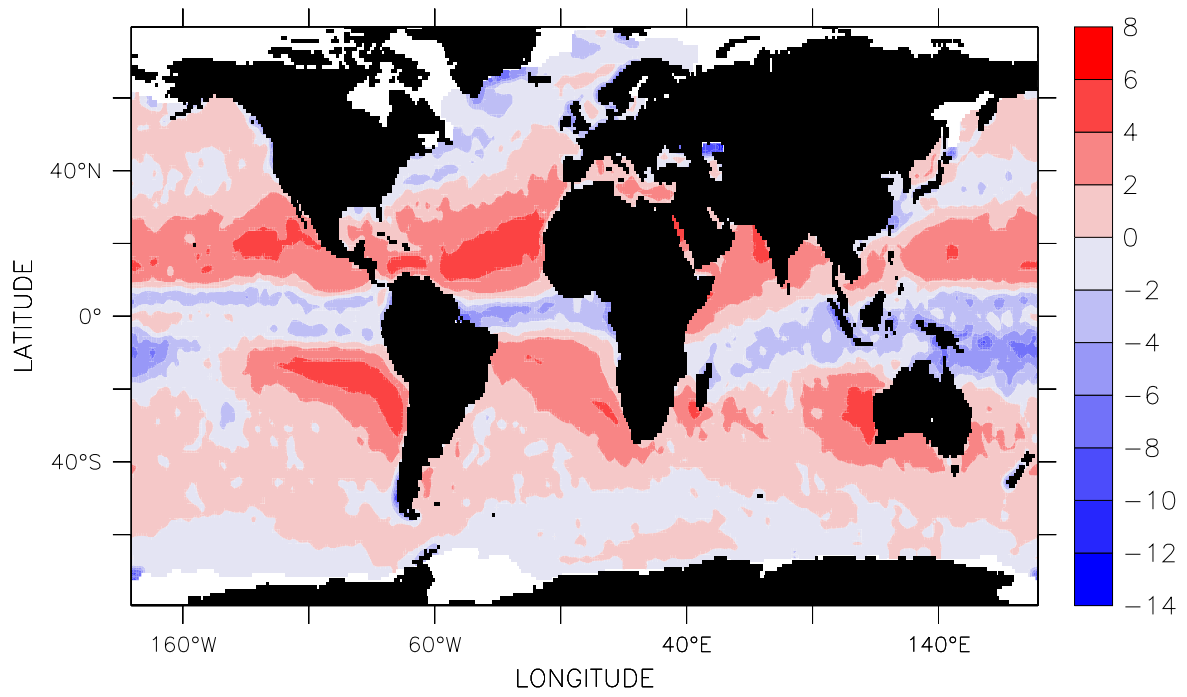
Fig.V.37 Freshwater Flux (mm/d), March
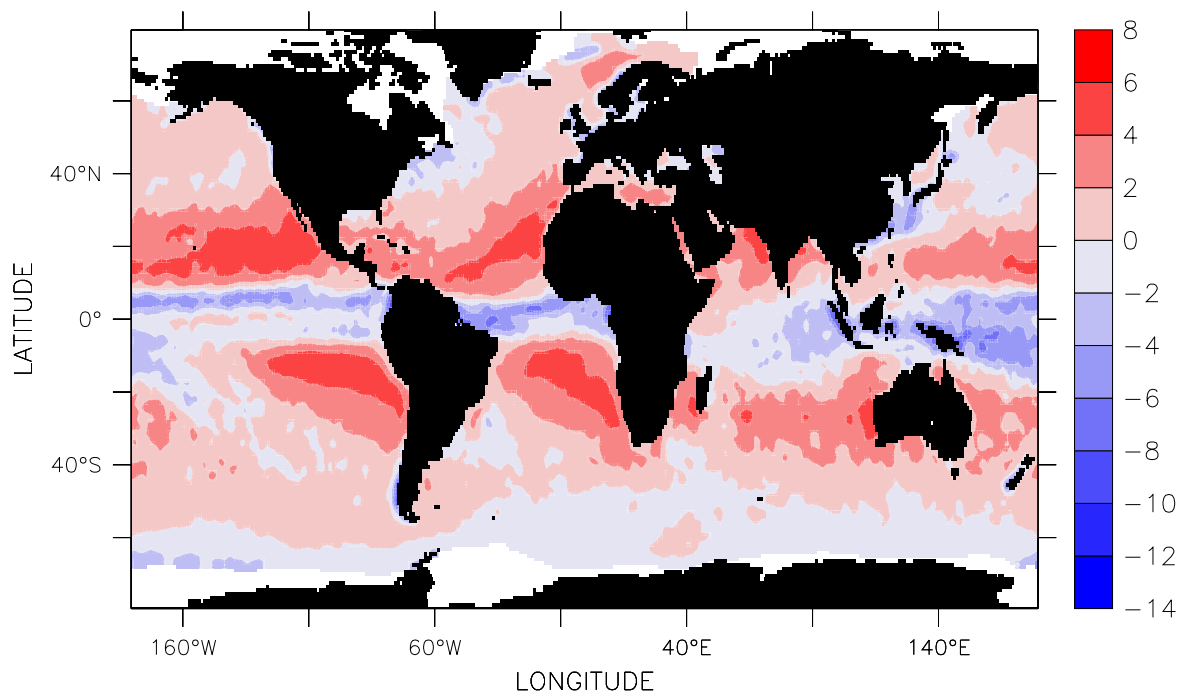
Fig.V.38 Freshwater Flux (mm/d), April

119
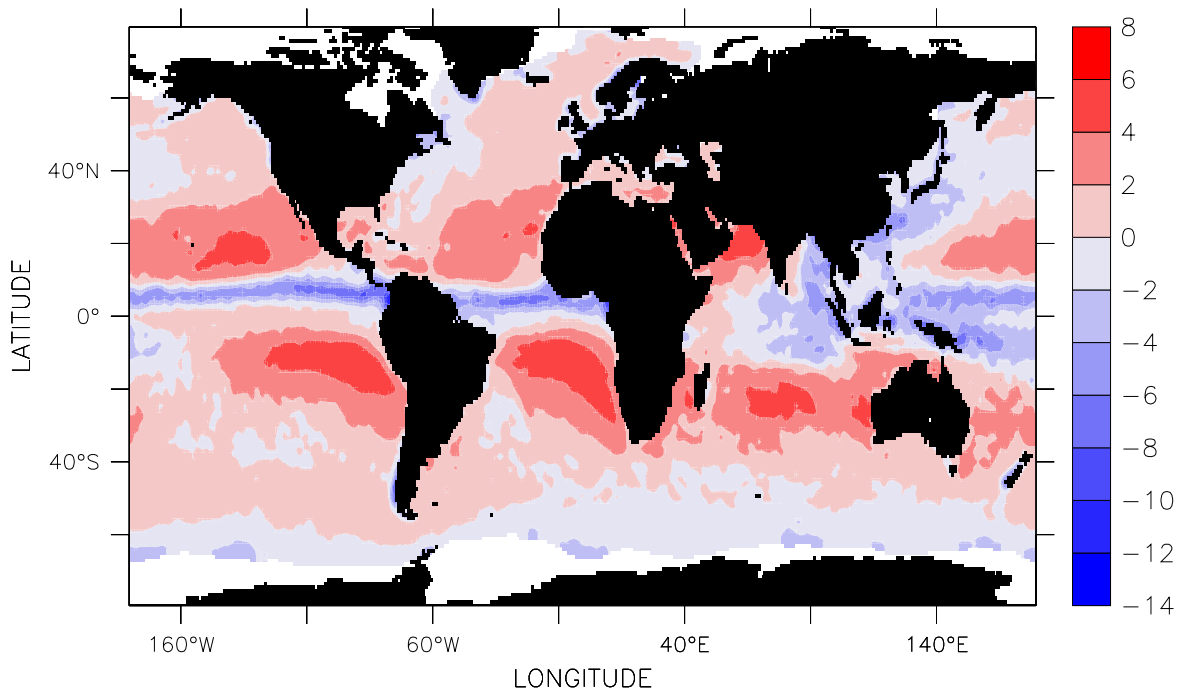
Fig.V.39 Freshwater Flux (mm/d), May
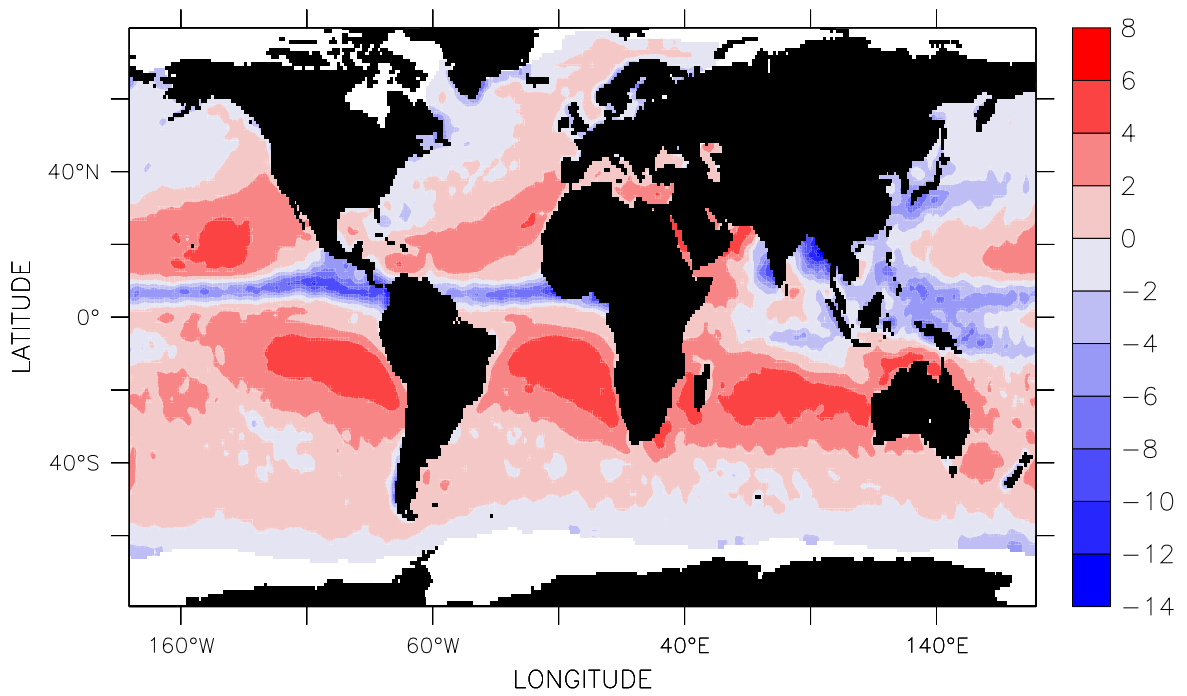
Fig.V.40 Freshwater Flux (mm/d), June

120
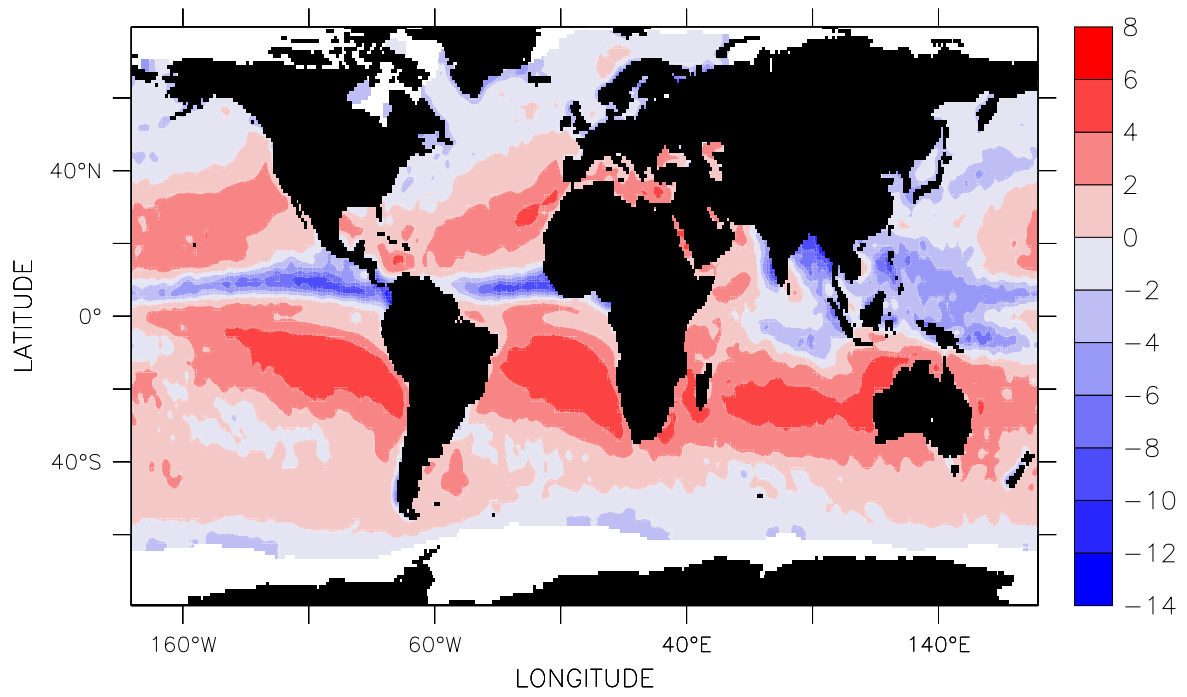
Fig.V.41 Freshwater Flux (mm/d), July
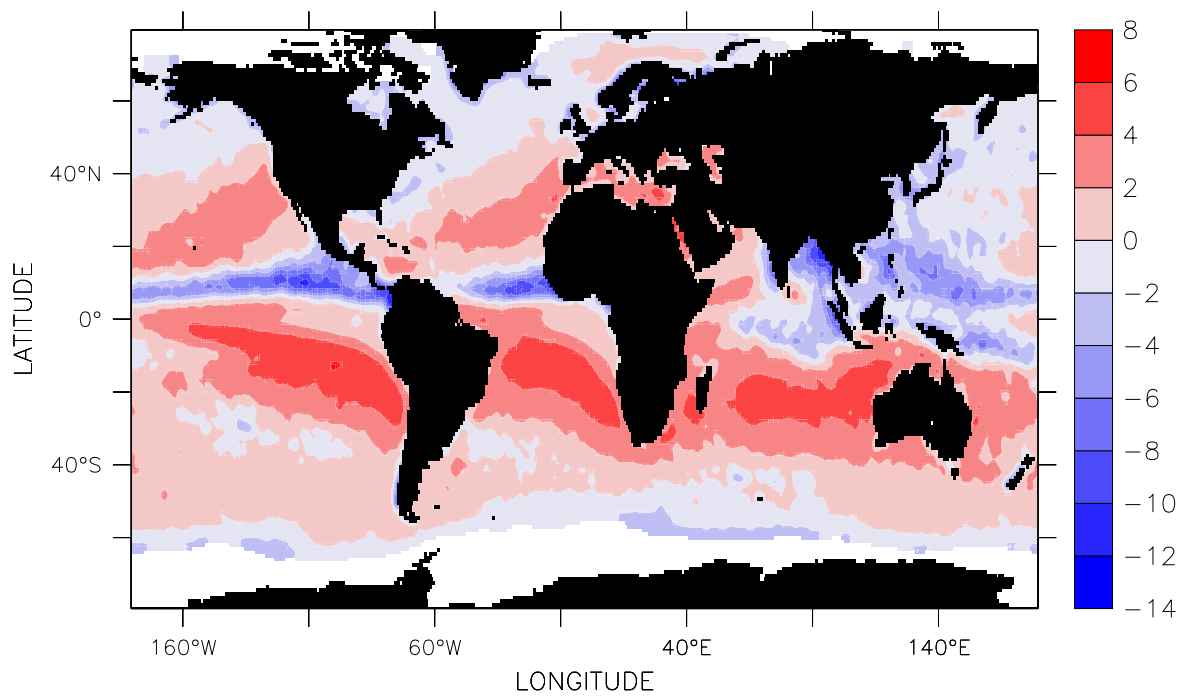
Fig.V.42 Freshwater Flux (mm/d), August

Fig.V.43 Freshwater Flux (mm/d), September
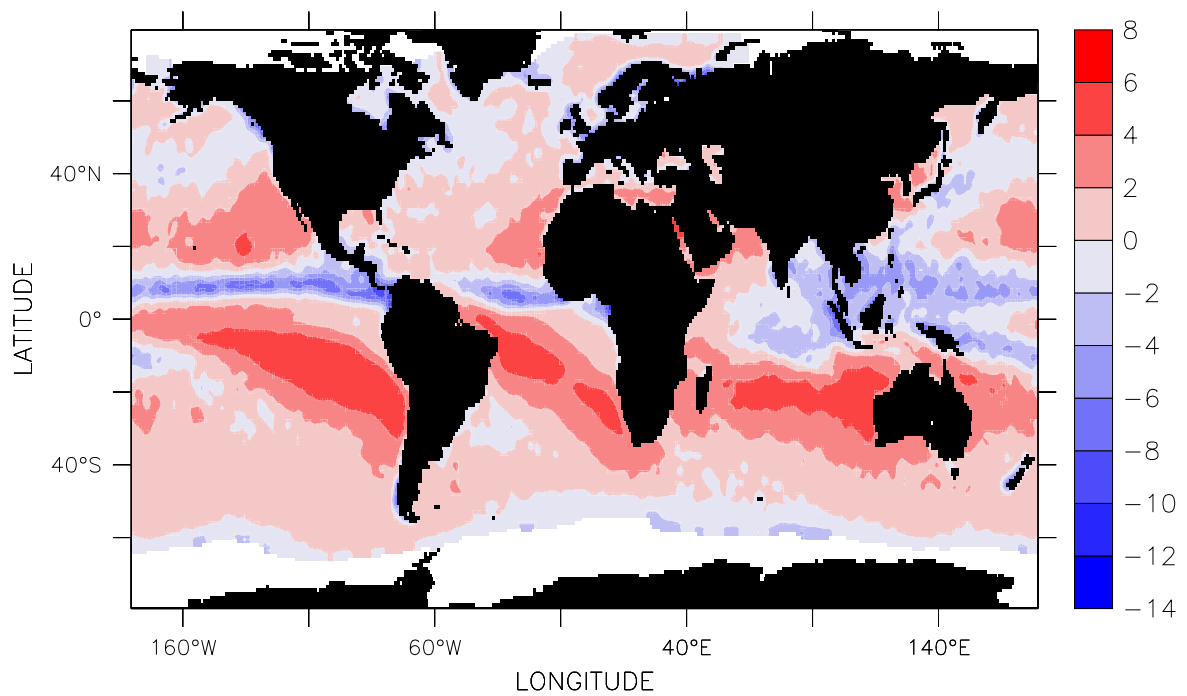
Fig.V.44 Freshwater Flux (mm/d), October
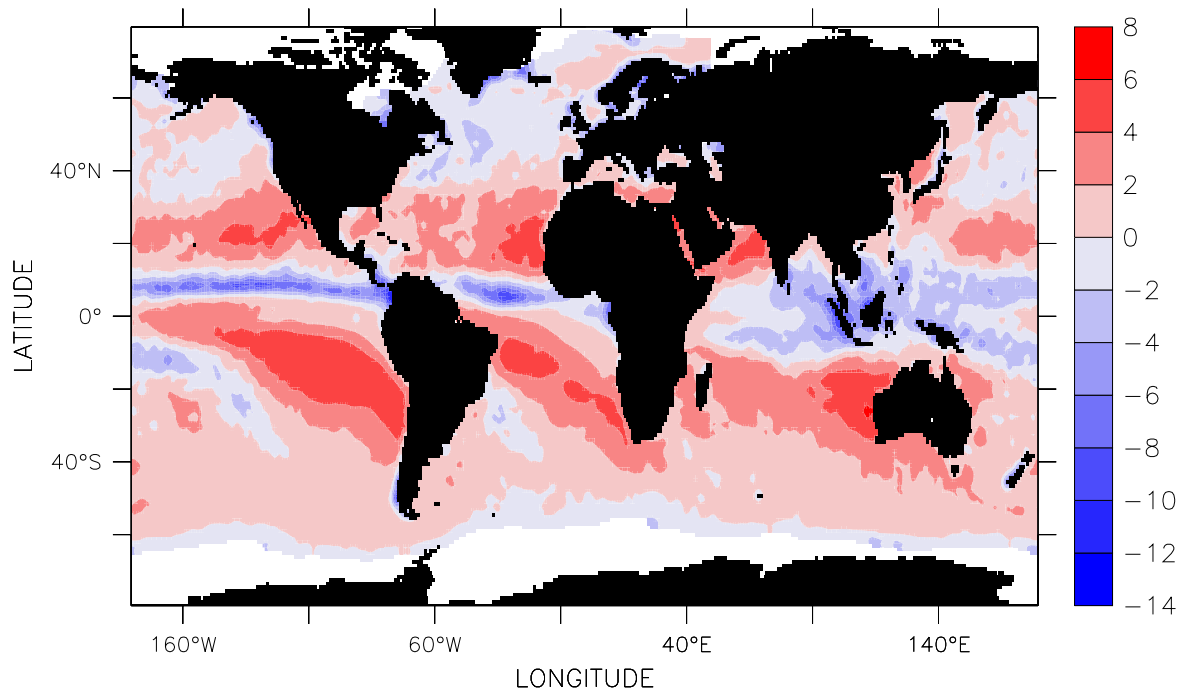
Fig.V.45 Freshwater Flux (mm/d), November
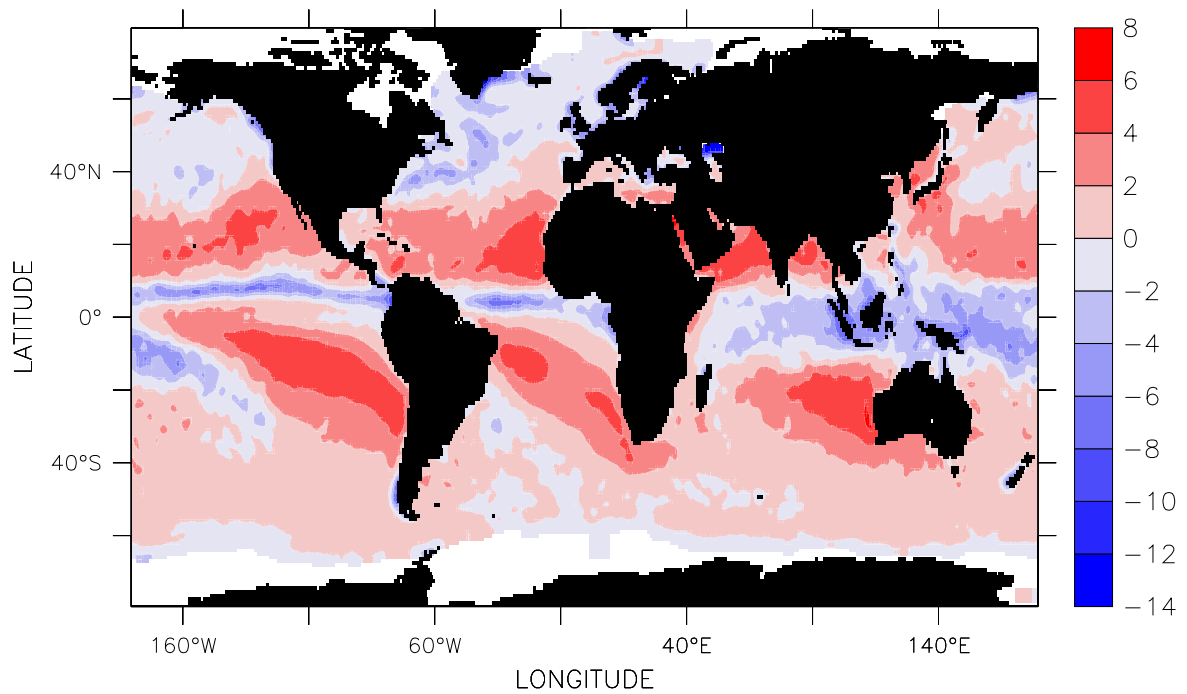
Fig.V.46 Freshwater Flux (mm/d), December
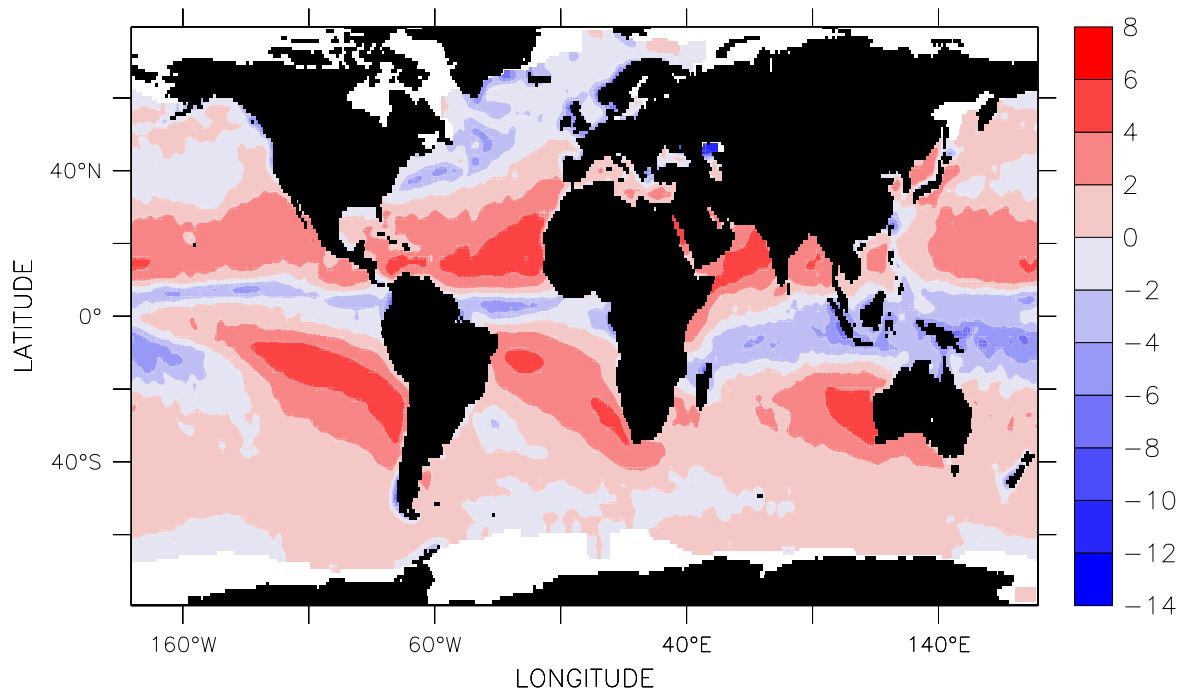
Fig.V.47 Freshwater Flux (mm/d), DJF
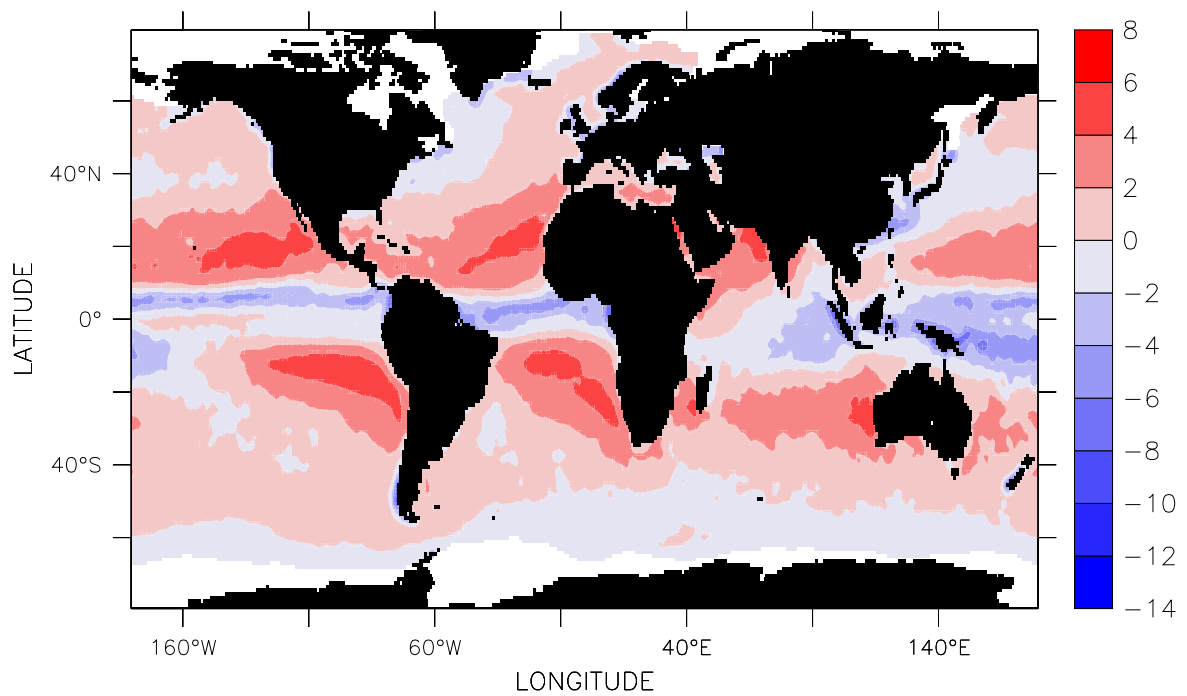
Fig.V.48 Freshwater Flux (mm/d), MAM
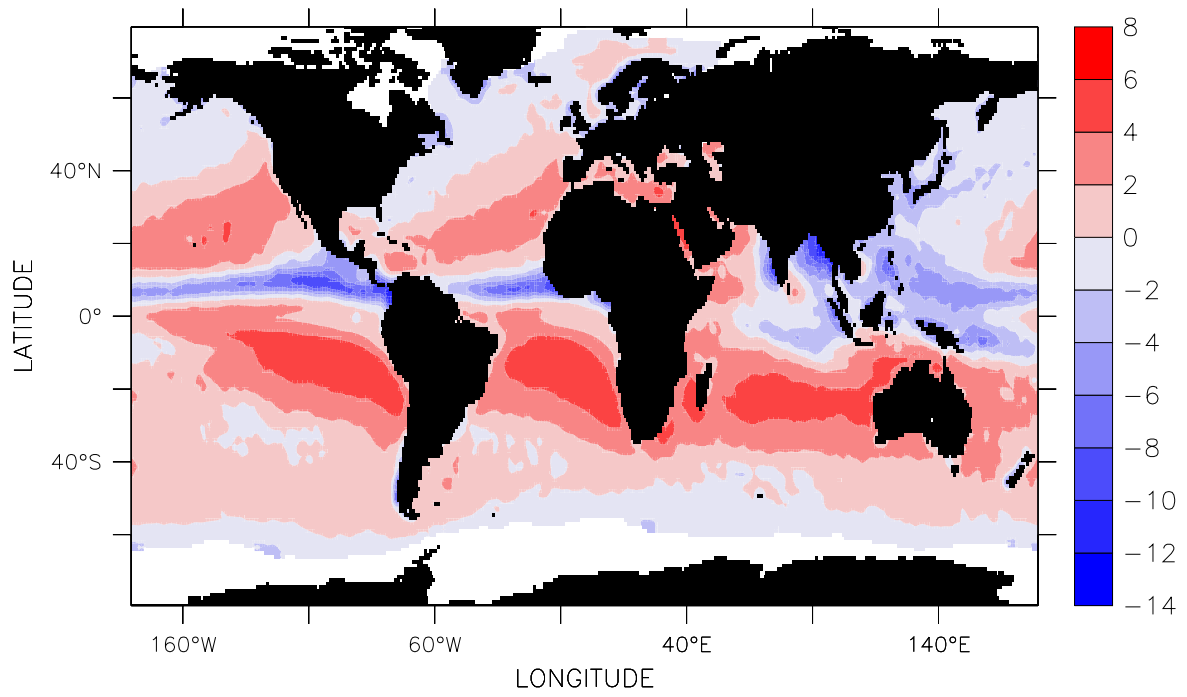
Fig.V.49 Freshwater Flux (mm/d), JJA
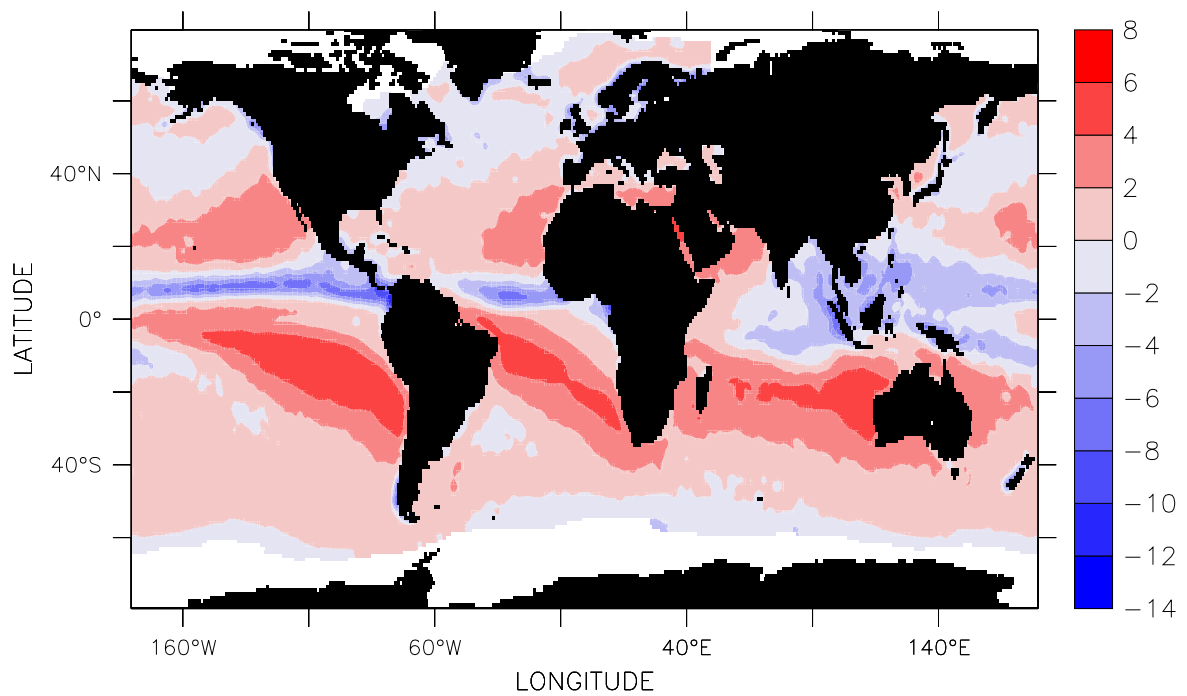
Fig.V.50 Freshwater Flux (mm/d), SON
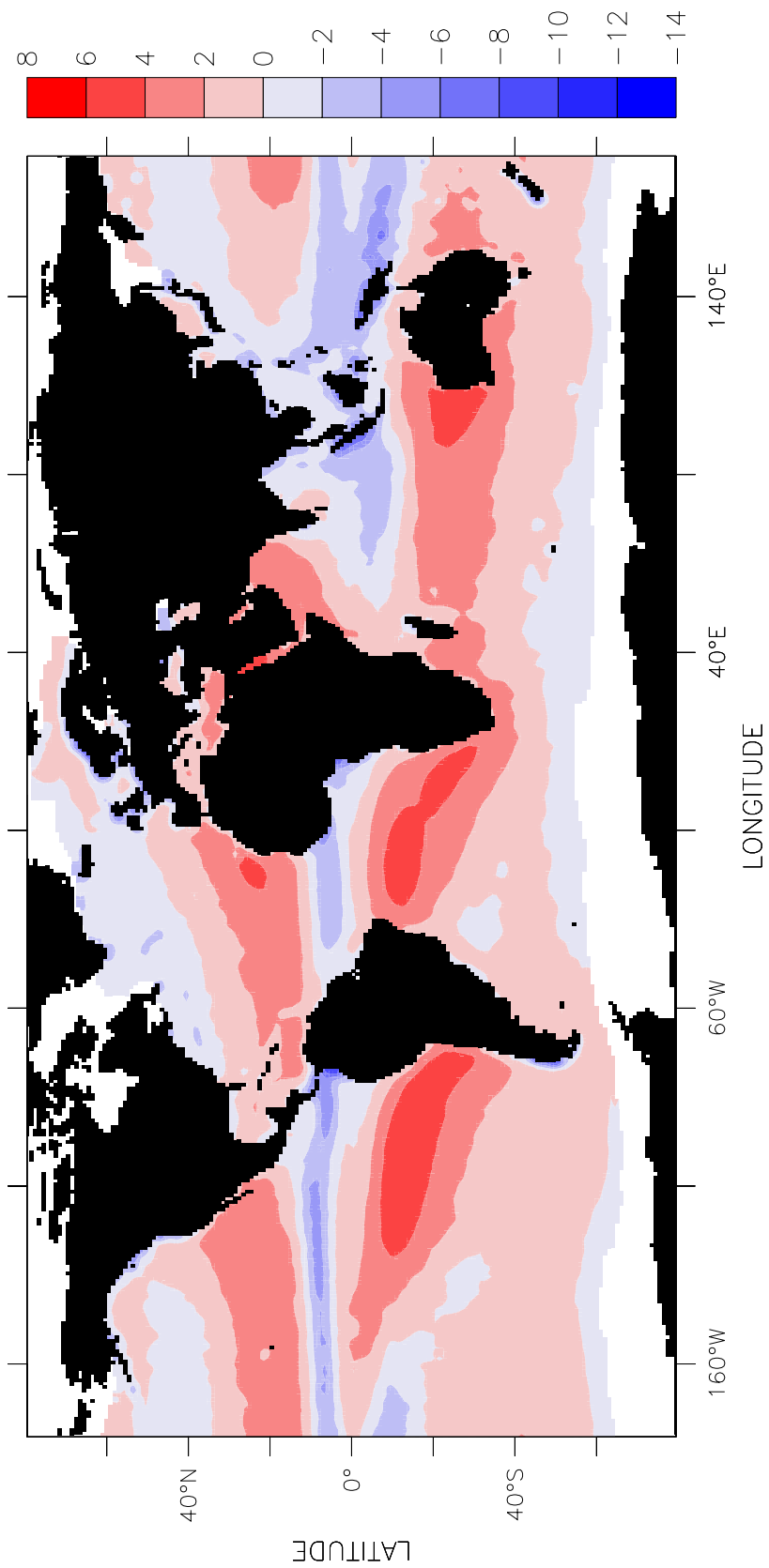
Fig.V.51 Freshwater Flux (mm/d), Annual

Chapter VI   Summary and Conclusions

This atlas presents for the first time a combination of various satellite-derived air-sea interaction parameters such as sea surface te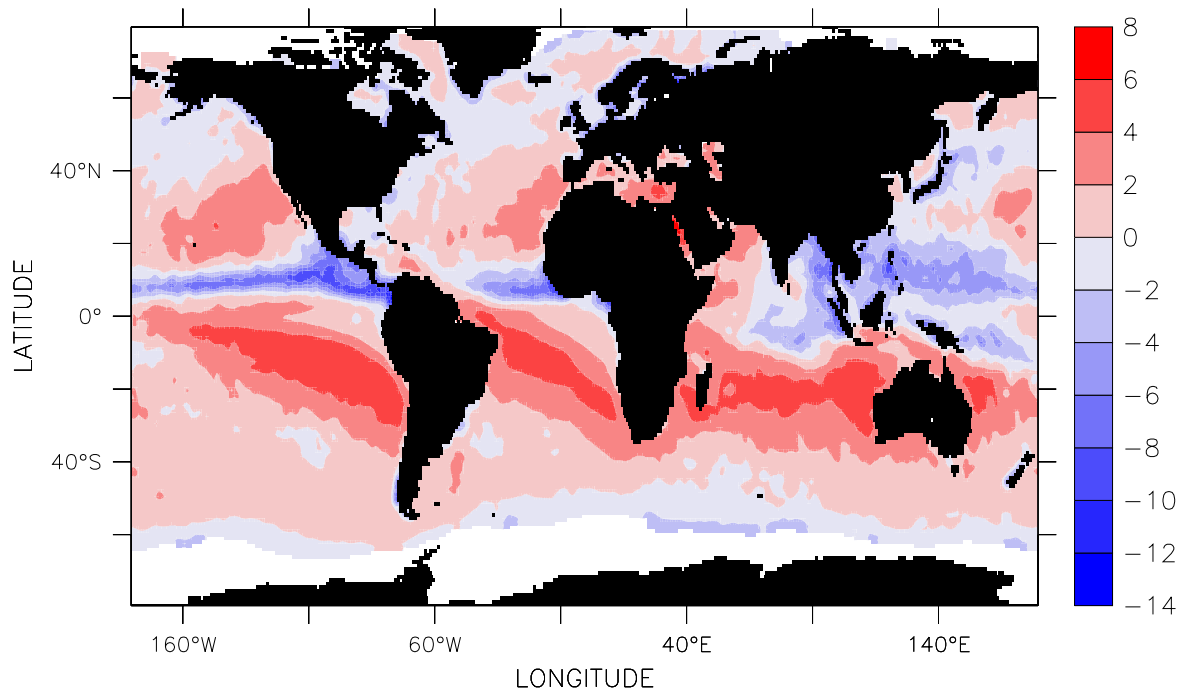mperature, specific humidity at sea surface and air temperatures, difference in humidity, wind speed, Dalton number as well as air-sea fluxes such as latent and sensible heat fluxes and longwave net radiation flux, and the hydrological cycle parameters evaporation, precipitation and freshwater flux derived from satellite data over the ice free global ocean. The instruments used are AVHRR and SSM/I that provide long data records. AVHRR data are only used in the derivation of sea surface temperature. All other parameters are computed from measurements of the SSM/I. The algorithms employed for the instantaneous retrieval and the construction of the monthly fields are explained comprehensively. As shown in several comparison studies the accuracy of the different passive microwave retrievals is sufficient to derive this climatology. The individual monthly and climatological fields have a much better spatial and temporal resolution as compared to conventional in-situ or ship measurements. Further the satellite measurements are well distributed in both space and time which is quite important for giving a meaningful monthly mean as compared to the traditional ship observations. This atlas, we hope will be useful as a reference material for students as well as research scientists who are working in the fields of climatology, meteorology, and oceanography and those engaged in similar activities.

Availability of Fields: The HOAPS climatology is freely available to interested users for non-commercial scientific research. For details of how to access the fields see http://www.mpimet.mpg.de/Depts/Physik/HOAPS.

References

Arkin, P. A., 1979: The relationship between fractional coverage of high cloud amount and rainfall accumulations during GATE over the B-scale array. *Mon. Wea. Rev.*, **107**, 1382-1387.

Arkin, P. A. and B. N. Meisner, 1987: The relationship between large-scale convective rainfall and cold cloud over the Western Hemisphere during 1982-1984. *Mon. Wea. Rev.*, **115,** 51-74.

Bauer, P. and P. Schluessel, 1993: Rainfall, total water, ice water, and water vapour over sea from polarized microwave simulations and Special Sensor Microwave/Imager data. *J. Geophys.Res.*, **98**, 20737-20759.

Baumgartner, A., and E. Reichel, 1975: *The World Water Balance: Mean Annual Global, Continental and Maritime Precipitation, Evaporation and Runoff*, Elsevier, 179 pp.

Berg, W. and R. Chase, 1992: Determination of mean rainfall from the Special Sensor Microwave/Imager (SSM/I) using a mixed lognormal distribution. *J. Atmos. Oceanic Tech.*, **9**, 129-141.

Cavalieri, D. J., P. Gloersen, and W. J. Campell, 1984: Determination of sea ice parameters with the Nimbus-7 SMMR. *J. Geophys. Res.*, **89**, 5355-5369.

Cavalieri, D. J., J. P. Crawford, M. R. Drinkwater, D. T. Eppler, R. R. Farmer, L. D. Jentz, and C. C. Wackermann, 1991: Aircraft active and passive microwave validation of sea ice concentration from Defense Meteorological Satellite Program Special Sensor Microwave/Imager. *J. Geophys. Res.*, **96**, 21989-22008.

Chou, S.-H., R. M. Atlas, C.-L. Shie, and J. Ardizzone, 1995: Estimates of surface humidity and latent heat flux over oceans from SSM/I data. *Mon. Wea. Rev.*, **123**, 2405-2425.

Chou, S.-H., C.-L. Shie, R. M. Atlas, and J. Ardizzone, 1997: Air-sea fluxes retrieved from Special Sensor Microwave/Imager data. *J. Geophys. Res.*, **102**, 12705-12726.

Da Silva, A., C.C.Young and S.Levitus, 1994: *Atlas of Surface Marine Data 1994 Vol.1. Algorithms and Procedure*s. NOAA Atlas NESDIS 6, U.S.Dept. of Commerce, Washington, D.C., 83 pp.

Ebert, E. E., 1996: Results of the 3rd Algorithm Intercomparison Project (AIP-3) of the Global Precipitation Climatology Project (GPCP). Revision 1. BMRC Research Rep. No. 55, 299 pp. [Available from Bureau of Meteorology Research Centre, GPO Box 1289K, Melbourne, Australia 3000.]

Ebert, E. E. and A. J. Manton, 1998: Performance of satellite rainfall algorithms during TOGA/COARE. *J. Atmos. Sci.*, **55**, 1537-1557.

Emery, W. J., Y. Yu, G. Wick, P. Schlüssel and R. W. Reynolds 1994: Correcting infrared satellite estimates of sea surface temperature for atmospheric water vapor contamination, *J. Geophys. Res.*, **99**, 5219-5236.

Fuhrhop, R. and C. Simmer, 1996: SSM/I brightness temperature corrections for incident angle variations. *J. Atm. Oceanic Tech.*, **13**, 246-254.

Gardashov, R. G., K. S. Shifrin, and J. K. Zolotova, 1988: Emissivity, thermal albedo and effective emissivity of the sea at different wind speeds. *Oceanologica Acta*, **11**, 121-124.

Gloersen, P. and D. J. Cavalieri, 1986: reduction of weather effects in the calculation of sea ice concentration from microwave radiances. *J. Geophys. Res.*, **91**, 3913-3919.

Goodberlet, M. A., C. T. Swift, and J. C. Wilkerson, 1989: Remote sensing of ocean surface winds with the Special Sensor Microwave/Imager. *J. Geophys. Res.*, **94**, 14547-14555.

Hastenrath, S., and P. J. Lamb, 1977: *Climatic Atlas of the Tropical Atlantic and Eastern Pacific Oceans*, University of Wisconsin Press, Madison, 340 pp.

Hastenrath, S., and P. J. Lamb, 1978: *Heat Budget Atlas of the Tropical Atlantic and Eastern Pacific Oceans*, University of Wisconsin Press, Madison, 104 pp.

Hastenrath, S., and P. J. Lamb, 1979a: *Climatic Atlas of the Indian Ocean, Part I: Surface Circulation and Climate*. University of Wisconsin Press, Madison, USA.

Hastenrath, S., and P. J. Lamb, 1979b: *Climatic Atlas of the Indian Ocean, Part II: The Oceanic heat budget*, University of Wisconsin Press, Madison, USA.

Hollinger, J. P., R. Lo, G. Poe, R. Savage, and J. Peirce, 1987: Special Sensor Microwave/Imager user's guide. Naval Research Laboratory, Washington, DC, 177 pp.

Isemer, H. J. and L. Hasse, 1987: *Air-Sea Interaction. Vol. 2, the Bunker Climate Atlas of the North Atlantic Ocean*, Springer-Verlag, 252 pp.

Josey S. A., E. C. Kent, and P. K. Taylor, 1999: New insights into the ocean heat budget closure problem from analysis of the SOC air-sea flux climatology. *J. Climate*, **12**, 2856-2880.

Oberhuber, J. M., 1988: An Atlas based on the COADS Data Set: The budgets of Heat, Buoyancy and Turbulent Kinetic Energy at the surface of the Global Ocean. Max-Planck-Institut fur Meteorologie, Rep.No.15

Reynolds, R. W., 1993: Impact of Mount Pinatubo aerosols on satellite-derives sea surface temperatures, *J. Climate*, **6**, 768-774.

Reynolds, R. W. and T. M. Smith, 1994: Improved global sea surface temperature analyses. *J. Climate*, **7**, 929-948.

Schanz, L. and P. Schluessel, 1997: Atmospheric back radiation in the tropical Pacific: Intercomparison of in-situ measurements, simulations, and satellite retrievals. *Meteor. Atmos. Phys.*, **63**, 217-226.

Schluessel, P., 1995: Passive Fernerkundung der unteren Atmosphäre und der Meeresoberfläche aus dem Weltraum. Berichte aus dem Zentrum für Meeres- und Klimaforschung, Reihe A: Meteorologie, 20, 175 pp. [Available from Universität Hamburg Meteorologisches Institut, Bundesstraße 55, D-20146 Hamburg, Germany.]

Schlüssel, P., W. J. Emery, H. Graßl, T. Mammen 1990: On the bulk-skin temperature difference and its impact on satellite remote sensing of sea surface temperature, *J. Geophys.Res.*, **95**, 13341-13356.

Schluessel, P. and H. Luthardt, 1991: Surface wind speeds over the North Sea from Special Sensor Microwave/Imager observations. *J. Geophys.Res.*, **96**, 4845-4853.

Schluessel, P., L. Schanz, and G. Englisch, 1995: Retrieval of latent heat flux and longwave irradiance at the sea surface from SSM/I and AVHRR measurements. *Adv. Space Res.*, **16**, (10)107-(10)116.

Schulz, J., P. Schluessel and H. Grassl, 1993: Water Vapour in the atmospheric boundary layer over oceans from SSM/I measurements. *Int. J. Remote Sens.*, **14**, 2773-2789.

Schulz, J., J.Meywerk, S. Ewald and P. Schluessel, 1997: Evaluation of satellite derived latent heat fluxes. *J. Climate*, **10**, 2782-2795.

Schulz, J., V. Jost and S. Bakan., 1998: A New satellite derived freshwater flux climatology (Hamburg Ocean Atmosphere Parameters and Fluxes from Satellite Data). *International WOCE Newsletter*, **32**, 20-26.

Smith, S. D. (1988): Coefficients for sea surface wind stress, heat flux, and wind profiles as a function of wind speed and temperature. *J. Geophys. Res.*, **93**, 2859-2874.

Smith, E., X. Xiang, A. Mugnai, and G. I. Tripoli, 1994: design of an inversion-based precipitation profile retrieval algorithm using an explicit cloud model for initial guess microphysics. *Meteor. Atmos. Phys.*, **54**, 53-78.

Smith E., J. Lamm, R. Adler, J. Alishouse, K. Aonashi, E. Barrett, P. Bauer, W. Berg, A. Chang, R. Ferraro, J. Ferriday, S. Goodman, N. Grody, C. Kidd, C. Kummerow, G. Liu, F. Marzano, A. Mugnai, W. Olson, G. Petty, A. Shibata, R. Spencer, F. Wentz, and T. A. Wilheit, 1998: Results of the WetNet PIP-2 project. *J. Atmos. Sci.*, **55**, 1483-1536.

Stogryn, A. P., C. T. Butler, and T. J. Bartolac, 1994: Ocean surface wind retrievals from Special Sensor Microwave/Imager data with neural networks. *J. Geophys. Res.*, **99**, 981-984.

Taurat, D., 1996: Windfelder über See unter Verwendung von Satellitendaten und Druckanalysen, Berichte aus dem Zentrum für Meeres- und Klimaforschung, Reihe A: Meteorlogie, 22. [Available from Universität Hamburg Meteorologisches Institut, Bundesstraße 55, D-20146 Hamburg, Germany.]

Walton, C. C., 1988: Nonlinear multichannel algorithms for estimating sea surface temperature with AVHRR satellite data. *J. Appl. Meteor.*, **27**, 115-124.

Wentz, F. J., 1991: User's manual SSM/I antenna temperature geophysical tapes, tech. Rep. 120191, Remote Sensing Systems, Santa Rosa, California, US.

Wilheit, T. A., T. C. Chang, and L. S. Chou, 1991: Retrieval of monthly rainfall indices from microwave radiometry measurements using probability functions. *J. Atmos. Oceanic Tech.*, **8**, 118-136.